Optical Sum-Frequency Response of Lattice Vibrations and Pulse Timing at a Free-Electron Laser

Dissertation

zur Erlangung des Grades eines
Doktors der Naturwissenschaften
(Dr. rer. nat)

am Fachbereich Physik
der Freien Universität Berlin

vorgelegt von

Riko Kießling

Berlin 2019

This work was conducted in the Lattice Dynamics Group (Dr. Alexander Paarmann) of the Department of Physical Chemistry (Prof. Dr. Martin Wolf) at the Fritz Haber Institute of the Max Planck Society in Berlin between June 2015 and November 2019.

Erstgutachter: Prof. Dr. Martin Wolf
Zweitgutachter: Prof. Dr. Joachim Heberle

Tag der Disputation: 18.08.2020

Abstract

The vibrational characteristics of solids and interfaces are determined by the dynamics of the underlying atomic structures. Via resonant interaction, optical fields allow access to these fundamental low-energy excitations, and hence information about the interatomic bonding and structural phases. As a vibrational and interface-sensitive probe, sum-frequency generation (SFG) spectroscopy has emerged as valuable nonlinear optical technique. Combined with the brilliance and spectral tunability of free-electron laser-based infrared (IR) radiation, a variety of vibrational modes comes into reach.

In this thesis, an experimental infrared-visible SFG setup at an accelerator-driven free-electron laser (FEL) has been implemented and applied. First, the characteristics of the coherent radiation sources and their relative pulse timing are examined. Based on balanced optical cross-correlation (BOC), the jitter between the synchronized fs table-top and mid-IR FEL pulses is determined to be about 100 fs. Arrival time drifts are correlated to the energy fluctuations of the accelerated electron bunches. The micro-/macro-pulse structure of the FEL oscillator emission is studied in detail as function of the cavity length detuning. In the limit-cycle regime, pronounced optical sub-pulses within the picosecond-short FEL micro-pulse are observed. The experimental findings are in line with theoretical calculations based on classical Maxwell-Lorentz electrodynamics.

Second, zone-center optical phonons in polar dielectric crystals with broken inversion symmetry are investigated by SFG spectroscopy. Simultaneous IR and Raman activity of the vibrational modes causes a resonant enhancement of the second-order susceptibility. Linear optical effects (e.g. Reststrahlen bands) are found to strongly modify the sum-frequency response. The phase mismatch of the interacting optical waves determines the coherence length within the sample bulk, limiting SFG emission to a some micrometer thin layer. Both for silicon carbide and α-quartz, SFG spectra are well described by an analytical model taking into account all contributions. Symmetry properties of the $\chi^{(2)}$ tensor are revealed by polarization- and azimuth-dependent measurements.

Further, the possibility to modify the mid-IR response by localized phonon polaritons is explored in sub-diffractional dielectric nanostructures. Modifications of spectral position and amplitude of the modes are observed in dependence on the geometry and arrangement of the nanoresonator structures. A scanning-probe approach of tightly focused laser beams is used to spatially resolve the polariton-caused local electric field enhancement, and thus increased SFG intensity, at different resonant IR frequencies. In contrast to linear IR reflectance imaging, the second-oder response in SFG microscopy provides improved lateral resolution with vibrational contrast.

Finally, the temporal resolution provided by the short IR and visible pulses is utilized in time-domain SFG experiments, complementing the frequency-resolved spectra. Taking advantage of the BOC-based timing correction, the free-induction decay of the induced coherent IR polarization within a dielectric material is disclosed on a ps time scale. Excitation close to an optical resonance revealed a pronounced slowdown of the dephasing dynamics compared to the non-resonant case. Transient SFG spectra showed a narrowing of the linewidth at increased pulse delays, enhancing the spectral sensitivity to modes being close together in frequency.

The presented work lays the ground for FEL-based vibrational SFG spectro-microscopy, ultimately reaching interface-sensitivity with lateral resolution below the IR diffraction limit.

Kurzfassung

Die Schwingungseigenschaften von Festkörpern und Grenzflächen sind durch die Dynamik der zugrunde liegenden atomaren Struktur bestimmt. Mittels resonanter Wechselwirkung erlauben optische Felder Zugang zu diesen niederenergetischen Anregungen und somit Aussagen über die chemische Bindung und strukturelle Phasen. Aufgrund der Schwingungs- und Grenzflächen-Sensitivät ist die Summenfrequenzerzeugungs (SFG)-Spektroskopie eine nützliche nichtlineare optische Methode. Kombiniert mit der Brillanz und Abstimmbarkeit der Freie-Elektronen-Laser-basierten Infrarot (IR)-Strahlung werden eine Vielzahl von Moden erfassbar.

In der vorliegenden Arbeit wurde ein experimenteller Infrarot-Sichtbar-SFG-Aufbau an einem Beschleuniger-betriebenen Freie-Elektronen-Laser (FEL) implementiert und angewendet. Zuerst wurden die Charakteristika der kohärenten Strahlungsquellen und ihr relatives Puls-Timing untersucht. Basierend auf symmetrischer optischer Kreuzkorrelation (BOC) wurde der Jitter zwischen den synchronisierten fs-Labor- und mittleren Infrarot-FEL-Pulsen zu etwa 100 fs bestimmt. Zeitliche Drifts sind korreliert zu den Energiefluktuationen der beschleunigten Elektronenpakete. Die Mikro-/Makro-Puls-Struktur der FEL-Oszillator-Emission wird als Funktion der Kavitätslänge studiert. Im Grenzzyklus-Regime wurden ausgeprägte Sub-Pulse beobachtet. Die experimentellen Ergebnisse stimmen mit klassischen Elektrodynamik-Berechnungen überein.

Zweitens wurde optische Phononen in polaren Dielektrika mit gebrochener Inversionssymmetrie mittels SFG-Spektroskopie untersucht. Bei gleichzeitiger IR- und Raman-Aktivtät der Moden wird eine resonante Verstärkung der Suszeptibilität zweiter Ordnung beobachtet. Lineare optische Effekte (z.B. Reststrahlen-Bänder) modifizieren den Summenfrequenz-Respons. Die Phasendifferenz der beteiligten optischen Wellen limitiert die Kohärenzlänge innerhalb des Kristalls und somit die SFG-Emission auf eine wenige Mikrometer-dünne Schicht. Sowohl für Siliziumkarbid als auch α-Quarz konnten die SFG-Spektren durch ein analytisches Modell beschrieben werden. Die Symmetrie des $\chi^{(2)}$-Tensors wurde durch polarisations- und azimutabhängige Messungen aufgedeckt.

Weiterhin wird gezeigt, dass lokalisierte Phonon-Polaritonen in subdiffraktionalen dielektrischen Nanostrukturen den Respons im mittleren IR modifizieren. In Abhängigkeit von Geometrie und Anordnung der Nanoresonatoren werden Änderungen der spektralen Position und Amplitude der Moden beobachtet. Ein Rastersonden-Ansatz mit fokussierten Laserstrahlen wird verwendet, um die Polariton-bedingte lokale elektrische Feldverstärkung, resultierend in erhöhter SFG-Intensität, räumlich bei verschiedenen resonanten IR-Frequenzen aufzulösen. Im Gegensatz zur linearen IR-Reflektivität erlaubt der Respons zweiter Ordnung in der SFG-Mikroskopie eine bessere laterale Auflösung mit Schwingungskontrast.

Schließlich wird die kurze Dauer der IR- und VIS-Pulse in Zeitdomänen-SFG-Experimenten eingesetzt, ergänzend zu den frequenzaufgelösten Spektren. Unter Nutzung der BOC-basierten Zeitversatz-Korrektur wird der freie Induktionszerfall der induzierten kohärenten IR-Polarization im Dielektrikum auf der ps-Zeitskala gezeigt. Anregung nahe einer optischen Resonanz ergab eine deutlich verlangsamte Dephasierungsdynamik im Vergleich zum nicht-resonanten Fall. Transiente SFG-Spektren zeigten eine schmalere Linienbreite bei großem Pulsversatz und erhöhen damit die Sensitivität für spektral nah beieinander liegende Moden.

Diese Arbeit legt die Grundlage für FEL-basierte Schwingungs-Spektromikroskopie, um Grenzflächen-Sensitivität mit lateraler Auflösung unterhalb des IR-Beugungslimits zu erhalten.

Contents

1 Introduction

Nowadays, research in the natural sciences is becoming increasingly interdisciplinary. Among the branches of physics, condensed matter science has a prominent role and multiple connenctions to neighboring fields, such as materials science, chemistry and quantum physics. The practical application of the obtained fundamental understanding enables new technologies and thus, new methods for experimental and theoretical investigations. Within the last decades, research on matter has been focused increasingly on very short length and time scales, enabling nanotechnology and bringing this into everyone's life.

In a microscopic view, solid-state materials are not at rest at elevated temperatures. Instead, finite vibrational motions at the atomic level give rise to several physical properties. Thus, insights into the appearance and behavior of lattice dynamical modes are of crucial interest. Fundamental phenomena like thermal transport, phase transitions and scattering processes of electrons and light waves are related to phonons [Bar01]. The ongoing developments in optics and electronics towards nanoscale architectures entail alterations of the physical properties in reduced dimensions due to quantum confinement effects for electronic [Ali96] as well as lattice excitations [Sch00]. Besides advances in microscopic theory, experimental examinations are vital for proper understanding of the vibrational characteristics and, hence, interatomic forces.

Due to the interaction of lattice vibrations with photons, taking into account certain selection rules, optical spectroscopies are a suitable way to probe these quantum particles. On the other hand, the optical behavior of materials can be modified on the basis of coupled light-matter excitations, so-called phonon polaritons [Hil02; Dai14]. There, the energy of an optical wave is exchanged with a electric dipole-carrying phonon. Thus, user-defined nanostructures made of polar dielectric crystals have emerged as promising tools for the manipulation of light on length scales smaller than the optical wavelength [Li15]. Due to the characteristic energy of phonons of some tens of meV, phonon-based nano-photonic devices are highly beneficial for the control and manipulation of optical fields at IR and THz frequencies [Cal15]. Applications in e.g. molecular sensing [Aut18], waveguiding [Dai15], thermal emitters [Gre02] and nano-optical antennas [Tam18] show the potential of phonon polaritons.

A broad range of experimental optical techniques allows to gather information not only about the energy and lifetimes of vibrational modes in solids, clusters and (bio-)molecules, but also gives access to dielectric properties and nonlinear susceptibilities. In particular, infrared (IR) - visible (VIS) sum-frequency generation (SFG) spectroscopy has emerged

as workhorse technique to identify vibrational dynamics in bulk media, at interfaces and of molecular adsorbates [She89; Vid05]. Due to the inherent symmetry sensitivity, interface-specific measurements are readily obtained, in contrast to linear optical techniques. Concerning the increased surface-to-volume ratio in low-dimensional material systems, the impact of interface states is particular relevant. Also, due to the selection rules for the SFG activity of vibrational modes, complementary information to IR and Raman experiments are revealed. Moreover, the characteristic fingerprint response of molecular species allows for chemical sensitivity. Various fields have benefited from vibrational SFG spectroscopy, for instance heterogeneous catalysis [Fre11], environmental science [Ric02] or electrochemistry [Liu14].

The enormous developments in laser-based coherent light sources facilitate today reliable spectroscopic studies in an extremely broad spectral range, reaching from hard X-rays to long-wavelength THz radiation. Notably, free-electron lasers (FELs) provide intense optical fields covering a wide, continuously tunable frequency region [McN10]. Regarding vibrational SFG spectroscopy, resonant mid- to far-IR photons from FELs profit from the high peak brilliance, making them ideal candidates for nonlinear optical experiments. Comparable table-top sources are still lacking in that frequency window. In addition, short IR pulses of ps to fs duration can be created at FELs, corresponding to few cycles of the electric field [Kni95]. Such light bursts allow for time-resolved investigations, such as ultrafast surface dynamics or chemical reactions.

Since free-electron lasers are accelerator-based facilities, profound knowledge about the interaction of charged relativistic particles with electromagnetic radiation is required to deliver ultrashort and coherent light pulses. After demonstration of generating spontaneous synchrotron radiation from an electron beam in a magnetic undulator field [Mad71], much technical work has been devoted to the development and optimization of the collective electron bunching process [McN10], essential for the creation of coherent optical fields [Dea77]. As fourth generation accelerator-driven light source, FELs are nowadays able to provide highly brilliant radiation at wavelengths down to 1 Å and pulse durations of 10 fs [Ney18]. Such extreme time scales demand for precise sychronization of the accelerator components and external laser systems when using two-color spectroscopy. Hence, advanced techniques for a priori setting or a posteriori determination of the pulse timing have to be employed, enabling e.g. single-shot X-ray crystallography for structure exploration [Cha11] or ultrafast pump-probe spectroscopy of non-equilibrium processes [Mit15].

This work wants to add a contribution by enabling nonlinear vibrational optical spectroscopy using FEL-based IR excitation and investigating the sum-frequency response of optical phonons and phonon polaritons. To this end, the necessary experimental techniques are implemented, in particular allowing for precise temporal tracking of the accelerator-driven IR pulses. Further, the imprint of resonant lattice vibrations of polar dielectric materials on spectrally, temporal and spatially resolved sum-frequency emission processes will be studied.

First, the theoretical and experimental fundamentals of the used ingredients are presented (Chap. 2), encompassing lattice dynamics, linear and nonlinear light-matter interaction as well as the concepts of vibrational SFG spectroscopy and coherent radiation emission from a free-electron laser. Next, details of the developed experimental system are described (Chap. 3), in particular the characteristics of the employed IR free-electron laser oscillator, the technique of pulse synchronization with a femtosecond table-top light source and the SFG setup for FEL pulse characterization as well as phonon spectroscopy.

The relative timing between synchronized accelerator-based and external source optical pulses is examined by the method of balanced optical cross-correlation. Based on phase-matched SFG from a strongly nonlinear medium, direct conversion of the measured observable to the desired timing information on a single-shot level is achieved. Thus, statistical statements about short- and long-term temporal fluctuations are obtained (Chap. 4). Moreover, pulse envelope and bandwidth of the ps-short FEL radiation have been analyzed. Pronounced features of sub-pulse formation are experimentally observed, corroborated by classical electrodynamics simulations. The consequential intensity oscillations are related to the combination of slippage and cavity detuning effects in the IR FEL oscillator (Chap. 5).

Regarding the spectroscopic studies, the different contributions to the SFG response from polar dielectric phonon systems are investigated at first. Besides the resonant enhancement of the nonlinear susceptibility, lattice vibrations are found to significantly modulate the Fresnel behavior and coherence length of the SFG process within the bulk material (Chap. 6). Further, localized surface phonon polaritons in sub-diffractional nanostructures are explored to modulate the nonlinear behavior at solid interfaces. Modifications of the amplitude and spectral position of the sum-frequency emission due to the polariton mode are found to depend on the geometry of the structures (Chap. 7).

Subsequently, the confinement of the optical field on the micron length scale is revealed by means of SFG scanning probe imaging. Utilizing the advantage of nonlinear optical microscopies to provide lateral resolution below the incident radiation free-space wavelength, IR polaritonic resonances are mapped out in the far-field with spectral contrast (Chap. 7). Finally, the dephasing dynamics of the FEL-induced polarization is probed in the time-domain, providing insights into the free-induction decay of the IR polarization (Chap. 8). Transient SFG spectra with different time delays after IR excitation reveal a resonance narrowing, thus enhanced spectral sensitivity.

2 Fundamentals

In the following, the basic concepts necessary for the optical spectroscopy of lattice vibrations in solid-state materials are introduced. Besides pure phonons in polar dielectric crystals, polaritonic modes are discussed. Linear as well as nonlinear light-matter interaction processes are described, relevant for the technique of vibrational IR-VIS sum-frequency generation spectroscopy. Further, the underlying principle of a free-electron laser oscillator will be presented.

2.1 Lattice Dynamics: Phonons

2.1.1 General Concept

For any solid material, the constituting components are the atoms, connected via chemical bonds. Besides the atomic specifications, the nature of the binding mechanism – for instance, ionic, van der Waals, or metallic interatomic forces – has a pronounced impact on the physical properties of the solid. Typically, one cubic centimeter of solid-state matter is made up of $1/a^3 \sim 10^{22}$ atoms, with an atomic spacing a being in the range of a few angstroms [Kit05]. The periodic arrangement of the elemental atoms in crystalline solids allows a rather strict mathematical treatment of the material's microscopic properties. Spatial symmetries are utilized to classify three-dimensional crystals according to their static geometry in one of the seven lattice families or, more finely, in one of the 230 existing crystallographic space groups. Thereby, the lattice is a reduction of the real crystal structure – featuring certain defects and irregularities – to a perfect mathematical construct.

The dynamics of the lattice is responsible for several fundamental effects of condensed matter, such as thermal expansion, electrical resistance or superconductivity [Kit05]. By the term lattice dynamics one characterizes the small oscillatory displacement of the bound atoms around their equilibrium positions [Bor98]. At room temperature, the vibrational amplitudes are in the order of 0.1 Å [Rei73], i.e. smaller than $a/10$. The first postulation of quantizied crystal vibrations has been given by A. Einstein in 1907 [Ein07]. Soon later, Born and von Kármán carried out a detailed description of the dynamical lattice model [Bor12]. A modern and elegant treatment of the atomic-scale crystal dynamics is given by the second quantization formalism in the quantum-mechanical analysis [Rei73; Kit05]. The principal ansatz to find the vibrational modes of a solid lies in the disentanglement of the lattice and electronic degrees of freedom. This adiabatic or Born-Oppenheimer approximation allows to determine the atomic nuclei dynamics while leaving the electron system in the ground state. Now, consider a three-

dimensional harmonic potential $\mathcal{V}(\boldsymbol{x}^2)$ governing the motion of each of pN atoms (mass m) within the crystal. Then, the Hamiltonian reads

$$\mathcal{H} = \mathcal{T} + \mathcal{V} = \sum_{i=1}^{pN} \frac{\hat{\boldsymbol{p}}_i^2}{2m} + \frac{1}{2} m\omega^2 \hat{\boldsymbol{x}}_i^2, \tag{2.1}$$

where $\hat{\boldsymbol{x}}$ denotes the real-space atomic displacement and $\hat{\boldsymbol{p}}$ its momentum. In reciprocal space, the normal-mode coordinates $\hat{\boldsymbol{q}}_{\boldsymbol{q}}$, $\hat{\boldsymbol{p}}_{\boldsymbol{q}}$ are obtained by Fourier transformation. Usage of the creation and annihilation operators, defined as $\hat{\boldsymbol{a}}^\dagger = \sqrt{m\omega/(2\hbar)}(\hat{\boldsymbol{q}}_{\boldsymbol{q}} - \mathrm{i}\hat{\boldsymbol{p}}_{\boldsymbol{q}}/(m\omega))$ and $\hat{\boldsymbol{a}} = \sqrt{m\omega/(2\hbar)}(\hat{\boldsymbol{q}}_{\boldsymbol{q}} + \mathrm{i}\hat{\boldsymbol{p}}_{\boldsymbol{q}}/(m\omega))$, respectively, gives

$$\mathcal{H} = \sum_{\boldsymbol{q},p} \hbar\omega_{\boldsymbol{q}} \left(\hat{\boldsymbol{a}}^\dagger \hat{\boldsymbol{a}} + \frac{1}{2} \right). \tag{2.2}$$

This form of the Hamiltonian is equivalent to a set of independent harmonic oscillators, where the summation includes all wavevectors $|\boldsymbol{q}| = 2\pi m/Na$ with $m = 0, \pm 1, ..., \pm N/2$ and branches p (see below). Then, the energy eigenvalues of the stationary problem $\mathcal{H}\,|n\rangle = E\,|n\rangle$ are

$$E = \sum_{\boldsymbol{q},p} \hbar\omega_{\boldsymbol{q},p} \left(n_{\boldsymbol{q},p} + \frac{1}{2} \right). \tag{2.3}$$

Therefore, the energy of the collectively oscillating atoms is given in multiples of the quantum $\hbar\omega$: the phonon, which describes the particle-like nature of the lattice vibration. The discrete excitation of the crystal vibrational state $|n\rangle$ is characterized by the quantum number $n = 0, 1, 2, \ldots$. Thus, even the ground-state level $|0\rangle$ possesses a finite zero-point energy. In terms of the real-space dynamics, the larger the phonon population of the mode $\omega_{\boldsymbol{q}}$, the stronger is the mean-square displacement of the atoms, $\langle \hat{\boldsymbol{x}}^2 \rangle \propto n$ [Rei73].

Of particular interest, the relation between wavevector and mode frequency, $\omega(\boldsymbol{q})$, equivalent to momentum $\hbar\boldsymbol{q}$ versus energy $\hbar\omega$, is described by the phonon dispersion. Due to the translational crystal periodicity, consideration of only the first Brillouin zone of the reciprocal lattice is sufficient to display all feasible modes of the vibrational spectrum [Kit05]. In general, the eigenvalues of the Hamiltonian Eq. (2.1) depend on the form of the potential energy $\mathcal{V}(\boldsymbol{x}^2)$, or the strength of the interatomic force constant $f = \partial^2\mathcal{V}/\partial x^2$, respectively. Depending on the number of atoms p per unit cell of the crystal, $3p$ distinct dispersion branches exist; the pre-factor is due to the number of polarizations possible for an elastic wave within three-dimensional space (one longitudinal, two transverse).

The three lowest-energetic modes constitute the acoustic phonons [Bor98], whose dispersion

$$\omega_{\mathrm{ac}}(\boldsymbol{q}) = v_{\mathrm{g}}|\boldsymbol{q}| \tag{2.4}$$

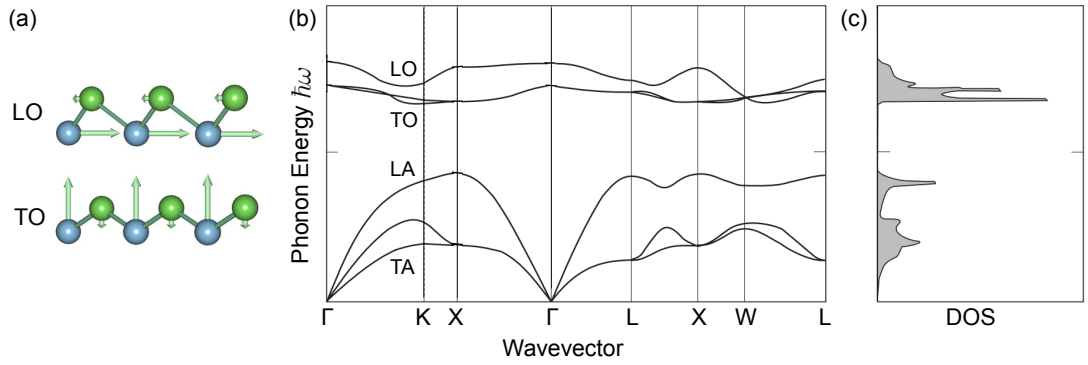

Fig. 2.1 Lattice vibrations of a diatomic cyrstal. (a) Real-space motion of the two different atom types (masses) in the longitudinal and transversal optical phonon mode at the Γ point. (b) Typical dispersion relation of optical and acoustic phonon branches in momentum space, shown for the entire first Brillouin zone of a simple diatomic cyrstal lattice. Longitudinal and transversal optical (acoustic) modes are labeled as TO and LO (TA and LA), respectively. (c) Corresponding phonon density of states (DOS), exhibiting van Hove singularities. Graphs are taken from Ref. [Mad01], based on *ab initio* calculations [Gia91]. A visualization of the lattice vibrations for other wavevectors and phonon modes of (b) can be found in Ref. [Per19a].

depend linearly on the wavevector close to the origin of the Brillouin zone. Furthermore, the slope, being equal to the group velocity $v_\mathrm{g} = \mathrm{d}\omega/\,\mathrm{d}q = a\sqrt{f/m}$, is decisive for the propagation speed of sound waves within solid material. For a diatomic basis ($p = 2$), this one has the value $v_\mathrm{g} = a\sqrt{f/2(m_1 + m_2)}$, with adjacent atoms oscillating in phase in the long-wavelength limit [Kit05; Bor98].

The remaining $3p - 3$ higher-frequency branches are called optical phonons, only present for non-monoatomic unit cells. In the center of the reciprocal space $\boldsymbol{q} = \mathbf{0}$, denoted by the Γ point, the optical phonon dispersion is characterized by a constant frequency, which is, for instance in the case $p = 2$, given by [Bor98]

$$\omega_\mathrm{op}(\boldsymbol{q} \simeq \mathbf{0}) = \sqrt{2f\left(\frac{1}{m_1} + \frac{1}{m_2}\right)}. \tag{2.5}$$

In contrast to acoustic lattice vibrations, the non-vanishing energy arises due to the out-of-phase motion of the atoms within the unit cell, see Fig. 2.1(a). The optical modes at $q \to 0$ have oscillation amplitudes of $x_1/x_2 = -m_2/m_1$, leading to a zero group velocity of the center of mass. If the lattice atoms are charged, e.g. in the case of ionic crystals, the oscillating dipoles can couple to an external electromagnetic field [Kit05; Bor98].

Figure 2.1(b) shows a typical behavior of the acoustic and optical phonon dispersion $\omega(\boldsymbol{q})$ over the entire first Brillouin zone, illustrated for a crystal with diatomic basis, $p = 2$. Depending on the crystallographic symmetry of the potential $\mathcal{V}$, a number of longitudinal and transverse vibrational dispersion curves can coincide, resulting in degenerated states. In addition, at certain frequencies between the acoustic and optical

branch, lattice vibrations can not propagate, leaving an energy gap. The width of the forbidden spectral region depends on the mass difference of the unit cell atoms [Rei73; Kit05].

In Fig. 2.1(c), a graph of the density of states $D(\omega)$ is given, defined as spectral distribution of the lattice modes per unit volume in the momentum space. The density $D(\omega)$ is an integral of the number of phonon states across the full Brillouin zone. The function obeys the phonon band-structure via an inverse dependence on its slope, characterized by the group velocity $\nabla_{\boldsymbol{q}}\omega(\boldsymbol{q})$,

$$D(\omega) = \frac{V}{(2\pi)^3} \int_{S(\omega)} \frac{\mathrm{d}S}{|\nabla_{\boldsymbol{q}}\omega(\boldsymbol{q})|}, \tag{2.6}$$

where V is the crystal volume and $\mathrm{d}S$ an area element of constant vibrational energy in reciprocal space [Kit05]. For the low-frequency acoustic phonons, the density of states is in good approximation quadratic, $D(\omega) \propto \omega^2$. In case of high-energetic optical modes, the distribution exhibits a characteristic structure in the spectral range of their occurrence. In sections where the slope of the dispersion tends towards zero, $\nabla_{\boldsymbol{q}}\omega(\boldsymbol{q}) \to 0$, the mode density features van Hove singularities at critical points, implying a large number of excitable states, e.g. close to the TO phonon energy level at the K point in Fig. 2.1(b,c).

Since the lattice-vibrational particles are classified as bosons [Rei73], the population probability of a phonon state $\omega_{\boldsymbol{q},p}$ of the material in thermal equilibrium at temperature T is governed by Bose-Einstein statistics:

$$f(\omega, T) = \frac{1}{\mathrm{e}^{\frac{\hbar\omega_{\boldsymbol{q},p}}{k_\mathrm{B}T}} - 1}, \tag{2.7}$$

where k_B denotes Boltzmann's constant. Importantly, the mean occupation number of a vibrational mode is not limited, and the total number of phonon particles n is not obliged to a conservation law, but strongly temperature-dependent. At room temperature, $k_\mathrm{B}T \sim 25\,\mathrm{meV}$, the acoustic vibration branches are usually highly populated ($f \gg 1$), whereas the optical modes are less excited. In case of $\hbar\omega_{\boldsymbol{q},p} << k_\mathrm{B}T$, the equilibrium distribution can be expressed as $f(\omega, T) \propto T$, approaching the classical limit.

Consequently, by combination of the density of states $D(\omega)$ with the occupation probability $f(\omega, T)$, the temperature-dependent number of vibrational excitations within a solid is given according to the relation:

$$n(T) = \int D(\omega) f(\omega, T)\, \mathrm{d}\omega. \tag{2.8}$$

Phonons, besides e.g. plasmons or magnons, are elementary excitations of the crystalline solid [Kit05]. Apart from the frequency ω, each vibrational mode is characterized by a wavevector $\boldsymbol{q}$, whose magnitude is inversely proportional to the wavelength. Thus, phonon states near the origin of the first Brillouin zone, Γ, are considered as the long-

wavelength limit. The quantity $\hbar\boldsymbol{q}$ describes the quasi momentum of the vibration, however, an elastic lattice wave does not carry a real physical momentum [Rei73]. In case of the interaction of phonons with other wave-like particles, for instance photons or electrons, one might has to invoke an additional contribution $\hbar\boldsymbol{G}$, where $\boldsymbol{G}$ is a reciprocal lattice vector, from the crystal lattice to satisfy the law of momentum conservation.

Compared to the quantum harmonic oscillator model with $\mathcal{V} \propto x^2$ in Eq. (2.1), a realistic description of the crystal potential has to include higher-order terms, $\mathcal{V}(x) = V_0 + ax^2 + bx^3 + cx^4 + \dots$. These anharmonic contributions allow an interaction of the vibrational modes among themselves, i.e. phonon-phonon scattering. As a consequence, phonons possess a finite lifetime, that manifests, for instance, as limited linewidth in vibrational spectroscopy measurements. Moreover, the coupling between the lattice oscillations introduces a temperature dependence of the phonon frequencies, taken into account by renormalized phonon energies [Rei73]. Also, phonon-phonon scattering processes are responsible for non-equilibrium material properties like lattice expansion and the conductivity of heat mediated by lattice vibrations, which presents the main transport channel in dielectric crystals [Kit05].

Ab initio calculations of the phonon bandstructure and related properties like lifetimes and interatomic force constants employ techniques such as density-functional perturbation theory, a detailed description thereof can be found in, e.g., Ref. [Bar01].

2.1.2 Polar Dielectric Media

When dealing with dielectric, i.e. non-conducting, materials, the crystals often exhibt an ionic, covalent or van der Waals chemical bonding structure. In the case of polar dielectrics, elements with different degrees of electronegativity take part in the bond, creating a 'biased' electron distribution among the crystal atoms instead of a symmetrically shaped one. Therefore, the interatomic forces are mediated via electrostatic Coulomb attraction of oppositely charged atomic ions. This is in analogy to polar molecules (e.g. H_2O), where the charge distribution is shifted to the atoms possessing higher electronegativity, resulting in a permanent dipole moment.

For a crystal unit cell with an at least diatomic basis, optical phonons are present in the vibrational spectrum. In the case of polar crystals, the energy dispersion of the longitudinal (LO) and transverse optical (TO) phonon branches differs. The LO/TO splitting arises due to the different potentials $\mathcal{V}(\boldsymbol{x})$ being present along the certain crystallographic directions. This is caused by long-range Coulomb forces associated with the ionic charges [Bor98]. For the LO lattice vibrations, the eigenfrequency in the long-wavelength limit is generally higher in comparison to both transverse modes,

$$\omega_{\mathrm{LO},\boldsymbol{q}\to\boldsymbol{0}} > \omega_{\mathrm{TO},\boldsymbol{q}\to\boldsymbol{0}}. \tag{2.9}$$

In order to understand the origin behind this, one has to consider the electric polarization

for the different optical modes in the ionic crystal. The resulting contribution to the local Coulomb field, termed depolarization field [Bor98; Bru82],

$$\boldsymbol{E}_{\mathrm{pol}} = -\frac{1}{\epsilon_0}\frac{\boldsymbol{x}\cdot\boldsymbol{P}}{|\boldsymbol{x}|^2}\boldsymbol{x} \tag{2.10}$$

depends on the relative orientation of displacement vector $\boldsymbol{x}$ and polarization $\boldsymbol{P} = \sum_i \boldsymbol{\mu}_i/V$, with the microscopic dipole moment $\boldsymbol{\mu}_i$ and crystal volume V. Thus, for transversal lattice waves with $\boldsymbol{x} \perp \boldsymbol{P}$ the field term vanishes, whereas it is $\boldsymbol{E}_{\mathrm{pol}} = -\boldsymbol{P}/\epsilon_0$ for the longitudinal mode since $\boldsymbol{x} \uparrow\uparrow \boldsymbol{P}$. Consequently, the local electric field acts against the atomic displacement in case of LO phonons, increasing the potential energy function $\mathcal{V}(\boldsymbol{x})$ and thereby the eigenfrequency ω_{LO}. For TO modes, on the other hand, the local field supports the lattice vibration, hence softening the interatomic forces compared to neutral, i.e. non-ionic, atoms [Bru82].

Considering, for example, the polar dielectric material 4H-silicon carbide, the energetic difference between the LO and TO phonon branch at the Brillouin zone center accounts for $\sim 21\,\mathrm{meV}$ or $170\,\mathrm{cm}^{-1}$ [Mut99]. The broad range originates from the strong polarity of the atomic elements (electronegativity on Pauling scale of silicon $\chi = 1.90$, carbon $\chi = 2.55$). Besides the LO/TO splitting, an energy gap ΔE_{OA} between the optical and acoustic branches is present in ionic crystals. Background is the mass difference of the cationic and anionic unit cell atoms. Due to the distinct optical properties, the spectral region between the LO and TO phonon frequencies is called Reststrahlen band (see Sec. 2.2.2) [Bor98].

For the appearance of optical phonons in optical spectroscopy experiments, certain selection rules have to be taken into account. Direct, i.e. resonant, excitation of a lattice vibration by one-photon absorption requires, on the one hand, infrared (IR) radiation equivalent to the phonon energy (in the order of $\lambda \sim 10\,\mu\mathrm{m}$). Besides energy conservation, the momentum during the interaction with the electromagnetic field needs to be matched. Therefore, only vibrational modes near the Brillouin zone center $\boldsymbol{q} \simeq 0$ are accessible by IR spectroscopy, due to the small wavevector $|\boldsymbol{k}| = 2\pi/\lambda$ of mid-infrared (MIR) photons [Bru86]. Furthermore, the excitable lattice vibration must carry an electric dipole moment $\boldsymbol{\mu}$ which has to be spatially modulated during the interaction with the light field $\boldsymbol{E}$ in order to be IR active. According to Fermi's golden rule, the probability for the creation of a phonon, i.e. the transition rate of the crystal from initial vibrational state $|n\rangle$ to final state $|n+1\rangle$, is given by [Bru86]

$$\Gamma = \frac{2\pi}{\hbar}|\langle n+1|\boldsymbol{\mu}\cdot\boldsymbol{E}|n\rangle|^2\,\delta(E_{n+1} - E_n - \hbar\omega), \tag{2.11}$$

with the matrix element $\langle n+1|\boldsymbol{\mu}\cdot\boldsymbol{E}|n\rangle$. For the most probable transition, the dipole moment should be aligned with the electric field polarization, $\boldsymbol{\mu} \uparrow\uparrow \boldsymbol{E}_0$. Thus, transverse optical phonon modes are predominately excited in near-normal incidence transmission or reflectivity measurements. This will become apparent in the expression of the infrared dielectric function for the linear response in Sec. 2.2.1, where ω_{TO} is the reso-

nance frequency in the denominator. On the contrary, relevant absorption by LO lattice vibrations can be observed under non-normal incidence conditions for thin films [Bru86].

Another spectroscopic technique to probe optical lattice vibrations, but e.g. also magnons, is provided by the Raman effect [Rei73; Bru86]. There, the light is inelastically scattered at a low-frequency excitation of the solid, leading to the following conservation laws for energy and momentum, respectively:

$$\hbar\omega' = \hbar\omega \pm \hbar\omega_{\boldsymbol{q}}, \quad \boldsymbol{k}' = \boldsymbol{k} \pm \boldsymbol{q}, \tag{2.12}$$

where the incident (scattered) photon is characterized by $\hbar\omega, \boldsymbol{k}$ ($\hbar\omega', \boldsymbol{k}'$). Depending on the sign of the frequency shift, either the creation of a phonon (Stokes process) or an annihilation of a phonon (Anti-Stokes process) is taking place. As in the case of IR spectroscopy, only optical phonons with $|\boldsymbol{q}| \simeq 0$ can be probed, since $\boldsymbol{k}, \boldsymbol{k}'$ are much smaller than the zone-boundary wavevector $2\pi/a$. Additionally, the selection rule necessitates the vibrational mode to modulate the electronic polarizability tensor $\boldsymbol{\alpha}$ of the crystal in order to be Raman active [Bru86]. Thus, a dipole moment $\boldsymbol{\mu} = \boldsymbol{\alpha}\boldsymbol{E}$ oscillating at the frequencies given by Eq. (2.12) is induced by the incident light field $\boldsymbol{E}$. From a classical point of view, the derivative of the polarizability α_{ij} with respect to the normal-mode coordinate q_k, so-called (first-order) Raman tensor

$$R_{ijk} = \frac{\partial \alpha_{ij}}{\partial q_k}, \tag{2.13}$$

must have non-vanishing components. In a quantum-theoretical perturbation calculus, the scattering probability is

$$\Gamma = \frac{2\pi}{\hbar} \left| \sum_{\alpha,\beta} \frac{\langle 0|\mathcal{H}_{\mathrm{er}}(\omega')|\beta\rangle \langle \beta|\mathcal{H}_{\mathrm{el}}(\omega_{\boldsymbol{q}})|\alpha\rangle \langle \alpha|\mathcal{H}_{\mathrm{er}}(\omega)|0\rangle}{(\hbar\omega' - E_\beta)(\hbar\omega - E_\alpha)} \right|^2 \delta(\hbar\omega - \hbar\omega' \pm \hbar\omega_{\boldsymbol{q}}), \tag{2.14}$$

with the interaction of electron-radiation field $\mathcal{H}_{\mathrm{er}} = \boldsymbol{\mu} \cdot \boldsymbol{E}$ and electron-lattice vibration $\mathcal{H}_{\mathrm{el}}$. Here, the Raman effect is represented as three-step process of electron excitation from ground state $|0\rangle$ to intermediate (virtual) level $|\alpha\rangle$ by photon $\hbar\omega$, then scattering into state $|\beta\rangle$ due to phonon creation/elimination, and finally returning to $|0\rangle$ while emitting photon $\hbar\omega'$. By the symmetry of the equilibrium polarizability and that of the vibrational modes, the Raman tensor $\boldsymbol{R}$ reflects the crystal symmetry [Bru86]. Thus, the selection rules can be obtained from a group-theoretical analysis of the real-space crystal structure. As such, vibrational transitions can be classified as being dipole-allowed, and/or Raman-active or neither of them (silent modes). In the case of solids (as well as molecules) with a center of inversion, the rule of mutual exclusion holds, that is, a phonon might be either IR- or Raman-active, but not both. In general, the irreducible representation of the crystal point group is used to deduce the symmetry elements, and thus, the activity of the normal modes [Bru86].

As it becomes apparent in the IR or Raman spectra of lattice excitations, the resonances feature a nonzero spectral width. Due to the anharmonic coupling among the

phonons, the linewidth is limited by the lifetime $\tau(\boldsymbol{q})$ of the vibrational modes [Bar01]. In case of optical phonons in polar dielectrics, the dominant scattering mechanism is provided by the interaction with two lower-frequency modes away from the Γ point, in order to fulfill energy and momentum conservation:

$$\omega_1(\boldsymbol{q}_1) = \omega_2(\boldsymbol{q}_2) \pm \omega_3(\boldsymbol{q}_3), \quad \boldsymbol{q}_1 = \boldsymbol{q}_2 \pm \boldsymbol{q}_3 + \boldsymbol{G}. \tag{2.15}$$

Predominately, optically excited zone-center phonons decompose into two acoustic phonons (OAA scattering) [Deb99]. Due to the energy gap ΔE_{OA} between optic and acoustic phonon branches present in polar crystals, the number of decay channels can be limited, resulting in extended optical phonon lifetimes. This is the case for materials with a large mass difference of the unit cell atoms. On the other hand, a strong LO/TO splitting in solids enables the decay of an optical phonon into an acoustic mode and another lower-energetic optic phonon (OOA scattering). Crystals with strong Coulomb forces between the atomic ions have to be considered here. Therefore, lifetimes and linewidths of excited optical lattice vibrations depend strongly on the phonon dispersion relations, and hence, on the crystal structure. For ionic non-conducting materials, the intrinsic lifetimes of bulk optic phonons near the zone-center are in the order of a few picoseconds [Deb99].

Besides the decay channels arising in a perfect crystal, extrinsic scattering partners can further degradate the lifetime of the vibrational modes. There, scattering processes due to differing masses of the atomic isotopes are relevant, as well as impurities within the crystal bulk or lattice defects like domain boundaries and stacking faults [Kit05]. As consequence of the enhanced decay process, a broadening of the resonance linewidth appears.

2.2 Light-Matter Interaction

In general, the dielectric response of a material to an incident optical field $\boldsymbol{E}(\omega)$ is described by a Taylor series of the induced electric polarization $\boldsymbol{P}$ [Boy08]:

$$\boldsymbol{P} = \varepsilon_0 \left[\boldsymbol{\chi}^{(1)} \cdot \boldsymbol{E}(\omega) + \boldsymbol{\chi}^{(2)} : \boldsymbol{E}(\omega)\boldsymbol{E}(\omega) + \boldsymbol{\chi}^{(3)} \vdots \boldsymbol{E}(\omega)\boldsymbol{E}(\omega)\boldsymbol{E}(\omega) + ... \right]. \tag{2.16}$$

There, the medium's optical properties are characterized by the n-th order electric susceptibilities $\boldsymbol{\chi}^{(n)}$, expressed as tensors of rank $n+1$, whereas ε_0 denotes the permittivity of free space. Depending on the strength of the applied field, the cases of linear optics – determined only by the first term in Eq. (2.16) – and nonlinear optics – considering the higher-order contributions – are separated. In the linear regime, optical processes like the propagation velocity and attenuation of electromagnetic waves within a material system are concerned, as well as the refraction and reflection on its interfaces (Sec. 2.2.1). Since the nonlinear susceptibility values are several orders of magnitude smaller than unity, intense light fields have to be employed in order to observe nonlinear optical phenomena,

which can, for example, modify the frequency of the incident radiation by generating additional spectral components (see Sec. 2.2.3).

2.2.1 Linear Dielectric Response

In linear electromagnetism, the proportionality between the applied optical field and induced electric polarization of the medium is usually expressed in terms of the relative permittivity, also called dielectric function:

$$\boldsymbol{\varepsilon}(\omega) = \boldsymbol{\chi}^{(1)}(\omega) + \mathbf{1}. \tag{2.17}$$

The linear optical response of a material is, in general, characterized by a complex-valued, frequency-dependent second-rank tensor $\boldsymbol{\varepsilon}(\omega)$ [Bor99]. In case of an optically isotropic medium, the permittivity reduces to a scalar quantity,

$$\varepsilon(\omega) = \varepsilon'(\omega) + \mathrm{i}\varepsilon''(\omega). \tag{2.18}$$

Concerning the spectral dependence, a useful model for the dielectric function exhibiting multiple resonances is given by a sum of Lorentz oscillators [Bru86; Bor99]. These resonators might be electrons bound to positively charged atomic nuclei in metals (oscillating at UV/VIS frequencies), or optical phonons built of atomic ions in dielectrics (vibrating in the IR spectral range), thereby constituting electric dipoles that interact with an applied light field. Then, the dispersion relation is described by

$$\varepsilon(\omega) = \varepsilon_\infty + \sum_r \frac{A_r}{\omega_r^2 - \omega^2 - \mathrm{i}\gamma_r\omega}, \tag{2.19}$$

where A_r represents the oscillator strength, ω_r the resonance frequency and $\gamma_r = 1/\tau_r$ the damping constant of mode r. The high-frequency term ε_∞ characterizes a dielectric contribution arising outside the investigated spectral range. A nonzero imaginary part $\varepsilon''(\omega)$ directly indicates the stimulation of absorption processes in the material at the resonant frequencies. Outside these spectral regions, the dielectric function is purely real, $\varepsilon(\omega) = \varepsilon'(\omega)$, i.e. the optical wave does not experience an intensity loss while propagating through the medium.

In optics, it is convenient to use the complex refractive index $n^* = \sqrt{\varepsilon\mu}$ instead. Since the considered optical materials are electrically non-conducting and non-magnetic, i.e. with a relative permeability $\mu = 1$, the relation reduces to

$$n^* = n + \mathrm{i}\kappa = \sqrt{\varepsilon}, \tag{2.20}$$

with the real index of refraction $n = \sqrt{(|\varepsilon| + \varepsilon')/2}$ and the extinction coefficient $\kappa = \sqrt{(|\varepsilon| - \varepsilon')/2}$. Due to the causality of the dielectric material response with respect to the incident electric field, real and imaginary part are connected via the Kramers-Kronig relations [Bor99]. The refractive index n determines the phase velocity v of the

electromagnetic wave propagating within the medium,

$$v = \frac{c_0}{n} = \frac{\omega}{k}, \tag{2.21}$$

in relation to the speed of light in vacuum c_0. If the spectral derivative $\mathrm{d}n/\,\mathrm{d}\omega$ is positive, the medium is called normal dispersive. Otherwise, it obeys anomalous dispersion, which is the case close to a resonance frequency.

When dealing with optically anisotropic materials, the dielectric properties have to be described by a second-rank tensor. For a uniaxial crystal (e.g., members of the hexagonal crystallographic system), this one is of the form

$$\boldsymbol{\varepsilon}(\omega) = \begin{pmatrix} \varepsilon_\perp(\omega) & 0 & 0 \\ 0 & \varepsilon_\perp(\omega) & 0 \\ 0 & 0 & \varepsilon_\parallel(\omega) \end{pmatrix} = \begin{pmatrix} n_\mathrm{o}^2(\omega) & 0 & 0 \\ 0 & n_\mathrm{o}^2(\omega) & 0 \\ 0 & 0 & n_\mathrm{e}^2(\omega) \end{pmatrix}, \tag{2.22}$$

with the principal permittivities being on the main diagonal. The dielectric tensor can be illustrated as index ellipsoid where the semi-axes correspond to the values n_o and n_e [Bor99]. Therefore, the velocity of light propagation inside the crystal is generally dependent on both the wave polarization $\boldsymbol{E}$ and propagation direction $\boldsymbol{k}$. In case of the uniaxial anisotropic crystal, one single preferred optical axis exists, here chosen to coincidence with the z direction. Then, the refraction along the principal axes of the crystal is described by n_o and n_e for the ordinary and extraordinary ray, whose polarization is normal (o) to or within (e) the principal plane spanned by the z axis and the wavevector $\boldsymbol{k}$, respectively [Dmi99].

For an arbitrarily incidenting extraordinary beam with angle $\theta \in [0°, 90°]$ relative to the optical axis, the refractive strength $n_\mathrm{e}(\theta)$ of the crystal has a value between n_o and n_e, as specified by

$$\frac{1}{n_\mathrm{e}^2(\theta,\omega)} = \frac{\sin^2\theta}{n_\mathrm{e}^2(\omega)} + \frac{\cos^2\theta}{n_\mathrm{o}^2(\omega)}. \tag{2.23}$$

This phenomenon of birefringence is routinely used to achieve the same propagation speed of two light waves of different color in a nonlinear optical crystal by utilizing different polarization conditions (method of velocity or phase matching, see Sec. 2.2.3), which is otherwise not possible in dispersive media [Boy08].

Another quantity has to be introduced to characterize the speed of energy transport, defined as group velocity

$$v_\mathrm{g} = \frac{\partial\omega}{\partial k} \tag{2.24}$$

or $\boldsymbol{v}_\mathrm{g} = \nabla_{\boldsymbol{k}}\,\omega(\boldsymbol{k})$ in three-dimensional space. Depending on the dispersion relation $\omega(k)$, the value might be different from the phase velocity v, Eq. (2.21). In case of anisotropic crystals, the direction of wavefront propagation given by $\boldsymbol{v} \parallel \boldsymbol{k}$ differs slightly from the

way of energy flow represented by the Poynting vector $\boldsymbol{S} \parallel \boldsymbol{v}_\mathrm{g}$ for beams with extraordinary polarization [Bor99]. Thus, the resulting spatial walk-off might limit the usable interaction length in frequency-conversion crystals [Boy08; Dmi99].

At the interface between different optical media, the light field is subject to reflection and transmission. Therefore, the ratio of the electric field amplitudes relative to the incident wave is given by the Fresnel equations. In case of the interface of a uniaxial anisotropic crystal to vacuum ($\varepsilon^\mathrm{I} = 1$, or air, approximately), with the optic axis z being parallel to the surface normal, the following expressions hold for the amplitude coefficients of s- and p-polarized electric fields, respectively [Dru87; Mos68]:

$$\begin{aligned} r_\mathrm{s} &= \frac{g^\mathrm{I} - g_\mathrm{o}^\mathrm{II}}{g^\mathrm{I} + g_\mathrm{o}^\mathrm{II}}, \qquad t_\mathrm{s} = \frac{2g^\mathrm{I}}{g^\mathrm{I} + g_\mathrm{o}^\mathrm{II}} \\ r_\mathrm{p} &= \frac{\varepsilon_\perp g^\mathrm{I} - g_\mathrm{e}^\mathrm{II}}{\varepsilon_\perp g^\mathrm{I} + g_\mathrm{e}^\mathrm{II}}, \; t_\mathrm{p} = \frac{2g^\mathrm{I}}{\varepsilon_\perp g^\mathrm{I} + g_\mathrm{e}^\mathrm{II}}. \end{aligned} \tag{2.25}$$

There, $g = |k_\mathrm{z}|$ is the absolute component of the wave vector along the optic axis, defined as $g^\mathrm{I} = \frac{\omega}{c_0}\cos\theta$, $g_\mathrm{o}^\mathrm{II} = \frac{\omega}{c_0}\sqrt{\varepsilon_\perp - \sin^2\theta}$ and $g_\mathrm{e}^\mathrm{II} = \frac{\omega}{c_0}\sqrt{\frac{\varepsilon_\perp}{\varepsilon_\parallel}}\sqrt{\epsilon_\parallel - \sin^2\theta}$, with the angle of incidence θ in medium I. For an isotropic medium ($\varepsilon_\parallel = \varepsilon_\perp = \varepsilon^\mathrm{II}$), Eqs. (2.25) reduce to the well-known usual Fresnel formulae [Bor99]. In any case, the intensity reflectivity of the electromagnetic radiation at the material surface, i.e. the reflectance, is determined according to $R_\mathrm{s,p} = |r_\mathrm{s,p}|^2$.

2.2.2 Phonon Polaritons

The particular properties of IR-active phonon modes in polar dielectrics have been discussed in Sec. 2.1.2. Now, the consequences on the linear optical response are considered. From a general derivation [Lyd41] it is found that the ratio of the longitudinal, $\omega_\mathrm{LO}(q \simeq 0)$, and transverse optic, $\omega_\mathrm{TO}(q \simeq 0)$, lattice eigenfrequencies determines the behavior of the dielectric function $\epsilon(\omega)$, known as the Lyddane-Sachs-Teller (LST) relation for multiple modes r:

$$\prod_r \left(\frac{\omega_{\mathrm{LO},r}}{\omega_{\mathrm{TO},r}}\right)^2 = \frac{\varepsilon_0}{\varepsilon_\infty}. \tag{2.26}$$

The value ε_0 describes the static dielectric response (DC-field permittivity), whereas ε_∞ characterizes the dielectric medium in the high-frequency limit ($\omega \gg \omega_\mathrm{LO}$). Due to the relation $\omega_\mathrm{LO} > \omega_\mathrm{TO}$, Eq. (2.9), the static permittivity exceeds the value in the visible range, i.e. $\varepsilon_0 > \varepsilon_\infty$. Since electromagnetic waves $\boldsymbol{E}(\omega)$ are of transverse nature, the excitation of longitudinal optical phonons in bulk crystals by light near normal incidence is not possible. Therefore, the solid does not respond to an external field at this frequency, $\epsilon(\omega_\mathrm{LO}) = 0$ in the absence of damping [Bru86]. Contrary, the polarization component of TO vibrational modes can interact with photons. Thus, the resonances

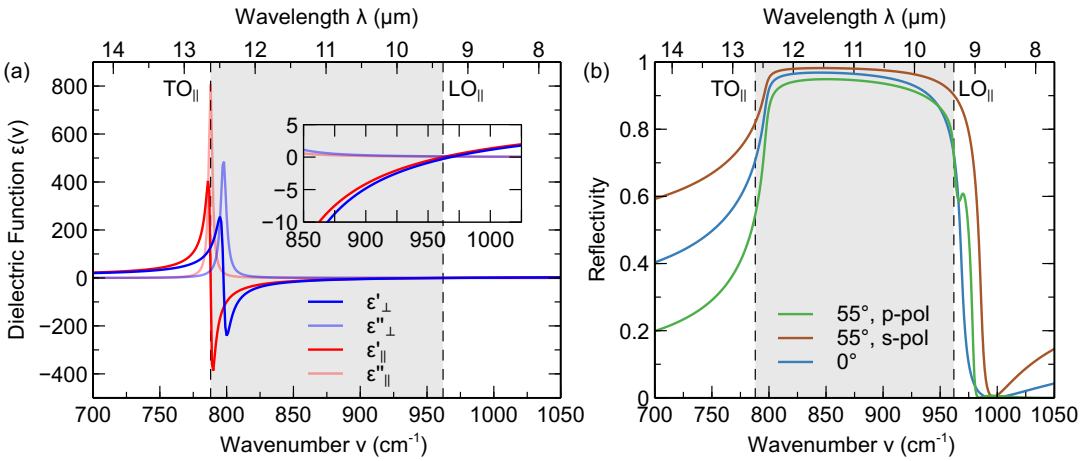

Fig. 2.2 Typical mid-infrared dispersion of the linear optical susceptibility and Reststrahlen reflectivity of a polar dielectric, 4H-SiC. (a) Dielectric function $\varepsilon_{\perp,\parallel}(\nu)$, exhibiting different resonance frequencies ν_{TO} and zero-crossings at ν_{LO} for the extraordinary ($\parallel$) and ordinary ($\perp$) component of the uniaxial susceptibility tensor, Eq. (2.22), respectively. Inset shows a magnified view of the spectral region close to the LO phonon. (b) Reflectance $R_{\mathrm{s,p}}(\nu)$ for s- and p-polarized light under oblique angle of incidence and normal irradiation, obtained from Eq. (2.25). The Reststrahlen band is indicated by the gray-shaded area between TO and LO phonon mode. Experimental values for 4H-SiC are taken from Ref. [Mut99].

in the dielectric function of Eq. (2.19) correspond to the transversal eigenfrequencies of the polar ionic crystal in the long-wavelength limit, $\omega_{\mathrm{TO}}(q \to 0)$. In case of diatomic insulators, one obtains

$$\varepsilon(\omega) = \varepsilon_\infty \left(1 + \frac{\omega_{\mathrm{LO}}^2 - \omega_{\mathrm{TO}}^2}{\omega_{\mathrm{TO}}^2 - \omega^2 - \mathrm{i}\gamma_{\mathrm{TO}}\omega}\right). \tag{2.27}$$

Exemplary, the real and imaginary part of the dispersion relation $\varepsilon(\omega)$ for the strongly polar and anisotropic dielectric 4H-SiC are plotted in Fig. 2.2. The calculated reflectivity $R(\omega)$, according to Eq. (2.25), is also depicted. At the infrared frequencies of interest, contributions due to excitation of electronic transitions are neglectable. Depending on the spectral position within the IR region, the optical behavior of insulators can be differentiated in the following way: For $\omega \ll \omega_{\mathrm{TO}}$, normal dispersion is present, related with finite transmittance of the material. Around $\omega = \omega_{\mathrm{TO}}$, strong optical absorption due to $\epsilon'' \neq 0$ occurs, combined with anomalous dispersion of $\epsilon'(\omega)$ in a range of width $\sim \gamma_{\mathrm{TO}}$. Then, as the permittivity is negative, $\epsilon' < 0$, the reflectivity becomes significant until the zero-crossing at $\omega = \omega_{\mathrm{LO}}$. At high frequencies, the dielectric function approaches ϵ_∞.

The change from reflective to transmissive response of the dielectric at ω_{LO} is similar to the behavior of metals or electron-ion plasmas at their natural eigenfrequency. There, the spectral point of $\epsilon(\omega_{\mathrm{p}}) = 0$ corresponds to the energy of a plasmon, the quantum of the coherent longitudinal oscillation of the charge density [Kit05]. In case of polar

dielectrics, the optical phonons take on the role of screening the external electromagnetic field. Owing to the negative dielectric function, the light waves can not propagate within the material, causing nearly perfect reflectivity. This material-specific frequency range is termed Reststrahlen band [Rei73]. There, only an evanescent field $E\mathrm{e}^{-\kappa z}$ at the surface, attenuated by the extinction coefficient κ towards the bulk, is present.

Due to the energy of TO and LO phonons in the order of 100 meV, the Reststrahlen effect is pronounced in the MIR spectral region, $\lambda \sim 10\,\mu\mathrm{m} - 30\,\mu\mathrm{m}$. Electromagnetic fields $E(\omega)$ with a frequency outside the forbidden gap, $\omega > \omega_{\mathrm{LO}}$ or $\omega < \omega_{\mathrm{TO}}$, can penetrate the medium, accompanied by the excitation of transverse lattice vibrations. If the wavenumber of the photon within the material, $|\boldsymbol{k}| = 2\pi n/\lambda$, is matched to the phonon's wavevector, $\boldsymbol{q} \simeq \boldsymbol{k}$, which is the case close to the Brillouin-zone center, coupling of both modes occurs. As consequence of the interaction between optic phonon and electromagnetic field, the formation of a phonon polariton emerges. This bosonic quasiparticle is present in the momentum space where one would expect the intersection of phonon and light dispersion. However, a mixed state appears instead, according to the avoided crossing-principle. Inserting the material's dielectric function Eq. (2.27) into the linear photon dispersion, $\omega^2 = \frac{c_0^2}{\epsilon(\omega)}k^2$, the bulk polariton solution is given by [Bru86]

$$q^2 = \frac{\varepsilon_\infty}{c_0^2}\frac{\omega_{\mathrm{LO}}^2 - \omega_{\mathrm{TO}}^2}{\omega_{\mathrm{TO}}^2 - \omega^2 - \mathrm{i}\gamma_{\mathrm{TO}}\omega}\omega^2, \tag{2.28}$$

which converges, under employment of the LST formula Eq. (2.26), to the relations

$$\omega = \frac{c}{\sqrt{\varepsilon_\infty}}q \quad \text{for } \omega \gg \omega_{\mathrm{LO}}, \tag{2.29}$$

$$\omega = \frac{c}{\sqrt{\varepsilon_0}}q \quad \text{for } \omega \ll \omega_{\mathrm{TO}}. \tag{2.30}$$

The two (bulk) polariton dispersion curves, as determined by Eq. (2.28), are plotted in Fig. 2.3, together with the derived limits. Depending on the region within the momentum space, each polariton branch, labelled as α and β, respectively, exhibits either a more photonic, or phononic, or strongly coupled character. Considering, for example, the polariton α, a nearly pure electromagnetic nature is present close to the Brillouin zone origin, characterized by the linear dispersion Eq. (2.30). There, the mechanical displacement of the oppositely charged atomic ions is small, whereas the energy is preferably stored in the electromagnetic field [Bru86]. Towards larger momentum k, the weight of the lattice vibrational character is increased, in trade-off for the reduced optical amplitude. Consequently, the coupling is strongest at wavevectors around $k \sim 3 \times 10^5\,\mathrm{m}^{-1}$. At larger values, the α-polariton dispersion is almost flat, approaching the uncoupled, pure TO phonon frequency, $\omega \approx \omega_{\mathrm{TO}}$. Note that the k-space relevant for the phonon-photon interaction is still much smaller than the extent of the Brillouin zone with the boundary at $q \sim 1\,\text{Å}^{-1}$.

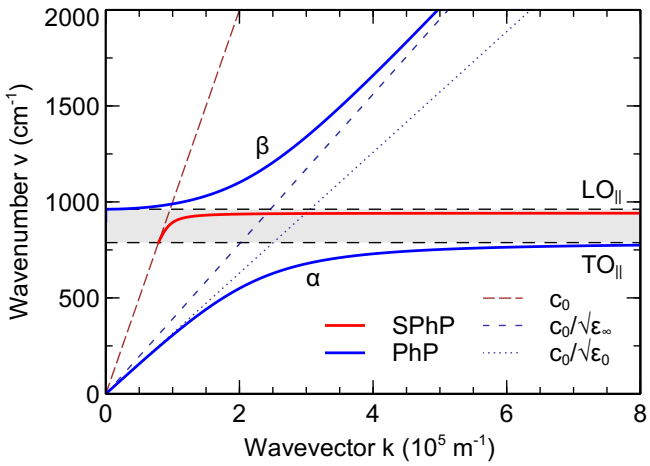

Fig. 2.3 Dispersion relation for bulk (PhP) and surface (SPhP) phonon-polariton modes in 4H-SiC. The two branches of the volume mode are labelled α and β, respectively. The photon dispersion curves for light propagation in air (velocity c_0) and within the dielectric material in the low- ($c_0/\sqrt{\varepsilon_0}$) and high-frequency ($c_0/\sqrt{\varepsilon_\infty}$) limit are given for comparison. Extraordinary optical wave polarization has been used. The polariton dispersions are obtained from Eqs. (2.28) and (2.31).

As mentioned, bulk phonon polariton modes are not supported within the Reststrahlen band. There are, however, also optical surface vibrations present in polar dielectrics. Due to the structural difference in the environment of bulk and interface atomic ions, the potential $\mathcal{V}$ governing the lattice dynamics in Eq. (2.1) is affected as well, resulting in modified vibrational frequencies at the surface. Such optical crystal excitations, whose amplitudes are confined to the interface and decaying exponentially towards the bulk, are also called Fuchs-Kliewer modes [Fuc65]. The mixing of these transverse polar vibrations with light gives rise to surface phonon polaritons (SPhPs), with the dispersion [Bru86]

$$q^2 = \frac{\epsilon(\omega)}{\epsilon(\omega)+1}\frac{\omega^2}{c_0^2}. \tag{2.31}$$

For the ease of understanding, insertion of the dielectric function Eq. (2.27) with zero damping $\gamma = 0$ in Eq. (2.31) and using the relation Eq. (2.26), yields the SPhP frequency at large wavevectors,

$$\omega_{\mathrm{SPhP}} = \sqrt{\frac{\epsilon_0+1}{\epsilon_\infty+1}}\omega_{\mathrm{TO}}. \tag{2.32}$$

Because $\epsilon_0 > \epsilon_\infty$, surface polaritons propagate within the spectral region of the Reststrahlenband, $\omega_{\mathrm{LO}} > \omega_{\mathrm{SPhP}} > \omega_{\mathrm{TO}}$, where the bulk modes Eq. (2.28) are not allowed. The SPhP dispersion relation is plotted in Fig. 2.3 as well.

The hybrid surface phonon-light excitations discussed so far are classified as *propagating* modes, being free to expand along the crystal interface. As an example, two-

dimensional polar dielectric van der Waals heterostructures allow to control the dispersion of such modes [Dai14]. In contrast, *localized* SPhPs are created by a specific design of the material surface, e.g. via nanostructures [Cal15]. There, the coupled mode is spatially confined in all three dimensions. The character of the polariton can be modified in a way similar to propagating or localized surface plasmon polaritons, respectively, which arise at metal/dielectric interfaces [Mai07]. Due to the general momentum mismatch between the photon and propagating surface polariton dispersion (see also Fig. 2.3), different methods can be employed to accomplish optical excitation, for instance, by the near field of evanescent waves [Cal15; Mai07].

2.2.3 Nonlinear Optics

Nonlinear optical effects are nowadays routinely employed to produce radiation of specific properties otherwise difficult to create as well as to probe light-induced processes in matter under advanced conditions. The observation of such phenomena is closely connected with the availability of coherent laser light, as shown by the seminal work about optical second-harmonic generation in the 1960s [Fra61]. Basically, the occurrence of nonlinear optical processes in media is caused by the higher-order induced electric polarization terms of Eq. (2.16),

$$\begin{aligned} \boldsymbol{P}^{\mathrm{NL}} &= \varepsilon_0 \left[\boldsymbol{\chi}^{(2)} : \boldsymbol{E}(\omega)\boldsymbol{E}(\omega) + \boldsymbol{\chi}^{(3)} \vdots \boldsymbol{E}(\omega)\boldsymbol{E}(\omega)\boldsymbol{E}(\omega) + ... \right] \\ &= \boldsymbol{P}^{(2)} + \boldsymbol{P}^{(3)} + ... \,. \end{aligned} \tag{2.33}$$

These nonlinear polarization contributions $\boldsymbol{P}^{\mathrm{NL}}(\boldsymbol{r},t)$ act as radiation sources, as described by the wave equation for the propagation of electromagnetic waves $\boldsymbol{E}(\boldsymbol{r},t)$ in a nonlinear optical material, which can be derived from Maxwell's equations [Boy08]:

$$\Delta\boldsymbol{E} - \frac{\varepsilon(\omega)}{c_0^2}\frac{\partial^2}{\partial t^2}\boldsymbol{E} = \frac{1}{\varepsilon_0 c_0^2}\frac{\partial^2}{\partial t^2}\boldsymbol{P}^{\mathrm{NL}}. \tag{2.34}$$

Consequently, light fields at new frequencies are generated. As an example, the irradiation of two laser beams $\boldsymbol{E}_1 \mathrm{e}^{\mathrm{i}(\boldsymbol{k}_1\boldsymbol{r}-\omega_1 t)} + \text{c.c.}$ and $\boldsymbol{E}_2 \mathrm{e}^{\mathrm{i}(\boldsymbol{k}_2\boldsymbol{r}-\omega_2 t)} + \text{c.c.}$ of different color, $\omega_1 \neq \omega_2$, onto matter with a second-order optical nonlinearity $\boldsymbol{\chi}^{(2)} \neq \boldsymbol{0}$ will be considered. The resulting nonlinear polarization fields $\boldsymbol{P}(\omega_3)\mathrm{e}^{\mathrm{i}(\boldsymbol{k}_3\boldsymbol{r}-\omega_3 t)}$ are

$$\boldsymbol{P}(2\omega_1) = \varepsilon_0 \boldsymbol{\chi}^{(2)} : \boldsymbol{E}_1^2, \tag{2.35}$$

$$\boldsymbol{P}(2\omega_2) = \varepsilon_0 \boldsymbol{\chi}^{(2)} : \boldsymbol{E}_2^2, \tag{2.36}$$

$$\boldsymbol{P}(\omega_1+\omega_2) = 2\varepsilon_0 \boldsymbol{\chi}^{(2)} : \boldsymbol{E}_1\boldsymbol{E}_2, \tag{2.37}$$

$$\boldsymbol{P}(\omega_1-\omega_2) = 2\varepsilon_0 \boldsymbol{\chi}^{(2)} : \boldsymbol{E}_1\boldsymbol{E}_2^*, \tag{2.38}$$

$$\boldsymbol{P}(0) = 2\varepsilon_0 \boldsymbol{\chi}^{(2)} : (\boldsymbol{E}_1\boldsymbol{E}_1^* + \boldsymbol{E}_2\boldsymbol{E}_2^*)\,. \tag{2.39}$$

Therefore, electromagnetic waves at several frequencies ω_3 arise due to the four frequency-mixing processes of second-harmonic generation [SHG, Eqs. (2.35,2.36)], sum-frequency generation [SFG, Eq. (2.37)], difference-frequency generation [DFG, Eq. (2.38)] and optical rectification [OR, Eq. (2.39)]. The SHG and OR interaction can be seen as special case of the SFG and DFG process, respectively, with $\omega_1 = \omega_2$. Also, the effects of optical parametric oscillation (OPO) and amplification (OPA) belong to the class of three-wave coupling caused by the second-order susceptibility $\chi^{(2)}$ [Boy08].

In order to obtain efficient emission of optical radiation at frequency ω_3 from bulk media, the light wave $\boldsymbol{E}(\omega_3)$ is required to propagate at the phase velocity $v = c_0/n(\omega_3)$ supporting constructive interference with the input fields $\boldsymbol{E}(\omega_1)$ and $\boldsymbol{E}(\omega_2)$, i.e. to enable energy transfer between the fundamental and mixed frequencies over some spatial distance. In terms of the wavevectors, this phase-matching condition takes [Boy08; Dmi99]

$$\boldsymbol{k}_3 = \boldsymbol{k}_1 \pm \boldsymbol{k}_2, \tag{2.40}$$

where the plus (minus) sign is valid for the SFG (DFG) process and $|\boldsymbol{k}_j| = \omega_j/v(\omega_j) = \omega_j n(\omega_j)/c_0$. In case of a collinear input beam geometry ($\boldsymbol{k}_1 \parallel \boldsymbol{k}_2$), Eq. (2.40) reduces to a scalar expression, $\omega_3 n(\omega_3) = \omega_1 n(\omega_1) \pm \omega_2 n(\omega_2)$, otherwise non-collinear phase-matching is required. Due to the usually normal dispersion $\mathrm{d}n/\,\mathrm{d}\omega > 0$ of the dielectric function in the spectral range where the material is optically transparent, the anisotropy of crystals is utilized by differently polarized light fields (cf. Sec. 2.2.1) to satisfy the phase-matching relation, Eq. (2.40). Depending on the polarization combinations, the cases of type I phase-matching (same polarization of input fields) and type II phase-matching (orthogonal polarization of fundamental waves) are distinguished. The detailed polarization states of the involved light beams are subject to the optical crystal symmetry and can be found, e.g. for uniaxial media, in Ref. [Dmi99].

A common method to achieve phase-matching is provided by the angular dependence of the extraordinary refractive index $n_\mathrm{e}(\theta)$ [Eq. (2.23)]. There, the orientation of the crystal axis has to be adjusted with respect to the irradiating optical beams (angle tuning or critical phase-matching) [Dmi99]. However, this application implies spatial beam walk-off, restricting the conversion efficiency (cf. Sec. 2.2.1). Other techniques of non-critical phase-matching exist, for example, by temperature tuning of the anisotropic dielectric functions of the crystal [Boy08].

Similar to the linear optical properties given by $\boldsymbol{\chi}^{(1)}$, the second (third, ...)-order electric susceptibilities are affected by the spatial symmetry of the medium. In general, the complex-valued, frequency-dependent third-rank tensor $\boldsymbol{\chi}^{(2)}$ has 3^3 components, but the number of nonzero independent values is reduced due to the symmetry restrictions. Group theory provides a way to classify crystalline material according to their symmetry elements (e.g. mirror planes, n-fold axes of rotation). The second-order optical properties are differentiated by the 32 crystallographic point groups [Boy08]. As a particular symmetry operation, inversion symmetry implies that $\boldsymbol{\chi}^{(2)} = \mathbf{0}$ (see proof in Sec. 2.3.1).

The remaining 21 non-centrosymmetric point groups exhibit one or more non-vanishing independent components, that are tabulated in, e.g., Ref. [Boy08]. For instance, crystals with cubic lattice belonging to point group $\bar{4}3m$ (Hermann-Mauguin notation), like zinc selenide (ZnSe), possess only a single unique $\chi^{(2)}$-component.

In contrast, the third-order optical susceptibility does not vanish at all, $\boldsymbol{\chi}^{(3)} \neq \mathbf{0}$, being allowed for centrosymmetric media as well due to the odd-order nature of the contributing force terms. However, the strength is several orders of magnitude smaller than $\chi^{(2)}$. Third-order processes include, e.g., the optical Kerr effect, leading to an intensity-dependent index of refraction $n = n(|\boldsymbol{E}|^2)$, two-photon absorption or four-wave mixing within the material [Boy08]. Furthermore, if an additional static electric field $E(0)$ is applied to the medium, $\chi^{(3)}$ gives rise to a contribution to the second-order polarizability $P^{(2)}(\omega_3)$, Eqs. (2.35)-(2.39), also in case of an isotropic bulk. This effect, called field-induced SHG/SFG/DFG, can be naturally present at charged gas-liquid or solid-liquid interfaces, such as the α-quartz/water system [Ohn16].

The typical dispersion behavior of the second-order susceptibility $\chi^{(2)}(\omega_3, \omega_1, \omega_2)$ can be obtained from a classical model, the anharmonic Lorentz oscillator [Boy08], which is an extension of the approach known from the dielectric function in linear optics [cf. Eq. (2.19)]. This model does not account for the energy eigenstates of the atoms and subsequent band structure formation in solids as revealed by quantum-mechanical calculations. Nevertheless, it provides a correct description of the actual nonlinear optical response of several materials, including dielectric media in the IR spectral range. The dynamics of a charged entity q situated in a non-parabolic potential $V(x) = m\omega_0^2 x^2 + ax^3$ with additional damping γ responding to an electric field $E(t)$ is determined by the equation of motion [Boy08]

$$\ddot{x} + 2\gamma\dot{x} + \omega_0^2 x + ax^2 = qE/m. \tag{2.41}$$

For an optical field consisting of two frequency components, $E_1 \mathrm{e}^{-\mathrm{i}\omega_1 t} + E_2 \mathrm{e}^{-\mathrm{i}\omega_2 t} + \text{c.c.}$, the amplitude of the oscillating solution $x^{(2)}(\omega_1 + \omega_2)\mathrm{e}^{-\mathrm{i}(\omega_1+\omega_2)t}$ reads

$$x^{(2)}(\omega_1 + \omega_2) = \frac{-2a(q/m)^2 E_1 E_2}{D(\omega_1 + \omega_2) D(\omega_1) D(\omega_2)} \tag{2.42}$$

with the function $D(\omega) = \omega_0^2 - \omega^2 - \mathrm{i}\gamma\omega$, whose inverse characterizes the resonance behavior of a classical Lorentz oscillator, $\chi^{(1)} \propto 1/D(\omega)$. Calculation of the nonlinear polarization $P(\omega_1 + \omega_2) = nqx^{(2)}$, where n is the density of the oscillating particles, and comparison with Eq. (2.37) yields the second-order susceptibility

$$\chi^{(2)}(\omega_1 + \omega_2, \omega_1, \omega_2) = \frac{na(q^3/m^2)}{\epsilon_0 D(\omega_1 + \omega_2) D(\omega_1) D(\omega_2)}. \tag{2.43}$$

Thus, the nonlinear susceptibility is essentially a product of the first-order susceptibilities $\chi^{(1)}(\omega)$ at the corresponding frequencies [Boy08],

$$\chi^{(2)}(\omega_1+\omega_2,\omega_1,\omega_2)=\frac{\varepsilon_0^2 ma}{n^2q^3}\chi^{(1)}(\omega_1+\omega_2)\chi^{(1)}(\omega_1)\chi^{(1)}(\omega_2). \tag{2.44}$$

This behavior is known as Miller's rule [Mil64]. The relationship allows to express the magnitude and dispersion of the nonlinear optical coefficient in terms of known dielectric constants $\varepsilon(\omega)$ [Bel72], indicating that a stronger nonlinearity is present for a larger index of refraction. However, the condition is not valid near resonances [Fau66], i.e. only if all frequencies are within the transmission region. An expression of the second-order susceptibility derived from the quantum-mechanical analysis is given in the next section, see Eq. (2.48).

2.3 Vibrational Sum-Frequency Generation Spectroscopy

As a second-order nonlinear optical process, SFG requires electromagnetic radiation with strong field amplitudes, applied to a medium of non-vanishing $\boldsymbol{\chi}^{(2)}$-tensor. Due to the spectral dispersion of the susceptibility components $\chi^{(2)}_{ijk}(\omega_3,\omega_1,\omega_2)$ and the sensitivity of the third-rank tensor to the symmetry of the investigated system, SFG spectroscopy is a versatile method to probe resonant vibrational modes at interfaces, which have inherently broken inversion symmetry, such as molecular adsorbates at surfaces, gas/liquid interfacial layers, or buried interfaces [She89]. Applications extend to time-resolved studies of (photo)chemical processes [Bon00; Bac05] and high-resolution nonlinear microscopy of biological material [Ji06; Chu13].

2.3.1 Theoretical Background

The phenomenon of sum-frequency generation relies on the interaction of two optical fields with amplitudes $\boldsymbol{E}(\omega_1)$ and $\boldsymbol{E}(\omega_2)$ and different (angular) frequencies ω_1 and ω_2 within a medium of finite $\chi^{(2)}$-susceptibility, Fig. 2.4(a). Consequently, a polarization $\boldsymbol{P}^{(2)}(\omega_3)$ of the medium oscillating at the sum-frequency $\omega_3=\omega_1+\omega_2$ is induced [cf. Eq. (2.37)]:

$$\boldsymbol{P}^{(2)}(\omega_3)=\epsilon_0\boldsymbol{\chi}^{(2)}(\omega_3,\omega_1,\omega_2):\boldsymbol{E}(\omega_1)\boldsymbol{E}(\omega_2). \tag{2.45}$$

This electric polarization acts as radiation source for the emitted field $\boldsymbol{E}(\omega_3)$, whose intensity $I\propto|\boldsymbol{E}|^2$ is given by

$$I(\omega_3)\propto\left|\boldsymbol{P}^{(2)}(\omega_3)\right|^2\propto\left|\chi^{(2)}\right|^2 I(\omega_1)I(\omega_2). \tag{2.46}$$

In general, the nonlinear susceptibility tensor components $\chi^{(2)}_{ijk}$ can be separated in terms of non-resonant and resonant contributions [She16]:

$$\chi^{(2)}(\omega)=\chi^{(2)}_{\mathrm{NR}}+\chi^{(2)}_{\mathrm{R}}=|\chi^{(2)}_{\mathrm{NR}}|\mathrm{e}^{\mathrm{i}\phi}+\sum_r\frac{\chi^{(2)}_r}{\omega_r-\omega-\mathrm{i}\Gamma_r}. \tag{2.47}$$

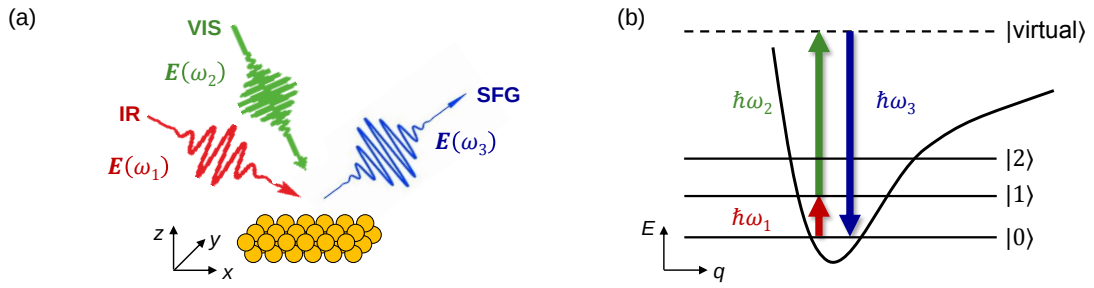

Fig. 2.4 Principle of IR-VIS SFG. (a) Two optical waves at ω_{IR} and ω_{VIS} frequency are overlapped in time and space on a nonlinear medium. Radiation at the sum-frequency $\omega_3 = \omega_1 + \omega_2$ is generated. (b) Energy level diagram of the process. The IR radiation excites a vibrational mode and is upconverted by the VIS field to a virtual state. The incident energy is released by photon emission at frequency ω_3.

Here, the resonance r is characterized by a Lorentz oscillator of amplitude $\chi_r^{(2)}$, center frequency ω_r and damping constant Γ_r, whereas the non-resonant contribution is determined by the amplitude $|\chi_{\mathrm{NR}}^{(2)}|$ and relative phase ϕ. The non-resonant SFG arises due to a collective electronic response from the polarized material.

In case of vibrational SFG spectroscopy, the technique utilizes the infrared spectral dependence of the second-order susceptibility $\chi^{(2)}(\omega_3, \omega_1, \omega_2)$ to probe vibrational modes [She16]: While the frequency of one input field, ω_2, is fixed, the other one, ω_1, is tuned to excite the vibration ω_r of the investigated material system. The photon energies of both the constant frequency (ω_2) and sum-frequency (ω_3) radiation are usually chosen to do not match other material resonances. Caused by the resonant enhancement in $\chi^{(2)}(\omega_1)$, the observed SFG spectra of Eq. (2.46), plotted as function of the variable input frequency, $I_{\mathrm{SFG}}(\omega_1)$, contain information about the activated vibrational modes, which show up as Lorentzian-shaped lines. The derived information might be the oscillator strength $|\chi_r^{(2)}|$, the frequency (shift) ω_r, the orientation or the dephasing constant Γ_r of the mode, each affected by the coupling among the vibrations and the chemical composition of the environment [She16].

The energy levels of the involved vibrational modes and the incident as well as emitted photons are depicted in Fig. 2.4(b). There, the ground, first and second excited vibrational state of the system are denoted as $|0\rangle$, $|1\rangle$ and $|2\rangle$, respectively. The SFG process involves the resonant excitation of the transition $|0\rangle \rightarrow |1\rangle$ by the photon $\hbar\omega_1$, while the second incident radiation $\hbar\omega_2$ promotes the material to a virtual, i.e. non-eigenstate, quantum level $|\mathrm{virtual}\rangle$ [Vid05]. The transferred energy is released as a photon $\hbar\omega_3$ of higher energy compared to the input, thereby bringing the system back to the vibrational ground state. These processes occur simultaneously within the material. Due to the conservation of total energy, $\hbar\omega_3 = \hbar\omega_1 + \hbar\omega_2$, SFG is a parametric process, also termed parametric up-conversion since $\omega_3 > \omega_1$.

An alternative description of the SFG process is provided by the following picture [Mor18]: The pump radiation ω_1 is absorbed by an IR-active transition to populate the excited eigenstate $|1\rangle$. Subsequently, the photon ω_2 interacts with the coherent state via anti-Stokes Raman scattering, resulting in a blue-shift of the frequency towards $\omega_3 > \omega_2$. Thus, the vibrational mode ω_r is required to be IR- as well as Raman-active in order to take part in SFG spectroscopy, see also Eq. (2.49).

The strength of the resonant contribution $\chi^{(2)}_{\mathrm{R}}$ is related to the microscopic properties of the molecular or crystalline normal modes, as described by the hyperpolarizability β. Taking into account the coordinate transformation from the molecular (a, b, c) to the laboratory (i, j, k) framework and weighting by the density n of vibrating units, the relation reads [Vid05]

$$\chi^{(2)}_{ijk} = n \left\langle \beta_{abc} \right\rangle_{ijk} . \tag{2.48}$$

Then, in the quantum mechanical formalism, the hyperpolarizability is given by [Vid05]

$$\beta_{abc} = \frac{2}{\hbar} \frac{\left\langle 0 \left| \frac{\partial \mu_c}{\partial q} \right| 1 \right\rangle \left\langle 1 \left| \frac{\partial \alpha_{ab}}{\partial q} \right| 0 \right\rangle}{\omega_{10} - \omega - \mathrm{i}\Gamma_{10}}. \tag{2.49}$$

There, $\partial \mu_c / \partial q$ and $\partial \alpha_{ab} / \partial q$ denote the derivatives of the electric dipole transition moment $\boldsymbol{\mu}$ and the polarizability tensor $\boldsymbol{\alpha}$ in the electronic ground state, respectively, with regard to the normal mode coordinate q; ω_{10} and Γ_{10} being the frequency and damping of the vibration. This indicates that, as discussed above, for a vibrational mode to be observed in the SFG spectrum, it has to be IR active ($\partial \mu / \partial q \neq 0$) as well as Raman allowed ($\partial \alpha / \partial q \neq 0$). The selection rule differs from other vibration-sensitive optical techniques (IR spectroscopy, Raman scattering, cf. Sec. 2.1.2) and can be used to provide complementary information.

For a large number of bulk media, including liquids, amorphous solids (like glass) and many crystals which are characterized as centrosymmetric, the second-order susceptibility vanishes, $\boldsymbol{\chi}^{(2)} = \mathbf{0}$, within the electric dipole approximation [Boy08]. The reason is the inherent inversion symmetry of these media (i.e. $\chi^{(2)}_{ijk} = \chi^{(2)}_{-i,-j,-k}$). This can be derived from the condition that if the directions of the incident electric fields are reversed, the induced polarization has to invert its sign as well, whereas $\chi^{(2)}$ is invariant to the inversion [Mor18]:

$$-\boldsymbol{P}^{(2)}(\omega_3) = \epsilon_0 \boldsymbol{\chi}^{(2)} : (-\boldsymbol{E}(\omega_1))(-\boldsymbol{E}(\omega_2)). \tag{2.50}$$

To satisfy both Eqs. (2.45) and (2.50), $\chi^{(2)}$ must be zero. More generally, all even-order susceptibilities of centrosymmetric media are parity-forbidden. In the case of crystalline solids, a wide range of elemental metals and semiconductors are affected by that [McG96]. Higher-order terms in the multipole expansion of the fields, however, can give rise to electric quadrupole or magnetic dipole contributions to the bulk second-order

nonlinear susceptibility. In general, these are neglegible in comparison to the SFG intensity generated from the interface between two media. There, the inversion symmetry is broken in any case, resulting in a nonzero quadratic susceptibility caused by electric dipoles, $\chi^{(2)} \neq 0$, even if the adjacent materials are centrosymmetric. Therefore, SFG spectroscopy is an intrinsically surface-sensitive technique when applied to media possessing inversion symmetry [She89].

The fact that centrosymmetric solids (or molecules) are not allowed to take part in SFG (or DFG) processes is also directly obtained from the rule of mutual exclusion (cf. Sec. 2.1.2). Since modes can not be both IR and Raman active there, the hyperpolarizability contribution of Eq. (2.49) vanishes at all.

The information regarding the presence, strength and symmetry of vibrational modes has to be obtained by a thorough quantitative analysis of the measured SFG spectra. In the following, a brief description of the exact relation between emitted SFG intensity and incident light fields will be given, considering several factors [Mor18].

First, the second-order polarization $\boldsymbol{P}^{(2)}(\omega_3)$ is induced by the electric fields according to Eq. (2.45). However, the field $\boldsymbol{E}(\omega_{1,2})$ inside the material differs from the incident radiation due to Fresnel reflections at the sample surfaces. Thus, Fresnel factors $F(\omega, \theta)$ have to be included, deduced from the field amplitude transmission coefficients and depending on wavelength ω and angle of incidence θ. Due to the boundary conditions valid for an electromagnetic field at the interface between two optically different media, the $F(\omega, \theta)$ factor is polarization-dependent. A derivation of the Fresnel factors, summarized by the diagonal tensor $\mathbf{F}(\omega) = \mathrm{diag}(F_{xx}, F_{yy}, F_{zz})$, can be found in Ref. [Mor18]. The modified equation for the induced polarization reads

$$\boldsymbol{P}^{(2)}(\omega_3) = \epsilon_0 \left(\boldsymbol{\chi}^{(2)} : \mathbf{F}(\omega_1)\hat{\boldsymbol{e}}^{\mathrm{I}}(\omega_1)\, \mathbf{F}(\omega_2)\hat{\boldsymbol{e}}^{\mathrm{I}}(\omega_2) \right) E^{\mathrm{I}}(\omega_1) E^{\mathrm{I}}(\omega_2), \tag{2.51}$$

with the unit vector of the electric field polarization $\hat{\boldsymbol{e}}(\omega) = \boldsymbol{E}(\omega)/|\boldsymbol{E}(\omega)|$ and the superscript indicating the surrounding linear optical medium I.

Second, the nonlinear susceptibility is composed of two contributions, $\boldsymbol{\chi}^{(2)} = \boldsymbol{\chi}^{(2)}_{\mathrm{S}} + \boldsymbol{\chi}^{(2)}_{\mathrm{B}}$, originating from the surface (S) and the bulk (B) of the sample. Depending on the medium, one of them might be dominant. In general, the emitted sum-frequency field $\boldsymbol{E}^{\mathrm{I}}(\omega_3)$ outside the sample is given by [She16]

$$\hat{\boldsymbol{e}}^{\mathrm{I}}(\omega_3)\boldsymbol{E}^{\mathrm{I}}(\omega_3) \propto \left(\mathbf{F}(\omega_3)\hat{\boldsymbol{e}}^{\mathrm{I}}(\omega_3) \cdot \boldsymbol{\chi}^{(2)}_{\mathrm{eff}} : \mathbf{F}(\omega_1)\hat{\boldsymbol{e}}^{\mathrm{I}}(\omega_1)\, \mathbf{F}(\omega_2)\hat{\boldsymbol{e}}^{\mathrm{I}}(\omega_2) \right) E^{\mathrm{I}}(\omega_1) E^{\mathrm{I}}(\omega_2) \tag{2.52}$$

with

$$\boldsymbol{\chi}^{(2)}_{\mathrm{eff}} = \boldsymbol{\chi}^{(2)}_{\mathrm{S}} + \frac{\mathrm{e}^{\mathrm{i}\Delta k_z l} - 1}{\mathrm{i}\Delta k_z} \boldsymbol{\chi}^{(2)}_{\mathrm{B}}. \tag{2.53}$$

There, the phase mismatch Δk_z of the propagating waves inside the sample of length l has been taken into account [She16].

Finally, the intensity of the SFG radiation $I(\omega_3)$ can be determined from the field amplitude. According to the general relation, $I(\omega) = \frac{n(\omega)c_0\varepsilon_0}{2}|E(\omega)|^2$, and assuming air as surrounding medium, the measured observable is

$$I^{\mathrm{I}}(\omega_3) \propto \left|\mathbf{F}(\omega_3)\hat{\boldsymbol{e}}^{\mathrm{I}}(\omega_3) \cdot \boldsymbol{\chi}^{(2)}_{\mathrm{eff}} : \mathbf{F}(\omega_1)\hat{\boldsymbol{e}}^{\mathrm{I}}(\omega_1)\, \mathbf{F}(\omega_2)\hat{\boldsymbol{e}}^{\mathrm{I}}(\omega_2)\right|^2 I^{\mathrm{I}}(\omega_1)I^{\mathrm{I}}(\omega_2). \tag{2.54}$$

Thus, the sum-frequency response is modified by dispersive linear optical properties, entering via the Fresnel tensor $\mathbf{F}(\omega)$ and, in case of bulk-dominated SFG, additionally via the wavevector mismatch $\Delta\mathbf{k}(\omega)$. If an optical anisotropy is present in the nonlinear medium, the involved dielectric function $\varepsilon(\omega)$ depends on the polarization state of the light waves.

The relevant quantity of interest in SFG spectroscopy is, however, the second-order susceptibility tensor $\boldsymbol{\chi}^{(2)}(\omega_3, \omega_1, \omega_2)$. The sensitivity to the incident frequency ω_1 provides the spectral contrast necessary for the identification of the vibrational mode. Information regarding the symmetry of the tensor, and thus of the material system, is acquired by a particular geometry selection. This includes the chosen combination of polarizations $\boldsymbol{E}(\omega)$ (s or p) for input and output electric fields at the frequencies $\omega_1, \omega_2, \omega_3$ as well as the angles of incidence θ_1, θ_2. By taking multiple SFG spectra under different experimental conditions, the individual $\chi^{(2)}_{ijk}$ components are disentangled [Mor18].

Due to the coherence of the SFG process, the generated signal possesses a well-defined directionality. The direction of the sum-frequency emission is determined by the conservation law of photon momentum. In case of a reflection geometry, the angle of propagation of the generated sum-frequency light θ_3 is set by the wave vector components of the incident fields parallel to the interface,

$$\begin{aligned} \boldsymbol{k}_{\parallel}(\omega_3) &= \boldsymbol{k}_{\parallel}(\omega_1) + \boldsymbol{k}_{\parallel}(\omega_2) \\ \Rightarrow\ n(\omega_3)\omega_3 \sin\theta_3 &= n(\omega_1)\omega_1 \sin\theta_1 + n(\omega_2)\omega_2 \sin\theta_2, \end{aligned} \tag{2.55}$$

with the angle of incidence θ_1 (θ_2) of the input field at frequency ω_1 (ω_2) and the refractive index n of the nonlinear medium. Thus, besides the geometric arrangement of the electromagnetic waves, their frequencies determine the SFG emission direction as well.

2.3.2 Experimental Methods

When using sum-frequency generation to probe vibrational modes at interfaces, of adsorbates or bulk materials, various experimental approaches have been developed. Usually, IR-VIS SFG spectroscopy is applied to analyze resonances in the so-called fingerprint region. On the one hand, MIR radiation with a photon energy in the order of $\hbar\omega_1 \sim 50\,\mathrm{meV} - 100\,\mathrm{meV}$ resonantly excites the vibrational mode ω_r. On the other hand, light at a fixed VIS frequency $\omega_2 \gg \omega_1$ is used for up-conversion, generating

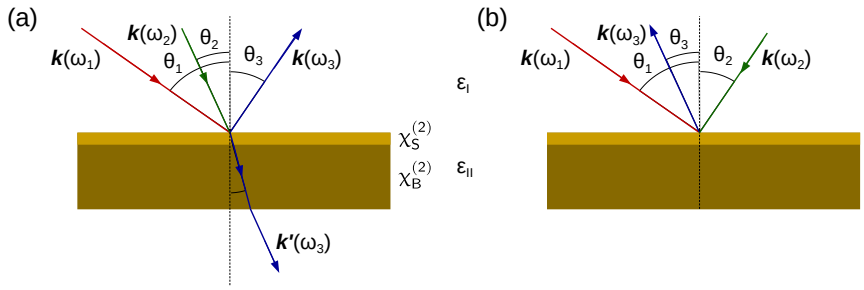

Fig. 2.5 Reflection geometry of beam propagation in IR-VIS SFG spectroscopy. (a) Co-propagation scheme: The input beams ω_1 and ω_2 are incident from the same side relative to the surface normal (dashed). (b) Counter-propagation arrangement: The IR and VIS beam have nearly the same angle of incidence θ_1 and θ_2, but propagate from opposite directions. The emission angle θ_3 of the SFG light has to obey the condition $k(\omega_3)\sin\theta_3 = k(\omega_2)\sin\theta_2 \pm k(\omega_1)\sin\theta_1$, where the positive sign is valid for co-propagation, the negative one for counter-propagation.

easily measurable SF radiation $\omega_3 \approx \omega_2$, in contrast to the more difficult to detect IR range [Boy08].

The critical component in IR-VIS spectroscopy is the source of the MIR radiation ω_1. For that, either table-top optical parametric amplifier (OPA) systems [GS87] or accelerator-based free-electron lasers (FEL) [Bar94] are available. While OPA systems need additional stages of frequency conversion (like DFG) in nonlinear optical crystals to obtain a sufficient spectral tuning range, the FEL output can be directly employed. However, FEL facilities require a larger infrastructure (see Sec. 2.4).

Depending on the bandwidth of the applied IR radiation, two approaches to collect the vibrational spectra can be differentiated [She16]: If narrowband radiation ($\Delta\lambda/\lambda < 0.5\,\%$) is utilized, the center frequency ω_1 is continuously scanned over the spectral range of the modes ω_r. In contrast, broadband fs light sources ($\Delta\omega > 250\,\mathrm{cm}^{-1}$) covering multiple resonances at once are used in connection with a multi-channel spectrometer for faster spectra acquisition. In case of scanning-type SFG spectroscopy, the spectral resolution is limited in general by the bandwidth $\Delta\omega_1$ and hence by the duration τ of the IR pulse, according to the uncertainty principle, $\Delta\omega\,\tau \geq 1/2$. Since short pulses are preferred for a higher efficiency of the SFG process, a trade-off has to be found. Commonly, pulses of 1 ps FWHM are employed, providing $5\,\mathrm{cm}^{-1}$ spectral resolution [She16]. For broadband IR measurements, the resolution is set by the light source with the smallest bandwidth. Thus, narrowband VIS radiation ($\Delta\omega_2 \sim 5\,\mathrm{cm}^{-1}$) is advised to obtain a good spectral resolution.

In order to access vibrational spectra of surfaces, the SFG signal is usually probed in reflection geometry, see Fig. 2.5. There, two types of beam arrangements can be distinguished: On the one hand, IR and VIS beams are incident onto the sample from the same quadrant spanned by the surface and its normal, Fig. 2.5(a), the so-called

co-propagating geometry. Otherwise, in the counter-propagating scheme, the two input beams are directed from opposite quadrants, Fig. 2.5(b). Depending on the polarizations, this can enhance the coupling of electric field and dipole moment, and hence the sensitivity to certain vibrational modes [Din09]. Also, spatial separation of the SFG beam from the fundamental reflections is simplified, increasing the detectable dynamic range. However, some effort is required to identify the propagation direction of the weak sum-frequency light given by momentum conservation. Thus, the co-propagation arrangement is commonly preferred.

A measurement of the SFG intensity, given by Eq. (2.54), just contains information about the absolute value of the complex quadratic susceptibility, $|\chi^{(2)}|$. However, knowledge about the spectral phase $\arg(\chi_2)$ provides additional insights into the material response. For example, the absolute out-of-plane orientation of the adsorbed molecule on the surface can be directly determined from the sign of $\mathrm{Im}(\chi^{(2)})$ of the resonant contribution. A sign change, or equivalently, a phase shift of $\arg(\chi^{(2)})$ by π, then corresponds to a flip-flop re-orientation of the molecule [Nih09]. Such investigations are enabled by phase-sensitive SFG spectroscopy. For that, it is necessary to interfere the sum-frequency wave with a reference field, the local oscillator [Tha18]. Thus, the technique is based on heterodyne detection, in contrast to the phase-insensitive homodyne scheme described above.

2.4 Free-Electron Laser Radiation

Since its invention in the 1970s [Mad71; Dea77], free-electron laser radiation has enabled a variety of new experimental investigations, such as protein crystallography in biology [Cha11], ultrafast carrier dynamics in condensed matter physics [Mit15], or the imaging of excited states in complex materials [Wan12]. Due to the ability to generate coherent, intense and ultrafast light pulses at any desired optical wavelength, the free-electron laser (FEL) enables optical spectroscopy and imaging at high spectral, spatial and temporal resolution scales. The general advantage of the FEL concept is based on the continuous tunability of the emitted photon energy, ranging from the low-frequency terahertz and infrared region to the ultraviolet and X-ray regime with sub-Angstrom wavelengths. The technical realization of the FEL differentiates for the long- and short-wavelength region due to physical restrictions of having highly reflective cavity mirrors available for the desired wavelength [Sch14]. In the infrared, FEL oscillators are used, whereas UV/X-ray FELs are built as single-pass amplifiers. In the following, the operation principle of the FEL oscillator is detailed and the characteristics of the emitted electromagnetic radiation are discussed.

2.4.1 FEL Oscillator: Principle of Operation

In contrast to a conventional quantum laser, the FEL does not employ electronic transitions between discrete energy levels of atomic or molecular states as in condensed matter or gases. Instead, highly energetic unbound electrons propagating in a magnetostatic field are utilized, therefore the name *free-electron* laser [Sch14].

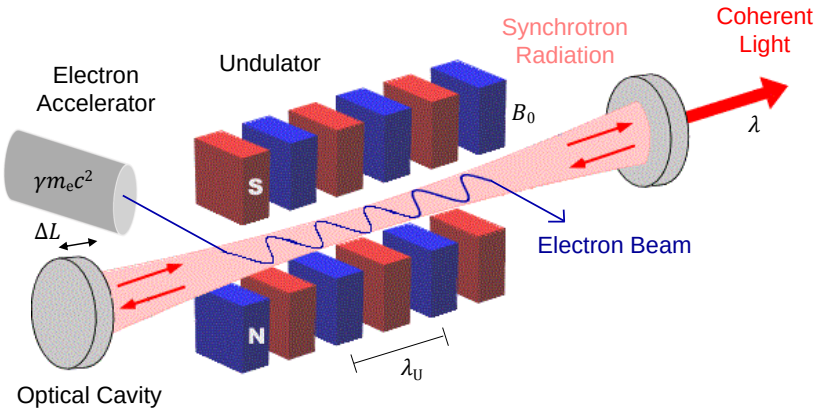

Fig. 2.6 Setup of a free-electron laser oscillator. The kinetic energy of the relativistic electron beam generated in a linear accelerator is transferred into electromagnetic energy due to the wiggling motion in the undulator magnet. The radiation is captured within an optical resonator and amplified by multiple passes.

The setup of an FEL oscillator is sketched in Fig. 2.6. The light source consists of a relativistic electron beam, an undulator and an optical cavity. The electron beam acts simultaneously as pump source and gain medium, which is supplied by a linear accelerator (linac). To operate an infrared FEL, the required kinetic energy $\gamma m_e c_0^2$ of the accelerated electrons is a few tens of MeV [Col90]. Consequently, the velocity is close to the speed of light and the particle dynamics has to be treated relativistically (Lorentz factor $\gamma \sim 10$). The undulator consists of a magnetic structure of periodically alternating poles with amplitude B_0 and period length λ_U. Due to the Lorentz force acting transversely, electrons undergo a sinusoidal motion along the longitudinal undulator axis (named z-axis hereafter). Thus, the charged particles emit incoherent electromagnetic radiation (synchrotron light), which is captured within the optical cavity.

The interaction of the generated optical wave and the co-propagating electrons results in an energy transfer which can amplify the optical field while decelerating the electrons, depending on their relative phases. Thus, a density modulation of the electron beam evolves, called micro-bunching [Sch14]. Optical waves emitted from the charged micro-bunches overlap in phase, consequently generating coherent FEL radiation. By performing multiple round trips of the light field within the cavity and overlapping with the electron bunches at the resonant wavelength, the radiation intensity is successively amplified by a small gain. Finally, a fraction of the intra-cavity optical power is extracted through a hole in one resonator mirror, whereas the electrons are collected by a beam dump after passing the undulator.

The center wavelength λ of the fundamental FEL radiation is determined by the kinetic energy of the electrons as well as the strength and period of the undulator field.

The so-called resonance condition is given by [Col90; Sch14]

$$\lambda = \frac{\lambda_\mathrm{U}}{2\gamma^2}\left(1 + \frac{K^2}{2}\right), \tag{2.56}$$

where the undulator parameter is

$$K = \frac{\mathrm{e}B_0\lambda_\mathrm{U}}{2\pi m_\mathrm{e}c_0}. \tag{2.57}$$

A deviation of the relation can be found in Ref. [Col90]. From a qualitative point of view, on the one hand, the undulator period λ_U is shortened for the highly relativistic electrons to $\lambda_\mathrm{U}/\gamma$ due to Lorentz contraction. On the other hand, the emitted light is observed in the laboratory framework, inserting a second Lorentz factor due to the relativistic Doppler shift of the optical wavelength, $\lambda/2\gamma$. The emitted wavelength λ can be changed either by tuning the Lorentz factor γ in Eq. (2.56) via the linac's electron energy or by varying the undulator parameter K via the magnetic field strength, which is usually done by adjusting the gap size between the two magnet banks. Typical values for the undulator parameter are $0.5 \lesssim K \lesssim 3$ [Col90].

In most cases, the linac operates at radio frequencies (RF) [Sch14], producing a beam of electron pulses separated by the repetition period $1/f_\mathrm{rep}$. Since the electron beam provides the gain medium, the FEL output consists of light pulses with the same repetition frequency. Therefore, the length of the cavity L has to be chosen to be of a round-trip time corresponding to (a multiple of) the electron bunch spacing, $2L = c_0/f_\mathrm{rep}$. However, exact temporal synchronism between the electron bunches and the generated FEL light pulses does not allow a steady-state laser oscillation [Col90; Jar93]. This effect, called 'laser lethargy', is caused by the slippage of the electron bunches while transversing the undulator. Due to the slower velocity of the particles, they fall behind with respect to the optical wave. As a result, the optical pulse experiences gain only at the rear end and does not grow in intensity. In order to reach efficient optical energy extraction, the light pulse has to be shifted towards the peak of the electron pulse. This is realized by the cavity detuning ΔL as an additional degree of freedom, enabling a shortening of the cavity length to $L = L_0 - \Delta L$. By means of ΔL, the pulse shape and spectral bandwidth of the FEL radiation can be altered [Col90].

2.4.2 Classical FEL Theory

The theory describing the motion of the electrons in the undulator magnetic field and the evolution of the optical field within the resonator has been developed shortly after invention of the FEL [Mad71; Col77]. For an accurate description, it is sufficient to consider classical electrodynamics within the relativistic regime [Col77; Col90]. Quantum effects like discrete electron momentum recoil can be neglected in most cases [Kli15]. The deviation of the classical FEL theory starts from the Lorentz force equation governing the electrons' trajectories within the undulator. The accelerated charges give rise to electromagnetic fields; both mutually interact via the Maxwell's equations. A

complete description is provided in Ref. [Col90]. Rigoros calculus under the assumption of a slowly varying envelope of the optical field reduces the problem to a set of fairly simple differential equations, the universal FEL equations [Col90; McN10]: First, the pendulum equation,

$$\ddot{\zeta} = |a| \cos(\zeta + \varphi), \tag{2.58}$$

governing the motion of each electron particle with phase ζ and phase velocity $\nu = \dot{\zeta}$ inside the bunch, and secondly, the wave equation,

$$\dot{a} = -j \left\langle \mathrm{e}^{-\mathrm{i}\zeta} \right\rangle, \tag{2.59}$$

describing the complex optical field $a = |a|\mathrm{e}^{\mathrm{i}\varphi}$ with amplitude $|a|$ and phase φ. For each electron, a seperate pendulum equation (2.58) has to be solved. The optical wave in Eq. (2.59) is driven by the electron beam current j, thus the average $\langle ... \rangle$ goes over all sampled electrons. The set of equations is valid for both weak and well as strong optical fields and constitutes the basis of the Maxwell-Lorentz theory of the FEL [Col90]. A closer look at the nonlinear differential equation Eq. (2.58) resembles that it is similar to the physical pendulum equation without small-angle approximation. Consequently, nonlinear electron dynamics is expected to occur. From inspection of Eq. (2.59) it is clear that there is only amplification of the optical intensity $I = |a|^2$ if there is a change in the initially randomly distributed electron phases, meaning that the average value $\left\langle \mathrm{e}^{-\mathrm{i}\zeta} \right\rangle$ has to become nonzero. This bunching process of the electron particles is depicted in Fig. 2.7(a) for a typical set of FEL oscillator parameters. The electron bunch evolves after some time τ of interaction with the radiation field towards the end of the undulator ($\tau = 1$). Thus, the gain during one pass increases, as defined by

$$g(\tau) = \frac{\Delta I}{I_0} = \frac{|a(\tau)|^2 - |a_0|^2}{|a_0|^2} = \frac{I}{I_0} - 1. \tag{2.60}$$

A plot of $g(\tau)$ is shown in Fig. 2.7(b). Usually, FELs for IR generation are operated as small-gain oscillators. Therefore, multiple passes through the undulator embedded within the resonator cavity are necessary to extract a powerful optical beam (typically ~ 500 round trips).

2.4.3 Radiation Characteristics and Applications

Free-electron laser facilities are in increasing demand due to the unique properties of the emitted electromagnetic radiation [Sch14; Mur09]:

- Coherence: A narrow spectral linewidth and tight spatial focusing of the light onto the sample can be obtained.

- Spectral tunability: Due to the construction of the FEL and its classical physical operation principle, the optical wavelength λ can be continuously changed. Most

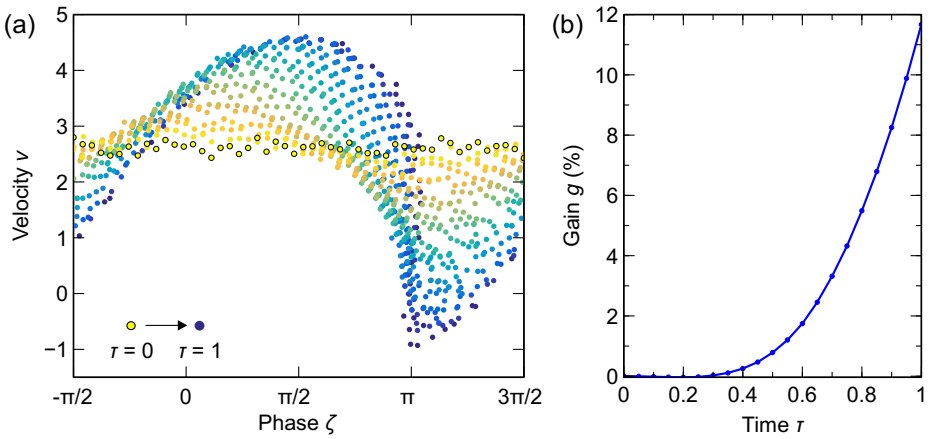

Fig. 2.7 Micro-bunching of electrons in phase space and FEL gain development. (a) The trajectories show the temporal development of each electron's phase ζ and velocity ν while transversing the undulator (start $\tau = 0$, end $\tau = 1$). Initially, the phases are randomly distributed in the range of 2π and the velocity $\nu_0 \neq 0$. During the interaction with the light waves, the charge density is modulated to bunch at phase $\phi = \pi$. Some electrons experience an increase in energy, but the major part slows down ($\nu < \nu_0$) and loses energy to the optical field. (b) Exponential growth of the optical gain $g(\tau)$ [Eq. (2.60)] towards the end of the undulator where bunching is significant.

importantly, spectral regions not accessible by other light sources can be addressed (e.g. far-IR or X-ray photon energies).

- Brightness: Highly energetic pulses together with the short pulse duration create an optical beam of high peak intensity. Nonlinear processes of light-matter interaction or strong-field phenomena are therefore easily probed.

- Ultrashort pulses: Near-transform-limited pulses with durations τ_p in the order of picoseconds (for IR) to some femtoseconds (for x-rays) are directly generated, corresponding to few cycles of the optical field. This is advantageous for the investigation of ultrafast dynamics. In the case of the FEL oscillator, it can be manipulated also by the length L of the resonator.

- Narrowband radiation: The width of the fundamental FEL line is essentially determined by the gain bandwidth to be $\Delta\lambda/\lambda \approx 1/N_\mathrm{U}$, where N_U is the number of undulator periods [Sch14]. In the case of an FEL oscillator, the cavity detuning parameter ΔL controls the spectral bandwidth as well. Near-monochromatic radiation can be obtained (relative bandwidth down to $\Delta\lambda/\lambda < 0.3\,\%$).

- Polarization: The polarization state of the generated light is defined by the undulator geometry. In the case of infrared FEL oscillators, usually equipped with a planar undulator, linearly polarized optical output is delivered. For a helical undulator design circular polarization is created [Col90].

- Higher harmonics: A detailed FEL analysis gives a modified resonance condition $\lambda_n = \lambda/n$ with λ from Eq. (2.56) and $n = 1, 2, 3, \ldots$. However, only the odd frequency components ($n = 1, 3, 5, \ldots$) are emitted in direction of the z-axis in case of a planar undulator [Sch14].
- Repetition rate: FELs are capable of delivering energetic optical pulses with repetition frequencies in the MHz range up to 1 GHz, which is comparable to mode-locked solid-state lasers. This is beneficial for a high photon flux and efficient data acquisition due to the higher duty cycle.

In contrast to previous advanced photon sources (synchrotrons), FELs are classified as fourth generation accelerator-based light sources. In the first generation, synchrotron radiation (SR) generated as by-product at electron storage rings has been used. Later, SR from dedicated storage ring facilities was employed. In the 1990s, pure optical emission user facilities have been built (3^{rd} gen). There, the synchrotron radiation is produced by undulators reaching a peak brightness in the order of 10^{24} photons per (s mrad^2 mm^2 0.1 % bandwidth) [Sch14]. Nowadays, FELs are capable of delivering peak intensity values up to 10^{33}. Besides the much higher brilliance, the radiation emitted from FELs is coherent, whereas SR is incoherent due to the absence of micro-bunching.

As a current topic in the development of the FEL technology, X-ray FELs are reaching new records in terms of smaller wavelengths (down to $\lambda = 1\,\text{Å}$), shorter pulses ($\tau \sim 100\,\text{fs}$) and higher intensities (e.g., European XFEL, SwissFEL) [McN10]. At the other end of the optical spectrum, THz FELs are emerging (e.g., TELBE with $\lambda = 300\,\mu\text{m} - 3000\,\mu\text{m}$ [Kov17]). For wavelengths in betweeen, the possibility of two-color operation of an FEL has been demonstrated [Jar94]. An overview of the currently active large-scale FEL facilities, including the FHI FEL, can be found in Ref. [Ney18].

The mentioned characteristics of FEL radiation facilitate a variety of applications in different areas of scientific research, like structural biology, chemistry or condensed matter physics. X-ray FELs provide the potential for imaging the structure and dynamics of crystals or protein structures on the atomic length and time scales [Cha11]. On the other side, narrrow-band and tunable radiation can be utilized for selective excitation of quantum states in solid-state material, for example low-energetic, THz-frequency phonons, magnons or Landau level transitions [Mit15]. Additionally, the synchronization of the ultrafast FEL pulses with external lasers enables time-resolved two-color studies in a pump-probe fashion.

3 Experimental Methods

In order to perform sum-frequency generation spectroscopy experiments of crystalline materials, a wavelength-tunable free-electron laser is chosen, covering the full MIR spectral region for resonant excitation of lattice vibrations. After a description of the technology and key parameters of the used FEL, the implemented sub-ps precision synchronization system and optical spectroscopy setup is outlined. Here, a table-top fiber oscillator is employed for upconversion of the FEL radiation, enabling two-color IR-VIS SFG spectroscopy in the frequency- and time-domain at ambient conditions.

3.1 FHI Infrared Free-Electron Laser

The free-electron laser at the FHI is an RF-based low-gain FEL oscillator-type source of coherent radiation, generating ps-short optical pulses in the MIR spectral region. The design is similar to other FEL oscillator facilities like FELIX (Netherlands) [Oep95] or CLIO (France) [Jar94]. The technical description of the FHI FEL system in the following details the electron source and linear accelerator (linac) section, the magnetic undulator within the optical cavity and the beamline part. A sketch of the FHI FEL system is depicted in Fig. 3.1. Further information is given in Ref. [Sch15a].

3.1.1 Accelerator Section

As it has been deduced from the resonance condition in Sec. 2.4.1, relativistic electrons with an energy in the range of a few tens of MeV are necessary to obtain IR FEL radiation. In a first step, electron bunches are emitted from a thermionic cathode ('electron gun') made of a tungsten metal filament alloyed with rhenium to lower the work function. Due to an electric current of 7.8 A, the cathode reaches temperatures of 1100 °C − 1200 °C. The charge carriers are extracted into an ultra-high vacuum tube of 10×10^{-9} mbar, where an electric potential difference of 38 kV accelerates the particles to the anode. In order to be accelerated efficiently, the electron bunch has to be compressed in time by a buncher cavity from around some hundreds of ps down to a few ps.

The RF master oscillator (MO) serving as clock for all FEL system components operates at a frequency of $f_{\mathrm{MO}} = 2.998$ GHz. It is composed of an 100 MHz quartz oscillator and an electronic unit for upconversion. The electron source is operated at the third sub-harmonic of the RF MO, $f_{\mathrm{MO}}/3 \sim 1$ GHz. This has been chosen due to the limited performance of a metal cathode at high frequencies, whereas the length requirement of the linac is reduced at higher frequencies, i.e. smaller RF wavelengths.

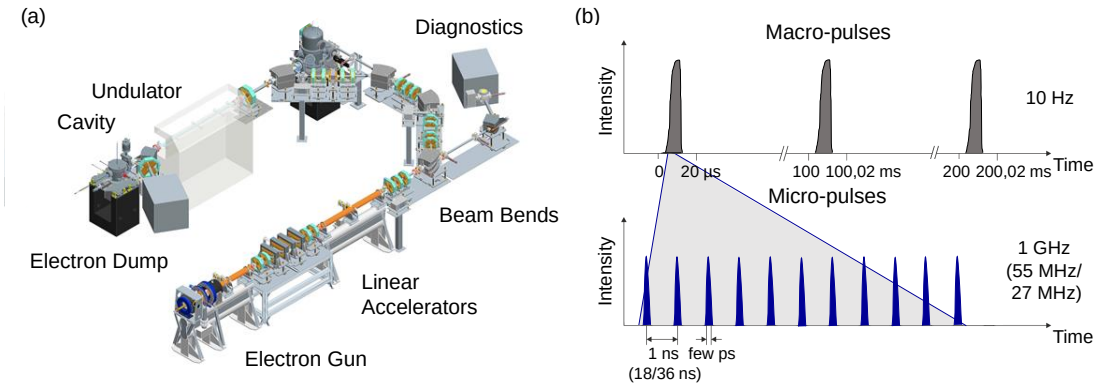

Fig. 3.1 Overview of the IR free-electron laser at the FHI. (a) FEL setup consisting of source and acceleration part for MeV electrons and undulator and cavity section for MIR radiation. (b) Temporal structure of generated coherent radiation. Macro-pulses of 10 µs duration, repeating at 10 Hz, are made up of ps-short micro-pulses with a repetition rate of 1 GHz (normal operation) or 55 MHz (low-repetition mode), matched to the table-top laser pulse frequency.

The electron accelerator section consists of two normal-conducting copper linacs operating at f_{MO}. The first one is used to accelerate the charged particles to a fixed energy of 20 MeV, whereas the second one decelerates or accelerates the electron bunches to the desired energy between 15 MeV $-$ 50 MeV. The energy spread of the final electron beam is less than 0.3 %. The particle beam consists of micro-bunches with around 200 pC charge each, repeated at the rate of $f_{\mathrm{MO}}/3$ within a macro-bunch time window (so-called shot) of usually 10 µs duration and 10 Hz repetition frequency. The macro-bunch structure is due to the necessity to fade out the Joule heating of the copper-made accelerators, which is in contrast to the continuous (cw) operation of a superconducting electron linac [Bha11]. The microwave power for the accelerators ($\sim$ 12 MW/10 µs) is delivered by klystrons via RF waveguides. A magnetic chicane in the accelerator section is available to shorten the electron bunch length even further, however, it has not been used throughout this work.

Besides the standard 1 GHz mode of the electron micro-bunch rate, sub-harmonics can be deduced from the RF MO to drive the electron gun at the lower frequencies of 27.8 MHz and 55.5 MHz, respectively. This corresponds to a micro-bunch spacing of 36 ns (or 18 ns) and has been chosen to match the round-trip time of an optical pulse within the FEL cavity, thus enabling single-bunch (or double-bunch) operation. The reduced repetition rates are delivered by a custom-made pulse generator providing voltage pulses of 160 V amplitude and $\sim$ 500 ps length to the gridded electron gun. The MHz pulse rates are useful to investigate FEL-induced dynamics in matter exceeding beyond the 1 ns relaxation time scale, as well as for the synchronization of the FEL with external table-top lasers operating at MHz repetition rates.

The path of the accelerated electron beam within the evacuted tube system towards the undulator is steered by quadrupole and dipole (electro-)magnets, see Fig. 3.1(a). While the quadrupoles are primarily used for (re-)collimation of the particle bunches, the dipoles are employed to bend the beam. For the 90° bending magnets, isochronous achromats are used. In principle, these allow a deflection of the electron bunches independent of the energy of the particles and do not affect the temporal bunch profile.

3.1.2 Undulator and Cavity

The undulator employed at the FHI FEL to generate IR radiation from the relativistic particles is of a planar type, thus producing linearly polarized light. The hybrid-magnet design of the undulator consists of $N = 50$ periods with $\lambda_U = 40\,\mathrm{mm}$ wavelength. Radiation-resistant NdFeB permanent magnets arranged in an alternating order are employed in the undulator. By adjusting the gap between the magnet banks, the magnetic field B_0 and thus the undulator parameter K, cf. Eq. (2.57), can be varied between 0.5 and 1.6. The typical magnetic flux density is in the order of 0.3 T. For a minimum gap size of 17 mm, the maximum value $K = 1.6$ is reached.

To capture the emitted IR waves and amplify them via multiple passes through the undulator, the optical cavity is formed by gold-plated concave spherical mirrors. At one end of the $L_0 = 5.4\,\mathrm{m}$ long resonator, the out-coupling of the laser radiation is accomplished by a 2.5 mm diameter hole within the mirror, set concentrically with the undulator axis. Although different hole sizes are available for efficient FEL power extraction depending on the optical wavelength, they are rarely changed. An essential degree of freedom is the length L of the cavity, which can be altered with a 1 µm step size via a translation stage. Conveniently, the cavity detuning ΔL is given in terms of the IR wavelength. The FHI FEL parameters of the accelerator, undulator and cavity are summarized in Tab. 3.1.

The temporal arrangement of the optical FEL pulses is determined by the sequence of the gain-providing electron bunches. Thus, IR micro-pulses of 1 GHz, 55.5 MHz or 27.8 MHz repetition frequency are emitted within a 10 µs long macro-pulse repeated at a 10 Hz rate, see Fig. 3.1(b).

The spectral range of the FHI FEL fundamental radiation, as given by Eq. (2.56), covers the entire MIR region, i.e. the wavelength of $\lambda = 3\,\mu\mathrm{m} - 50\,\mu\mathrm{m}$, corresponding to a wavenumber $\nu = 200\,\mathrm{cm}^{-1} - 3333\,\mathrm{cm}^{-1}$ or a photon energy of 25 meV – 400 meV. The extracted optical power depends on the emitted wavelength and the cavity detuning. In the 1 GHz mode, macro-pulse energies of several tens of mJ are available, corresponding to several µJ for each micro-pulse. At the low-repetition rates, the typical energy per macro-pulse is about 5 mJ.

Tab. 3.1 Parameters of electron accelerator, undulator and cavity of the FHI free-electron laser.

Parameter	Value
Electron kinetic energy E_{kin}	15 MeV - 50 MeV
Electron energy spread	< 50 keV
Electron bunch charge	~ 200 pC
Electron bunch length σ_{z}	1 ps - 5 ps
Normalized rms transverse emittance	$< 20\ \pi$ mm mrad
Lorentz factor γ	30 - 100
Undulator length L_{U}	2.0 m
Undulator periods N_{U}	50
Undulator wavelength λ_{U}	40.0 mm
Undulator parameter K	0.5 - 1.6
Cavity length L_0	5.4 m
Out-coupling hole diameter	2.5 mm
Optical wavelength λ	3 µm - 50 µm

Depending on the cavity detuning, the micro-pulse duration can be as short as 420 fs (FWHM) and increases up to several picoseconds, as it has been determined by second-order auto-correlation measurements [Sch15a]. The expected linear polarization of the generated light has been confirmed experimentally [Sch15a]. Intrinsically generated higher harmonics of the fundamental FEL radiation wavelength λ are observed up to the 11^{th} order.

Prior to the delivery of the IR beam to the user labs, a diagnostic station is used to monitor the FEL macro-pulse energy as well as the spectral profile using a Czerny-Turner grating spectrometer combined with a pyroelectric array detector. For a variation of the IR intensity, a set of five free-standing metal wire-grid attenuators with discrete power transmission levels (50 %, 33 %, 14.5 %, 13 %, 12 %) is available. A visible helium-neon laser can be used to align the IR beam path from the FEL cavity to the user setup. The radiation is transported to the lab via gold-coated mirrors in an evacuated beamline of approx. 50 m length. The out-coupling of the FEL light to the experimental setup is accomplished by a window made up of thallium bromo-iodide (KRS-5) material, which is transparent in the MIR range of 0.6 µm $-$ 40 µm.

3.2 Femtosecond Table-Top Laser – FEL Synchronization

To perform sum-frequency generation spectroscopy, the MIR FEL radiation is combined with NIR or VIS light provided by a table-top laser. Here, we employ a fiber-based Terbium-doped high-power femtosecond oscillator[1], operating at the center wavelength

[1] Origami HP, Onefive GmbH, Switzerland (now part of NKT Photonics A/S, Denmark)

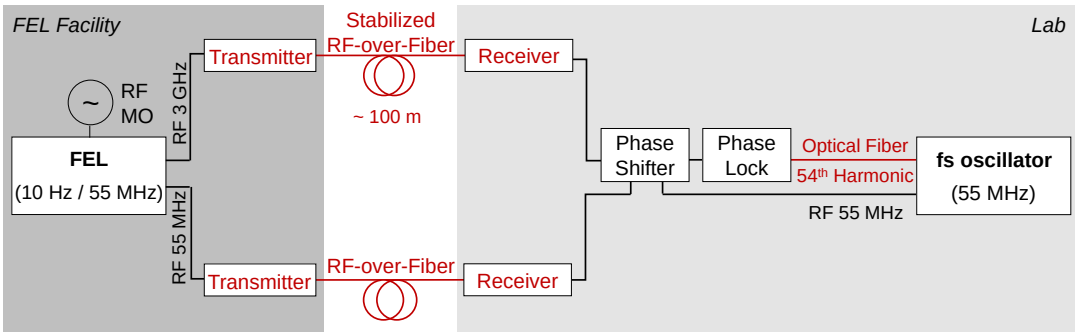

Fig. 3.2 Setup of RF electronics for laser synchronization. Provided by the master oscillator (MO) of the free-electron laser (FEL), the 3 GHz reference signal is transmitted via optical fibers to the experimental lab. Using the 54$^{\text{th}}$ harmonic of the optical output of the table-top laser, synchronization is achieved by a phase-locked loop. The actual pulse repetition rate of both light sources of 55 MHz is matched by an electronic phase shifter.

of $\lambda = 1052\,\text{nm}$ and delivering transform-limited sech^2-pulses of $\tau_\text{p} = 100\,\text{fs}$ duration (FWHM) and $\sim 50\,\text{nJ}$ energy at a repetition rate of $f_\text{FO} = 55.5\,\text{MHz}$ [One15]. Passive mode-locking is achieved by a saturable absorber (SESAM). The benefit of using a fiber laser is the extremely low phase noise [Cox10], resulting in a free running timing jitter $< 50\,\text{fs}$ rms ($1\,\text{kHz} - 10\,\text{MHz}$) [One15], which is advantageous for the synchronized operation.

The synchronization of the table-top laser pulses and the FEL micro-pulses, emitted at a reduced repetition rate of 55.5 MHz or 27.8 MHz, is accomplished by an electronic phase-locking technique (Fig. 3.2). In order to achieve a precise synchronization, the high-frequency signal f_MO of the master oscillator is used. This one is distributed from the FEL vault to the user lab via a timing-stabilized RF-over-fiber connection (approx. 100 m length). The commercial clock transfer system[2] features a very low phase noise ($< 6\,\text{fs}$ rms [10 Hz-10 MHz]) and low drift ($< 40\,\text{fs/day}$) [Ins15]. This is realized by two optical fiber links to compensate for phase drifts within the cable due to environmental fluctuations (temperature, humidity) of up to 400 ps [Zor15]. For a later relocation of the synchronization setup, two fiber cables, each consisting of six single-mode fibers[3], have been installed between the basement of the FEL facility and the user lab in the neighboring building.

In order to phase lock the fiber oscillator (FO) to the RF MO signal, the 54$^{\text{th}}$ harmonic of the table-top laser output, received by a fast photodiode, is supplied to a custom-made synchronization module[4]. Comparison of the phase of both signals yields the input for a PID controller of the phase-lock loop (PLL) to manipulate the length of the FO cavity

[2] Libera Sync 3, Instrumentation Technologies d.d., Slovenia
[3] OS2, optical carrier wavelength $\lambda = 1550\,\text{nm}$, Corning Inc., USA
[4] S. Hunziker et al., Timing and Synchronization Group, Paul Scherrer Institut (PSI), Switzerland

accordingly for synchronized operation at 55.5 MHz. This is realized in two ways: On the one hand, a piezoelectric drive is used to adjust the repetition rate (capture range > 250 Hz). On the other hand, a coarse tuner is employed to keep the FO frequency within the piezo locking range, realized via a temperature control of the table-top laser cage (capture width 2.5 kHz).

For the temporal overlap of the repetition rate-matched FEL micro-pulses and the FO pulses in the experimental setup, the MO signal phase can be varied via an electronic phase-shifter[4] prior to feed-in to the synchronization module. The phase variation is based on an RF vector modulator [Sch16], allowing a time delay change from 80 fs up to several tens of nanoseconds. Since the MO frequency f_{MO} used for the synchronization is a multiple of the actual optical pulse rate f_{FO}, the reduced-repetition rate signal of the FEL micro-pulses is also transferred to the user lab via a separate, non-stabilized RF-over-fiber link[5] [MIT15]. In principle, this allows for additional superperiod synchronization with the FO, providing a perfect overlap of FEL and FO pulses. However, the unreliable performance of the built-in function has been replaced by a manual phase adjustment.

The intensity of the FEL radiation is usually measured by home-built pyroelectric detectors. If it is required to resolve the individual micro-pulses a fast ($\tau < 1$ ns) IR-sensitive uncooled photoelectromagnetic (HgCd)Te-based detector[6] is applied. This is used in connection with a broadband oscilloscope for a rough determination of the relative timing of the MIR FEL and FO pulses, giving a temporal resolution of about 100 ps. In the final step, the FEL – table-top laser pulse timing can be adjusted within a 1 ns-range using a high-precision delay stage (minimum increment 0.1 µm $\widehat{=}$ 0.7 fs).

3.3 SFG Spectroscopy Setup

The sum-frequency generation experiments are possible in either transmission or reflection geometry. A schematic arrangement of the incident and emitted optical beams for both methods is shown in Fig. 3.3. In the SFG transmission scheme, Fig. 3.3(a), the wavelength-tunable MIR FEL and fundamental NIR FO radiation are incident onto the sample in a non-collinear geometry. Due to momentum conservation, Eq. (2.55), the created sum-frequency light is emitted close to the propagation direction of the refracted table-top laser radiation. Both the polar (θ) and azimuthal (φ) angle of the sample can be varied without changing the SFG emission direction. The difference in the angles of incidence of the input beams is held constant, chosen to be 15°. In case of the reflection geometry, Fig. 3.3(b), both input beams are non-collinearly arranged as well. There, the FEL radiation is incident under oblique incidence to increase the out-of-plane component of the MIR electric field (for p-polarization). For upconversion, VIS radiation derived from the FO by frequency doubling in a nonlinear crystal is employed in order

[5] Fiber Optic Link, RF frequency range 50 kHz to 4.5 GHz, MITEQ Inc., USA
[6] IR Photoelectromagnetic Detector PEM-10.6, VIGO Systems S.A., Poland

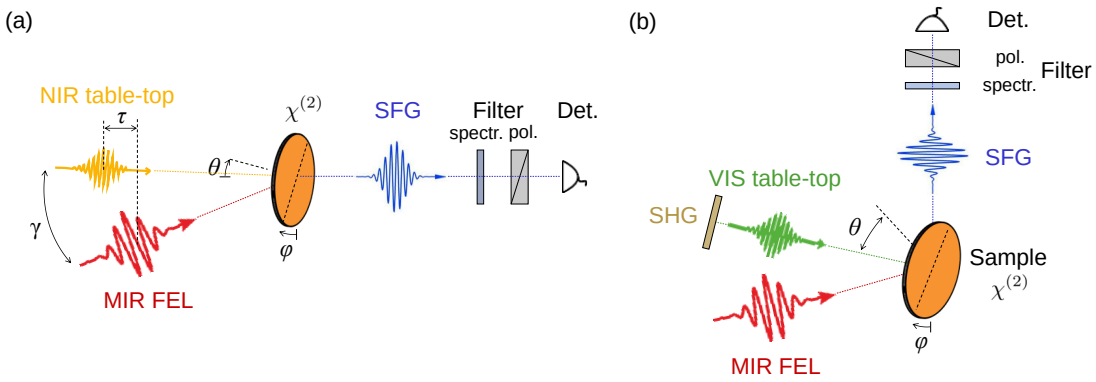

Fig. 3.3 Schematic sum-frequency generation geometries. (a) SFG transmission geometry. A non-collinear beam propagation arrangement (angle $\gamma = 15°$) of the temporally (τ) and spatially overlapped mid-infrared FEL and near-infrared ($\lambda = 1052\,\text{nm}$) FO pulses is used together with an adjustable polar (θ) and azimuthal (φ) orientation of the sample ($\chi^{(2)} \neq 0$). Spectral and polarization filtering prior SFG intensity detection is used. (b) SFG reflection geometry. After frequency doubling (SHG) in a nonlinear crystal, the visible table-top ($\lambda = 526\,\text{nm}$) and FEL radiation are focused onto the sample with an angle of incidence of $\theta_{\text{VIS}} = 30°$ and $\theta_{\text{IR}} = 55°$ relative to the sample surface normal, respectively.

to utilize more sensitive SFG light detectors available in the VIS spectral range. The angle of incidence of the FEL radiation is 55°, whereas the table-top light is incident under $\theta = 30°$. Then, the SFG radiation can be probed near the propagation direction of the reflected VIS FO beam. The azimuthal sample orientation is adjustable, whereas the polar angle is fixed by the experimental geometry. Thus, the transmission geometry (a) is preferred for the phase-matched SFG at fixed wavelengths λ_{IR} and λ_{VIS} to find the temporal overlap of FEL and FO pulses. On the other hand, the vibrational SFG spectroscopy is performed in the reflection setup (b).

An overview of the implemented experimental setup for the various SFG measurements is given in Fig. 3.4. The collimated MIR radiation supplied by the FEL, having a beam diameter of several millimeter, is focused by gold-coated off-axis parabolic mirrors (reflected focal lengths 388 mm and 191 mm) onto the sample to about 400 µm and 200 µm FWHM spot sizes (at $\lambda = 10\,\mu\text{m}$) in the transmission and reflection geometry, respectively. A combination of two holographic wire-grid polarizers can be used as polarization rotator of the FEL light, set 45° and 90° relative to the linear *p*-polarization of the FEL beam, respectively, if *s*-polarized MIR radiation is required. Longpass filters (cut-off $\lambda = 7\,\mu\text{m}$) are usually employed to restrict the FEL beam to the fundamental wavelength. To normalize the measured SFG signal to the incident FEL intensity, a caesium iodide (CsI) broadband beamsplitter (reflectance $\sim 7\,\%$) is used to separate an FEL reference detector signal. Since the transmission and reflection SFG geometries, Fig. 3.3(a) and Fig. 3.3(b), are realized in separate setups in order to be able to use them in parallel, another beamsplitter made of thallium bromo-iodide (KRS-5) is employed to distribute the FEL power ($\sim 15\,\%$ used for the phase-matched SFG transmission setup).

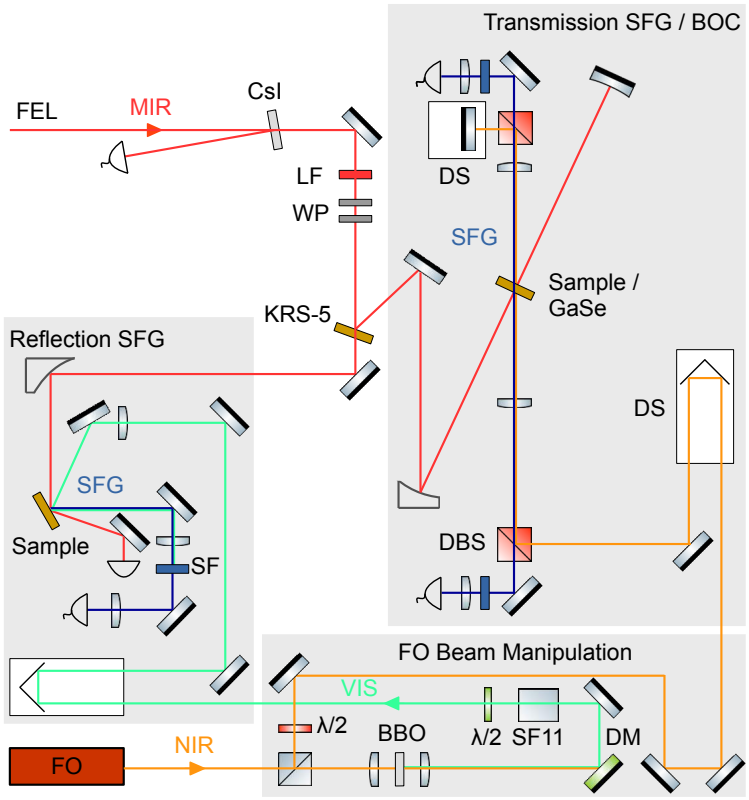

Fig. 3.4 Experimental SFG spectroscopy setup. The optical output of the FO is manipulated to provide the fundamental NIR ($\lambda = 1052\,\mathrm{nm}$) and also VIS ($\lambda = 526\,\mathrm{nm}$) radiation after frequency-doubling in a BBO crystal (bottom part). Half-wave plates are used to set the polarization state of the table-top beam; an SF11 crystal can be used to stretch the VIS pulse for increased temporal pulse overlap. The experimental setup for the SFG spectroscopy in transmission geometry (right part) is usually used for the balanced optical cross-correlation. The reflection-type SFG measurements are performed in a separate setup (left part), where the MIR reflectivity response of the sample can be captured as well. The FEL radiation is splitted by a KRS-5 window (15/85) for the two setups, while a CsI crystal (7/93) is used to separate an FEL beam for reference power detection. DM: dichroic mirror, DBS: dichroic beamsplitter, SF: spectral filter, DS: delay stage. Parts of the optical components used in the layout are from Ref. [Fra06].

The table-top FO is employed to provide NIR light ($\lambda = 1052\,\mathrm{nm}$) and VIS radiation ($\lambda = 526\,\mathrm{nm}$) via frequency doubling. There, a custom-cut β-barium borate (BBO) crystal (thickness 1 mm) is used for type I phase-matched second harmonic generation. Anti-reflective coatings on both crystal sides are used to minimize optical losses. Due to the strong focusing by a $f = 5\,\mathrm{cm}$ lens, a conversion efficiency up to 30 % has been achieved. Residual NIR radiation is removed by a dichroic mirror, being highly reflective only at the VIS wavelength. Afterwards, the VIS pulse can be stretched in time by a strongly dispersive medium of SF11 glass (length 10 cm, group velocity dispersion (GVD) $\sim 400\,\mathrm{fs}^2/\mathrm{mm}$) from $\tau_\mathrm{p} \sim 120\,\mathrm{fs}$ to about 1 ps (FWHM) duration. Thus, the temporal overlap of MIR and VIS pulses is increased, beneficial to reduce the sensitivity of the SFG signal to timing drifts during frequency-resolved spectroscopy scans. The spectral resolution in the IR frequency-scanning SFG approach is limited by the FEL linewidth. The linear polarization of NIR and VIS beam can be adjusted by the respective half-wave plate. After passing a delay stage to vary the arrival time τ relative to the FEL pulses, the NIR/VIS radiation is focused by transmissive optics (focal length $f = 20\,\mathrm{cm}$) onto the sample (60 µm FWHM of NIR spot, 80 µm size of VIS spot).

Subsequently, the created SFG radiation is re-collimated. Due to conservation of momentum, cf. Eq. (2.55), the angle of the SFG emission θ_SFG depends on the frequency of the input beams. The angular variation for the used MIR wavelengths is below 1°. Thus, the position of the SFG beam focused on the detector (lens focal length $f = 5\,\mathrm{cm}$) is nearly identical when scanning the FEL frequency ω_IR. Due to the similar propagation angle of reflected FO and SFG radiation, spatial separation is not possible. Therefore, to block the spectrally nearby table-top laser wavelength, two shortpass [cut-off $\lambda = 1000\,\mathrm{nm}$, Fig. 3.3(a)] or bandpass [FWHM range $\lambda = 500 \pm 5\,\mathrm{nm}$, Fig. 3.3(b)] filters are placed in front of the SFG light detector, providing a total suppression level of optical density (OD) 10. The particular sum-frequency electric field polarization being probed can be selected by a Glan-Thompson calcite prism polarizer. Depending on the intensity of the generated NIR or VIS sum-frequency light, either a silicon photodiode[7], silicon avalanche photodetector[8] or bialkali photomultiplier tube[9], the most photon-sensitive device, is employed. The whole setup can be flooded with nitrogen gas to avoid absorption of the MIR radiation by the water vapor contained in ambient air. Measurements are performed on samples held at room temperature.

During a certain beamtime (one day), the kinetic energy E_kin of the FEL machine is fixed to a value suitable for the desired wavelength range. The wavenumber-resolved spectroscopy measurements are performed by scanning the undulator gap size. During such a wavelength sweep, the length of the cavity is adjusted accordingly to retain a constant detuning ratio $\Delta L/\lambda$, and thus a fixed relative bandwidth and spectral resolution. The cavity detuning can be set to a value in between $\Delta L = (0.5 \ldots 5)\,\lambda$.

[7] DET10A/M, Thorlabs Inc., USA
[8] APD410A/M, Thorlabs Inc., USA
[9] H11901P-210, Hamamatsu Photonics K.K., Japan

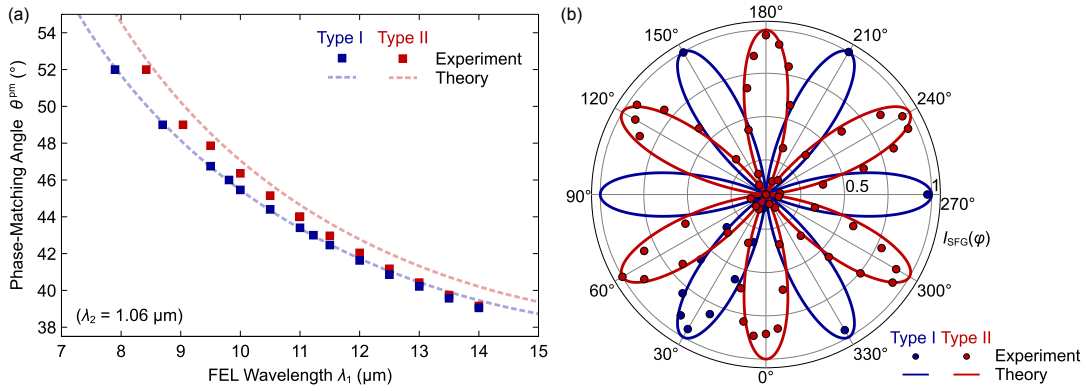

Fig. 3.5 Phase-matched sum-frequency generation in GaSe. (a) Experimental and calculated phase-matching angle θ_{pm} for mixing the MIR FEL radiation λ_1 with the NIR table-top light at $\lambda_2 = 1.06\,\mu\mathrm{m}$. (b) Azimuthal dependence of normalized SFG intensity $I_{\mathrm{SFG}}(\varphi)$ for type I and type II phase-matching (see text for analytical expressions). Measurement values are obtained with a 1 mm thick z-cut crystal; the theoretical result are based on Refs. [Dmi99; Abd75].

The FHI FEL parameters are controlled and monitored via an EPICS software interface. All detector signals are captured via a 4 GHz bandwidth oscilloscope, triggered by the FEL macro-pulse frequency signal. The experimental setup (control and readout of delay stage positions, FEL parameters, oscilloscope data) is operated via a LabView program. Subsequent analysis of the GB-sized data (due to single-shot storage of macro-pulse time-domain traces and FEL radiation spectra) is performed with Matlab.

Phase-matched sum-frequency mixing

Prior to the spectroscopy measurements, the actual temporal overlap of FEL and FO pulses is identified by non-resonant sum-frequency generation in a nonlinear optical crystal. For that, phase-matched SFG in gallium selenide (GaSe) [Kai99], a layered semiconductor, can be used in the wavelength range of $\lambda = 0.6\,\mu\mathrm{m} - 18\,\mu\mathrm{m}$. Due to the large nonlinearity ($\left|\chi^{(2)}(10\,\mu\mathrm{m})\right| > 100\,\mathrm{pm/V}$ [Dmi99]), the material provides a strong SFG intensity. Depending on the polarization of both input beams, type I and II phase-matching can be realized by angle tuning of the anisotropic crystal. In case of non-collinear type I phase-matching in the negative uniaxial crystal ($n_{\mathrm{e}} < n_{\mathrm{o}}$), the following equation holds for the polar angle θ_{pm} [Dmi99]:

$$\tan^2\theta_{\mathrm{pm}} = \frac{1-(k_{\mathrm{o1}}^2+k_{\mathrm{o2}}^2+2k_{\mathrm{o1}}k_{\mathrm{o2}}\cos\gamma)/k_{\mathrm{o3}}^2}{(k_{\mathrm{o1}}^2+k_{\mathrm{o2}}^2+2k_{\mathrm{o1}}k_{\mathrm{o2}}\cos\gamma)/k_{\mathrm{e3}}^2-1}, \tag{3.1}$$

where $k_{\mathrm{o1}} = n_{\mathrm{o}}(\lambda_1)/\lambda_1$, $k_{\mathrm{o2}} = n_{\mathrm{o}}(\lambda_2)/\lambda_2$, $k_{\mathrm{o3}} = n_{\mathrm{o}}(\lambda_3)/\lambda_3$ and $k_{\mathrm{e3}} = n_{\mathrm{e}}(\lambda_3)/\lambda_3$ with the angle γ between the wave vectors $\boldsymbol{k}_1$ and $\boldsymbol{k}_2$. A similar expression can be found for type II phase-matching [Dmi99]. Dispersion relations of the refractive indices of the ordinary beam $n_{\mathrm{o}}(\lambda)$ and the extraordinary beam $n_{\mathrm{e}}(\theta,\lambda)$ of the birefringent GaSe

are taken from Ref. [Abd75]. The calculated phase-matching angles θ_{pm} are shown in Fig. 3.5(a), together with the measured values obtained from a 1 mm thick z-cut crystal. In Fig. 3.5(b), the azimuthal dependence $I_{\mathrm{SFG}}(\varphi)$ is depicted, which affects the efficiency of the upconversion process as well. A good agreement between experiment and theory is found for type I and II phase-matching. Due to the threefold crystal symmetry, $I_{\mathrm{SFG}} \propto \left|\chi^{(2)} \cos\theta \sin 3\varphi\right|^2$ in the case of type I, whereas $I_{\mathrm{SFG}} \propto \left|\chi^{(2)} \cos^2\theta \cos 3\varphi\right|^2$ for type II velocity-matched sum-frequency generation [Dmi99].

In case of sum-frequency generation with the VIS table-top laser radiation, zinc selenide (ZnSe) has been used due to the larger band gap (transparency range $\lambda = 0.4\,\mu\mathrm{m} - 20\,\mu\mathrm{m}$), but without the phase-matching possibility. For the long-wavelength region of the FEL ($\lambda > 20\,\mu\mathrm{m}$), silicon carbide (SiC) might be a suitable material, as phase-matched DFG has been demonstrated by this [Fis17].

4 Timing Stability of the FEL Synchronization

In order to perform two-color FEL–table-top laser spectroscopy experiments, whether nonlinear or pump-probe, the stability of the relative pulse timing is a crucial issue. Therefore, the short-term fluctuations, i.e. jitter, as well as long-term variations, i.e. drift, of the pulse arrival time have to be known. Here, the method of balanced optical cross-correlation is used for the timing characterization. Implications of the experimental results are discussed.

Parts of this Chapter have been published in Ref. [Kie18].

4.1 Balanced Optical Cross-Correlation

In general, the intensity cross-correlation of two different, synchronized optical pulses reveals a convolution function in dependence of the relative pulse delay. Whenever the relative temporal delay of the input pulses jitters, the amplitude of the cross-correlation signal is changed. However, the relation between intensity change and time difference is not unambiguous. Therefore, the intensity cross-correlation can be performed a second time, after insertion of a small temporal offset between both pulses. After normalization, the substracted cross-correlation values obey a linear relationship with regard to the pulse delay. Thus, a reliable method to track the development of the relative timing of two synchronized lasers is obtained.

The principle setup of the balanced optical cross-correlator is depicted in Fig. 4.1. There, the spatial and temporal overlap of two input pulses in an appropriate nonlinear crystal generates a third optical beam at the sum frequency. The intensity of this first SFG signal, $\mathrm{XC}(\tau)$, is measured after blocking the fundamentals. Then, the two input pulses transmitted through the crystal are directed back to the nonlinear medium after introducing a fixed time delay Δt between them. The created second SFG signal $\mathrm{XC}(\tau + \Delta t)$ is collected as well. By scanning the relative time delay τ of the two input pulses, the whole cross-correlation functions $\mathrm{XC}(\tau)$ and $\mathrm{XC}(\tau + \Delta t)$ are sampled. Normalizing each to its maximum and subsequent calculation of the difference gives the balanced optical cross-correlation function $\mathrm{BOC}(\tau, \Delta t)$:

$$\mathrm{BOC}(\tau, \Delta t) = \frac{\mathrm{XC}(\tau)}{\max\left[\mathrm{XC}(\tau)\right]} - \frac{\mathrm{XC}(\tau + \Delta t)}{\max\left[\mathrm{XC}(\tau + \Delta t)\right]}. \tag{4.1}$$

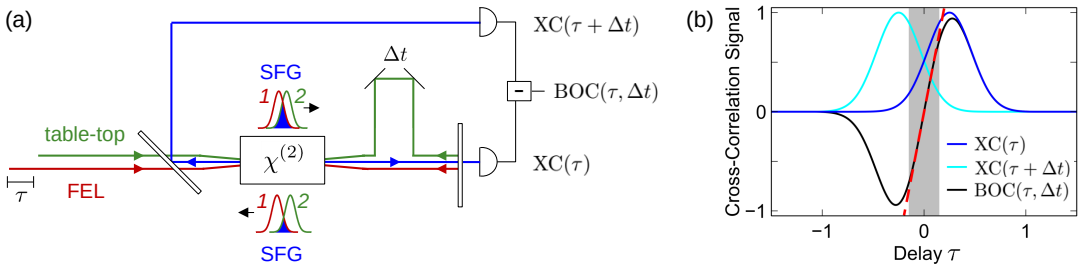

Fig. 4.1 Scheme of balanced optical cross-correlation (BOC). (a) Sketch of experimental setup. Optical pulses of FEL (red, 1) and table-top laser (green, 2) with relative delay τ are mixed within a single nonlinear crystal ($\chi^{(2)} \neq 0$). Sum-frequency radiation (blue) is generated twice: in forward direction [XC(τ)], and in backward direction [XC($\tau + \Delta t$)] after inserting a small, fixed time delay Δt between the transmitted input pulses. (b) Illustration of the normalized cross-correlation signals XC(τ) and XC($\tau + \Delta t$) as well as of the BOC function BOC($\tau, \Delta t$) calculated according to Eq. (4.1).

Close to time zero, $|\tau| \lesssim \Delta t/2$, the BOC profile can be approximated by a linear function,

$$\mathrm{BOC}(\tau, \Delta t) \approx c\,\tau. \tag{4.2}$$

The calibration coefficient c is revealed by a linear fit to the experimental data. When using the calibrated cross-correlator for a measurement of timing jitter or drift, the variable time delay τ is set to a constant value close to zero. Now, fluctuations of the relative arrival time of both input pulses transform in nonzero BOC values. Using the calibration coefficient, these values can be converted into the desired timing information. Then, the timing jitter δt is calculated as root-mean square (rms) value of the timing fluctuations within a certain real-time window (here, 3 min), whereas the drift is given as peak-to-peak variation during a long period of time (here, 15 min).

To obtain a maximum temporal range where the BOC function is almost linear, an optimum value for the fixed time delay Δt exists, depending on the duration of the two input pulses. It can be derived analytically, and is given by

$$\Delta t_{\mathrm{opt}} = \pm\sqrt{\frac{1}{2\ln 2}\left(\tau_1^2 + \tau_2^2\right)}, \tag{4.3}$$

where τ_1 and τ_2 are the FWHM durations of the input pulses, assuming Gaussian pulse profiles.

Besides a characterization of the timing stability by itself, the BOC tool can be used to measure the timing variations $\Delta\tau$ in parallel to an FEL pump – table-top probe experiment. Then, a post-correction of the transient signal can be performed, improving the temporal resolution of the experiment due to the elimination of timing drifts. To that end, the measured observable is re-arranged over the actual time delay $\tau + \Delta\tau$ instead

of the time delay τ set. As another approach, the timing drift during the time-resolved study can be eliminated in real time by applying an adequate feedback to the delay stage of the measurement setup.

The first BOC has been demonstrated in the synchronization of two mode-locked table-top lasers, yielding a timing jitter of $\delta t = 300\,\text{as}$ by supplying active feedback to the control loop [Sch03]. At accelerator-based light sources, the BOC can be applied to stabilize the timing of all accelerator components as well as of the table-top laser to a master oscillator clock. This has been proven, for example, at the X-ray FEL FLASH, where all-optical synchronization yields a timing jitter of $\delta t = 30\,\text{fs}$ using 90 fs short FEL light pulses [Sch15b]. Due to the inherent linearity of the measured observable to absolute timing conversion, the BOC technique is preferable over a simple SFG cross-correlator, which has been used so far at other IR FELs [Per93; Eli95].

The balanced optical cross-correlator of FEL and table-top laser pulses has been implemented using SFG in transmission geometry, cf. Fig. 3.3(a). For the BOC measurements, the *s*-polarized fundamental NIR wavelength of the table-top laser is mixed with the *p*-polarized MIR FEL radiation at wavelength $\lambda = 10\,\mu\text{m}$ and detuning $\Delta L = 3\lambda$. Both beams are focused into a *z*-cut GaSe crystal (thickness 1 mm) adjusted for type II phase-matching. The angle between the incident beams is 15°. The transmitted FEL radiation is refocused by a concave spherical mirror, whereas the NIR radiation is reflected back by a plane mirror behind a collimation/refocusing lens. Spectral separation of the nearly co-propagating fundamental NIR and SFG light is realized by dichroic mirrors. The relative delay τ as well as the fixed time delay Δt can be varied via motorized stages. The SFG intensities $\text{XC}(\tau)$ and $\text{XC}(\tau + \Delta t)$ are detected by photodiodes.

4.2 Jitter and Drift of FEL Pulse Timing

By using the balanced optical cross-correlation method, the jitter as well as drift of the FEL pulse arrival time has been measured relative to the synchronized table-top FO.

In Fig. 4.2(a), the measured BOC function is shown, obtained for 100 FEL shots at each delay point. Concerning the dynamic range of the timing tool, i.e. the delay window with a linear relationship, a range of about 3 ps can be captured. A histogram of the BOC values close to the delay $\tau = 0$ is depicted in Fig. 4.2(b). The extracted timing jitter, corresponding to the standard deviation σ of a Gaussian fit, is $\delta t = 103\,\text{fs}$ in the low-repetition FEL mode (27 MHz). In case of the standard micro-pulse rate of 1 GHz, a higher timing jitter of $\delta t = 200\,\text{fs} - 300\,\text{fs}$ has been measured. A dependence of the jitter on the FEL wavelength, i.e. undulator gap size, for a given accelerator electron energy or on the cavity detuning (i.e. mirror translation) has not been found, see Fig. 4.3. The larger jitter value in case of the standard repetition rate might be due to the higher overall beam-load of the linacs. Another source is probably the different electronic device used for the generation of the high-voltage pulses and applied to the electron grid in the 1 GHz mode (cf. Sec. 3.1.1).

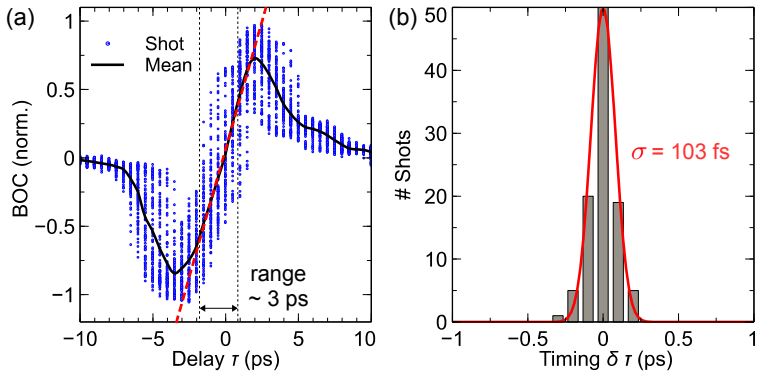

Fig. 4.2 FEL pulse jitter determination by balanced optical cross-correlation. (a) Record of the BOC value according to Eq. (4.1) as function of the relative time delay τ between FEL and table-top pulse. For each delay step, 100 subsequent macro-pulses (shots) have been captured. Calculation of the mean BOC function reveals a linear relationship between the BOC value and the delay around time $\tau = 0$. There, the dynamic range is about 3 ps. (b) Histogram of the FEL micro-pulse timing. The extracted jitter value is $\sigma = 103$ fs, derived as standard deviation of the Gaussian distribution.

The long-term fluctuations of the FEL pulse arrival time are depicted in Fig. 4.4. Simultaneously, the shift of the FEL center wavelength and the mean energy of the electron bunches have been recorded. For the latter, the kinetic energy of the charged particles is captured by a horizontal beam-position monitor placed behind a beam bending magnet downstream the two linacs. Thus, energy differences of the electrons transform into different spatial positions on the screen. The peak-to-peak timing fluctuations are

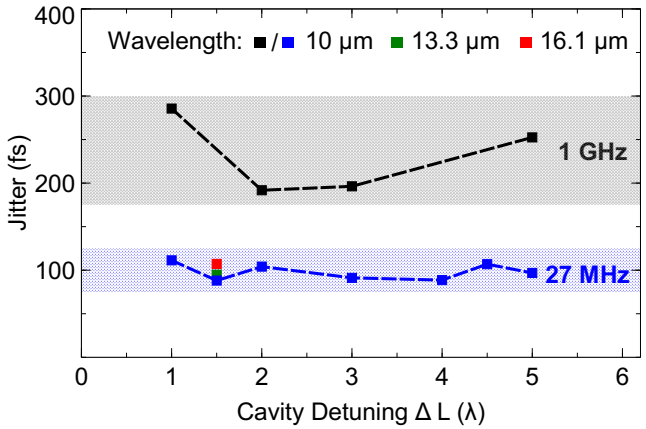

Fig. 4.3 Dependence of FEL pulse jitter on repetition rate and radiation wavelength. The short-time fluctuations of the FEL micro-pulse arrival time has been determined for the standard repetition rate ($f_{\mathrm{rep}} = 1$ GHz, black line) and reduced frequency (27 MHz, other colors) at various cavity lengths. Different lasing wavelengths have been used in the low-rate mode by varying the undulator gap (fixed electron energy).

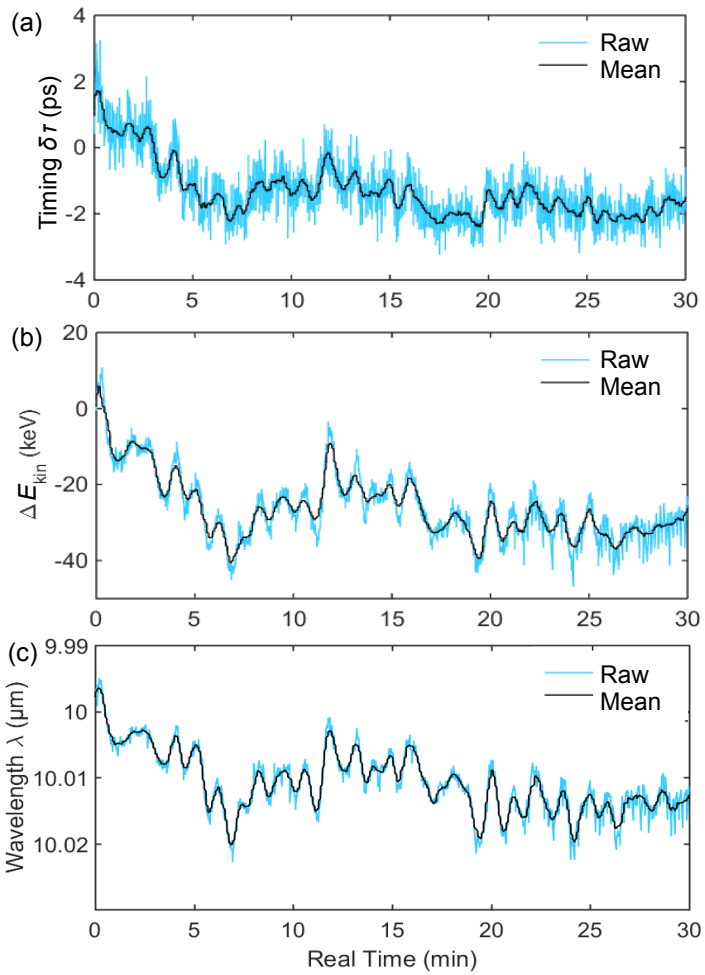

Fig. 4.4 Drift of FEL pulse timing. (a) Variation of the FEL pulse arrival time δt with respect to the table-top pulse during a 30 min time range. The data are obtained from a calibrated BOC measurement. (b) Kinetic energy fluctuations ΔE_{kin} of the electron bunches after traversing both linear accelerators. This has been determined by a beam position monitor behind a bend of the electron beam. (c) Wavelength variation measured by the FEL spectrometer. In each graph, a moving average with half-minute window is displayed (black line).

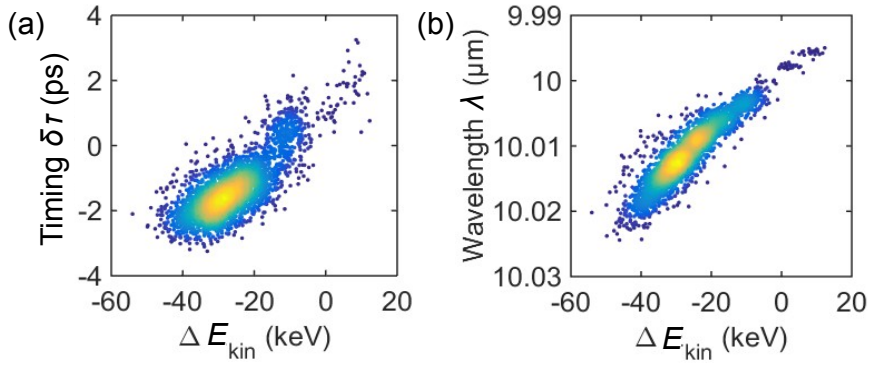

Fig. 4.5 Correlation of optical pulse timing and accelerator behavior of the FEL. The long-term fluctuations of the (a) FEL pulse arrival time and (b) center wavelength of the FEL radiation are plotted against the variations of the kinetic energy ΔE_{kin} of the accelerated electrons. Data density of the scatter plots is indicated by color (blue low, yellow high). A strong linear correlation is present in both cases, expressed by the Pearson coefficients $\rho = 0.78$ and 0.98, respectively.

3 ps over a period of 30 min, Fig. 4.4(a). Obviously, there is a clear correlation with the energy variations of the electrons generating the light pulse, Fig. 4.4(b). The measured energy fluctuations ΔE_{kin} of the electron bunches are in the same order of magnitude as the energy spread of the accelerated electrons (cf. Tab. 3.1). This is accompanied by shifts of the center wavelength λ_0 of the optical radiation, Fig. 4.4(c). The behavior can be directly explained by means of the resonance condition Eq. (2.56): Due to the unchanged magnetic undulator field during the experiment, the K parameter is fixed. Thus, variations in the kinetic electron energy are imprinted on the optical wavelength.

A calculation of the Pearson correlation coefficient ρ for the linear relationship gives a value of $\rho = 0.78$ in the case of the micro-pulse timing vs. electron energy, Fig. 4.5(a), and $\rho = 0.92$ between FEL wavelength and electron energy, Fig. 4.5(b), respectively. Thus, the accelerator system is seen as the main source of the timing fluctuations. In detail, these can be amplitude and/or phase instabilities in the RF fields of the thermoelectric electron injection, the buncher cavity, or the two linac modules. As a consequence of dispersive effects along the electron beam path, bunch energy differences result in timing variations. Other sources of pulse arrival time changes might be the thermal expansion of the beamline or mechanical vibrations due to mounting on the building. As a rough estimate, for a 100 m long stainless steel beamline, the arrival time difference for $\Delta T = 1$ K is in the order of 3 ps. However, this would occur at a time scale of hours instead of the 30 min period depicted in Fig. 4.4(a). The contribution from the RF distribution system is of minor impact since the fiber-based clock transfer employed exhibits a high timing stability. Also, the table-top fiber oscillator exhibits a low phase noise (cf. Sec. 3.2).

Taking into account that the synchronization relies solely on radio frequency-based phase-locking, a high stability of the table-top pulse timing is achieved. Compared to other FEL facilities, the jitter value of about 100 fs is the lowest reported so far [Kni98; Bha11; Wan12]. This is also the lower limit which can be reached by means of conventional electronic phase-locking techniques [Grg12; Azi09]. The implemented experimental setup is suited for sub-ps-resolved FEL – table-top experiments, since the timing jitter is one order of magnitude smaller than the FEL pulse duration. In principle, the information about the clear relationship between electron energy and timing drift can be used to eleminate the temporal variations by applying an appropriate feedback to the accelerator components. In this work, the way chosen to compensate for timing variations in time-resolved measurements is done via post-correction of the time delay, similar to other accelerator-based systems [Kov17].

Conclusion

In summary, a robust method for the precise timing determination of IR FEL-based pulses with respect to an external laser has been established. Based on balancing of two slightly time-shifted optical SFG cross-correlation signals, a linear relationship between measured observable and pulse timing is provided by an all-optical technique. This extends the possibilities for experimental investigations with the FEL radiation to two-color spectroscopy studies. Due to the low timing jitter of about 100 fs of the electronic phase-locking architecture, nonlinear frequency-resolved spectroscopy of materials can be performed right off. In case of time-resolved measurements, recording of the actual relative pulse delay in parallel to the pump-probe study improves the time resolution on the femtosecond scale. Thus, the post-correction approach mitigates the requirement for a strict synchronization of table-top and accelerated-based light source.

The observation of a strong correlation between the temporal pulse drift and the electron energy fluctuations provides a way to reduce the timing shifts. For that, an active feedback might be applied to the amplitudes and phases of the accelerator RF fields. Besides the timing aspect, this would be beneficial for the spectral stability of the emitted FEL radiation.

5 Temporal and Spectral Structure of the FEL Radiation

The linewidth of the IR FEL radiation is a critical parameter for the spectral resolution of the measurements, requiring narrowband radiation. Besides that, knowledge about the temporal structure of the FEL radiation is essential when combined with optical pulses from other laser light sources to perform two-color spectroscopy. In the following, the temporal and spectral characteristics of the FHI FEL pulses are investigated in detail. Due to the oscillator configuration of the FEL, the length of the resonator provides a way to manipulate the pulse shape and spectrum. In particular, the formation of sub-pulses within a single FEL micro-pulse could be observed. This result will be explained as a consequence of the nonlinear electron-photon interaction in the free-electron laser.

Parts of this Chapter have been published in Ref. [Kie18].

5.1 Pulse Profile and Bandwidth

For a measurement of the time-domain profile of the FEL pulse $I_{\mathrm{FEL}}(\tau)$, the SFG cross-correlation method introduced in Sec. 4.1 has been employed. Therefore, the MIR FEL radiation at $\lambda = 10\,\mu\mathrm{m}$ is mixed with the NIR table-top laser pulses in a phase-matched GaSe crystal. Since the reference pulse $I_{\mathrm{ref}}(t)$ used from the FO laser is at least one order of magnitude shorter than the FEL micro-pulse, the measured convolution trace $\int I_{\mathrm{FEL}}(\tau) I_{\mathrm{ref}}(\tau - t) d\tau$ represents in good approximation the actual FEL pulse shape $I_{\mathrm{FEL}}(\tau)$.

In Fig. 5.1(a), the dependence of the FEL micro-pulse profile $I(\tau)$ on the cavity detuning ΔL is displayed. The depicted profile is acquired by integration of the SFG signal over the whole macro-pulse. In the following diagrams, the leading edge of the FEL micro-pulse is placed at negative delay times. In case of zero detuning, $\Delta L = 0$, no stable lasing can be observed (not shown). This is a consequence of the laser lethargy (cf. Sec. 2.4). At small cavity detuning, $0 < \Delta L \lesssim 1\lambda$, an FEL pulse of Gaussian-shaped intensity envelope is emitted. The integrated micro-pulse duration (FWHM) determined from the cross-correlation is about 1.5 ps, see inset of Fig. 5.1(a). By further shortening of the FEL cavity, the pulse length is increased up to 4 ps at $\Delta L = 5\,\lambda$. At the same time, an asymmetric pulse profile evolves with an exponential rising edge. In Fig. 5.1(b), the corresponding spectral signature of the generated FEL light is displayed. Whereas for a short detuning value, the relative bandwidth $\Delta\lambda/\lambda$ amounts to a few percent, see inset of Fig. 5.1(b), narrowband radiation down to $\Delta\lambda/\lambda = 0.3\,\%$ can be produced at large cavity detunings ($\Delta L \sim 5\,\lambda$).

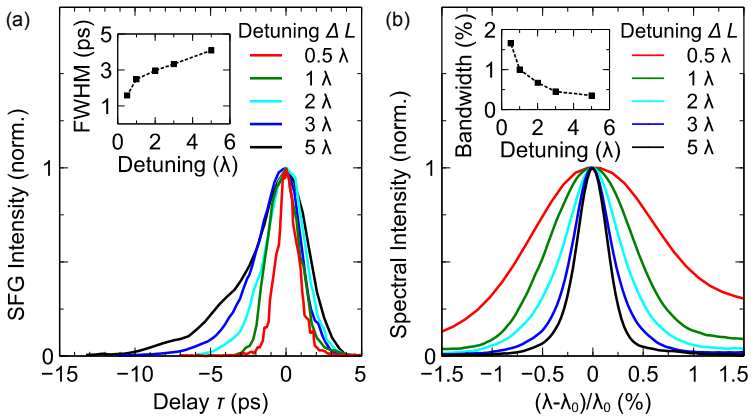

Fig. 5.1 Pulse profile and spectral bandwidth of the FEL radiation. (a) Intensity profile $I(\tau)$ of the micro-pulse determined by SFG cross-correlation with integration over the full macro-pulse time. The inset displays the pulse duration (FWHM) as function of the cavity detuning ΔL. (b) Spectral structure of the FEL light normalized to the center wavelength λ_0. The relative bandwidth (FWHM) is depicted in the inset. Narrowband IR radiation of 0.3 % relative bandwidth can be generated.

The change of the pulse profile as function of the detuning is a result of the varying temporal overlap between the ps-short electron bunches and the generated optical field: Whereas the repetition rate of the electron pulses is fixed by the accelerator frequency, the round-trip time of the light waves within the resonator is determined by the shortened cavity length $L = L_0 - \Delta L$. Consequently, the optical pulses are advanced relative to the gain-providing free-electron medium, stretching the micro-pulse duration. Due to the lack of contact with the electron bunches, the intensity of the light pulse at the front is attenuated by cavity losses. Thus, the exponential form of the leading pulse edge is governed by the cavity Q factor.

In the frequency domain, the broadening of the pulse duration is accompanied by a narrowing of the spectral linewidth. Calculation of the time-bandwidth product gives $\tau\,\Delta\omega = 0.78$ in the case of $\Delta L = 0.5\,\lambda$ and $\tau\,\Delta\omega = 0.42$ at $\Delta L = 5\lambda$. For a Gaussian-shaped transform-limited pulse, the time-bandwidth product is $\tau\,\Delta\omega = 0.44$. Thus, the experimental value at small detuning is about a factor of two larger than required for the transform limit. Studies at other IR FEL oscillators have proven that Fourier transform-limited pulses are reasonable (Stanford FEL [Dlo91], FELIX [Kni99]). The difference might arise due to a change of the micro-pulse timing during the macro-pulse, i.e. an effective chirp. This means that the temporal profile, in this setting, has a significant inhomogeneous broadening, arising due to averaging of the micro-pulses with different timing across the macro-pulse.

A close look at the spectrum at small detunings ΔL reveals an asymmetry, i.e. deviation from a perfect Gaussian. The detailed investigation of the micro-pulse structure within the macro-pulse, explaining this behavior, will be given in the next section.

5.2 Sub-Pulse Formation and Limit-Cycle Oscillations

In the following, a detailed study of the evolution of the micro-pulse intensity profile within a single macro-pulse will be presented. As it turns out, there is a strong dependence on the cavity detuning, so that a non-constant amplitude and temporal shape can occur. On the one hand, these observations allow a better understanding of the underlying FEL physics, on the other hand, the particular optical characteristics have to be taken into account for the spectroscopic experiments.

5.2.1 Experimental Results

The two-dimensional plot in Fig. 5.2(a) shows the development of the FEL micro-pulse intensity envelope $I(\tau)$ (vertical axis) as function of the temporal position t within the macro-pulse (horizontal axis), measured by SFG cross-correlation. In the case of $\Delta L = 1.75\,\lambda$, a strong modulation of the micro-pulse shape appears, with a periodic repetition. This can also be clearly seen in the cross-sections of Fig. 5.2(b) and Fig. 5.2(c). In contrast to the macro-pulse integrated data, Fig. 5.1(a) and Fig. 5.2(b) (gray line), equally-spaced sub-pulses within the micro-pulse are resolved. Along the macro-pulse time axis, Fig. 5.2(c) (blue line), an oscillation period of the FEL power of $T = 1.1\,\mu s$ can be extracted. The strength of the intensity modulation is up to 50 % in the delay-specific macro-pulse trace, whereas it is hardly seen in the delay-integrated data, Fig. 5.2(c) (gray line).

To rationalize these observations, one has to consider the interplay of gain, provided by the free-electron medium, and the resonator losses within the cavity. The emission of light pulses from the FEL starts as soon as the gain exceeds the lasing threshold, i.e. at around 1 µs in Fig. 5.2(a). Due to the detuned cavity length, the peak position of the micro-pulse shifts to earlier delay times in the subsequent cavity round-trips. As a result, the contact to the gain medium is lost. However, after further passes of the optical wave through the undulator, a second so-called sub-pulse arises at the trailing edge ($\tau > 0$). Apparently, net gain is provided again to the electromagnetic field. This peculiar behavior can be explained by means of an analytical model, see Sec. 5.2.2. The generation and shifting of the sub-pulses occurs repeatingly by the aforementioned mechanism. Most importantly, the temporal arrangement, i.e. distance, of the sub-pulses does not change during the move 'through' the micro-pulse. Finally, at the leading edge ($\tau < 0$), the intensity decays exponentially due to cavity losses, now exceeding the FEL gain. Thus, the oscillation pattern of the emitted FEL power within one macro-pulse arises due to the regular occurrence of sub-pulses.

The dependence of the pulse formation dynamics on the length of the cavity is revealed by a series of 2D cross-correlation measurements as shown in Fig. 5.3. At small cavity detuning, $\Delta L = 1\,\lambda$ in Fig. 5.3(a), a short micro-pulse is observed, in agreement with the previous results of Fig. 5.1. The build-up and decay of optical sub-pulses can be clearly identified. In comparison with the case of $\Delta L = 1.75\,\lambda$ in Fig. 5.2, a longer

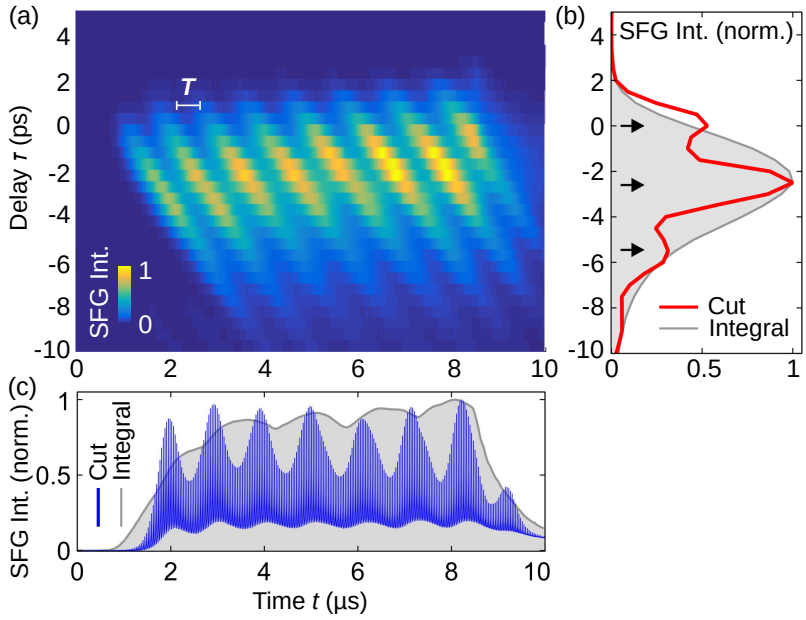

Fig. 5.2 Two-dimensional cross-correlation measurements of the FEL output in the case of sub-pulse formation and limit-cycle oscillations. (a) Evolution of the FEL micro-pulse shape $I(\tau)$ (vertical axis) during the macro-pulse of 10 µs duration (horizontal axis). Cross-sections from the 2D plot along a constant time of $t = 8\,\mu s$ and a constant delay of $\tau = -3\,ps$ are plotted in (b) and (c), respectively. In contrast to the time- or delay-integrated intensity envelopes (grey areas), the equally spaced sub-pulses (b, black arrows) and regular limit-cycle power oscillations (c) are clearly resolved. The temporal separation of the sub-pulses is 2.7 ps; the oscillation period T is indicated in (a). Cavity detuning has been $\Delta L = 1.75\,\lambda$.

power oscillation period is present. Further shortening of the FEL cavity results in a reduction of the period T as well as of the strength of the modulation. Consequently, at $\Delta L = 3\,\lambda$ in Fig. 5.3(d), oscillations of the micro-pulse intensity can no longer be resolved. Instead, a single-peaked micro-pulse is observed, featuring a nearly constant amplitude during the whole macro-pulse.

The start of the coherent light emission from the FEL depends on the cavity detuning, cf. Fig. 5.3. This is a consequence of the gain development required to overcome the lasing threshold. For a larger detuning, the optical power generation is established at earlier time t, meaning that the gain growth is faster, compared to the case of ΔL close to zero. Also, the saturation of the FEL power is reached sooner. In contrast to the begin of the optical macro-pulse, its temporal end is taking place mainly independent of the cavity detuning at around $t = 10\,\mu s$. This is determined by the switch off of the train of electron bunches. Thus, a clear edge of the saturated intensity appears in the 2D plots of Fig. 5.3(a)-(d). The final decay of the FEL power is governed by the cavity Q factor.

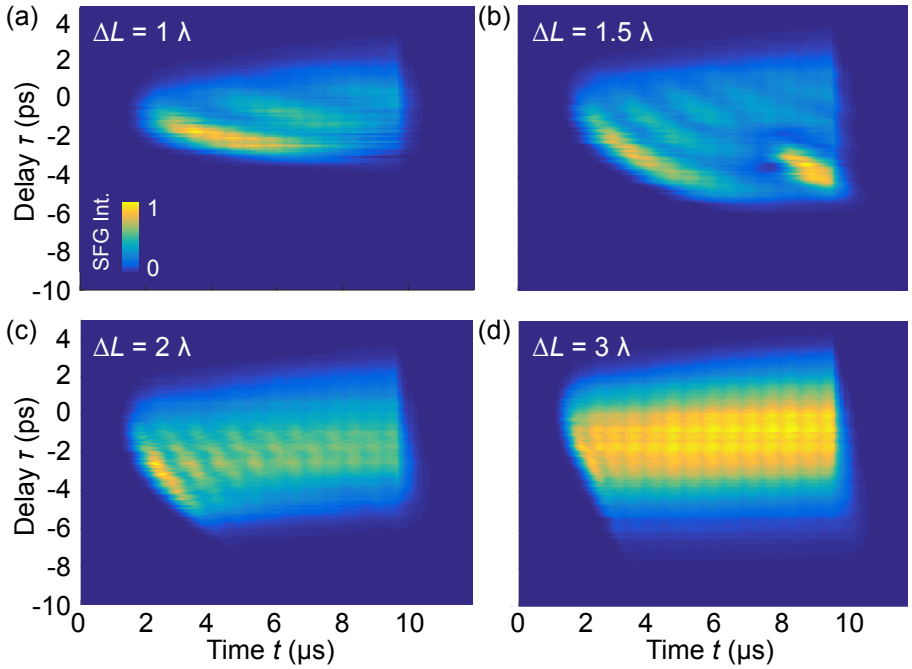

Fig. 5.3 Dependence of the FEL oscillator pulse development on the cavity detuning ΔL. The data for $\Delta L = 1\,\lambda - 3\,\lambda$ are obtained by SFG cross-correlation (linear intensity scale). Limit-cycle oscillations of the FEL power are clearly resolved in the cases of (a) – (c).

Various experimental and theoretical work has been concerned with the FEL power oscillations [Col82; Jar93; Hah93; Bak94]. The behavior is observed for FEL oscillators driven by short electron pulses. In the case of IR FELs, bunch durations in the ps range are required to create optical sub-pulses. The emerging FEL intensity modulation has been recognized as limit-cycle oscillation (LCO) [Col82].

The dependence of the oscillation period T on the detuning parameter ΔL is summarized in Fig. 5.4. The values are extracted from the measurements shown in Figs. 5.2 and 5.3. A clear trend of a decreasing LCO period for a shorter cavity length can be observed. In Ref. [Jar93], a simple analytic expression has been derived for the period T in a small-gain FEL oscillator. For this, the group velocity v_g of the light pulses has to be considered, which is determined by the gain-providing free-electron medium traveling at relativistic speeds. Thus, v_g is below c_0. When the FEL intensity begins to saturate, v_g is getting closer to the vacuum value c_0 [Bak94; Kni95]. At the same time, the modulation of the energy of the electrons is increasing. Finally, the charges are trapped by the strong optical field, performing synchrotron oscillations. During such an oscillation, the electrons are shifted back relative to the light pulse by one slippage length $s = N\lambda$.

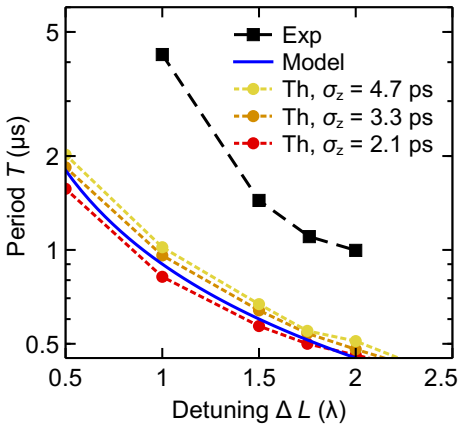

Fig. 5.4 Limit-cycle oscillation period T as function of the cavity detuning. The experimental values are extracted from the data shown in Figs. 5.2 and 5.3. The analytic model function is according to Eq. (5.1) and described in the text. Simulation results are from 4D Maxwell-Lorentz theory calculations for different electron pulse durations σ_z as described in Sec. 5.2.2.

Due to the particles' reabsorption of energy from the optical field, the gain is reduced to below the threshold. So, the previous group velocity of the light pulse recovers. In the end, the repeated variation of the group velocity causes the equally spaced sub-pulses. Thus, the LCO period of the FEL power within the macro-pulse is determined by the time a sub-pulse needs to propagate the slippage distance s [Jar93]:

$$T = \frac{s}{\Delta L}\frac{L_0}{c_0}. \tag{5.1}$$

The experimental results of the oscillation period T are in qualitative agreement with the analytical trend. However, there is a quantitative deviation of about a factor two. As known from literature [Col90], the FEL pulse formation is very sensitive to the position and angle of the electron beam injection into the undulator. This is supported by our measurements at different beamtimes, where variations of the pulse shapes have been identified (not shown). However, the condition of the electron beam is usually not monitored at the FHI FEL facility. Thus, we assign the deviation to the specific alignment of the particle beam relative to the undulator axis. Nevertheless, the conclusions concerning the fundamental physical process are the same.

The results of the FHI FEL pulse development are in agreement with other FEL oscillators [Jar93; Kni95]. However, in contrast to the auto-correlation experiments performed there, the cross-correlation measurements presented here resolve the evolution of the actual pulse shape, thus providing deeper insight into the FEL physics.

5.2.2 FEL Dynamics Simulations

The observed LCO pattern can be a characteristic feature of nonlinear dynamical systems without external perturbation. To this end, the theory introduced in Sec. 2.4.2 has been applied to describe the lasing behavior of an FEL oscillator operating with ps-short electron bunches [Col90]. There, the critical parameters are the bunch length σ_z, the slippage $s = N\lambda$, composed of the number of undulator periods N and the optical wavelength λ, and the detuning value ΔL. In the following, calculations of the optical intensity development within one macro-pulse will be presented for various cavity detunings. Thus, the simulated FEL micro-pulse profiles can be directly compared to the experimental observations.

The classical relativistic theory used to describe the temporal and spectral structure of the FEL emission is based on coupled Maxwell-Lorentz equations. The system of nonlinear differential equations is given by Eqs. (2.58) and (2.59). In order to simulate the temporal development of the pulse profile, at least two dimensions have to be included in the simulations: the time t and the longitudinal coordinate z along the undulator axis. For a complete description of the effects taking place in the FEL oscillator, e.g. optical wavefront distortion, also the transverse directions x, y have to be taken into account. Whereas 2D calculations are solvable on an office computer, the 4D simulations require dedicated hardware [Bla15].

2D FEL Dynamics Simulations

Method Due to the electron-photon interaction, energy is transferred from the gain medium to the electromagnetic field and vice versa. For the low-current electron pulses a Gaussian-shaped temporal profile $j(z) = j_0 \exp\left(-\frac{z^2}{2\sigma_z^2}\right)$ of width $\sigma_z = 3.3\,\mathrm{ps}$ has been assumed. Note that the z-axis in the calculations is equivalent to the delay axis τ in the experiments. Each undulator pass, the slower electron bunches, consisting of N sample electrons, slip back relative to the light pulse by one slippage length s. Multiple (n) round trips of the optical pulse within the cavity (of time $t_{\mathrm{pass}} = 2L_0/c_0$) are followed, giving the time axis $t = n\,t_{\mathrm{pass}}$ of the macro-pulse. The resonator losses are considered by a cavity Q factor, reducing the field intensity each pass, $|a_n|^2 = |a_{n-1}|^2\,\mathrm{e}^{-Q}$. Shortening of the cavity length due to detuning is included by advancing the optical pulse every round trip by the length ΔL. To start the growth of the light pulse from spontenous emission, noise is added to the phase of the electrons, creating a random distribution of $\zeta \in [-\pi/2, 3/2\pi[$ in phase space. Initially, each particle enters the undulator with velocity ν_0. The coupled differential equations for the particles, Eq. (2.58), and the optical envelope $a(z)$, Eq. (2.59), are solved numerically for each pass, see Appendix A.2.

Results The dependence of the calculated optical pulse shape $I(z,t) = |a(z,t)|^2$ on the cavity detuning ΔL is depicted in Fig. 5.5. Consistent with the experimental observations (cf. Fig. 5.3), sub-pulses and LCOs of the FEL power occur for a limited range of cavity lengths. Close to zero detuning, short but intense single-peaked optical pulses

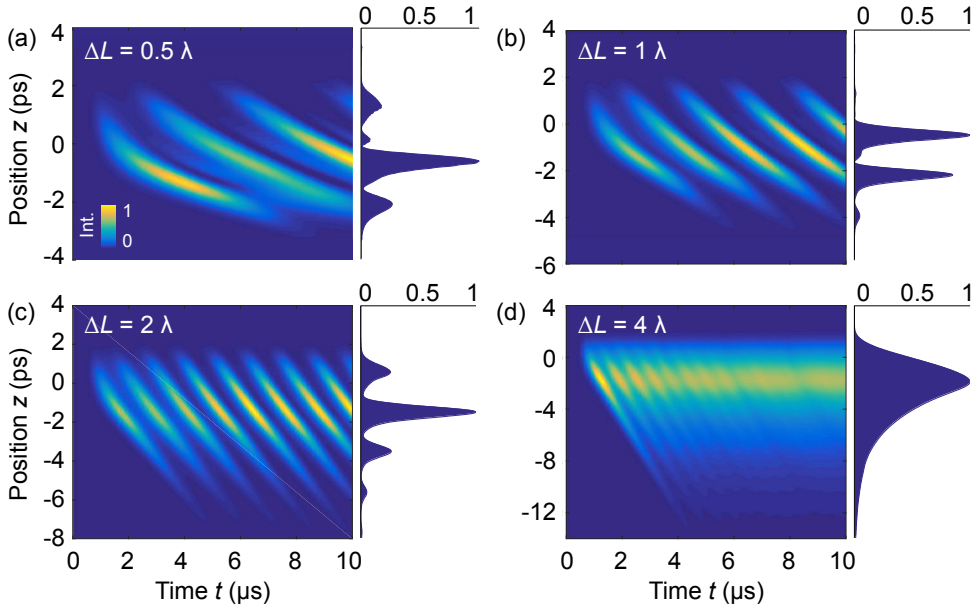

Fig. 5.5 Simulation of the optical emission based on 2D FEL theory. In the 2D images, the development of the micro-pulse intensity profile $I(z)$ is shown at various detuning values, $\Delta L = 0.5\lambda, 1\lambda, 2\lambda$ and 4λ, (a)-(d). The intensities are normalized for each plot; the ratio reads as 7.5:6:3:1 from (a) to (d). The pulse profile at the end of the macro-pulse, equivalent to $t = 10\,\mu s$, is depicted in the normalized line graphs. Note the different time scale of the vertical axes, due to the longer micro-pulse duration at larger cavity detunings. The formation of sub-pulses and the variation of the limit-cycle oscillation period is clearly present.

are generated. With a further advancement of the light pulses with respect to the electron bunches, a modulation of the gain during the pulse growth leads to the occurrence of sub-pulses within the micro-pulse. At large detuning ($\Delta L \gtrsim 4\lambda$), the FEL intensity saturates at a lower level. Consequently, the sub-pule formation sets in earlier and the modulation depth is smaller. Many sub-pulses arrange into a single-peaked, temporally long micro-pulse. Since the electric field amplitude is calculated, the maximum intensity at the different detuning settings can be compared, given in the legend to Fig. 5.5. It is found that the strongest FEL pulses are generated at around $\Delta L = 0.5\lambda$, which is in agreement with the experimental observations.

A further aspect revealed from comparison of the simulation data with the measured pulse shapes in Figs. 5.2 and 5.3 is related to the sharpness of the intensity peaks. Whereas the calculated FEL power oscillations along the macro-pulse time axis are rather clear, the experimental results show blurring. This is actuallly due to the measurement procedure of acquiring multiple shots and subsequent averaging. Hence, the individual FEL macro-pulses exhibit slightly different starting times due to gain fluctuations.

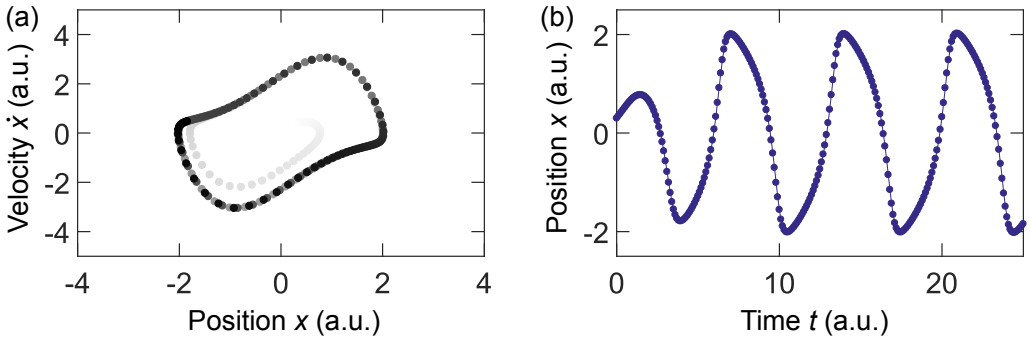

Fig. 5.6 Nonlinear dynamics of a van der Pol oscillator. (a) Temporal development of the system displayed in phase-space $(x, \dot{x})$. The trajectory shows a limit-cycle solution as time approaches infinity, $t \to \infty$ (light gray to black). (b) Plot of the corresponding limit-cycle oscillation $x(t)$ of the system observable in the time domain.

The generation of sub-pulses in an FEL oscillator has been first predicted by Colson using this theoretical model [Col82]. Due to the nonlinear equation of motion governing the dynamics of the electrons in the light field, Eq. (2.58), the coupled optical amplitude can be strongly modulated. As another exemplary nonlinear system, the van der Pol oscillator, present in mechanical and electrical problems [Man72], exhibits a limit-cycle solution as well. There, the time evolution is determined by a nonlinear damping term ($\mu \neq 0$):

$$\ddot{x} - \mu(1 - x^2)\dot{x} + x = 0. \tag{5.2}$$

The solution of the differential equation is displayed in Fig. 5.6. In Fig. 5.6(a), the temporal development of the oscillator in the phase space $(x, \dot{x})$ is shown. As time evolves towards $t \to \infty$, a closed trajectory occurs, the 'limit cycle'. The temporal evolution of the position $x(t)$ is depicted in Fig. 5.6(b), where pronounced oscillations with a fixed period T are observed. This can be seen as analogon to the behavior of the optical amplitude of the FEL emission, hence giving reason to the term limit-cycle oscillation.

4D FEL Dynamics Simulations

In order to obtain a detailed calculation of the complex optical field amplitude $a(x, y, z, t)$, the two-dimensional simulations are extended in the transverse dimensions. Thus, the diffraction of the light wave within the cavity, the actual overlap of electron beam and optical mode as well as the finite-size hole out-coupling are included. For efficient energy extraction, the photon beam cross-section πw_0^2 should be similar to the electron beam size πr_e^2, and the Rayleigh range $\pi w_0^2/\lambda$ in the order of the undulator length L_U [Col90].

Method For the four-dimensional optical field simulations, the general Maxwell-Lorentz equations are used instead of the reduced equations (2.58) and (2.59), yielding [Col90]

$$\frac{d\gamma}{dt} = \frac{\omega K (J_0(\xi) - J_1(\xi)) K_\mathrm{R}}{\gamma} \cos(\xi + \phi) \tag{5.3}$$

$$\left(\frac{\partial}{\partial z} + \frac{1}{c} \frac{\partial}{\partial t} \right) E \mathrm{e}^{\mathrm{i}\phi} = -2\sqrt{2}\pi e K (J_0(\xi) - J_1(\xi)) n_\mathrm{e}(z - \beta_z ct) \langle \frac{1}{\gamma} \mathrm{e}^{-\mathrm{i}\xi} \rangle_{(z-\beta_z ct)} \tag{5.4}$$

Here, $K_\mathrm{R} = eE\lambda/2\pi mc^2$ is the optical potential, $E\mathrm{e}^{\mathrm{i}\phi}$ the complex optical field, $n_e(z - \beta_z ct)$ describes the electron bunch traveling at speed β_z, $\langle ... \rangle$ indicates the average over the electrons and $J_0(\xi)$ and $J_1(\xi)$ are Bessel functions. This set of equations is routinely used for the design of FEL facilities [Bla15], allowing to study the influence of, e.g., the angle and position of the electron beam injection into the undulator, the energy spread of the particles and higher order optical modes. The self-consistent solution of Eqs. (5.3) and (5.4) using the FHI FEL parameters given in Tab. 3.1 and generation of the plots in Figs. 5.7 and 5.8 has been performed by collaborator William B. Colson[10].

Results The optical intensity $I(z,t)$ at different cavity detunings is depicted in Fig. 5.7. Obviously, the pulse shape evolution agrees qualitateively with the results of the 2D simulations (Fig. 5.5) as well as with the experimental data (Figs. 5.2, 5.3). This means that pronounced sub-pulses of 1 ps $-$ 2 ps duration (FWHM) are present at intermediate detuning values ($0.5\lambda \lesssim \Delta L \lesssim 2\lambda$), see Fig. 5.7(a)-(c). In contrast, a single-peaked micro-pulse is emitted for a strongly shortened FEL cavity, Fig. 5.7(d). This can be directly seen in the line graphs [right side of Fig. 5.7(a)-(d)], representing the optical micro-pulse shape $I(z)$ that has been developed towards the end of the macro-pulse, i.e. at $t = 10\,\mu\mathrm{s}$. The observed temporal shift of the optical intensity peak relative to the driving Gaussian-shaped current pulse $j(z)$ is caused by the pulse slippage as well as the detuning mechanism.

The LCO period T extracted from the 4D simulations is shown in Fig. 5.4 for comparison with the measurement. The trend of decreasing T values for a stronger cavity detuning ΔL is clearly present. Also, the simulation results are in good agreement with the simple analytical expression of Eq. (5.1). Nevertheless, there is a significant quanitative deviation from the experimental data. To check whether this might arise due to the value assumed for the electron bunch length σ_z, calculations for different current pulse durations have been performed (Fig. 5.4). However, the impact on the limit-cycle period is negligible. Therefore, the reason for the deviation might be the previously mentioned non-perfect electron beam alignment. Simulations dedicated to this aspect have not been conducted. A further issue is the uncertainty in the experimental cavity detuning ΔL, which amounts to $\pm 0.5\,\lambda$.

[10] Compass Scientific Engineering, Fremont, California, USA

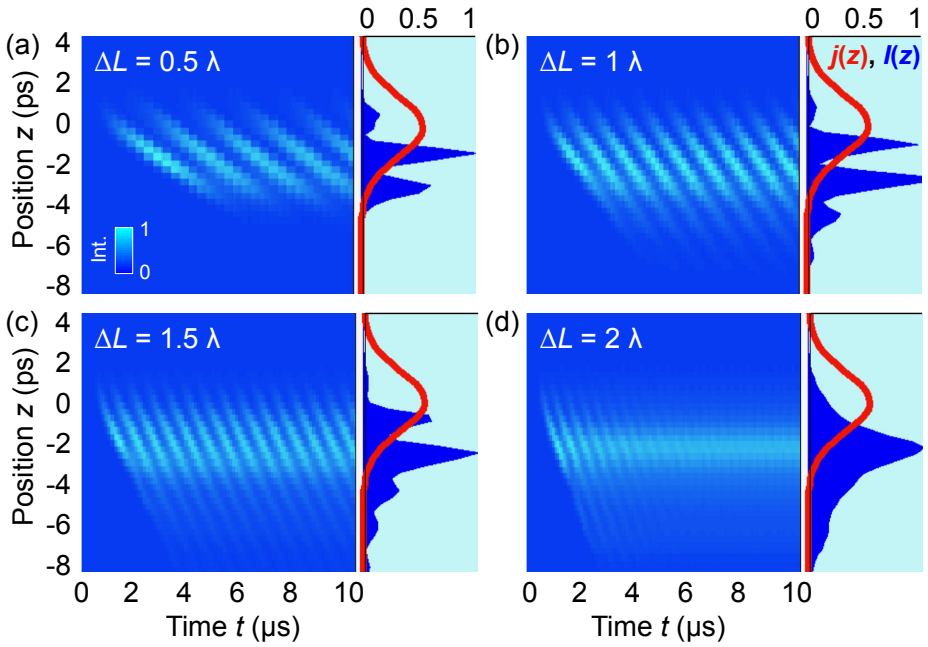

Fig. 5.7 FEL emission simulation based on 4D FEL theory. Depicted is the evolution of the optical intensity of the micro-pulse $I(z)$ (vertical axis) during a macro-pulse (horizontal axis), showing sub-pulse formation. The different detuning cases ΔL investigated are (a) 0.5 λ, (b) 1.0 λ, (c) 1.5 λ, and (d) 2.0 λ, respectively. The line graphs show the optical micro-pulse profile $I(z)$ (blue) and the electron bunch $j(z)$ (red) after passing the undulator.

The spectral structure $I(\lambda)$ of the FEL pulse is obtained by Fourier-transformation of the time-domain envelope $I(z)$. In Fig. 5.8, the development of the spectrum over successive cavity round trips at different detuning values ΔL is displayed. In the case of small cavity detuning, an additional frequency component λ_1 about 0.2 µm adjacent to the fundamental wavelength λ_0 appears in the FEL spectrum. This sideband arises due to the sub-pulse formation in the strong optical fields. Actually, the spectral separation is determined by the undulator geometry, $\lambda_1 - \lambda_0 = \lambda_0/N$ [Jar93]. Compared to the measured spectra in Fig. 5.1(b), which are integrated over the whole macro-pulse time, this sideband can be examined in the asymmetric spectral line shape at short cavity detuning ΔL. Moreover, a shift of the center wavelength λ_0 within the macro-pulse can be seen in the simulations (marked by arrows in the line graphs of Fig. 5.8). The larger the detuning, the stronger is the center wavelength shift. Since the FEL spectrum has not been measured time-resolved during the macro-pulse, a comparison is difficult. Concerning the spectral bandwidth of the FEL radiation, a narrowing is predicted by theory if the cavity length is shortened. This is in line with the experimental observations, cf. Fig. 5.1(b).

Overall, the full 4D simulations of the time-domain structure of the FEL oscillator radiation are in reasonable agreement with the 2D calculation results, justifying the complexity reduction for reproduction of the LCOs and sub-pulses. The benefit of the

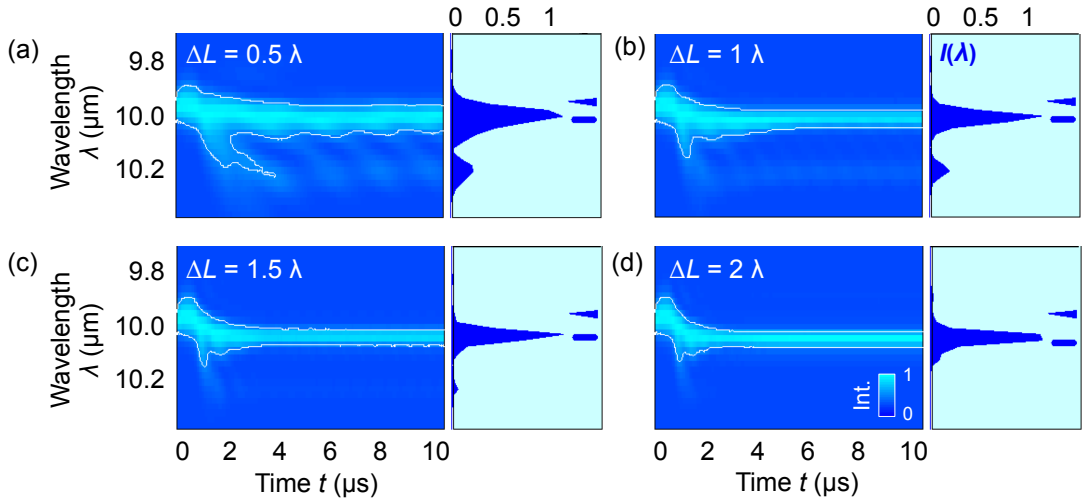

Fig. 5.8 Simulated FEL spectrum. The development of the spectral amplitude $I(\lambda)$ over the macro-pulse time is shown at different detunings, (a) $0.5\,\lambda$, (b) $1.0\,\lambda$, (c) $1.5\,\lambda$, and (d) $2.0\,\lambda$. The line graphs display the spectral structure at $t = 10\,\mu s$. In the case of (a) and (b), sidebands at $\Delta\lambda = 0.2\,\mu m$ away from the fundamental wavelength $\lambda_0 = 10\,\mu m$ are present due to the occurence of sub-pulses in the time-domain (cf. Fig. 5.7).

4D model, being sensitive to, e.g., electron beam alignment and energy spread, might be used in further investigations to clarify the discrepancy with the experimental LCO period and, moreover, to optimize the performance of the FHI FEL with respect to short, single-peaked optical pulses or a small linewidth in single-band spectral emission.

Conclusion

In summary, the experimentally and theoretically investigated pulse dynamics of an IR FEL oscillator on the ps scale provides a deep insight into the underlying FEL physics. Under certain conditions, the complex interaction between the relativistic, charged particles and the buildup of the optical field manifests in the generation of sub-ps short sub-pulses and regular power oscillations. In the spectral domain, the appearance of sidebands is observed, diminishing the resolution in spectroscopic applications of the FEL light. Thus, larger detuning values are preferred in that case, delivering narrow-band radiation. In contrast, if ultrafast optical pulses are desired for time-resolved measurements, a short cavity detuning has to be applied. Then, however, the occurence of multiple sub-pulses with shifting temporal positions during the macro-pulse has to be accepted.

6 Sum-Frequency Generation in Polar Dielectrics

Coherent radiation in the MIR spectral region is particular useful in condensed matter physics for the resonant stimulation of low-frequency excitations, such as lattice vibrations. Here, the second-order nonlinear optical response of polar dielectric materials is probed in the vicinity of optical phonon resonances. By means of IR-VIS SFG spectroscopy, the dispersion of the quadratic susceptibility tensor components is revealed. SFG spectra are found to be strongly influenced by linear optical effects.

Parts of this Chapter have been published in Ref. [Kie19].

6.1 Motivation

Sum-frequency generation spectroscopy is a valuable tool to obtain interface-specific information about vibrational resonances, adsorbate orientations and surface structures. Besides this, relevant properties of symmetry and phonon modes of bulk crystalline media can be accessed as well, provided that the solid material has an electric dipole-allowed second-order nonlinear response (cf. Sec. 2.3). Thus, bulk SFG/SHG studies are applied to reveal, e.g., structural phase transitions [She16], the domain orientation and boundaries of transition metal dichalcogenides [Li13; Li16], magnetic ordering of ferroic systems [Fie00] or lattice vibrational frequencies and forces within polar crystals [Dek03; Win18].

Due to the selection rules valid for SFG phenomena, only a subset of all bulk phonons can be probed at the Brillouin zone center. This might be advantageous to identify lattice modes of crystals with complex vibrational spectra. Moreover, SFG spectroscopy provides complementary information compared to other phonon-sensitive optical techniques, such as IR absorption and Raman scattering. In IR-VIS sum-frequency studies, the incident wavelength-tunable low-energy photon is in the same energy range as the lattice oscillations. Thus, if the IR frequency ω_1 is in resonance with an SFG-allowed phonon mode $\omega(\boldsymbol{q} \approx 0)$, the nonlinear susceptibility $\chi^{(2)}(\omega_3, \omega_1, \omega_2)$ exhibits a sharp enhancement. Depending on the behavior of the linear optical properties, the vibrational modes can be directly extracted from the SFG response. In addition, azimuthal measurements at the resonant frequencies inform about the symmetry character of the particular modes.

One should be aware that any medium possesses electric-quadrupole and magnetic-dipole contributions to the second-order susceptibility $\chi^{(2)}$. Hence, the SFG signal from the bulk of centrosymmetric solids might reveal useful information [Zha19], however, it is usually weak and potentially dominated by the sum-frequency radiation generated at the surface. Here, polar dielectric crystals without inversion symmetry are explored in nonlinear second-order spectroscopy in order to identify bulk phonon modes.

6.2 Theoretical Model

When using nonlinear bulk media with electric dipole-allowed sum-frequency generation, the contribution from the surface can be neglected in good approximation. Hence, the measured response in spectroscopy experiments is given by, following Eq. (2.54),

$$I(\omega_3) \propto \left| \mathbf{F}(\omega_3)\hat{\boldsymbol{e}}(\omega_3) \cdot \boldsymbol{\chi}_{\mathrm{B}}^{(2)} : \mathbf{F}(\omega_1)\hat{\boldsymbol{e}}(\omega_1)\, \mathbf{F}(\omega_2)\hat{\boldsymbol{e}}(\omega_2) \right|^2 / \Delta k^2, \tag{6.1}$$

after normalization to the input intensities, with the bulk second-order susceptibility tensor $\boldsymbol{\chi}_{\mathrm{B}}^{(2)}(\omega_3, \omega_1, \omega_2)$ and the wavevector mismatch $\Delta k = |\boldsymbol{k}(\omega_3) - \boldsymbol{k}(\omega_2) - \boldsymbol{k}(\omega_1)|$ inside the investigated material. Due to the conservation of momentum parallel to the interface, cf. Eq. (2.55), the mismatch yields $\Delta k = \Delta k_z$. In general, the wavevector is a complex quantity, reducing to $|\boldsymbol{k}| = \omega n / c_0$ only for non-absorbing media. Depending on the setup geometry used, the wavevector component $k_z(\omega_3)$ might be antiparallel (reflection type, backward propagating) or parallel (transmission type, forward propagating) to the input beams. The physical consequence of the wavevector mismatch is the limited volume part of the bulk contributing to the SFG signal, i.e. the region enclosed by the coherence length $L_c \sim 1/\Delta k$, strongly influenced by the dispersion of the dielectric function of the material.

The Fresnel tensors in Eq. (6.1) relate the actual field strength inside the nonlinear material to the incident electric field component of the optical waves. Besides the spectral dispersion, the optical symmetry of the crystal is relevant. In the case of an uniaxial anisotropic material (labeled II) interfacing with an isotropic medium (I) and the surface normal of the c-cut crystal being parallel to the z-axis, i.e. $c \parallel z$, the diagonal Fresnel factors are [Mor18; Paa15]

$$\begin{aligned} F_{xx} &= \frac{2\varepsilon^{\mathrm{I}} g_{\mathrm{e}}^{\mathrm{II}}}{\varepsilon_{\perp}^{\mathrm{II}} g^{\mathrm{I}} + \varepsilon^{\mathrm{I}} g_{\mathrm{e}}^{\mathrm{II}}}, \\ F_{yy} &= \frac{2g^{\mathrm{I}}}{g^{\mathrm{I}} + g_{\mathrm{o}}^{\mathrm{II}}}, \\ F_{zz} &= \frac{\varepsilon_{\perp}^{\mathrm{II}}}{\varepsilon_{\parallel}^{\mathrm{II}}} \frac{2\varepsilon^{\mathrm{I}} g^{\mathrm{I}}}{\varepsilon_{\perp}^{\mathrm{II}} g^{\mathrm{I}} + \varepsilon^{\mathrm{I}} g_{\mathrm{e}}^{\mathrm{II}}}. \end{aligned} \tag{6.2}$$

There, the dispersion functions are part of the dielectric tensor with $\varepsilon_{xx}(\omega), \varepsilon_{yy}(\omega) = \varepsilon_{\perp}(\omega)$ and $\varepsilon_{zz}(\omega) = \varepsilon_{\parallel}(\omega)$. The relevant z-components of the wavevector $g \equiv k_z$ read

$$
\begin{aligned}
g^{\mathrm{I}}(\omega,\theta) &= \frac{\omega}{c_0}\sqrt{\varepsilon^{\mathrm{I}}(\omega)}\cos\theta,\\
g_{\mathrm{o}}^{\mathrm{II}}(\omega,\theta) &= \frac{\omega}{c_0}\sqrt{\varepsilon_{\perp}^{\mathrm{II}}(\omega)-\sin^2\theta},\\
g_{\mathrm{e}}^{\mathrm{II}}(\omega,\theta) &= \frac{\omega}{c_0}\sqrt{\frac{\varepsilon_{\perp}^{\mathrm{II}}(\omega)}{\varepsilon_{\parallel}^{\mathrm{II}}(\omega)}}\sqrt{\varepsilon_{\parallel}^{\mathrm{II}}(\omega)-\sin^2\theta},
\end{aligned}
\tag{6.3}
$$

with the angle of incidence θ relative to the surface normal. Due to the birefringence of the crystal, the wavevector of the radiation propagating inside medium II is subject to the polarization of the electric field. Thus, ordinary and extraordinary beam are distinguished, denoted as o and e, respectively.

The dispersion of the second-order susceptibility tensor components $\chi_{ijk}^{(2)}(\omega_3,\omega_1,\omega_2)$ can be approximated by the sum of a non-resonant contribution and a Lorentz-oscillator term for each resonance, cf. Eq. (2.47). For the crystalline materials under study, the resonances arise due to phonons in the IR spectral region, whereas the medium is transparent for the VIS and upconverted optical fields. Thus, the spectral $\chi^{(2)}$-behavior can be modeled by an IR frequency dependence of the form [Fau66]

$$
\chi_{ijk}^{(2)}(\omega_3,\omega_1,\omega_2) = \chi_{ijk\,\infty}^{(2)}\left(1+\sum_r \frac{A_{r,ijk}}{\omega_r^2-\omega_1^2-\mathrm{i}\Gamma_r\omega_1}\right). \tag{6.4}
$$

Due to the spatial symmetry of the material, only a subset of the $\chi^{(2)}$-tensor components has a finite value and is independent. The number of non-vanishing components is governed by the point group of the crystal (cf. Sec. 2.2.3). In order to use the material-specific second-order tensor in accordance with the experimental arrangement, a transformation from the crystallographic framework $(i,j,k)\in(a,b,c)$ with the principal axes a,b and c to the laboratory coordinate system $(l,m,n)\in(x,y,z)$ is necessary. The change of the basis is specified by the definition

$$
\chi_{lmn}^{(2)} = \sum_{ijk}\chi_{ijk}^{(2)}(\boldsymbol{e}_l\cdot\boldsymbol{e}_i)(\boldsymbol{e}_m\cdot\boldsymbol{e}_j)(\boldsymbol{e}_n\cdot\boldsymbol{e}_k). \tag{6.5}
$$

With the experimental geometry as depicted in Fig. 3.3(a), where the surface normal of the c-cut sample is parallel to the z-axis and x-z describing the plane of incidence, one yields the basis vectors $\boldsymbol{e}_a = \cos\varphi\boldsymbol{e}_x + \sin\varphi\boldsymbol{e}_y$, $\boldsymbol{e}_b = -\sin\varphi\boldsymbol{e}_x + \cos\varphi\boldsymbol{e}_y$ and $\boldsymbol{e}_c = \boldsymbol{e}_z$ with the azimuthal angle φ.

The actual polarizations of the incident and detected electric fields $\boldsymbol{E}(\omega)$ are accounted for in the nonlinear response function Eq. (6.1) by the unit vectors $\hat{\boldsymbol{e}}_{\mathrm{p}}(\omega_i) = (\cos\theta_i, 0, \sin\theta_i)$ and $\hat{\boldsymbol{e}}_{\mathrm{s}}(\omega_i) = (0,1,0)$ for p- and s-polarized light, respectively. The angle of incidence/emission of beam ω_i relative to the surface normal is denoted by θ_i.

6.3 4H-Silicon Carbide

6.3.1 Material

Silicon carbide (SiC) appears in nature in a variety of more than 200 different crystal polytypes. One of the commonly encountered structure exhibits a hexagonal lattice with the repeating stacking sequence $ABCB$, termed 4H-SiC. The wurtzite crystal structure of this wide-gap semiconductor ($E_g = 3.23\,\text{eV}$, indirect), belonging to point group $6mm$ [Per19b], is depicted in Fig. 6.1(a). The unit cell constants are $a = 3.1\,\text{Å}$ and $c = 10.1\,\text{Å}$ [Par98], with the stacking of the alternating cubic and hexagonal character-type Si-C bilayers along the c-axis. Also shown are the vibrational properties, Fig. 6.1(b), as obtained by *ab initio* calculations of the phonon dispersion based on density-functional perturbation theory [Pet18]. Owing to the number of atoms within the unit cell, $p = 2 \cdot 4 = 8$, multiple modes exist within the optical phonon branch. The characteristics of the important modes are given in Tab. 6.1. Besides the optical absorption in the MIR due to the vibrational resonances, the material is transparent in two windows of $\lambda = 0.4\,\mu\text{m} - 6\,\mu\text{m}$ and $16\,\mu\text{m} - 300\,\mu\text{m}$ [Fis17].

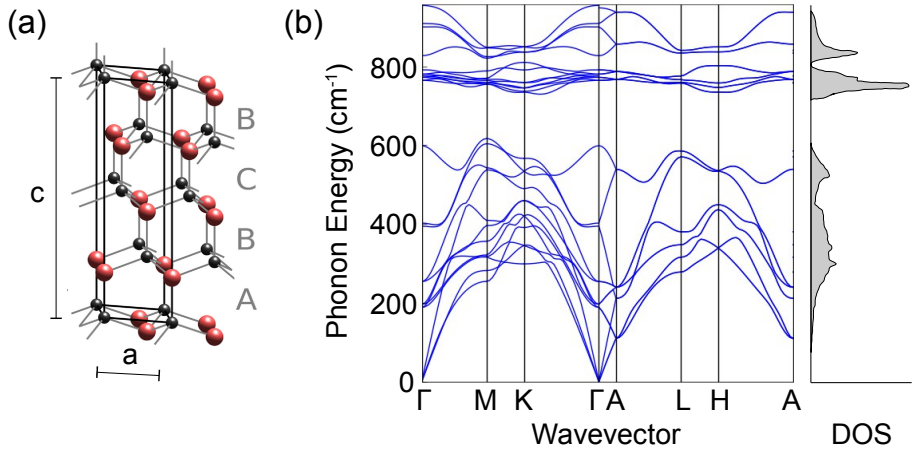

Fig. 6.1 Structure and lattice dynamics of 4H-SiC. (a) Hexgonal crystal structure consisting of Si (red) and carbon (black) atoms. Stacking order of Si-C bilayers is ABCB, lattice constants are $a = 3.1\,\text{Å}$ and $c = 10.1\,\text{Å}$. (b) Phonon dispersion in momentum space, together with the density of states, calculated by density-functional perturbation theory [Pet18]. Image (a) is taken from Ref. [Fis17], (b) from Ref. [Per19b].

4H-SiC possesses a number of promising mechanical and electronic properties, among them a high electric breakdown field, large thermal conductivity and strong Mohs hardness (9) [Par98], owing to the tight covalent Si-C bond. Therefore, it is suited for high-temperature, high-pressure and high-power applications in IR/THz optics and electronics. In particular, silicon carbide has a great technological importance due to the possibility to utilize the SiC surface for the well-ordered epitaxial growth of graphene mono- and multi-layer samples [Ber06; Has08]. Moreover, 4H-SiC can be synthesized in

Tab. 6.1 Optical phonon frequencies of 4H-SiC at the Brillouin zone center in the Reststrahlen band. The values of phonon energy and damping are extracted from a fit of the SFG spectra using Eq. (6.1). Symmetry properties are taken from Ref. [Hof94]. Planar modes ($\perp$) are IR active in the ordinary ray, axial modes ($\parallel$) are excited with the extraordinary ray.

Mode	Symmetry	ν (cm^{-1})	γ (cm^{-1})	IR activity	Raman activity
$\mathrm{TO}_{\parallel}$	A_1	787.2	3.8	x	x
$\mathrm{LO}_{\parallel}$	A_1	962.3			x
$\mathrm{TO}_{\perp}$	E_1	797.6	5.0	x	x
$\mathrm{LO}_{\perp}$	E_1	968.5			x

high quality as large-size single-phase crystals. Due to the hexagonal crystal structure, 4H-SiC exhibits birefringence regarding the linear optical properties. The point group symmetry allows for a nonzero electric dipole contribution to the second-order susceptibility [Boy08].

The investigated sample has been a semi-insulating, *c*-cut substrate made of monocrystalline 4H-SiC. The thickness is about 350 µm. U.S. Naval Research Laboratory, Washington, D.C., USA, provided the crystal. Measurements are performed in air atmosphere at room temperature. The experimental details for the acquisition of the SFG spectra of SiC using the reflection geometry and mixing of the IR FEL radiation with the VIS table-top laser light are described in Sec. 3.3.

6.3.2 Experimental Results

SFG spectra obtained from the 4H-SiC sample under different linear polarization combinations of input and output light fields are shown in Fig. 6.2(a). Note that the spectra are plotted as function of the incident IR wavenumber $\nu_{\mathrm{IR}} = 750\,\mathrm{cm}^{-1} - 1050\,\mathrm{cm}^{-1}$. The SFG intensity displayed is obtained after normalization of the measured value to the incident IR power $I(\omega_1 = \omega_{\mathrm{IR}})$ in order to remove the frequency-dependent variation of the FEL radiation intensity. The VIS power is held constant.

In case of PPP and SSP polarization, strong SFG emission is observed if the IR wavenumber is close to the LO phonon frequency at $\nu_{\mathrm{LO}\,\parallel} = 962\,\mathrm{cm}^{-1}$. No significant intensity is measured at all under SPP, PSP and PPS conditions. The TO phonon ($\nu_{\mathrm{TO}\,\parallel} = 787\,\mathrm{cm}^{-1}$) can not be identified in the SFG response. These experimental findings might be surprising at first sight since the TO mode is SFG active, i.e. IR- and Raman-allowed [Nak97], whereas the LO vibration does not absorb the IR radiation and thus does not contribute to a resonant enhancement of the second-order susceptibility. Also, there the SFG response is observed as a double peak, potentially pointing towards a linear optical effect where the crystallographic anisotropy of the hexagonal structure comes into play.

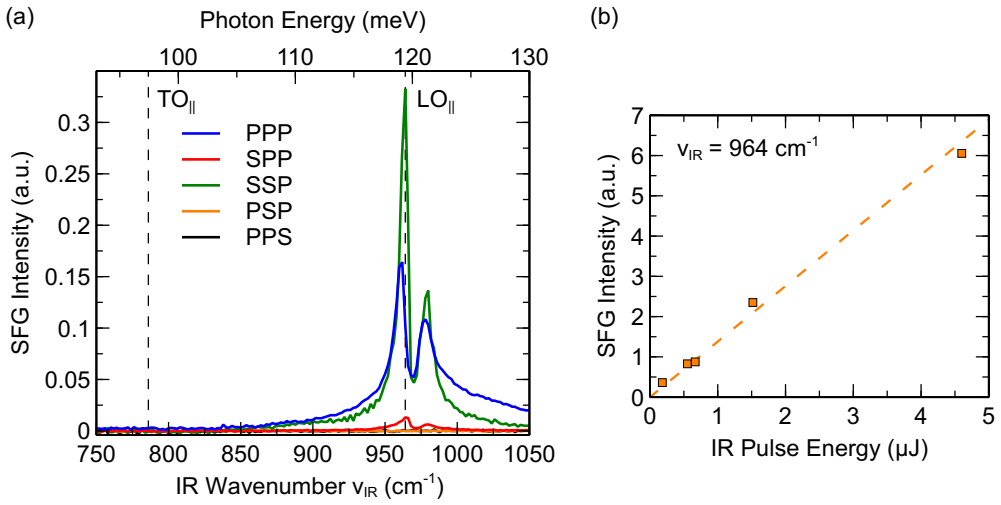

Fig. 6.2 Experimental SFG spectra and fluence dependence of 4H-SiC. (a) Polarization dependence of the nonlinear response around TO and LO phonon. (b) IR fluence dependence of the SFG intensity at $\nu_{\mathrm{IR}} = 964\,\mathrm{cm}^{-1}$ for constant VIS power and PPP polarization. The linear behavior is in accordance with a second-order SFG process.

The fluence dependence of the detected SFG intensity on the energy of the IR pulses has been tested in Fig. 6.2(b). Spectrally selective light detection is realized by a band-pass filter centered around the expected sum-frequency wavelength of $\lambda_{\mathrm{SFG}} \sim 500\,\mathrm{nm}$. The observed linear relation is in agreement with Eq. (2.54), valid for a second-order nonlinear optical process. Thus, the spectra shown originate from sum-frequency generation. Note that the angle of the sum-frequency emission is close to the intense, specularly reflected VIS radiation ($\theta(\omega_3) - \theta(\omega_2) \sim 1°$), thus, an effective suppression of the upconversion light is achieved by the spectral filter.

6.3.3 Theoretical Analysis

In order to understand and model the sum-frequency behavior of 4H-SiC according to Eq. (6.1), information about the dielectric dispersion and character of the nonlinear susceptibility tensor is required. For the linear optical function, a one-phonon term Lorentz oscillator of the form Eq. (2.19) is used within the Reststrahlen region [Mut99],

$$\varepsilon_{\perp,\parallel}(\omega) = \varepsilon_{\perp,\parallel\,\infty}\left(1 + \frac{\omega^2_{\mathrm{LO}\,\perp,\parallel} - \omega^2_{\mathrm{TO}\,\perp,\parallel}}{\omega^2_{\mathrm{TO}\,\perp,\parallel} - \omega^2 - \mathrm{i}\gamma_{\mathrm{TO}\,\perp,\parallel}\omega}\right) \tag{6.6}$$

with the high-frequency dielectric constant ε_∞, resonance frequency ω_{TO} and damping γ_{TO} for the phonon mode in the basal plane of SiC ($\perp$) and parallel to the crystal c axis ($\parallel$), respectively. The parameters at room temperature are taken from Ref. [Mut99].

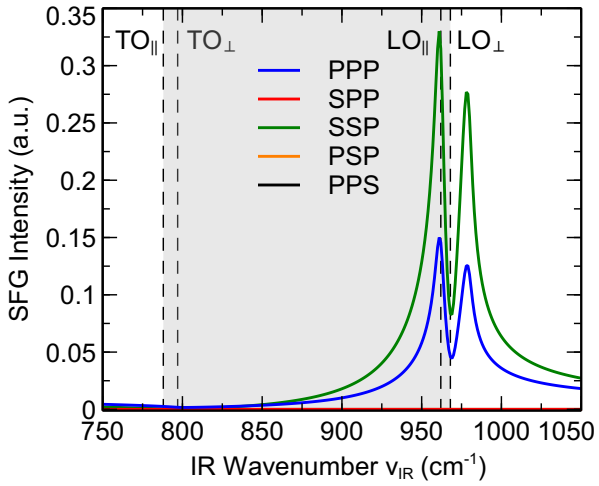

Fig. 6.3 Theoretical SFG spectra of 4H-SiC. Using the parameters of model Eq. (6.1) fitted to the PPP measurement (Fig. 6.2), the spectral response is calculated for different polarization configurations. The Reststrahlen band between the $\mathrm{TO}_{||}/\mathrm{TO}_{\perp}$ and $\mathrm{LO}_{||}/\mathrm{LO}_{\perp}$ phonon modes is indicated (gray area).

Due to the varying documented numerical values and to account for the specific crystal quality, the phonon-related properties are adjusted to fit the experimental results. In the transparent VIS/NIR region, Sellmeier equations for $\varepsilon_{\perp}(\omega) = n_{\mathrm{o}}^2(\lambda)$ and $\varepsilon_{||}(\omega) = n_{\mathrm{e}}^2(\lambda)$ are employed [Wan13].

The second-order susceptibility tensor $\boldsymbol{\chi}^{(2)}$ of the hexagonal crystal 4H-SiC of point group $6mm$ has the following non-vanishing components, given in Cartesian coordinates [Boy08]:

$$\chi^{(2)}_{zzz}, \chi^{(2)}_{zxx} = \chi^{(2)}_{zyy}, \chi^{(2)}_{xzx} = \chi^{(2)}_{yzy}, \chi^{(2)}_{xxz} = \chi^{(2)}_{yyz}. \tag{6.7}$$

Due to the crystal symmetry, just four independent components are present. Using the spectral dispersion of the nonlinear susceptibility according to Eq. (6.4), the only resonant contribution arises due to the TO phonon mode. Within the basal plane, the vibrational mode $\omega_{\mathrm{TO},\perp}$ at the Γ point obeys E_1 symmetry, whereas the lattice oscillation $\omega_{\mathrm{TO},||}$ polarized in the direction of the optic axis of the crystal is A_1 symmetric [Mut99]. The appropriate phonon frequencies have to be used in the resonant term of the $\chi^{(2)}_{lmn}(\omega_3, \omega_1, \omega_2)$ component for the IR field polarization $\boldsymbol{E}(\omega_1)$ parallel or perpendicular to the z-axis.

For the instructive case of PPP polarization, where a non-vanishing second-order signal is expected, the SFG response function obtained according to Eq. (6.1) reads:

$$\begin{aligned} I_{\mathrm{PPP}}(\omega_3) \propto |&(F_{\mathrm{xx}}(\omega_3)\cos\theta_3\, \chi^{(2)}_{\mathrm{xxz}}\, F_{\mathrm{xx}}(\omega_2)\cos\theta_2\, F_{\mathrm{zz}}(\omega_1)\sin\theta_1 \\ &+ F_{\mathrm{xx}}(\omega_3)\cos\theta_3\, \chi^{(2)}_{\mathrm{xzx}}\, F_{\mathrm{zz}}(\omega_2)\sin\theta_2\, F_{\mathrm{xx}}(\omega_1)\cos\theta_1)^2 \\ &+ (F_{\mathrm{zz}}(\omega_3)\sin\theta_3\, \chi^{(2)}_{\mathrm{zxx}}\, F_{\mathrm{xx}}(\omega_2)\cos\theta_2\, F_{\mathrm{xx}}(\omega_1)\cos\theta_1 \\ &+ F_{\mathrm{zz}}(\omega_3)\sin\theta_3\, \chi^{(2)}_{\mathrm{zzz}}\, F_{\mathrm{zz}}(\omega_2)\sin\theta_2\, F_{\mathrm{zz}}(\omega_1)\sin\theta_1)^2 |/\Delta k^2_{\mathrm{PPP}}. \end{aligned} \tag{6.8}$$

The curve fitted to the experimental data is shown in Fig. 6.4(a). The free parameters are the phonon center frequency ω_r and linewidth γ_r, entering into both the dielectric function and the second-order susceptibility, as well as the non-resonant constants $\chi^{(2)}_{ijk\,\infty}$ and resonance amplitudes $A_{r,ijk}$ contained in the nonlinear susceptibility. The obtained fit result is in good agreement with the measurement, allowing for disentanglement of the several contributions to the SFG spectrum as listed in Sec. 6.2.

The nonlinear origin of the emitted radiation is captured by the dispersive $\chi^{(2)}(\omega_1)$ tensor, whose absolute components $|\chi^{(2)}_{ijk}|^2$ are plotted in Fig. 6.4(b). Since the spectral variation of the upconverted radiation is rather small ($\lambda_3 = 498.5\,\mathrm{nm} - 506.0\,\mathrm{nm}$), only the IR frequency dependence of the second-order susceptibility is taken into account. Further, no electronic resonances of the material are expected as $\hbar\omega_2, \hbar\omega_3 \lesssim 2.5\,\mathrm{eV}$, being well below the band gap. In case of the PPP combination, all independent tensor components contribute to the detected SFG signal. Owing to the dispersion Eq. (6.4) with the SFG-active $\mathrm{TO}_{\parallel,\perp}$ phonon mode, a resonant enhancement of the nonlinear susceptibility $\chi^{(2)}_{ijk}(\omega_1)$ of about two orders of magnitude is observed in the model calculation. Depending on the relevant tensor component, the peak occurs at the IR photon energy $\hbar\omega_1$ matching either the axial ($\omega_{\mathrm{TO},\parallel}$) or planar ($\omega_{\mathrm{TO},\perp}$) TO vibration.

In order to explain the apparent discrepancy of the peak positions in the second-order susceptibilities with the measured spectrum, linear optical effects have to be invoked. On the one hand, these modify the actual field strength being present in the bulk material. The Fresnel factors, Eq. (6.2), calculated for the IR radiation $|F_{ll}(\omega_1, \theta_1)|^2$ under the used experimental geometry are depicted in Fig. 6.4(c). For a p-polarized field $\boldsymbol{E}(\omega)$, only F_{xx} and F_{zz} are relevant. Close to the TO phonon wavenumber, reduced transmission of the IR radiation occurs due to the strong absorption of the crystal. Still within the Reststrahlen band, the Fresnel factor is increased towards the LO vibration due to a diminishing real part of the permittivity (Fig. 2.2). Remarkably, the out-of-plane component $F_{zz}E_z$ of the electric field varies by three orders of magnitude. Due to the optical anisotropy of the 4H-SiC crystal, both $\omega_{\mathrm{LO}\,\parallel}$ and $\omega_{\mathrm{LO}\,\perp}$ enter as singularities into F_{zz}, Eq. (6.2), giving rise to two spectrally narrow peaks in the local field function. This effect is absent in the case of normal incidence ($\theta_1 = 0$), as shown for illustration in Fig. 6.4(c) as well, essentially recovering an isotropic linear response.

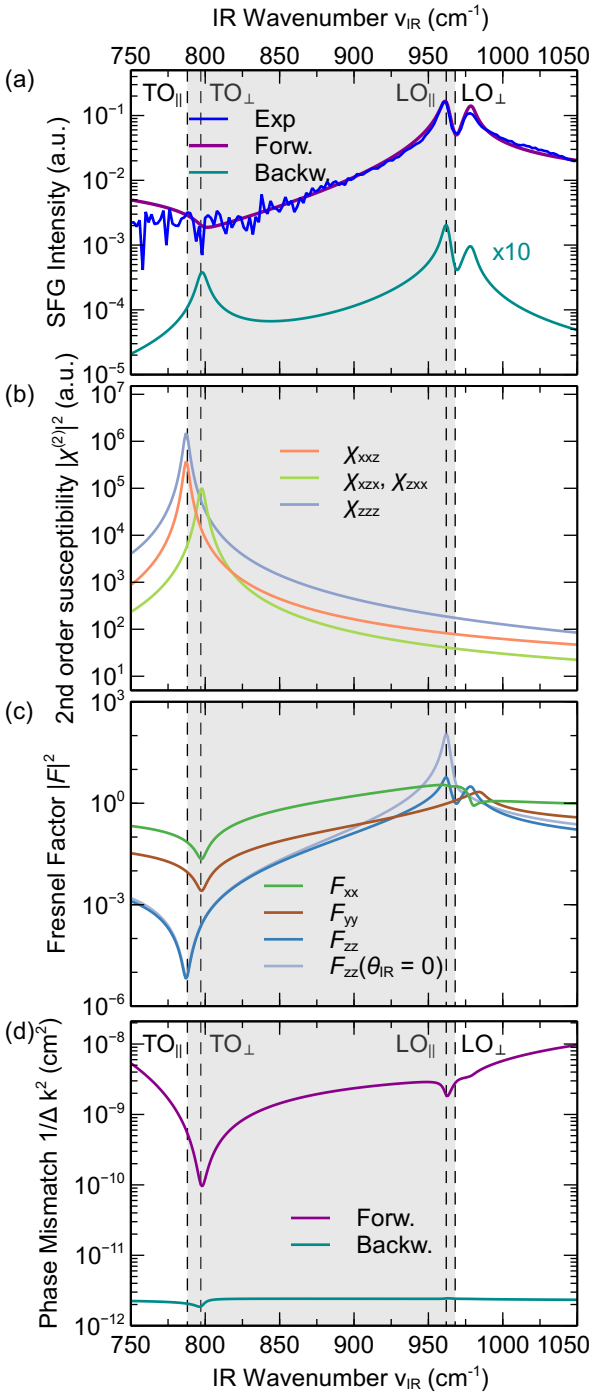

Fig. 6.4 Sum-frequency generation in the Reststrahlen region of 4H-SiC. Shown are the (a) the total intensity as measured and fitted with the model Eq. (6.1), (b) the IR dispersion of the quadratic susceptibility tensor components, (c) the Fresnel factors $|F_{ll}|^2$ governing the transmission of the IR field at the air/SiC interface and (d) the phase mismatch between IR, VIS and SFG wave inside the nonlinear medium. Depending on the propagation direction of the SFG radiation inside the crystal (forward, backward), the mismatch and hence the amplitude and spectral behavior of the emitted light are affected. The broad-range Reststrahlen band is marked (gray area). Data are for PPP configuration.

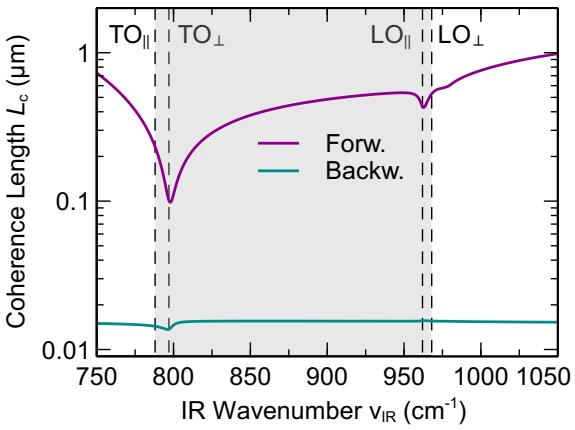

Fig. 6.5 Coherence length for SFG emission in 4H-SiC. The interaction depth of IR-VIS sum-frequency mixing is calculated for for- and backward propagation direction in PPP polarization.

On the other hand, the dielectric dispersion affects the length of the complex wavevector $k_z(\omega_1)$ inside the nonlinear medium and, hence, the mismatch of the spatial electric field phases $e^{ik_z(\omega)z}$. The inverse square of the phase difference, $1/\Delta k^2$, decisive for the sum-frequency intensity according to Eq. (6.1), is depicted in Fig. 6.4(d) for the PPP case. When considering the forward propagation of the SFG radiation through the transparent crystal, the wavevector mismatch Δk_z is rather small, compared to the backtraveling sum-frequency field, being antiparallel to the incident waves. Thus, the forward contribution of the SFG intensity dominates by about three orders of magnitude in the measured signal [Fig. 6.4(a)] due to reflection at the optically flat sample backside (reflectance at SiC/air interface $|r_p|^2 = 0.16$). The IR dispersion is less prominent in the backward-type phase-mismatch due to the large $\Delta k_z \approx 2k_z(\omega_2)$ and $|k_z(\omega_1)| \ll |k_z(\omega_2)|$.

In total, the consequence of the frequency-dependent permittivity is a strong modification of the nonlinear spectrum. The resonant enhancement in $\chi^{(2)}(\omega_1)$ at the TO phonon frequency is even more suppressed by the linear optical effects than at any other IR wavelength. Instead, a (double) peak in the SFG behavior at the LO mode is induced, mainly caused by the increased Fresnel transmission and, to a lesser extent, due to the smaller phase mismatch. As seen in Fig. 6.4(a), the variation in the SFG intensity is at least two orders of magnitude across the whole IR spectral range, strongly influenced by the dispersion of the out-of-plane component of the electric field $F_{zz}E_z$ inside the material.

The coherence length L_c, describing the effective bulk volume for the frequency mixing, is shown in Fig. 6.5. Whereas the interaction depth amounts to about one VIS wavelength in forward direction, $L_c \sim \lambda_2$, the backward-type SFG emission is concentrated to a smaller, largely wavelength-independent region of $L_c \sim 15\,\text{nm}$. Considering the lattice constant c along the z direction, the latter case corresponds to a length of about 15 crystal unit cell. If one investigates nonlinear material being opaque to

the VIS/SFG wavelength, absorption would reduce the interaction volume even further. Then, in reflection-type SFG measurements, the coherent SFG process is sensitive to a thin volume close to the interface, typically tens of nanometers [Hor19], although the bulk response is probed.

Regarding the fitted nonlinear susceptibility coefficients $\chi^{(2)}_{ijk}$, a stronger $|\chi^{(2)}_{zzz}|$ component is observed compared to the other tensor elements, cf. Fig. 6.4(b). However, one should be aware that a reliable extraction of the second-order optical constants from the measured SFG intensity is difficult. This is due to the currently low signal-to-noise ratio in the order of 10^2 whereas the variation just in the linear response of the investigated system amounts to $\sim 10^4$. For comparison, reported experimental values of the quadratic optical coefficients for 4H-SiC in the NIR region give a ratio of $\chi^2_{zzz}/\chi^2_{zxx} = -4.5$ [Nie99] and show a similar value for $\chi^2_{zxx} \approx \chi^2_{xzx} \approx 6.5\,\mathrm{pm/V}$ [Sat09], in reasonable agreement with the measurement. Calculated second-order susceptibilities based on density functional theory support the reported experimental values [Che94; Ado00; Hue11]. Moreover, it has been found that the optical nonlinearity is stronger for SiC polytypes of reduced lattice hexagonality (e.g. 6H, 3C), possessing also a smaller band gap [Nie99].

6.4 α-Quartz

6.4.1 Material

Quartz, chemical formula SiO_2, is one of the most common minerals on earth, due to the abundant nature of its constituents silicon and oxygen. Besides the amorphous form, also known as fused silica or glass, quartz can crystallize in a variety of polytypes. Among the different crystal structures, α-quartz, see Fig. 6.6(a), belongs to point group 32 with a trigonal lattice structure [Per19c]. A prominent feature of quartz is the strong piezoelectric effect [Har09], establishing its daily usage as crystal oscillator in quartz clocks. Intrinsically related to the occurence of piezoelectricity, the crystal does not exhibit a center of inversion. Hence, second-order nonlinear optical processes are dipole-allowed. Actually, quartz was used in the first demonstration of harmonic frequency conversion by nonlinear optics [Fra61]. The birefringent properties of quartz, owing to the positive uniaxial crystal structure, are of great technological importance, e.g. for optical wave retarders and polarizers.

The mineral α-quartz is characterized by a large electronic band gap, 5.7 eV (indirect) [Per19c], making it an excellent dielectric material. This is accompanied by a large transparency window, ranging from $\lambda = 3.5\,\mu\mathrm{m}$ down to the UV region at $\lambda \sim 200\,\mathrm{nm}$ [Dmi99]. Also, the crystal is transparent for wavenumbers below the phonon absorption band. The IR response of α-quartz is determined by its vast number of phonon branches, giving rise to several absorption lines [Spi61; Ger75]. Due to nine atoms per unit cell, three acoustic and 24 optical phonon modes are present, Fig. 6.6(b). Parameters of the relevant vibrational modes are shown in Tab. 6.2.

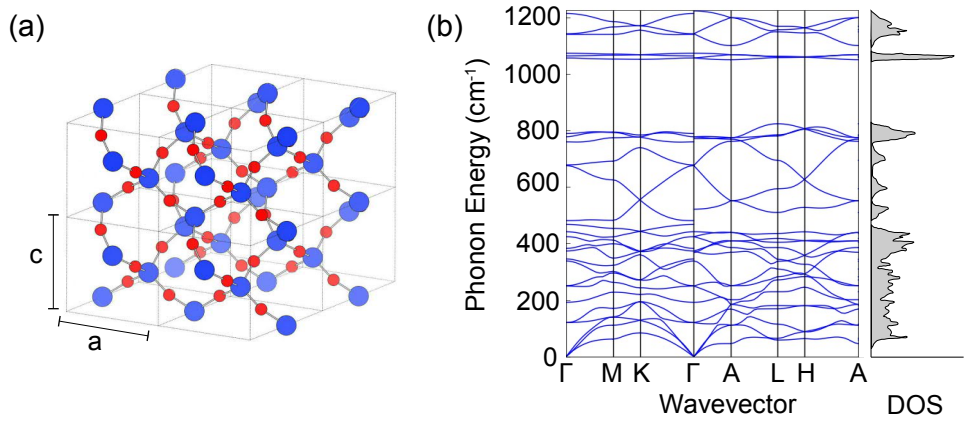

Fig. 6.6 Crystal structure and vibrational dynamics of α-quartz. (a) Arrangement of silicon (blue) and oxygen (red) atoms in the trigonal lattice with the unit cell parameters $a = 4.9\,\text{Å}$ and $c = 5.4\,\text{Å}$. (b) Phonon spectra as function of the wavevector, together with the density of states, obtained by *ab initio* calculations [Pet18; Per19c].

The sample used for the SFG spectroscopy experiment has been a monocrystalline, 8 mm thick, c-cut crystal of α-quartz, i.e. terminated with a (0001) oriented surface. It is mounted on a stage to allow for rotation about the surface normal, coinciding with the crystal c axis, in order to investigate the azimuthal dependence of the nonlinear response in reflection geometry. Besides the usual spectral and polarization filtering prior SFG light detection, a spatial filter has been applied to restrict the measurement to the sum-frequency field originating from the bulk in forward propagation direction, blocking the backward propagation.

6.4.2 Experimental Results

The SFG spectra of α-quartz taken by IR excitation in the wavenumber range of $\nu_{\text{IR}} = 680\,\text{cm}^{-1} - 1300\,\text{cm}^{-1}$ are depicted in Fig. 6.7. Different polarization conditions have been investigated, whereby a considerable SFG response is observed under SPP and PSP combinations. The expected transversal optical phonon resonances of the quadratic susceptibility are denoted in Fig. 6.7 as well, marked by the frequency of the in-plane lattice oscillations ($\text{TO}_\perp 5$, $\text{TO}_\perp 6$, ...). However, the measured SFG peak positions possess either a spectral shift closeby (e.g. at $\text{TO}_\perp 6$) or resonant enhancement seems to be absent at all ($\text{TO}_\perp 7$). For a detailed analysis of the spectra, linear Fresnel effects and wavevector mismatch have to be considered, see Sec. 6.4.3.

Since SFG spectroscopy is sensitive to the spatial symmetry of the investigated system, an azimuth-dependent measurement has been carried out at the $\nu_{\text{IR}} = 830\,\text{cm}^{-1}$ signal peak. The result for SPP configuration is plotted in Fig. 6.8. A threefold rotational symmetry in the (0001) plane is observed. The discussion relating the measurement to the symmetry of the $\chi^{(2)}$-tensor is performed in the next section.

Tab. 6.2 Optical phonon zone-center frequencies of α-quartz. The phonon energies and dampings of the SFG-active modes are used as fit parameters in Eq. (6.1). Other values are from Ref. [Ger75]. A_2 modes are IR active in the extraordinary ray, E modes in the ordinary one.

Mode	Symmetry	ν (cm^{-1})	γ (cm^{-1})	IR activity	Raman activity
E modes					
TO_5	E	692.3	5.0	x	x
TO_6	E	790.6	4.2	x	x
TO_7	E	1060.2	2.0	x	x
TO_8	E	1150.0	2.1	x	x
LO_5	E	697.6	13		x
LO_6	E	810	6.9		x
LO_7	E	1226	12.5		x
LO_8	E	1155	9.3		x
A_2 modes					
TO_1	A_2	363.5	4.8	x	
TO_2	A_2	495	5.2	x	
TO_3	A_2	777	6.7	x	
TO_4	A_2	1071	6.8	x	
LO_1	A_2	386.7	4.8		
LO_2	A_2	551.5	5.8		
LO_3	A_2	790	6.7		
LO_4	A_2	1229	12		

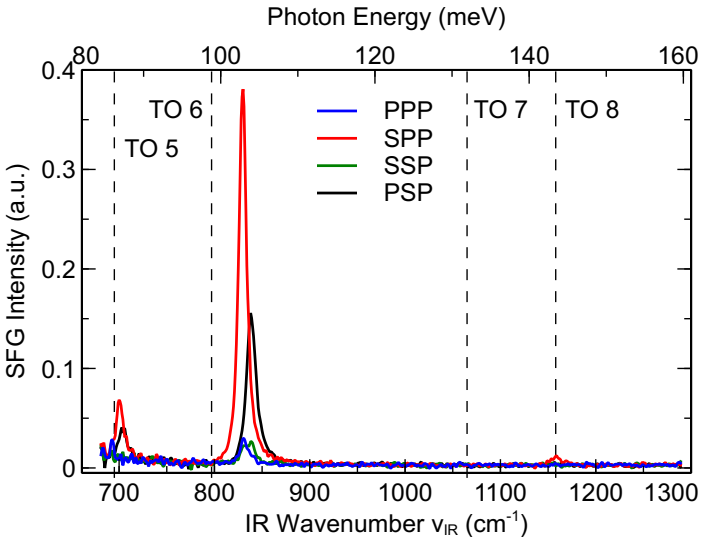

Fig. 6.7 SFG spectra of α-quartz under different polarization conditions. SFG-active transversal optical phonon modes are indicated.

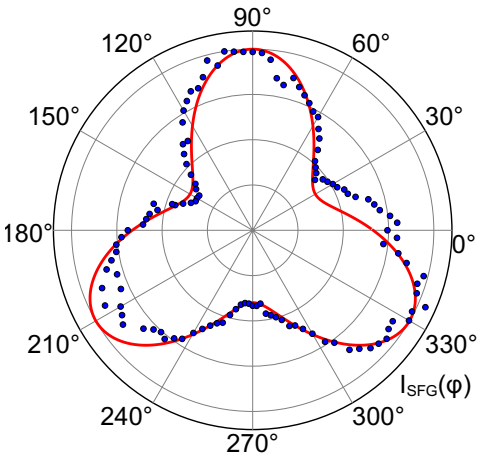

Fig. 6.8 Azimuthal dependence of the SFG response of α-quartz. The experimental (points) and calculated (line) normalized SFG intensities are shown for IR excitation at $\nu_{\mathrm{IR}} = 835\,\mathrm{cm}^{-1}$. A threefold symmetry is present for the case of SPP polarization.

6.4.3 Theoretical Analysis

For the analytical model of the IR-VIS sum-frequency emission originating from the bulk of α-quartz according to Eq. (6.1), the linear optical properties in the respective spectral regions are required. Since the quartz crystal exhibits multiple IR-active resonances due to polar lattice vibrations, several contributing terms to the dielectric function are relevant. In contrast to the single-Lorentz oscillator dispersion of SiC considering the distinct frequencies of TO and LO phonon, but only a single damping constant γ_{TO} (cf. Sec. 6.3.3), a more detailed approach is applied to quartz, where separate broadening quantities $\gamma_{\mathrm{TO}\,\perp,\parallel}$ and $\gamma_{\mathrm{LO}\,\perp,\parallel}$ are included for each branch r:

$$\varepsilon_{\perp,\parallel}(\omega) = \varepsilon_{\perp,\parallel\,\infty} \prod_r \frac{\omega^2_{\mathrm{LO}\,\perp,\parallel r} - \omega^2 - \mathrm{i}\omega\gamma_{\mathrm{LO}\,\perp,\parallel r}}{\omega^2_{\mathrm{TO}\,\perp,\parallel r} - \omega^2 - \mathrm{i}\omega\gamma_{\mathrm{TO}\,\perp,\parallel r}}. \tag{6.9}$$

Thus, the factorized dielectric function, also called four-parameter model, enables a better description of the dispersion behavior for multi-mode phonon crystals, in particular of the zero-crossing near the LO phonon frequencies [Sch00]. The reasoning for different damping rates γ of TO and LO modes even within the same phonon branch is due to the anharmonic coupling of the lattice vibrations, which is naturally more pronounced in crystals of complex vibrational properties [Ger74]. In this way, the classical model of the dielectric function incorporates the essential effects observed in quantum-mechanical calculations [Bar01]. The phonon parameters and dielectric constants for ordinary and extraordinary radiation rays in α quartz at room temperature are taken from Ref. [Ger75] in case of the IR spectral region and from Ref. [Gho99] for the VIS response.

The quadratic susceptibility tensor $\boldsymbol{\chi}^{(2)}$ of α-quartz contains, identical to other materials of point group 32, four independent components. Within the crystal framework, the nonvanishing elements are [Boy08]

$$\chi^{(2)}_{aaa} = -\chi^{(2)}_{abb} = -\chi^{(2)}_{bba} = -\chi^{(2)}_{bab}, \chi^{(2)}_{abc} = -\chi^{(2)}_{bac}, \chi^{(2)}_{acb} = -\chi^{(2)}_{bca}, \chi^{(2)}_{cab} = -\chi^{(2)}_{cba}. \tag{6.10}$$

Application of the crystal to laboratory coordinate transformation of Eq. (6.5) with $\boldsymbol{e}_a = \cos\varphi \boldsymbol{e}_x + \sin\varphi \boldsymbol{e}_y$, $\boldsymbol{e}_b = -\sin\varphi \boldsymbol{e}_x + \cos\varphi \boldsymbol{e}_y$ and $\boldsymbol{e}_c = \boldsymbol{e}_z$, where ϕ denotes the azimuthal angle within in the surface plane, yields

$$\chi^{(2)}_{xxx} = -\chi^{(2)}_{xyy} = -\chi^{(2)}_{yxy} = -\chi^{(2)}_{yyx} = \chi^{(2)}_{aaa} \cos 3\varphi, \tag{6.11}$$

$$\chi^{(2)}_{xxy} = -\chi^{(2)}_{xyx} = -\chi^{(2)}_{yxx} = -\chi^{(2)}_{yyy} = \chi^{(2)}_{aaa} \sin 3\varphi, \tag{6.12}$$

$$\chi^{(2)}_{xyz} = -\chi^{(2)}_{yxz} = \chi^{(2)}_{abc}, \tag{6.13}$$

$$\chi^{(2)}_{xzy} = -\chi^{(2)}_{yzx} = \chi^{(2)}_{acb}, \tag{6.14}$$

$$\chi^{(2)}_{zxy} = -\chi^{(2)}_{zyx} = \chi^{(2)}_{cab}. \tag{6.15}$$

The IR dispersion of the second-order nonlinear susceptibility as described by Eq. (6.4) takes into account the SFG-active vibrational modes of crystalline silica. Among the 24 fundamental optical phonons in α-quartz, only those belonging to the E-type symmetry class can take part in both Raman scattering and IR absorption if the incident electric field polarization is perpendicular to the optic axis of the crystal [Sak40]. Due to the selection rules, the number of zone-center modes observable in the SFG spectrum reduces to eight doubly degenerated vibrations, which can be accessed by IR radiation with ordinary polarization. From those, four TO modes are relevant in the investigated frequency range [Ger75]. As consequence of the symmetry restrictions, no resonant contribution is present in the $\chi^{(2)}_{abc}$ component. Further, the resonant amplitudes $A_{r,acb}$ and $A_{r,cab}$ as well as the accompanying non-resonant parts $\chi^{(2)}_{\mathrm{NR}}$ are assumed to be of the same order [Liu08a].

The center frequencies ω_r and damping values γ_r of the SFG-active lattice vibrations are free parameters in the dispersion of the nonlinear $\chi^{(2)}_{ijk}(\omega_{\mathrm{IR}})$ and linear response $\varepsilon(\omega_{\mathrm{IR}})$. Further, the resonance amplitudes $A_{r,ijk}$, high-frequency constants $\chi^{(2)}_{ijk\,\infty}$ and the azimuthal angle φ entering the second-order susceptibility tensor are fitted, giving a total number of 20 parameters for the SFG response function according to Eq. (6.1).

Results of the fit with the analytical model for the different polarization conditions are displayed in Fig. 6.9. The position of the TO and LO phonon modes for the ordinary polarized IR radiation is also indicated. Obviously, the resonant lattice vibrations do not dominate the SFG response. Instead, the strongest sum-frequency emission is observed around $\nu_{\mathrm{IR}} \sim 830\,\mathrm{cm}^{-1}$ for SPP and PSP polarization. Also in the cases of

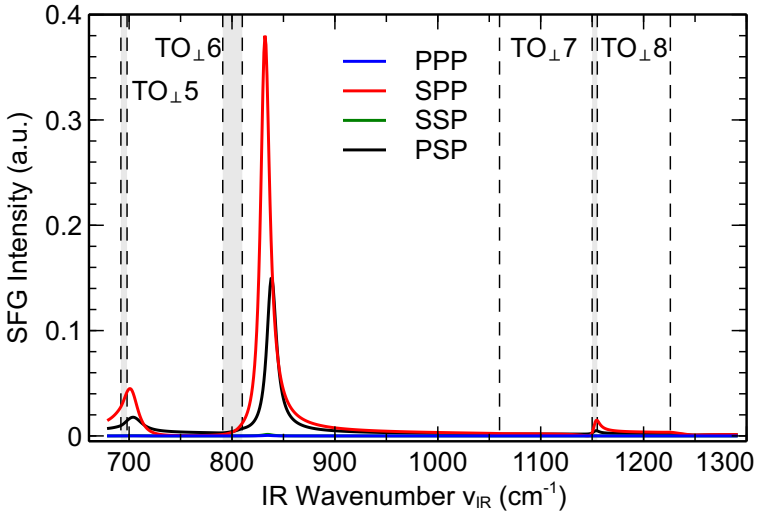

Fig. 6.9 Fitted polarization dependence of the SFG response of α-quartz. The different configurations are calculated from the model using the coefficients fitted for the SPP case. Forward SFG propagation is assumed. The IR frequencies of TO and LO phonons, appearing in the dielectric function for the ordinary radiation, are indicated, giving rise to several Reststrahlen bands (gray shaded).

PPP and SSP, an SFG response is allowed regarding the relevant tensor component $\chi^{(2)}_{aaa}$ in Eq. (6.11), however just a comparatively small signal peak is observed. Since the fit results are in good agreement with the experimental findings (cf. Fig. 6.7), a further analysis of the different contributions to the SFG response can be carried out.

The relevant contributions in the emission of sum-frequency radiation from the bulk of α-quartz are separated in Fig. 6.10(a)-(d) for the case of SPP. The signal yield is given by

$$\begin{aligned} I_{\mathrm{SPP}}(\omega_3) \propto & |F_{\mathrm{yy}}(\omega_3)\chi^{(2)}_{\mathrm{aaa}} \sin 3\varphi \, F_{\mathrm{xx}}(\omega_2)\cos\theta_2 \, F_{\mathrm{xx}}(\omega_1)\cos\theta_1 \\ & - F_{\mathrm{yy}}(\omega_3)\chi^{(2)}_{\mathrm{abc}} \, F_{\mathrm{xx}}(\omega_2)\cos\theta_2 \, F_{\mathrm{zz}}(\omega_1)\sin\theta_1 \\ & - F_{\mathrm{yy}}(\omega_3)\chi^{(2)}_{\mathrm{acb}} \, F_{\mathrm{zz}}(\omega_2)\sin\theta_2 \, F_{\mathrm{xx}}(\omega_1)\cos\theta_1|^2/\Delta k^2_{\mathrm{SPP}}. \end{aligned} \tag{6.16}$$

There, the nonlinear contribution originates from the tensor components $\chi^{(2)}_{yxx}$, $\chi^{(2)}_{yxz}$ and $\chi^{(2)}_{yzx}$ in the laboratory framework, consequently three of the four independent second-order susceptibility elements ($\chi^{(2)}_{aaa}$,$\chi^{(2)}_{abc}$ and $\chi^{(2)}_{acb}$) are involved in the SFG process. Resonant enhancement at the E-type TO phonon modes is allowed and observed for $\chi^{(2)}_{aaa}(\omega_{\mathrm{IR}})$ and $\chi^{(2)}_{acb}(\omega_{\mathrm{IR}})$, whereas $\chi^{(2)}_{abc}$ is dispersionless, i.e. only possessing a small, non-resonant part, see Fig. 6.10(b). Apparently, the resonant enhancement in the second-order susceptibility, which amounts up to two orders of magnitude in $|\chi^{(2)}|$, is hardly seen in the

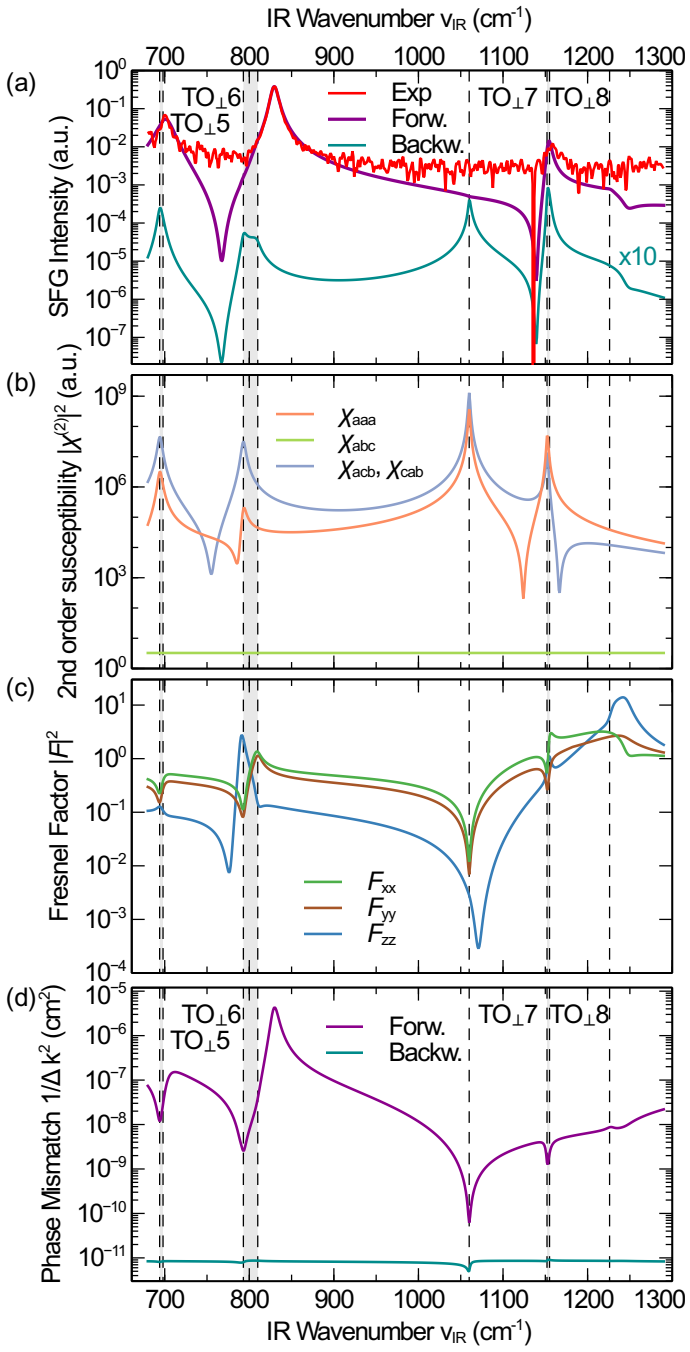

Fig. 6.10 Disentanglement of linear and nonlinear contributions to the SFG response of α-quartz. (a) Experimental and fitted SFG intensity using model Eq. (6.1). Forward and backward traveling SFG radiation are distinguished. (b) Dispersion of second-order susceptibility tensor components $\chi^{(2)}_{ijk}(\omega_{\mathrm{IR}})$ regarding the crystal framework. Displayed is the absolute value squared, entering into the SFG intensity. Resonant enhancement occurs at the SFG-active vibrational modes, i.e. at the TO phonons. (c) Fresnel tensor components $|F_{ll}|^2$ for the coupling of the IR field into the material. (d) Wavevector mismatch $1/\Delta k^2$ as function of the IR wavenumber ν_{IR}. Different magnitudes for forward and backward propagating radiation cause the varying SFG intensities in (a). SPP polarization configuration is used.

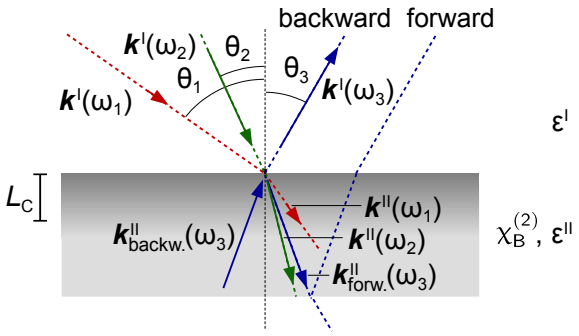

Fig. 6.11 SFG wavevector mismatch in a transparent medium. Incident IR, $\boldsymbol{k}^{\mathrm{I}}(\omega_1)$, and VIS radiation, $\boldsymbol{k}^{\mathrm{I}}(\omega_2)$, are mixed within the bulk of the nonlinear crystal $(\epsilon^{\mathrm{II}}, \chi_{\mathrm{B}}^{(2)})$, generating sum-frequency light in forward, $\boldsymbol{k}^{\mathrm{II}}_{\mathrm{forw.}}(\omega_3)$, and backward, $\boldsymbol{k}^{\mathrm{II}}_{\mathrm{backw.}}(\omega_3)$, propagating direction, respectively. The coherence length $L_{\mathrm{c}} = 1/|\Delta\boldsymbol{k}^{\mathrm{II}}|$ is determined by the wavefront phase difference inside the material, with $\Delta\boldsymbol{k}^{\mathrm{II}} = \boldsymbol{k}^{\mathrm{II}}(\omega_3) - \boldsymbol{k}^{\mathrm{II}}(\omega_2) - \boldsymbol{k}^{\mathrm{II}}(\omega_1)$ in forward and $\Delta\boldsymbol{k}^{\mathrm{II}} = \boldsymbol{k}^{\mathrm{II}}(\omega_3) + \boldsymbol{k}^{\mathrm{II}}(\omega_2) + \boldsymbol{k}^{\mathrm{II}}(\omega_1)$ in backward propagation, respectively.

SFG spectrum for forward propagation, Fig. 6.10(a). Thus, the linear optical effects have to be invoked. On the one hand, the Fresnel factors $\boldsymbol{F}(\omega)$ modify the electric field strengths being present in the nonlinear material for frequency-mixing. Particularly for SPP, the $F_{xx}(\omega_{\mathrm{IR}})$ component is relevant, leading to a slight reduction of the IR field at each TO resonance, Fig. 6.10(c). On the other hand, the phase-matching condition, necessary for the coherent SFG emission, is strongly affected by the dispersion of the dielectric constant in the Reststrahlen region. Therefore, the change in the factor $1/\Delta k^2(\omega_{\mathrm{IR}})$ of about five orders of magnitude in the forward direction, see Fig. 6.10(d), dominates the SFG spectrum, cf. Fig. 6.10(a). As a result, the main peak emerges around $\nu_{\mathrm{IR}} \sim 835\,\mathrm{cm}^{-1}$, whereas the vibrational resonances at the high-frequency side are almost completely suppressed.

Due to the experimental geometry, the measured SFG signal is generated by forward propagation of NIR, VIS and SFG radiation within the α-quartz crystal (i.e. in transmission direction), subsequently back-reflected at the quartz/air interface and detected along a beam path parallel to the VIS radiation specularly reflected at the first air/quartz interface, see Fig. 6.11. Similar to the experiment on SiC, the material is transparent for the SFG wavelength, allowing a significant nonlinear signal to be generated. The expected SFG emission in backward direction, in contrast, originating from a thin layer at the air/quartz interface, is also shown in Fig. 6.10(a). There, the TO phonon modes are clearly resolved as peaks in the SFG spectrum. This is due to the much less pronounced variation in the $1/\Delta k^2$ term, appearing almost flat in the IR range, see Fig. 6.10(d). However, the reduced effective source volume of the nonlinear signal entails a lower SFG intensity level compared to the forward propagation, difficult to acquire with the current signal-to-noise ratio.

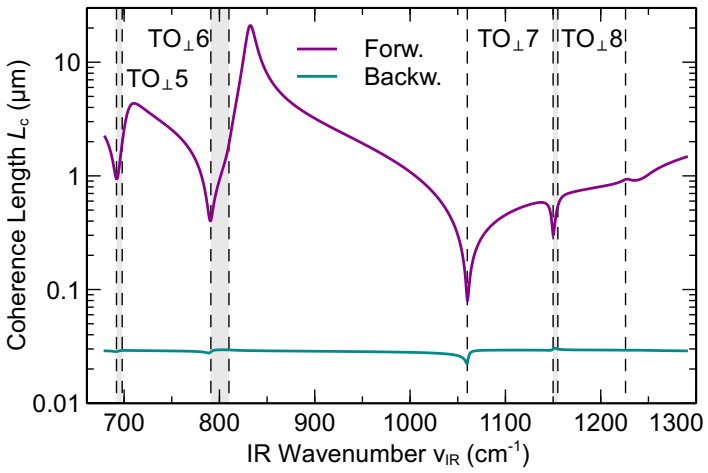

Fig. 6.12 Coherence length for SFG emission in α-quartz. Calculated interaction depths L_c for forward and backward propagating SFG radiation are plotted for the case of SPP configuration.

The depth of the crystal volume contributing to the generation of the SFG intensity is plotted in Fig. 6.12. In forward direction, a large coherence length of up to $L_c \sim 20\,\mu m$ is present, allowing for a strong bulk SFG signal. In contrast, the width of the crystal layer close to the air/quartz interface responsible for the backward propagation signal is only about 30 nm. This is in agreement with previous SFG measurements of α-quartz [Liu08a]. There, the SFG-allowed vibrational modes could be clearly resolved, owing to the backward propagation sensitivity. However, the analysis in Ref. [Liu08a] apparently neglects the anisotropy of crystalline quartz, which enters into the Fresnel tensor and the dielectric function of the system, questioning to some extent the derived nonlinear properties there. Spatial blocking of the forward-propagating bulk SFG in our setup has yielded no detectable light, due to the small backward SFG intensity.

An extraction of the quadratic suscpetibility coefficients is beyond the realms of possibility because of the limited signal-to-noise ratio in the present setup, compared to the order of magnitude variation in the linear optical effects. Absolute nonlinear susceptibilites $\chi^{(2)}_{ijk}$ of α-quartz in the MIR spectral region have been obtained experimentally in Ref. [Hor04] and by theory in Ref. [Zho93; Hua94].

The symmetry sensitivity of SFG spectroscopy is demonstrated on c-cut α-quartz by azimuth-dependent experiments. A polar plot of the measured nonlinear response at a fixed non-resonant frequency in SPP configuration is shown in Fig. 6.8. The threefold symmetry can be well described by the analytical model, Eq. (6.16). Due to the involved tensor components, the angle dependence is of the form $I_{SFG}(\varphi) \propto |\text{const.} + \sin 3\varphi|^2$. Observations at other polarization combinations can be derived in an analogous way.

Symmetry-related studies are particular important when investigating adsorbates on surfaces, revealing their orientation and structure. Due to the usually distinct point groups of bulk and surface, the different origins of the second-order susceptibility can be distinguished or, moreover, allow a suppression of the bulk contribution at certain azimuthal angles [Liu08b].

6.5 Summary

The investigated anisotropic polar dielectric materials, 4H-SiC and α-quartz, have shown a pronounced spectral dependence of the sum-frequency generation response due to the excitation of bulk lattice vibrations within the Reststrahlen region. A strong modification of the IR-VIS sum-frequency spectra by linear optical effects (Fresnel factor) can obscure the resonant enhancement of the second-order susceptibility at SFG-active phonons, which indicate the zone-center frequency of vibrational modes being both IR and Raman active. Depending on the geometry of the interacting optical fields and the crystal, the symmetry of the third-rank $\chi^{(2)}$ tensor and hence the point group can be determined. It is found that the phase-matching condition limits the probing depth of the frequency-mixing process to some micrometer distance from the surface at maximum, even for bulk-originating SFG radiation, as settled by the coherence length.

7 Resonant Enhancement of the Sum-Frequency Response by Localized Surface Phonon Polaritons

Vibrational, and thus chemical selective, contrast allows not just for spectroscopic information, but also for spatial imaging. Using surface phonon polaritons in nanoresonator structures, customizable MIR resonance frequencies can be created and observed in SFG spectroscopy. The underlying polaritonic field enhancement is employed in coherent nonlinear microscopy, demonstrating vibrational SFG contrast with increased spatial resolution compared to the linear IR absorption counterpart.

Parts of this Chapter have been published in Ref. [Kie19].

7.1 Motivation

The manipulation of the amplitude and frequency of resonant sum-frequency generation processes is of interest for, e.g., improved frequency conversion devices or vibrational molecule sensing applications. Within the last decades, free-electron excitations at metallic surfaces, known as surface plasmons, have emerged as a viable approach to guide light on the nanoscale, enabeling local electric field enhancements [Kau12]. Another way to achieve sub-diffractional light confinement, resulting in the enhancement of nonlinear optical effects, is provided by surface phonon polaritons (SPhPs). There, IR photons are coupled to transverse optical lattice vibrations in polar dielectrics, see Sec. 2.2.2. Localized SPhPs (LSPhPs) are excited on sub-wavelength-scale nanostructured surfaces of dielectric crystals, where the planar air/material interface is broken up. Thus, in contrast to propagating SPhPs, LSPhPs can be directly created by the incident light without the necessity of grating or prism coupling [Mai07; Cal15].

Due to the exploitation of optical phonons in non-conducting substrates, scattering processes involving charge carriers are almost completely suppressed. Thus, (bulk) phonon lifetimes in the order of some ps up to some tens of ps are routinely achieved in low-defect materials [Deb99; Cal15]. The actual lifetime of a SPhP, including scattering events on surface roughnesses created by the nanostructuring, is at maximum one order of magnitude lower than that of the bulk vibration [Cal15]. Due to the small imaginary contribution to the dielectric function, optical absorption losses are rather low, especially in comparison with plasmonic structures. Therefore, LSPhP spectral linewidth down to $2\Gamma \sim 5\,\mathrm{cm}^{-1}$ have been realized, combined with resonance (ω_0) tuning via the

nanostructure geometry, covering a large part of the MIR region [Che14]. When the electromagnetic energy is stored in a volume smaller than the resonant wavelength, $V < \lambda_0^3$, a strong enhancement of the incident IR field $\boldsymbol{E}(\omega_1)$ can be achieved. Thus, linear and nonlinear optical processes at the surface are intensified, being beneficial for, e.g., enhanced IR spectroscopy [And03] or the creation of nano-dipole antennas in nanophotonic devices [Tam18].

Different nanostructure designs with sub-IR-diffractional dimensions have been tested so far to realize LSPhP. A promising geometry, exhibiting a large quality factor $Q = \omega_0/2\Gamma$ up to ~ 300, is given by high aspect ratio cylindrical nanoresonators, also called nanopillars [Cal13; Che14]. There, different localized SPhP resonances are observed within the Reststrahlen region of the underlying substrate. A knowledge about the spatial confinement of the electromagnetic field is desirable for a control of the enhancement at the nanoscale. To this end, optical imaging of LSPhPs should rely on the mode-selective enhancement of the response. IR-VIS SFG microscopy has emerged as a valuable tool providing the vibrational contrast. Since the nonlinear response at the sum-frequency is probed, a spatial resolution below the diffraction limit of the IR-excitation wavelength can be reached, superior to conventional IR microscopy [Lab07]. Further, nonlinear optical imaging provides stronger signal contrast and access to higher-order material symmetries. Besides applications in the field of nanophotonics, investigations of biological specimens, electrochemical interfaces or surface-bound molecules on catalysts benefit from coherent nonlinear microscopy with vibrational sensitivity [Chu13].

In the following, the MIR resonances of LSPhP modes are analyzed in sub-wavelength geometries made from hexagonal silicon carbide material, possessing a high second-order nonlinearity $\chi^{(2)}$. SFG spectroscopy is applied to reveal a resonant enhancement of the response at the phonon-polariton frequencies. Further, the localized resonances are used as model system for the demonstration of scanning-probe SFG microscopy using long-wave IR radiation.

7.2 Experimental Details

Setup The sum-frequency generation in the sample is induced by the IR FEL radiation and VIS frequency-doubled table-top laser source as described in Sec. 3.3, using the reflection geometry depicted in Fig. 3.3(b) to capture the SFG light emitted from the nanostructured front-surface of the sample.

For the mapping of the resonances a spatial scan of the input beams across the sample will be performed. To this end, the material is mounted on a stage movable in two dimensions (x, y), orthogonal to the surface normal (z). Keeping the position and direction of the incident radiation fixed ensures a constant size and overlap of both FEL and table-top laser foci on the sample. The minimum incremental motion of the stepper motor actuators is 0.1 µm. For the chosen step size of 8 µm in Fig. 7.7, the image acquisition takes about 45 min time.

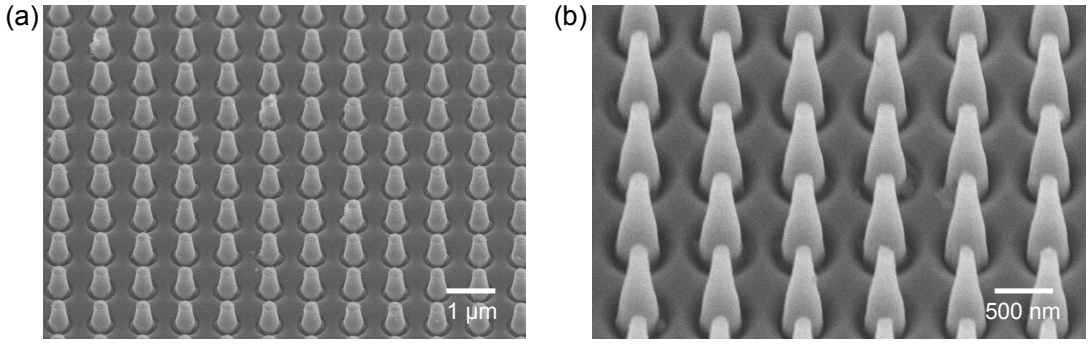

Fig. 7.1 SiC nanoresonator geometry and arrangement. Scanning electron microscopy images at different resolution levels are shown (tilted view angle of 15°).

The spatial resolution of the two-dimensional SFG sample imaging is increased by tightly focusing the incoming light beams. Thus, the off-axis parabolic mirror used for the IR FEL radiation is replaced by a potassium bromide (KBr) lens of shorter focal length ($f = 10\,\mathrm{cm}$), providing a FWHM spot diameter of $\sim 80\,\mu\mathrm{m}$. The VIS focal size is narrowed by inserting a Galilean beam expander in the frequency-doubled beam path, consisting of one concave ($f = -5\,\mathrm{cm}$) and one convex ($f = 20\,\mathrm{cm}$) lens placed 15 cm apart, ahead of the focusing lens ($f = 20\,\mathrm{cm}$). The resulting spot size at the sample position is about 20 µm FWHM. Fluences of IR and VIS radiation applied to the sample are $19\,\mathrm{mJ/cm^2}$ and $4\,\mathrm{mJ/cm^2}$ at maximum, respectively.

All spectroscopic measurements shown in this chapter are taken at an FEL cavity detuning of $\Delta L = 5\lambda$, resulting in a relative FEL linewdith of 0.3 % to obtain the best spectral resolution of the LSPhP modes. The emitted SFG intensity is collected by a photomultiplier. Additionally, the specularly reflected power of the (usually p-polarized) FEL radiation is measured by the photoelectromagnetic IR detector without polarization discrimination.

Samples For the excitation of LSPhPs two different samples, each made of semi-insulating c-cut 4H-SiC wafers (thickness 350 µm) with varying nanostructure arrays, have been investigated. One sample features nine 200 x 200 $\mu\mathrm{m}^2$ large square arrays of periodically arranged 1 µm high cylindrical nanopillars (same material as substrate) with systematically changing pillar diameters ($d = 450, 500, 550\,\mathrm{nm}$) and interpillar distances (pitch $p = 1000, 1100, 1200\,\mathrm{nm}$). The other sample possesses multiple arrays of smaller size (50 x 50 $\mu\mathrm{m}^2$) with pillar parameters of $d = 200, 300, 500, 750, 1000\,\mathrm{nm}$ and $p = 0.4, 0.7, 1, 1.5, 2, 5, 8\,\mu\mathrm{m}$.

The nanostructures are fabricated by reactive-ion etching in an SF_6 / O_2 environment. Prior to this process step, an etch mask coating is applied, subsequently structured by means of electron beam lithography. A typical scanning electron microscopy (SEM) image of the sample surface carrying the nanopillar structures is shown in Fig. 7.1. Note that, due to an additional H_2 etching process to remove the remaining surface-bound fluorine, the nanopillars exhibit a curved top.

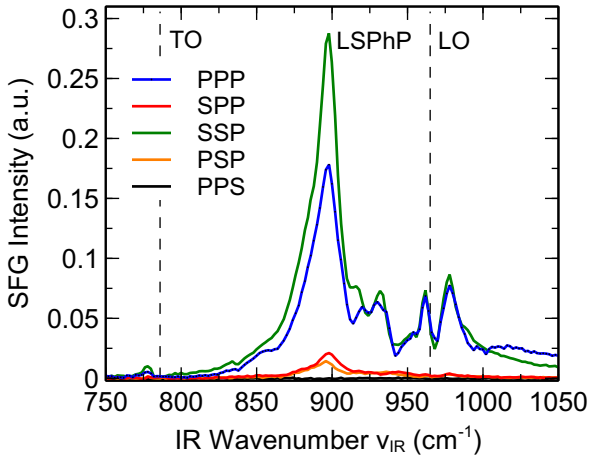

Fig. 7.2 SFG spectra of localized surface phonon polariton in SiC. The dependence of the nanoresonator array response on the polarization of incident and detected IR-VIS SFG radiation is shown. The monopolar mode of the resonator due to the localized surface phonon polariton (LSPhP) is situated in the Reststrahlen band of 4H-SiC, restricted by the TO and LO vibrations. LSPhP SFG intensity is strongly enhanced, compared to the bare substrate response. Pillar parameters are $p = 1100\,\text{nm}$ and $d = 450\,\text{nm}$.

Samples have been prepared by Alex J. Giles and Joshua D. Caldwell at U.S. Naval Research Laboratory. Fourier-transform infrared (FTIR) reflectance characterization of the various pillar arrays has been provided to identify the spectral position of the nanoresonator LSPhP modes. Further details on the fabrication process can be found in the supplementary information of Ref. [Cal13].

7.3 Results

In the first part, the modification of the amplitude and spectral behavior of the nonlinear response obtained with the excitation of LSPhP in SiC is investigated. Then, the spatial localization of the electromagnetic field enhancement is examined by SFG imaging.

7.3.1 Spectroscopy

The IR-VIS SFG spectra of a periodic array of nanopillars, are shown in Fig. 7.2, taken under various polarization conditions. The investigated nanostructures have diameter $d = 450\,\text{nm}$ and pitch $p = 1100\,\text{nm}$. In the plots, the transversal (TO) and longtidudinal bulk optical phonon (LO) frequencies are indicated as guide to the eyes. In comparison to the substrate response, discussed in the previous section (cf. Fig. 6.2), additional resonances within the broad Reststrahlen band of SiC are observed.

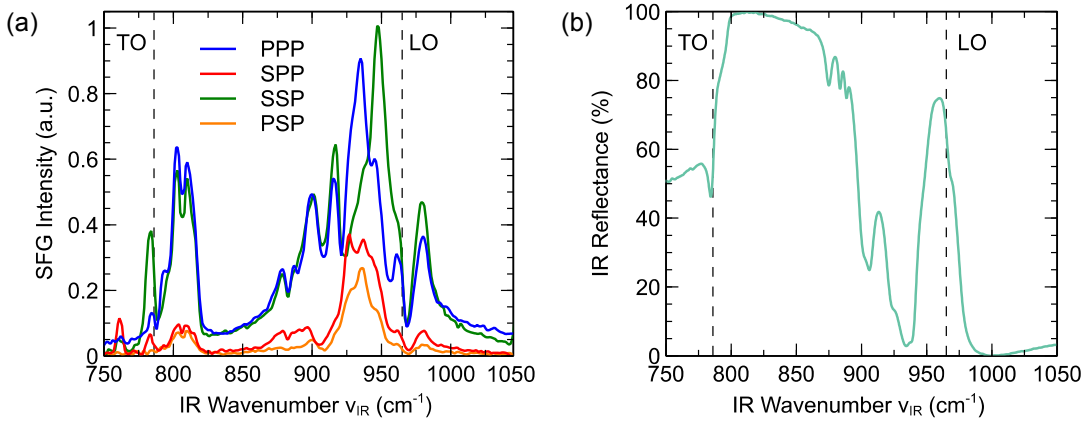

Fig. 7.3 Nonlinear and linear response of localized surface phonon polariton. (a) SFG spectra at different polarization configurations, (b) IR reflectance of the resonator array, characterized by $p = 1000\,\mathrm{nm}$ and $d = 200\,\mathrm{nm}$. Monopolar and dipolar modes within the Reststrahlen band are observed both in SFG and IR response. Reflectance data are measured by FTIR spectroscopy.

First, the spectrum acquired under PPP condition is analyzed. The strongest SFG response occurs at $\nu_0 = 898\,\mathrm{cm}^{-1}$ (FWHM $20\,\mathrm{cm}^{-1}$), possessing a higher intensity than the double-peak feature in the vicinity of the LO phonon mode ($\nu = 965\,\mathrm{cm}^{-1}$) originating from the bare substrate. Moreover, two smaller peaks appear at the high-frequency side of the $898\,\mathrm{cm}^{-1}$ mode, placed approximately $20\,\mathrm{cm}^{-1}$ and $30\,\mathrm{cm}^{-1}$ apart. Considering the different polarization combinations used to probe the nanostructure modes, Fig. 7.2, a similar sum-frequency response (number of appearing peaks, spectral position) is observed for the case of SSP. There, the SFG intensity at $\nu_0 = 898\,\mathrm{cm}^{-1}$ is increased by a factor of about 1.6 relative to the PPP spectrum. For SPP and PSP, only a weak nonlinear response at ν_0 is observed. No sum-frequency radiation is detected under PPS configuration.

The polarization conditions required to observe an SFG response of the nanopillars are identical with that of the pure substrate, cf. Fig. 6.2. Due to the nanostructuring, a modulation of the linear optical properties is induced. To corroborate this, another nanopillar array is investigated by SFG spectroscopy, complemented by IR reflectance measurements obtained from the sample provider. For the bare substrate near perfect reflectivity would be expected in the Reststrahlen region, cf. Fig. 2.2(b). In Fig. 7.3, the SFG and linear IR response of nanopillars with parameters $d = 200\,\mathrm{nm}$ and $p = 700\,\mu\mathrm{m}$ are shown. Again, the strongest SFG intensity is located below the LO phonon frequency within the Reststrahlen band, Fig. 7.3(a), now at around $948\,\mathrm{cm}^{-1}$ (FWHM $21\,\mathrm{cm}^{-1}$). Compared with the reflectivity spectrum in Fig. 7.3(b), the mode matches approximately the frequency of the largest IR reflectivity reduction. Moreover, the side-peak located towards the lower photon energy is in correspondence with the smaller dip in the reflectivity spectrum at $\nu_0 = 905\,\mathrm{cm}^{-1}$. Thus, the modification of the local electric field at certain resonance frequencies of the periodic nanostructure is the reason for the appearance of these modes in the nonlinear spectra.

Within the Reststrahlen band, the decrease of the reflectance is equivalent to enhanced optical energy absorption, due to the zero transmittance. Hence, the array of SiC nanopillars causes an extinction of the reflected IR field due to the strong light confinement. This local field enhancement is associated with the excitation of localized surface phonon polaritons in the nanoresonators, as it has been shown by finite-element method simulations of the electric near-field distribution [Cal13]. In detail, several resonant modes can be distinguished. On the one hand, the monopolar mode, resulting from the oscillation of the charged lattice atoms along the pillar axis, requires an out-of-plane polarized IR field for stimulation. In contrast, the occurence of multiple transverse dipolar LSPhP modes, where positive and negative charges are distributed across the nanopillar diameter, necessitates an in-plane component of the exciting electric field, i.e. parallel to the substrate surface. The simulations [Cal13] also revealed that the dipole resonances are of higher frequency than the monopole modes.

The SFG measurements of Figs. 7.2 and 7.3(a) are performed under non-normal incidence of the IR radiation so that both in-plane and out-of-plane eletric field components are present in case of p-polarization. Therefore, the monopole as well as dipole modes can be observed in the PPP and SSP spectra. For a s-polarized IR field in the PPS experiment, one can expect the excitation of the tranverse dipolar mode, however, the relevant component of the $\chi^{(2)}$ tensor vanishes, hence, no sum-frequency light is emitted in this polarization combination. Due to the same reason, no SFG radiation is expected in case of the SPP and PSP spectra. However, some small contribution is experimentally observed in Figs. 7.2 and 7.3, which might arise due to similar reasons as for the bare substrate response, cf. Fig. 6.2, where residual SFG light has been measured in SPP configuration.

The peak in the SFG spectra of both samples occuring at ν_0 ($898\,\mathrm{cm}^{-1}$ and $905\,\mathrm{cm}^{-1}$, respectively) is assinged to the monopole mode of the LSPhP resonators. Due to the angle of incidence of the IR radiation, determined by the experimental geometry, the out-of-plane component of the electric field E_z is slightly larger than the in-plane field E_x, favoring the monopolar resonance. The SFG peaks at frequencies larger than ν_0 correspond to the dipolar modes. Since the local electric field distribution of each resonator mode depends on the size and spacing of the nanopillars [Che14], the SFG amplitudes vary for the investigated arrays. In case of the first sample, Fig. 7.2, the field enhancement is stronger for the monopole mode, whereas for the other sample the dipole resonances appear more intense, Fig. 7.3.

In Fig. 7.4, the spectral dependence of the localized modes as function of the interpillar distance is shown. The diameter of the nanoresonators is fixed at $d = 300\,\mathrm{nm}$, while the pitch size has been varied between $p = 1\,\mu\mathrm{m}$ and $2\,\mu\mathrm{m}$. At first, the transversal dipole mode, located around $\nu_{\mathrm{IR}} = 940\,\mathrm{cm}^{-1}$, exhibits a spectral shift as well as amplitude changes. Whereas the increase in the wavenumber is about $5\,\mathrm{cm}^{-1}$ and $8\,\mathrm{cm}^{-1}$ for the arrays of $p = 1.5\,\mu\mathrm{m}$ and $2\,\mu\mathrm{m}$, compared to the case of $1\,\mu\mathrm{m}$, the magnitude of the nonlinear response is reduced by a factor of 1.7 and 2.8, respectively. For the monopole

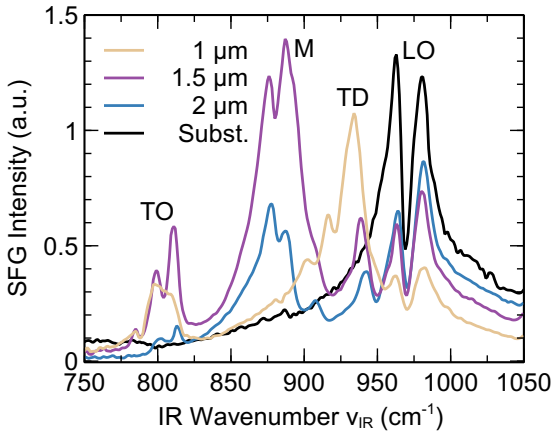

Fig. 7.4 SFG spectra of nanoresonator arrays with varying spacings. The nonlinear response is shown for the 4H-SiC substrate and pillars of pitch $p = 1\,\mu\text{m}$, $1.5\,\mu\text{m}$ and $2\,\mu\text{m}$ with $d = 300\,\text{nm}$. Monopolar (M, $\nu_{\text{IR}} \approx 890\,\text{cm}^{-1}$) and transverse dipolar modes (TD, $\nu_{\text{IR}} \approx 930\,\text{cm}^{-1}$) are observed, in addition to the reduced amplitude of the substrate double peak near the LO vibration ($\nu_{\text{IR}} \approx 965\,\text{cm}^{-1}$) and the TO phonon-resonant SFG ($\nu_{\text{IR}} = 810\,\text{cm}^{-1}$). Polarization is chosen as PPP.

LSPhP mode, the situation is less clear from the measured data. Depending on the pillar distance, a modification of the SFG intensity is observed. Finally, a third contribution in the spectra of the nanostructures occurs at $\nu_{\text{IR}} = 800\,\text{cm}^{-1}$. This can be assigned to the substrate TO phonon due to the spectral position.

To understand the spectral shift behavior of the different modes, one has to consider the associated electric near-field distributions [Che14]. For the transverse dipolar resonance, the change in the charge density from positive to negative sign occurs across the nanopillar diameter. Thus, an expansion of the interpillar gap results in a decrease of the Coulomb attraction of the neighboring oscillating dipoles, raising the eigenfrequency. Besides the blue shift of the spectral position, a reduction of the IR field enhancement and hence SFG amplitude is caused by the lowered coupling of adjacent resonators. These characteristics are in line with FTIR reflectance measurements of similarly structured nanoarrays [Che14]. In case of the monopole resonance, the opposite spectral behavior would be expected since the single-signed charge of the nanopillar entails a strong electric repulsion, decaying for increased pitch size and thus red-shifting the mode frequency. The experimental data of Fig. 7.4, however, do not provide a conclusive proof of that trend.

7.3.2 Spectro-Microscopy

Besides the spectral position and amplitude of the LSPhP modes, the spatial extent and homogeneity of the field enhancement is of relevance as well. Therefore, in order to acquire SFG information with lateral resolution, the spectroscopy method is combined

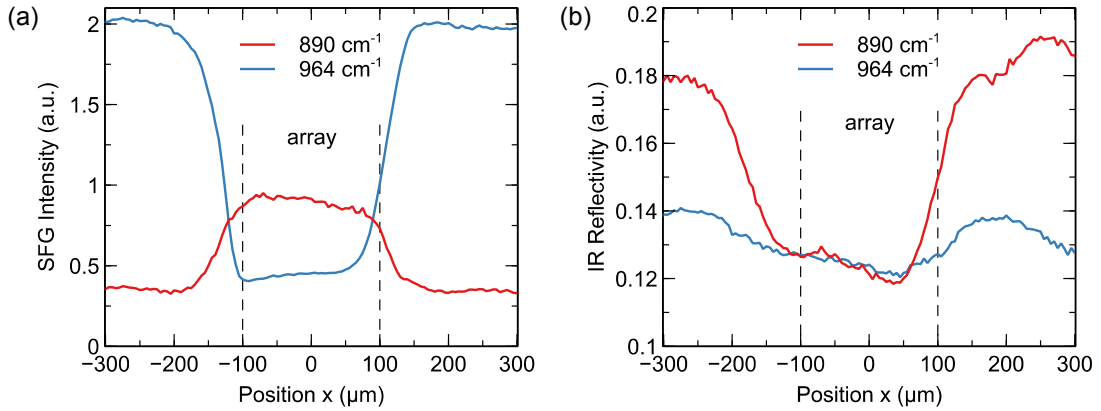

Fig. 7.5 Nonlinear and linear optical response across the nanoresonator array. (a) SFG intensity and (b) IR reflectivity measurements for resonant excitation at the monopole mode ($\nu_{\mathrm{IR}} = 890\,\mathrm{cm}^{-1}$) or the LO phonon frequency ($\nu_{\mathrm{IR}} = 964\,\mathrm{cm}^{-1}$). The SFG signal at $\lambda_{\mathrm{SFG}} \sim 500\,\mathrm{nm}$ provides a higher spatial resolution than the linear optical detection at $\lambda_{\mathrm{IR}} \sim 10\,\mu\mathrm{m}$.

with a scanning probe approach. Imaging contrast is provided by the IR excitation frequency if tuned to the LSPhP mode. Strongly focused laser beams are utilized to improve the spatial resolution of the far-field microscopy technique [Boy86].

The SFG response and IR reflectivity obtained during a lateral scan across a nanoresonator array of 200 µm size is depicted in Fig. 7.5. There, both the on-resonance and off-resonance cases are investigated, with the monopole mode of this nanostructure being located at $\nu_{\mathrm{IR}} = 890\,\mathrm{cm}^{-1}$. When the LSPhP is resonantly excited, the SFG intensity is amplified by a factor of ~ 2 relative to the surrounding SiC substrate, Fig. 7.5(a). At the same time, the reflectance of the IR radiation is decreased by about 33 %, Fig. 7.5(b), due to the capture of the electromagnetic energy in the LSPhP mode. For off-resonant IR excitation at $\nu_{\mathrm{IR}} = 964\,\mathrm{cm}^{-1}$, close to the bulk LO phonon, the nonlinear optical behavior is inverted, Fig. 7.5(a). That is, the SFG power is suppressed on the array with a ratio 1:4 in comparison to the strong signal originating from the bare substrate. On the contrary, the IR reflectance is much less sensitive to the nanopillar area, nevertheless, a small reduction is observed, Fig. 7.5(b), probably caused by Rayleigh scattering of the light on the nanostructures.

Tab. 7.1 Spatial resolution of IR and SFG imaging. The given values (2σ) are extracted from Fig. 7.5 using the fit function Eq. (7.1). Resonant excitation of the LSPhP mode of the nanoresonator is at $\nu_{\mathrm{IR}} = 890\,\mathrm{cm}^{-1}$, the off-resonance at $\nu_{\mathrm{IR}} = 964\,\mathrm{cm}^{-1}$.

	on-resonance	off-resonance
IR	70.7 µm	95.1 µm
SFG	55.4 µm	46.5 µm

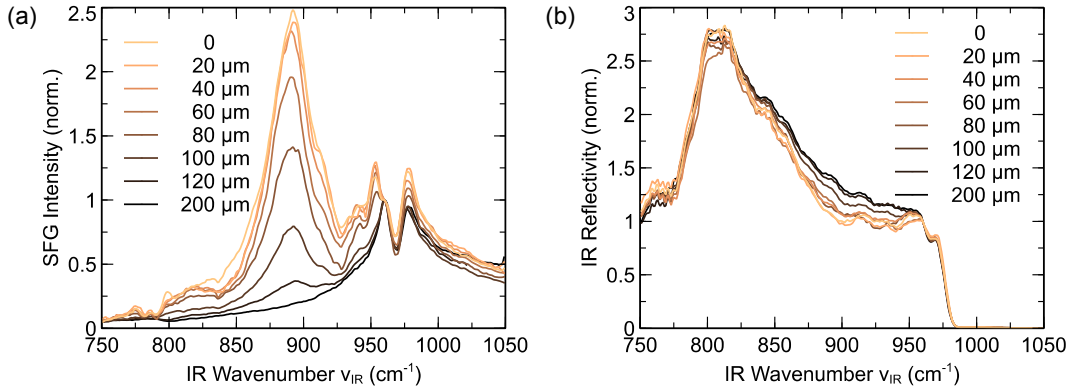

Fig. 7.6 Spatial sensitivity of SFG and IR reflectivity across the nanostructure. Spectra of (a) SFG intensity and (b) IR reflectivity are normalized to the response at $\nu_{\mathrm{IR}} = 960\,\mathrm{cm}^{-1}$. The nanostructured surface is sampled from the center (0) towards the substrate (200 µm), crossing the edge at 100 µm. The resonator-covered area (pillars of $p = 1100\,\mathrm{nm}$ and $d = 500\,\mathrm{nm}$) exhibits a strong SFG resonance at the monopole mode around $\nu_{\mathrm{IR}} = 890\,\mathrm{cm}^{-1}$.

To quantify the spatial resolution of the SFG and IR imaging, the response at the edges of the pillar array has been fitted by a cumulative normal distribution function,

$$I(x) = \frac{1}{2}\left(1 + \mathrm{erf}\left(\frac{x-\mu}{\sqrt{2}\sigma}\right)\right). \tag{7.1}$$

The edge widths extracted from Fig. 7.5 for the on- and off-resonant excitation are summarized in Tab. 7.1. There, the width is given as 2σ value, describing the lateral region enclosed between $1/e^2 \approx 14\,\%$ and 86 % of the maximum intensity. The FWHM equivalent is $2\sqrt{2\ln 2}\,\sigma$. The spatial resolution of the used scanning probe method is at best $2\sigma \sim 70\,\mu\mathrm{m}$ in the linear IR imaging and $\sim 45\,\mu\mathrm{m}$ for the SFG microscopy. Thus, the nonlinear approach provides a better lateral sensitivity, effectively limited by the focal profile of the VIS upconversion radiation. In principle, sub-IR wavelength resolution can be realized by using an appropriate objective lens [Rag11].

Spatially resolved measurements of the SFG and IR spectra are plotted in Fig. 7.6 to see the development of the LSPhP mode amplitude across the nanoresonator array. The strongest sum-frequency enhancement of the monopole resonance relative to the LO phonon peak is observed in the center of the nanostructured area. Moving towards the edge at 100 µm, the local field amplification decreases, until the nonlinear substrate response is the only dominating contribution, Fig. 7.6(a). In case of the IR reflectivity, excitation of the LSPhP modes within the Restrahlen band is identified by a reduction of the reflected IR intensity, strongest in the center of the array, Fig. 7.6(b). However, in contrast to the FTIR measurements, cf. Fig. 7.3, the clarity of the indiviual peaks is diminished. One reason might be the larger FEL focal spot size (80 µm FWHM compared to 50 µm for FTIR), being less sensitive to the restricted nanopillar area. On the other hand, the spectral resolution of the applied FEL radiation is about a factor 10 lower compared to the FTIR spectrometer.

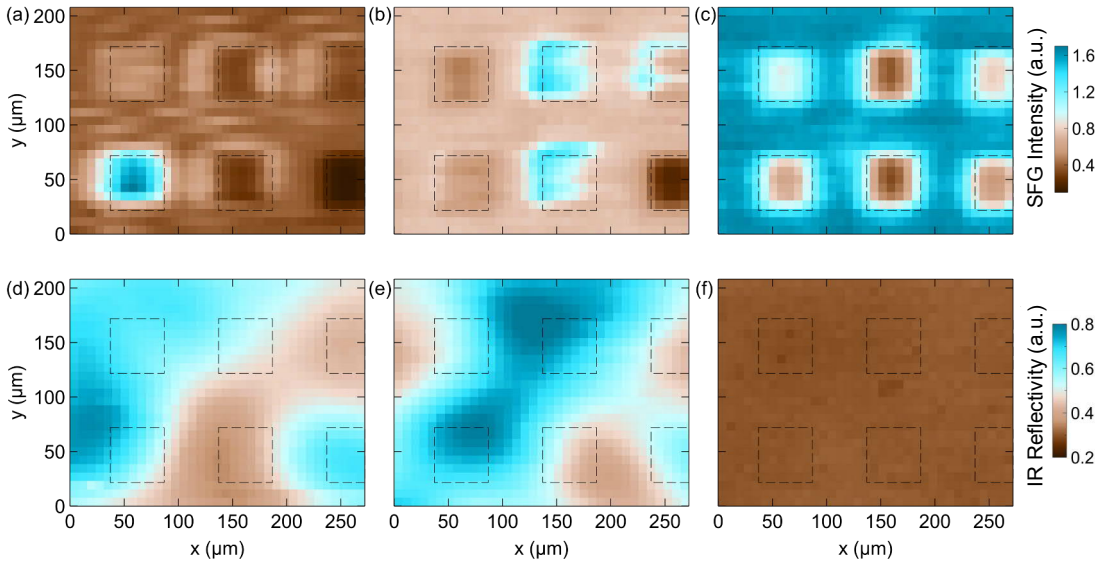

Fig. 7.7 Nonlinear and linear microscopy of phonon polariton resonances. (a)-(c) SFG intensity and (d)-(f) IR reflectivity are acquired by sampling with 8 µm step size. Exciting IR frequency has been selected to match the nanoresonator modes at $\nu_{\mathrm{IR}} = 888\,\mathrm{cm}^{-1}$ (a,d) and $\nu_{\mathrm{IR}} = 935\,\mathrm{cm}^{-1}$ (b,e) or the strongest substrate response at $\nu_{\mathrm{IR}} = 985\,\mathrm{cm}^{-1}$ (c,f). The 50 x 50 µm^2 areas of the nanostructured surface are indicated by dashed squares. P-polarization of incident and detected optical fields is used.

An illustrative application of the spectro-microscopy is a map out of the SFG response of a heterogeneously nanostructured surface. Figure 7.7 provides SFG images of 50x50 µm^2-sized arrays at three different IR frequencies, together with the simultaneously measured IR reflectivity maps. In case of $\nu_{\mathrm{IR}} = 888\,\mathrm{cm}^{-1}$, the excitation frequency is resonant with the monopolar mode of the array in the bottom left (pillar parameter $d = 300\,\mathrm{nm}$, $p = 1.5\,\mu\mathrm{m}$). This is recognized by the enhancement of the SFG intensity (factor ~ 2) in Fig. 7.7(a), which is limited to the nanopillar area. The intensity of the SFG radiation from the other arrays is hardly different compared to the substrate response. Switching the FEL wavenumber to $\nu_{\mathrm{IR}} = 935\,\mathrm{cm}^{-1}$, matching the dipolar LSPhP mode of the $p = 1\,\mu\mathrm{m}$ nanoresonator ensembles, causes an SFG enhancement in other sample areas as seen in Fig. 7.7(b), which is less sensitive to the pillar parameter d. The observed inhomogeneity of the SFG response across the arrays is probably due to a laser-induced modification of the nanopillar shape, and hence the resonance frequency, as discussed below. Finally, an inversion of the SFG intensity ratio of substrate versus nanostructure area is observed in the case of $\nu_{\mathrm{IR}} = 985\,\mathrm{cm}^{-1}$, close to the bulk LO phonon frequency, see Fig. 7.7(c). There, the SFG intensity is suppressed at the structured domains, providing a clear imaging contrast for all arrays independent of the resonator geometries.

The corresponding IR reflectivity maps of the sample are shown in Fig. 7.7(d)-(f). At first sight, the nanopillar arrays are hardly identified at all investigated excitation frequencies. This can be anticipated from the fact that the lateral IR resolution of at best

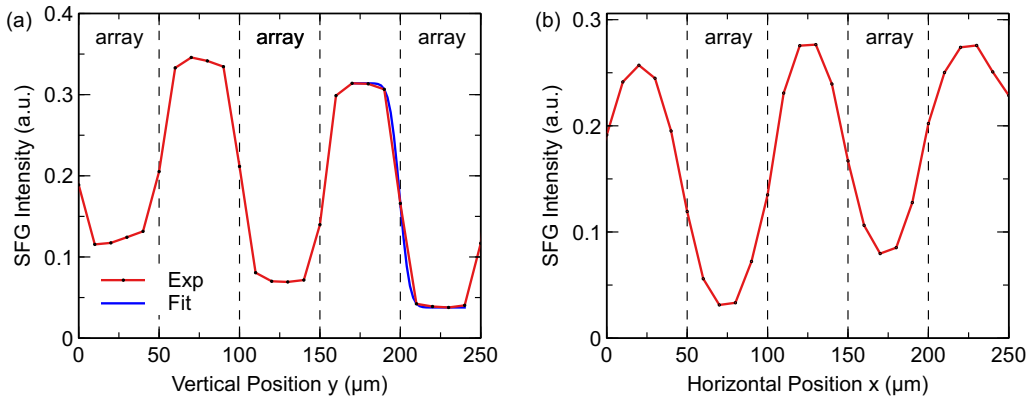

Fig. 7.8 Lateral SFG imaging resolution of nanostructures. (a) Vertical scan across nanopillar arrays with increasing nanopillar diameter from $d = 500\,\text{nm}$ (left), 750 nm (center) to 1000 nm (right) and $p = 2\,\mu\text{m}$. (b) Horizontal SFG intensity measurement of nanostructures with $d = 1000\,\text{nm}$ and varying pitch size of $p = 5\,\mu\text{m}$ (left) and $8\,\mu\text{m}$ (right). The edge positions of the $50\,\mu\text{m}$ wide arrays are marked by dashed lines. A fit of Eq. (7.1) to extract the resolved edge width is indicated in (a). Due to IR excitation at $\nu_{\text{IR}} = 968\,\text{cm}^{-1}$, the LO phonon frequency of the substrate, a reduction of the SFG intensity at the nanopillar arrays is observed.

70 µm (cf. Tab. 7.1) is not sufficient to distinguish the arrays of 50 µm size placed 50 µm apart. Further, the variation of the reflected IR intensity is small across the probed surfaces. This is in line with the modest contrast measured at various positions within the array, Fig. 7.6(b). Therefore, SFG microscopy is a viable tool to map the vibrational resonances of the sub-diffractional structures with IR radiation.

Optimization of the VIS beam to a minimal focal spot on the sample surface, described in Sec. 7.2, is used to figure out the best achievable lateral resolution, see Fig. 7.8. There, an one-dimensional probe scan in the vertical, Fig. 7.8(a), and horizontal direction, Fig. 7.8(b), has been performed. Depending on the nanoresonator dimensions, a varying SFG intensity contrast is observed compared to the substrate. The extracted edge widths, using the fit function Eq. (7.1), are summarized in Tab. 7.2. One reason for the different resolution values in the two directions might be the oblique incidence of the VIS beam, maintaining the focal size on the sample in the vertical direction, but stretching the diameter in the horizontal. Using the angle of incidence for an estimation, a horizontal value of $10\,\mu\text{m}/\cos(30°) = 11.5\,\mu\text{m}$ would be expected. Thus, the focused beam cross-section might be asymmetric. Comparable far-field SFG microscopy studies achieved a similar ($\sim 10\,\mu\text{m}$) [Cim06] or better resolution [Rag11].

Tab. 7.2 Best spatial resolution of SFG imaging obtained with scanning-probe approach. The edge width 2σ is extracted from a fit to Fig. 7.8.

	horizontal	vertical
SFG	$20.7 \pm 0.9\,\mu\text{m}$	$9.6 \pm 0.5\,\mu\text{m}$

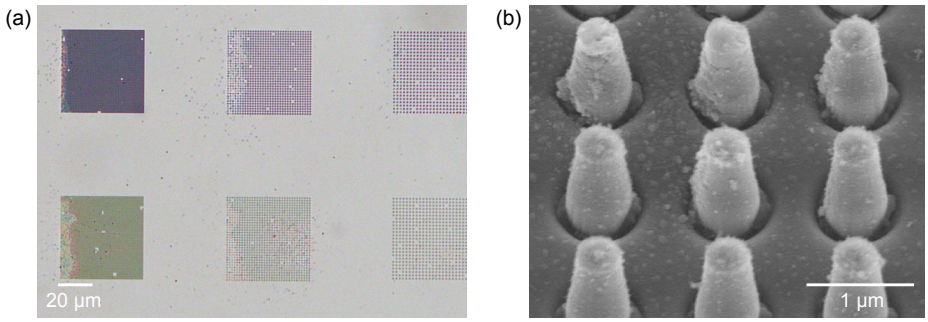

Fig. 7.9 Laser-induced changes of the nanoresonator shape. (a) Optical microscope image of the sample surface measured in Fig. 7.7. (b) SEM picture of individual nanopillars exhibiting structural modifications.

The inhomogeneities observed in the SFG images of the nanopillar arrays in Fig. 7.7(b) are probably caused by structural changes of the individual nanoresonators. An optical microscope and SEM image taken of the sample surface after the SFG experiment are shown in Fig. 7.9. For the used focal sizes and power levels of the laser beams, structural modifications of the nanopillar shape are present. The strong focusing results in a damage of the nanostructures, which is induced only if both IR and VIS radiation are applied. Due to the excitation resonant to the monopole mode, the strong energy absorption likely results in a melting and recrystallization of the material. In addition, the small volume of the nanoresonators restricts the heat transport in spite of the efficient thermal conductivity of SiC (cf. Sec. 6.3). The alterations of the pillar shape on the nanoscale influence the LSPhP resonance frequency ω_{SPhP} and, hence, the SFG emission intensity at the original IR excitation wavenumber ν_{IR}. However, this might prevent the complete destruction of the array due to a self-limitation of the IR absorption. As consequence of the damage, a trade-off between focusing size and pulse energy of the applied IR and VIS radiation has to be found in the scanning-probe microscopy approach. Alternatively, wide-field SFG imaging allows for capturing a large area of the specimen at once, avoiding the strong focusing [Hof02].

7.4 Summary

Localized surface phonon polaritons represent a versatile and efficient approach to enhance the local electric field at surfaces. Here, the consequences of the resonant IR excitation for the sum-frequency yield of such modes in nanoresonators on top of a non-centrosymmetric substrate are demonstrated. Spectral and spatial measurements show the occurrence of monopolar and dipolar modes to due strong light confinement within an array of identical nanopillars in contrast to the surrounding pristine substrate. SFG intensity enhancement relative to the bulk phonon resonance is obtained. Scanning of the IR-VIS probe across the sample with lateral SFG resolution of $\sim 10\,\mu\mathrm{m}$ allows to identify the extent of the field enhancement and imaging of the nanophotonic structures due to the vibrational contrast.

The study shows that IR-resonant phonon polaritons constitute an alternative to VIS-resonant plasmon polaritons in IR-VIS SFG enhancement [Ham99]. Applications of localized field enhancements might be beneficial for more sensitive IR absorption spectroscopy studies of molecular species at surfaces [Aut18] or amplified nonlinear optical conversion processes [Raz16]. The coherent nonlinear SFG microscopy can be used to resolve not only solid-state nanostructures, but also molecular adsorbates on surfaces or biological specimen [Lab07].

8 Polarization Dephasing in Time-Domain SFG Spectroscopy

Besides the investigation of vibrational transitions in solids via the nonlinear optical response in frequency-domain spectroscopy, the induced coherent polarization can also be probed in a time-resolved way. There, the observed dephasing dynamics is linked to the vibrational line profile. In this chapter, IR excitation of a polar dielectric by the FEL radiation followed by fs-short upconversion pulses is used to analyze the free-induction decay in the resonant and non-resonant case. Taking advantage of the timing correction method, the resolution of the transient signal is clearly improved. At nonzero time delays, a spectral narrowing of the resonance is found.

8.1 Motivation

While spectral and structural information about interface and bulk vibrations can be obtained by static IR-VIS SFG spectroscopy, time-domain experiments enable the study of ultrafast vibrational dynamics. This is in particular attractive for an understanding of energy transfer and the competition between different relaxation channels during chemical reactions and transient processes at surfaces, both of fundamental and technological importance, e.g. in catalysis [Bon00]. Depending on the arrangement of IR and VIS pulses, either the decay of the excited vibrational state's population $\Delta\rho(\tau)$ [GS90] or the dynamics of the optically induced linear polarization $P^{(1)}(\tau)$ [GS91] is revealed. In the case of two time-delayed IR and VIS pulses, the dephasing of the dielectric polarization can be measured, i.e. the loss of phase coherence among the dipole oscillators. The extracted time constant T_2 is connected to the spectral linewidth of the normal mode in the frequency domain, being usually a Lorentzian function [Ueb97]. In contrast, to probe the vibrational population lifetime T_1 via SFG, an additional pump excitation is required before the simultaneously arriving IR and VIS pulses. This IR pump – SFG probe approach also allows the recording of complete SFG spectra to discover, e.g., mode frequency shifts during desorption processes on surfaces [Bon00; Hes02].

The time-domain measurement of the dephasing is beneficial where ultrashort IR and VIS laser pulses are available: Scanning the time delay between the IR and a short upconversion pulse (i.e. duration at least one order of magnitude smaller than the dephasing time) to obtain the full dynamics and subsequent Fourier transformation yields the SFG spectrum. The same information would be obtained from a frequency-resolved SFG measurement, employing, in contrast, narrowband upconversion radiation. However, the time-domain acquisition of spectra can provide certain advantages [Rok03; Laa11]:

In reality, frequency narrowing of the VIS pulse is limited and entails loss of radiation power and SFG signal strength. Moreover, the resolution of the SFG spectrum can be easily scaled by the time range measured before Fourier transform [Laa11]. The increased spectral resolution facilitates more detailed line shape information, whether Gaussian or Lorentzian, and thus allows determination if inhomogeneous broadening contributions are present [Rok03]. Note that the actual SFG spectrum is only obtained by heterodyne detection of the time-domain electric field, whereas the homodyne-measured intensity trace only informs about the temporal free-induction decay.

The decoherence time T_2 of lattice vibrations can also be directly measured by other optical techniques, e.g. time-resolved coherent anti-Stokes Raman scattering (tr-CARS) or four-wave mixing experiments, as demonstrated on gallium phosphide polaritons [Juh89] and localized modes in fluorite [Wel00], respectively. Time-domain SFG measurements so far have concentrated on the vibrational dynamics of surfaces and adsorbates [GS91; Bon00; Arn10]. In the following, the free-induction decay of the IR polarization close to a bulk phonon mode in a polar 4H-SiC crystal is studied.

8.2 Experimental Details

For a time-domain SFG spectroscopy measurement of the polarization dephasing constant T_2, the two-pulse scheme has to be applied. There, the coherent optical polarization of the material is induced by the ps-short IR FEL pulse, subsequently probed by the frequency-doubled VIS table-top upconversion radiation. Variation of the time delay τ between both pulses yields the dynamics of the background-free SFG intensity. Whereas the time-domain SFG intensity traces and spectra have been aquired using the original $\tau_\mathrm{p} \sim 120\,\mathrm{fs}$ short VIS pulse, the static SFG spectrum is recorded by means of the $\sim 1\,\mathrm{ps}$ stretched VIS pulse. The arrangement of the incident beams, focal spot sizes and VIS fluence are the same as in the previous measurements (cf. Fig. 3.3(b) and Sec. 7.2). However, the sample is mounted with its surface normal parallel to the VIS wavevector, the FEL fluence is about $35\,\mathrm{mJ/cm^2}$ and the transmitted SFG radiation is detected.

In parallel to the time-domain SFG setup (Fig. 3.4, left part), the balanced optical cross-correlator (right part of Fig. 3.4) has been used to monitor and correct for the actual FEL – table-top laser pulse timing on a single-shot basis. For that, a part of the NIR output (50 %) of the fiber oscillator is separated before frequency-doubling of the remaining laser light. Thus, phase-matched sum-frequency mixing with a portion (15 %) of the FEL power is achieved in the GaSe crystal. All SFG intensities shown in this chapter are acquired under PPP polarization configuration.

The investigated sample is a 350 µm thin semi-insulating 4H-SiC crystal, which has been previously studied by static SFG spectroscopy (cf. Sec. 6.3). There, a single SFG-active phonon mode is present in the relevant IR frequency range.

8.3 Results

For the time resolution of the accelerator-based optical spectroscopy, the actual delay between FEL and table-top laser pulse is critical. Thus, the impact of the timing correction technique on the signal quality of the measured SFG dynamics will be analyzed first. Then, the dephasing constant of the polarization at different excitation frequencies is revealed from the free-induction decay data. Together with an analytical model, the transient SFG spectra at distinct temporal delays are dicussed, explaining the observed resonance narrowing.

8.3.1 Time Delay Correction

The ability of the implemented balanced optical cross-correlator to characterize the relative timing jitter and drift between FEL and table-top laser pulses has been demonstrated in Sec. 4.2. Here, this tool is used to adjust the delay τ set in the time-domain SFG measurement to the real temporal distance of the pulses. For that, the BOC-obtained relative timing value is added to the delay stage setting, $\tau+\delta\tau$, for each FEL macro-pulse, and the SFG intensity at the original delay points $I(\tau)$ is retrieved by linear interpolation. Subsequent averaging over multiple ($\sim$ 20) macro-pulses per delay coordinate is used to improve the statistics.

The results of the timing correction are illustrated in Fig. 8.1. Due to the occurence of multiple sub-pulses within an FEL micro-pulse and varying temporal peak positions during the real-time length of the macro-pulse, cf. Fig. 5.2(a) and Sec. 5.2, all time-domain SFG traces are displayed for a fixed real-time value t before the onset of the second sub-pulse. Otherwise, the real-time-integrated SFG data would hide the specific material response and diminish the delay resolution, cf. Fig. 5.2(b). The uncorrected measurement is shown in Fig. 8.1(a), whereas the more accurate BOC-readjusted SFG dynamics is plotted in Fig. 8.1(c). In order to quantify the 'smoothness' of the delay traces, a convolution integral of the Gaussian sub-pulse profile with an exponentially decaying material response is fitted to the corrected data. The ex-Gaussian convolution function reads

$$I(\tau) = I_0 \exp\left(\frac{\sigma^2}{2\kappa^2} - \frac{\tau-\tau_0}{\kappa}\right)\left(1 - \operatorname{erf}\left(\frac{\sigma^2 - \kappa(\tau-\tau_0)}{\sqrt{2}\sigma\kappa}\right)\right), \tag{8.1}$$

with the pulse width σ and decay constant κ. A comparison of the uncorrected and BOC-corrected experimental data with the reference model function yields a root-mean-square error (RMSE) of 9.6×10^{-3} and 6.5×10^{-3}, respectively, demonstrating the improvement of the signal quality due to the actual pulse delay recording. In addition, the electron beam-position monitoring (BPM) of the FEL has been tested for timing correction, see Fig. 8.1(b), due to the known correlation between kinetic electron energy and pulse arrival time (cf. Fig. 4.5). With a correlation coefficient of $\rho = 0.65$ for the relation of energy vs. timing, the BPM-corrected delay trace results in a RMSE of 8.2×10^{-3}. Thus, the adjustment of the synchronized FEL pulse timing solely by the accelerator-

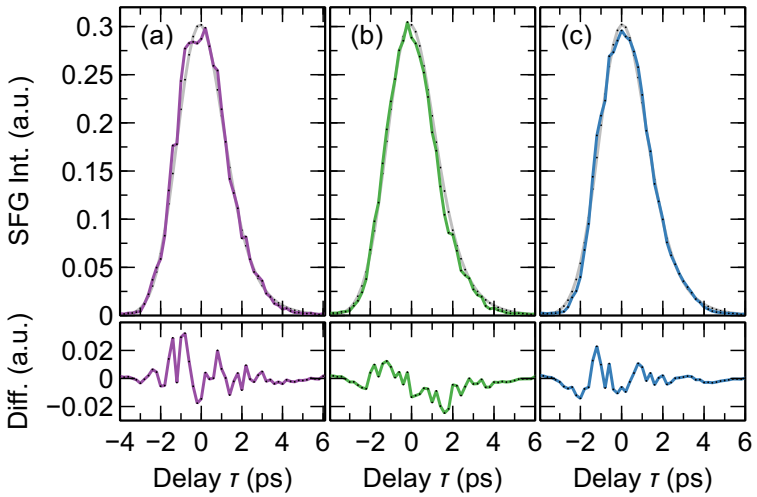

Fig. 8.1 Post-correction of FEL pulse timing. The time-domain SFG intensity trace is shown in the upper panel as measured (a) and after application of the delay correction using the kinetic electron energy monitoring (b) or the balanced optical cross-correlation (c), respectively. Corrections are done on a single-shot level, yielding the displayed delay traces after shot-averaging. The quality of the results is determined by comparison with the best-fit function to the BOC-corrected SFG transient (gray line) from (c), repeated in (a) and (b). Intensity differences are depicted in the lower panel.

based diagnostics might be an alternative method if the SFG cross-correlation is difficult to obtain (e.g., due to the used IR wavelength). However, the precision is reduced compared to the all-optical pulse timing monitoring.

8.3.2 Free-Induction Decay of IR Polarization

The dephasing dynamics of the induced dielectric polarization in SiC has been studied by IR excitation close to the LO phonon mode, $\nu_{\mathrm{LO},\parallel} = 962\,\mathrm{cm}^{-1}$. Although this vibration is not SFG-active, the measured SFG intensity, and thus the induced linear polarization $P^{(1)}$, is strongest there within the accessible spectral range, as discussed previously (cf. Sec. 6.3). The peak originates actually from the zero-crossing of the real part of the dielectric function of SiC, increasing the Fresnel factor by several orders of magnitude. For excitation of the first-order polarization $P^{(1)}$, the length of the IR FEL (sub-)pulse has been chosen as short as possible by setting a small FEL cavity detuning, $\Delta L = 1\lambda$. The measured SFG transients $I_{\mathrm{SFG}}(\tau)$ after BOC correction are plotted in Fig. 8.2. Depending on the wavenumber ν_{IR} of the exciting IR field, different polarization dynamics are observed. Whereas the spectral dependence of the SFG amplitude is explained in terms of the Fresnel factor, i.e. linear optical effects (cf. Sec. 6.3), the excitation frequency-sensitive dephasing manifests itself in different temporal peak positions as well as decay times. With the chosen delay increment of $\Delta\tau = 200\,\mathrm{fs}$, a slight temporal shift of the SFG peak position for $\nu_{\mathrm{IR}} = 960\,\mathrm{cm}^{-1}$ by about 400 fs towards positive delay times is

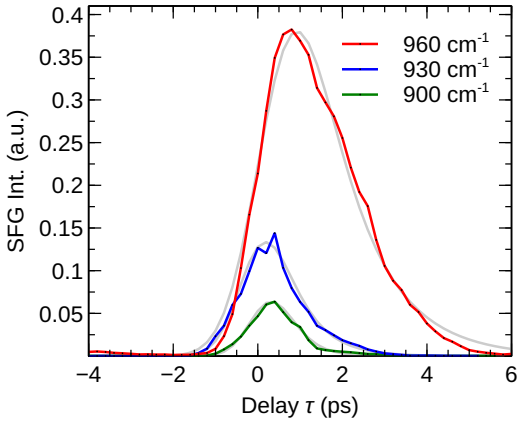

Fig. 8.2 IR polarization dynamics in 4H-SiC. Induced by a ps-short MIR pulse, the sum-frequency light is generated by the VIS upconversion pulse, delayed by time τ relative to the excitation. Different IR wavenumbers ν_{IR} close to the LO phonon mode are applied. The model fit of Eq. (8.1) to the SFG response is shown (gray lines). A semilogarithmic plot of the normalized data is given in Fig. 8.4(c).

detected, compared to the trace at $\nu_{\mathrm{IR}} = 900\,\mathrm{cm}^{-1}$. The free-induction decay of the SFG intensity can be fitted by the ex-Gaussian function of Eq. (8.1), see Fig. 8.2. The extraction of the decay constants κ is described below.

The polarization dephasing is also apparent in the 2D plots of Fig. 8.3. There, the BOC-corrected SFG intensity $I_{\mathrm{SFG}}(\tau)$ is shown during the whole FEL macro-pulse time t. The dependence of the dynamics on the excitation wavenumber ν_{IR} can be directly identified on basis of the intensity contrast within the delay range between the FEL sub-pulses, being more pronounced for the case $\nu_{\mathrm{IR}} = 900\,\mathrm{cm}^{-1}$, Fig. 8.3(a), due to the faster decay. Note that the SFG traces shown in Fig. 8.2 are extracted at a time t where a single sub-pulse is present. The decay constants κ for the different excitation wavenumbers are revealed from the 2D plots. To this end, a non-resonant SFG measurement is shown in Fig. 8.3(d), obtained by phase-matched frequency-mixing of MIR FEL ($\nu_{\mathrm{IR}} = 900\,\mathrm{cm}^{-1}$) and NIR table-top laser pulses in the GaSe crystal in transmission geometry [Fig. 3.3(a)]. A cross-correlation between FEL and VIS pulses in a ZnSe crystal or Au surface did not yield a useful signal. The SFG intensity decay times κ are obtained from a fit of the convolution of the reference FEL pulse shape with a step-like exponential function

$$f(\tau) = H(\tau)\,\mathrm{e}^{-\tau/\kappa}, \tag{8.2}$$

where $H(\tau)$ is the Heaviside distribution. An overview of the time constant fit results is given in Fig. 8.5. For the case of detuning $\Delta L = 1\lambda$, resonant excitation in the vicinity of the LO phonon reveals a slower free-induction decay of $\kappa = 1.66 \pm 0.01\,\mathrm{ps}$, compared to the spectrally offset case at $\nu_{\mathrm{IR}} = 900\,\mathrm{cm}^{-1}$ with $\kappa = 0.15 \pm 0.01\,\mathrm{ps}$. A simulation of the free-induction decay with the fitted time constant for excitation at $\nu_{\mathrm{IR}} = 960\,\mathrm{cm}^{-1}$ is shown in Fig. 8.3(e), comparing well with the measurement in Fig. 8.3(c).

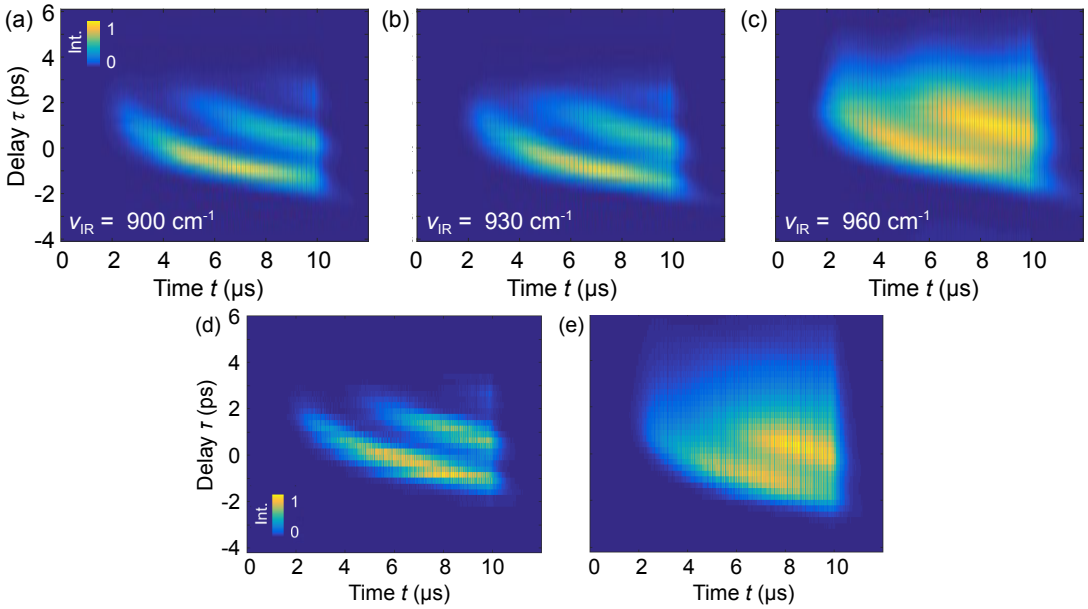

Fig. 8.3 Two-dimensional graphs of the near-resonance and non-resonant SFG response. The delay-resolved polarization dephasing is tracked during the macro-pulse real-time t at different IR photon energies, (a) $\nu_{\mathrm{IR}} = 900\,\mathrm{cm}^{-1}$, (b) $930\,\mathrm{cm}^{-1}$ and (c) $960\,\mathrm{cm}^{-1}$. The position shift of the IR sub-pulses is closely followed by the decay dynamics of the induced polarization. Excitation fluences are similar in all cases. The traces isolated at $t = 3.5\,\mu\mathrm{s}$ are depicted in Fig. 8.2. (d) Non-resonant reference SFG revealed by intensity cross-correlation of the FEL macro-pulse and NIR table-top laser pulse in GaSe. (e) Simulation of the material response by convolution of the FEL pulse envelope (d) along the delay axis with the exponential function Eq. (8.2) for the fitted decay constant $\kappa = 1.66\,\mathrm{ps}$ of $\nu_{\mathrm{IR}} = 960\,\mathrm{cm}^{-1}$. In all cases, short IR micro-pulses generated at cavity detuning $\Delta L = 1\lambda$ are used.

For completeness, time-domain SFG intensity decays have been measured with temporally longer FEL pulses (i.e. larger cavity detuning), see the semilogarithmic traces in Fig. 8.4. The convolution fitting analysis of the 2D data with the corresponding reference cross-correlation yields the decay constants κ shown in Fig. 8.5. All the extracted experimental values support the trend of an increased polarization dephasing time T_2 close to the LO phonon frequency. The dependence of the decay time κ on the FEL pulse duration at a certain IR center wavelength ν_{IR} might reflect the influence of the excitation bandwidth: For smaller FEL cavity detuning ΔL, i.e. larger IR bandwidth [cf. Fig. 5.1(b)], additional spectrally offset polarization contributions with an asymmetric frequency distribution are excited [see Fig. 8.6(a)].

The dephasing time of the IR polarization $P^{(1)}$ is related to the SFG intensity decay I_{SFG} via $T_2 = 2\kappa$, since $I \propto |P^{(2)}|^2$ and $P^{(2)} \propto P^{(1)}$ [Hes02]. Thus, the constant of the free-induction decay in bulk 4H-SiC varies between $T_2 = 3.32 \pm 0.02\,\mathrm{ps}$ (LO phonon resonant) and $T_2 = 0.30 \pm 0.02\,\mathrm{ps}$ (off-resonant) in case of short IR excitation pulses. Comparable values in literature for the dephasing time in solids are found to be

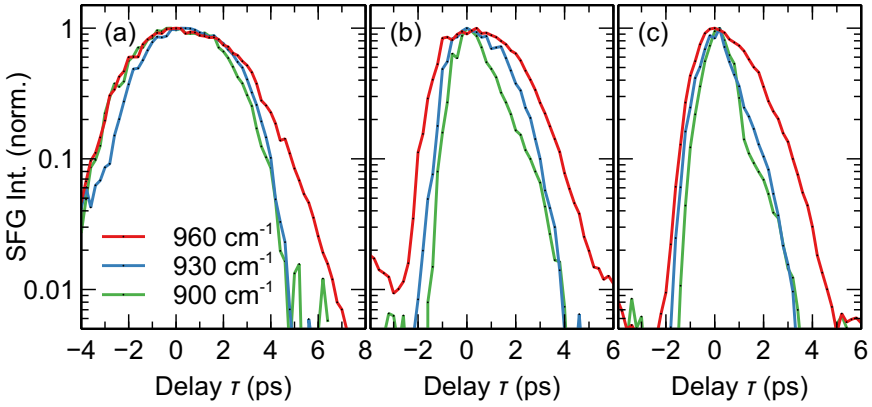

Fig. 8.4 Time-domain SFG spectroscopy. The polarization dynamics is induced with various IR pulse lengths, adjusted via the FEL cavity detuning: (a) $\Delta L = 4\lambda$, (b) $\Delta L = 2\lambda$ and (c) $\Delta L = 1\lambda$. The used IR excitation wavenumbers are $\nu_{\mathrm{IR}} = 960\,\mathrm{cm}^{-1}, 930\,\mathrm{cm}^{-1}$ and $900\,\mathrm{cm}^{-1}$. All transients are normalized for intensity and zero delay at maximum. The traces are extracted from the corresponding 2D plots like in Fig. 8.3 at a certain time t approximately 1 µs apart from the beginning of the macro-pulse, in order to obtain the response initiated by a single IR (sub-)pulse.

$T_2 = 4.2 \pm 0.4\,\mathrm{ps}$ for the LO phonon [Val94] and $T_2 = 2.9 \pm 0.3\,\mathrm{ps}$ for the TO phonon in a semiconducting polar GaAs crystal [Gan97] or $T_2 = 5.8 \pm 0.6\,\mathrm{ps}$ for the TO mode in insulating diamond [Lau71] using tr-CARS at room temperature.

In general, the dynamics observed in time-resolved vibrational spectroscopies is determined by two contributions: On the one hand, the rate T_1 at which the population or energy of the excited vibrational mode relaxes back to equilibrium and, on

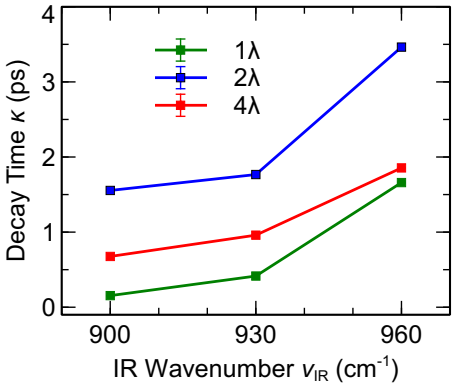

Fig. 8.5 Dephasing time at different IR excitation wavenumbers. The decay constant κ is extracted from a convolution fit of Eq. (8.2) with the reference pulse shape to the SFG SiC traces, see e.g. Fig. 8.3. Different FEL cavity detunings ΔL are applied at each IR wavenumber ν_{IR}. The dephasing time is related via $T_2 = 2\kappa$.

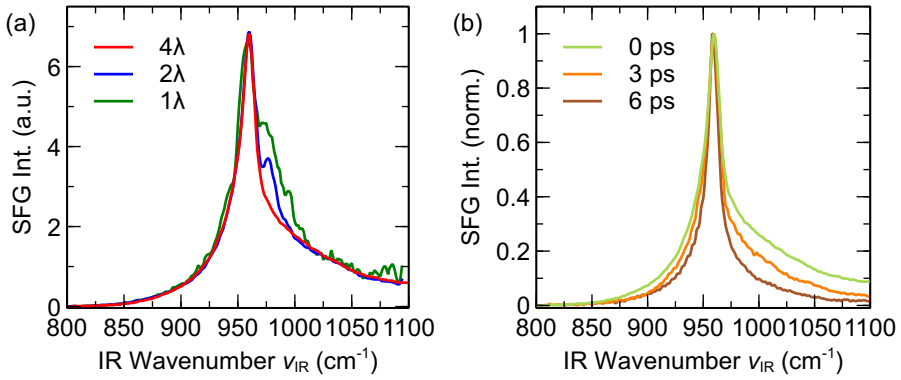

Fig. 8.6 Static and transient SFG spectra of 4H-SiC. (a) Static spectra obtained with different IR pulse bandwidths, varied via the FEL cavity detuning ΔL. (b) Normalized transient SFG spectra measured at distinct time delays τ with narrowband IR FEL radiation ($\Delta L = 4\lambda$).

the other hand, the pure dephasing or coherence loss of the vibrational polarization, characterized by the time constant T_2^* [Ueb97]. Since SFG is a coherent probing technique, the measured polarization dephasing in the time domain incorporates both mechanisms via $2/T_2 = 1/T_1 + 2/T_2^*$. In the absence of inhomogeneous broadening, resulting in a Gaussian spectral lineshape, the dephasing time T_2 is related to the bandwidth (FWHM, cm^{-1}) of a homogeneously broadened, Lorentzian-shaped spectral line via $2\Gamma = 1/\pi c_0 T_2$ [Lau78]. Thus, from the dephasing constant at $\nu_{IR} = 960\,\mathrm{cm}^{-1}$ excitation, $T_2 = 3.3\,\mathrm{ps}$, one would expect a FWHM linewidth of $2\Gamma = 3.2\,\mathrm{cm}^{-1}$. Spectra for comparison with the time-domain data are provided in the next section. Actually, the experimental data in Fig. 8.2 can not sufficiently well described by an exponential decay at large positive delays. The cause of the non-Lorentzian line shape is explained below.

8.3.3 Transient SFG Spectra

In order to further characterize the polarization dephasing, static and transient IR-VIS SFG spectra have been acquired, see Fig. 8.6. There, the wavenumber ν_{IR} of the IR excitation is scanned while keeping the time delay τ relative to the upconversion pulse constant. For the static spectra taken at maximum pulse overlap ($\tau = 0$) in Fig. 8.6(a), different FEL pulse lengths are used in combination with the stretched VIS pulse. Note that the timing correction can not be applied to the frequency-domain measurements. A comparison with the SFG spectrum measured in the reflection geometry under PPP configuration, cf. Fig. 6.2, reveals that just a single resonance peak at $\nu_{IR} = 960\,\mathrm{cm}^{-1}$ is observed for the smallest FEL bandwidth. This fact is due to the smaller angle of incidence of the IR field ($\sim 25°$) used in the SFG transmission geometry, modifying the angle-dependent Fresnel factor $F(\nu_{IR}, \theta_{IR})$, as illustrated for normal incidence in Fig. 6.4(c). At shorter IR pulses, i.e. smaller FEL cavity detuning, a side-peak $\sim 15\,\mathrm{cm}^{-1}$ apart emerges in Fig. 8.6(a). This might be due to the presence of sub-pulses within the FEL radiation, causing spectral sidebands as discussed in Sec. 5.2.2 and seen in Fig. 5.8,

Tab. 8.1 Temporal development of center frequency ν_{IR} and bandwidth $\Delta\nu$ of the SFG resonance. The values are extracted from the transient spectra shown in Fig. 8.6(b).

Delay τ	0 ps	3 ps	6 ps
Peak Frequency ν_{IR} (cm^{-1})	959.3 ± 0.2	959.3 ± 0.1	958.9 ± 0.1
FWHM $\Delta\nu$ (cm^{-1})	21.8 ± 0.7	18.1 ± 0.5	13.1 ± 0.3

thus being not related to the material response. The linewidth (FWHM) extracted from the static spectrum taken at $\Delta L = 4\lambda$ amounts to $21.8 \pm 0.7\,\mathrm{cm}^{-1}$. This is much larger than expected for a vibrational lineshape from the time-domain data ($3.2\,\mathrm{cm}^{-1}$). Also, the observed resonance has an asymmetric, non-Lorentzian form. Actually, as discussed in Sec. 6.3.3, the peak in the SFG spectrum around $\nu_{\mathrm{IR}} \sim 960\,\mathrm{cm}^{-1}$ is not related to a vibrationally enhanced contribution to the resonant part of the second-order susceptibility $\chi^{(2)}(\nu_{\mathrm{IR}})$, giving a Lorentzian shape, but due to a resonance in the Fresnel factor $F(\nu_{\mathrm{IR}})$, i.e. linear optical effects, of the bulk material. Therefore, the nonlinear response has a frequency-dependent modulation.

The time-resolved SFG spectra are summarized in Fig. 8.6(b), obtained with the narrowband FEL radiation ($\Delta L = 4\lambda$). Comparing the width of the normalized spectra, a narrowing of the spectral lineshape is observed at larger time delays τ between IR excitation and VIS upconversion pulse. The extracted FWHM and center wavenumber of the resonance are displayed in Tab. 8.1. Whereas the center wavenumber stays constant, the linewidth has nearly halved at time delay $\tau = 6\,\mathrm{ps}$. In addition, the spectral shape of the resonance undergoes a transition from an asymmetric to a symmetric function. The change in the resonance profile is linked to the wavenumber-dependent dephasing constants T_2 observed in the time-domain SFG measurements, cf. Fig. 8.4. Faster off-resonant decay of the induced polarization entails an effective spectral narrowing at larger delays.

8.3.4 Model of Time-Domain SFG

To corroborate the experimentally observed behavior of the SFG intensity in the time domain, an analytical model has been used to simulate the nonlinear response, following Ref. [Bor05]. The involved components of the SFG process are illustrated in Fig. 8.7. Starting in the frequency-domain, a Gaussian-shaped IR pulse of center wavenumber ν_{IR} and fixed width $\sigma_\nu = 0.441/2\sqrt{2\ln 2}\tau_{\mathrm{IR}}$, derived from the pulse duration τ_{IR},

$$\boldsymbol{E}_{\mathrm{IR}}(\nu) = \hat{\boldsymbol{E}} \mathrm{e}^{-\frac{(\nu-\nu_{\mathrm{IR}})^2}{2\sigma_\nu^2}}, \tag{8.3}$$

has been considered and multiplied with the Fresnel tensor $\boldsymbol{F}(\nu, \theta)$ to account for the occurrence of the resonance near the LO phonon mode. The absolute value of the

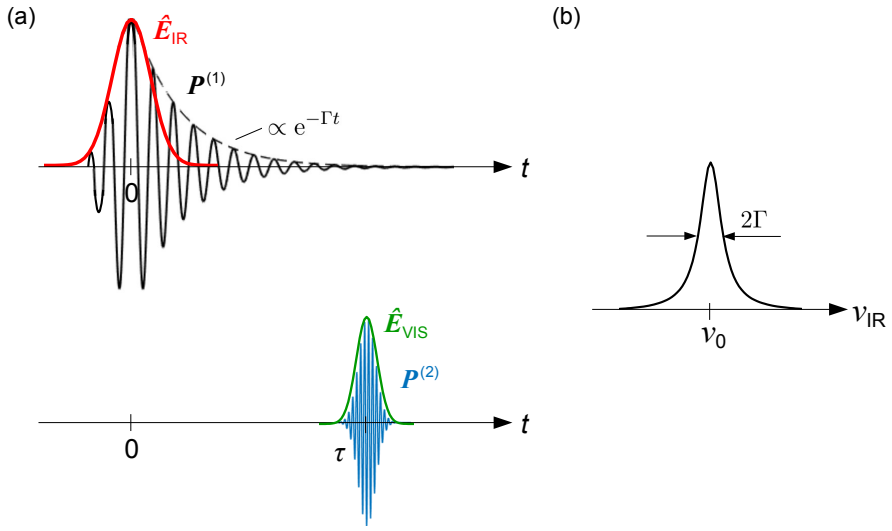

Fig. 8.7 SFG response of a vibrational resonance. (a) Process in the time-domain. Due to an IR pulse, $\boldsymbol{E}_{\mathrm{IR}}(t) = \hat{\boldsymbol{E}}_{\mathrm{IR}}\mathrm{e}^{-\mathrm{i}2\pi\nu_{\mathrm{IR}}t}$, resonant with a vibration ν_0, a linear polarization $\boldsymbol{P}^{(1)} \propto \mathrm{e}^{-\mathrm{i}2\pi\nu_0 t-\Gamma t}$ is induced, whose envelope dephases with decay rate Γ. For upconversion, a VIS pulse $\boldsymbol{E}_{\mathrm{VIS}}(t,\tau) = \hat{\boldsymbol{E}}_{\mathrm{VIS}}\mathrm{e}^{-\mathrm{i}2\pi\nu_{\mathrm{VIS}}(t-\tau)}$ is applied to create the nonlinear polarization $\boldsymbol{P}^{(2)}(t,\tau) = \hat{\boldsymbol{P}}^{(2)}\mathrm{e}^{-\mathrm{i}2\pi\nu_{\mathrm{SFG}}(t-\tau}$, generating the SFG radiation $I_{\mathrm{SFG}}(\tau)$. (b) In the frequency-domain, the free-induction decay entails a finite spectral linewidth 2Γ of the vibration ν_0.

resulting linear IR polarization

$$P^{(1)}(\nu) \propto |\boldsymbol{F}(\nu)\boldsymbol{E}_{\mathrm{IR}}(\nu)| \tag{8.4}$$

is subsequently Fourier-transformed to obtain the time-domain free-induction decay

$$P^{(1)}(t) = \mathcal{F}(P^{(1)}(\nu)). \tag{8.5}$$

The upconversion with the short time-delayed VIS pulse is assumed to be instantaneous, i.e. the convolution is taken as a product, yielding the second-order polarization

$$P^{(2)}(t,\tau) \approx E_{\mathrm{VIS}}(t-\tau)P^{(1)}(t). \tag{8.6}$$

Finally, the SFG intensity is received by

$$I_{\mathrm{SFG}}(\tau) \propto \int \mathrm{d}t|P^{(2)}(t,\tau)|^2. \tag{8.7}$$

The spectral dependence $I_{\mathrm{SFG}}(\tau,\nu_{\mathrm{IR}})$ on the excitation frequency is obtained via tuning the IR wavenumber ν_{IR} in Eq. (8.3).

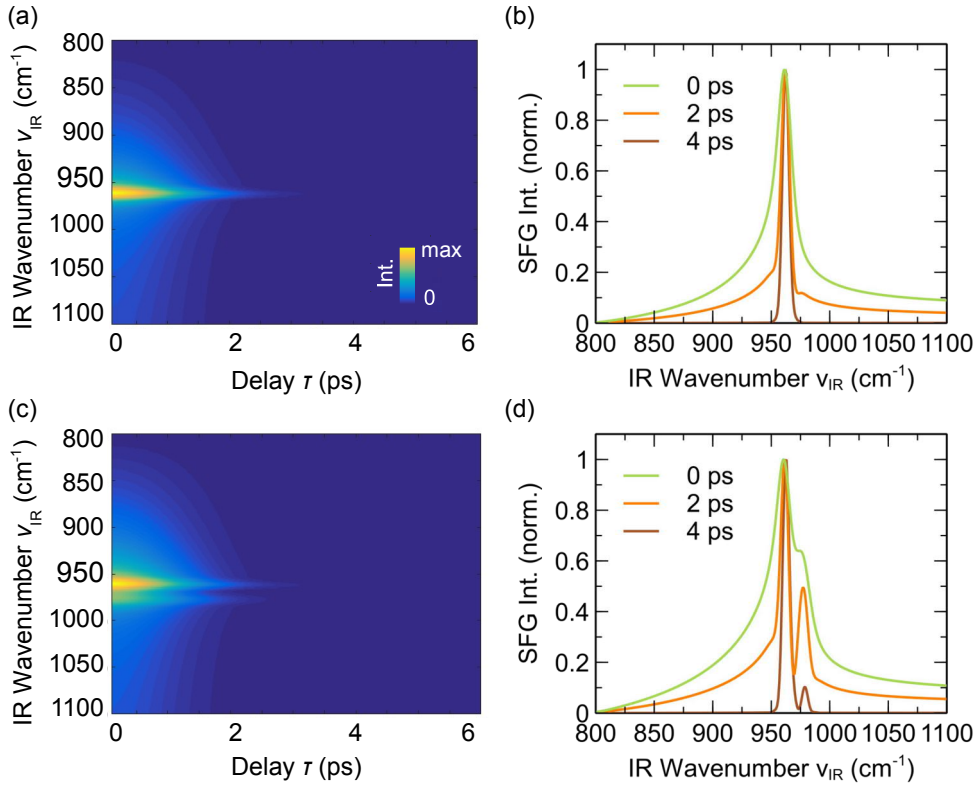

Fig. 8.8 Simulation of time-domain SFG response of a single (a,b) and two resonances (c,d). (a,c) Two-dimensional plot of the SFG intensity $I_{\mathrm{SFG}}(\tau, \nu_{\mathrm{IR}})$ showing the decay due to polarization dephasing for a single resonance. (b,d) Transient normalized SFG spectra $I_{\mathrm{SFG}}(\nu)$ extracted at certain time delays τ. The single resonance at $\nu_0 = 962\,\mathrm{cm}^{-1}$ (a,b) is obtained for IR incidence under $\theta_{\mathrm{IR}} = 25°$, whereas the double peak occurs at the angle of incidence $\theta_{\mathrm{IR}} = 55°$ (c,d).

Theoretical results of the time- and frequency-domain SFG intensity for two different angles of incidence of the IR field are shown in Fig. 8.8. For the case of close to normal incidence IR excitation under $\theta_{\mathrm{IR}} = 25°$ with $\tau_{\mathrm{IR}} = 2\,\mathrm{ps}$ and PPP configuration, corresponding to the measurement conditions, the 2D plot of $I_{\mathrm{SFG}}(\tau, \nu_{\mathrm{IR}})$ is given in Fig. 8.8(a). A single resonance, located around $\nu_{\mathrm{IR}} = 962\,\mathrm{cm}^{-1}$, is present, decaying on a ps-time scale. Cross-sectional normalized SFG spectra $I_{\mathrm{SFG}}(\nu_{\mathrm{IR}})$ at certain time delays τ are plotted in Fig. 8.8(b). A narrowing of the spectral linewidth is observed, e.g. to 32 % of the original FWHM after $\tau = 4\,\mathrm{ps}$. These findings are in qualitative agreement with the measured behavior, Fig. 8.6.

If the IR field is incident with the angle $\theta_{\mathrm{IR}} = 55°$, the simulations result in SFG spectra as depicted in Fig. 8.8(c,d). There, the Fresnel factor gives rise to two resonances in the vicinity of the LO phonon mode. Each resonance decays on a ps time scale, Fig. 8.8(c). However, the noticeable observation is a clear distinction of the spectrally narrowed resonance peaks at nonzero time delay, Fig. 8.8(d). Thus, SFG with a pair

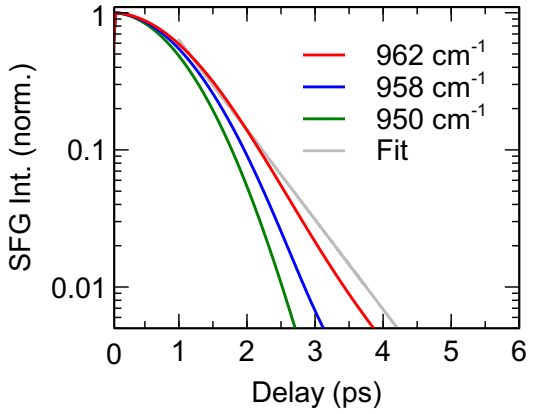

Fig. 8.9 Resonant and non-resonant free-induction decay. The time-domain SFG intensity $I_{\mathrm{SFG}}(\tau)$ is depicted for different IR excitation wavenumbers ν_{IR} in the single resonance case [Fig. 8.8(a,b)]. An exponential fit to the trace at $\nu_0 = 962\,\mathrm{cm}^{-1}$ is also shown (gray line). A similar result is obtained for the case of two SFG resonances [Fig. 8.8(c,d)].

of time-delayed IR and VIS pulses seem to provide a better spectral resolution than for the case of $\tau = 0$. Actually, time-domain SFG spectroscopy experiments have shown that they provide a higher sensitivity to the resonant contribution in the SFG process if IR and VIS pulses are not temporally overlapping, avoiding the non-resonant, instantaneous part [Rok03; Lag07]. Then, after Fourier transformation, the line shape in the frequency-domain is determined by the resonance dephasing. However, one should note that spectral distortions might occur caused by phase shifts [Laa11].

The SFG intensity $I_{\mathrm{SFG}}(\tau)$ depicted in Fig. 8.9 reflects the free-induction decay of the induced linear polarization $P^{(1)}$. Obviously, off-resoantn IR exciatuon results in a faster polariatuion depahsing than in the resonnat case. For the excitation at the LO phonon wavenumber, $\nu_{\mathrm{IR}} = 962\,\mathrm{cm}^{-1}$, a decay time of 0.7 ps might be extracted from an exponential fit. However, the calculated SFG trace deviates from the exponential form, see Fig. 8.9. This is in accordance with the non-Lorentzian spectral lineshape, Fig. 8.8(b). Also, the experimentally measured SFG time-domain traces in Fig. 8.4 exhibit a non-exponential decay.

8.4 Summary

In conclusion, the dephasing dynamics of the induced dielectric polarization in SiC has been probed in the time-domain, using the established pulse timing correction scheme. Resonant IR excitation close to a non-SFG-active vibrational mode reveals a slower free-induction decay of the polarization (total dephasing time $T_2 = 3.3\,\mathrm{ps}$) than with a spectrally offset excitation. The time-domain trace deviates from an exponential function, in accordance with the non-Lorentzian lineshape in the measured spectra, due to

the frequency-dependent Fresnel factor responsible for the SFG resonance. The transient spectral response exhibits a linewidth narrowing for temporal delays of the upconversion pulse far from the IR excitation. The observed dynamics is attributed to the development of the polarization decoherence. Results from an analytical model of the time-domain SFG response are in qualitative agreement with the experimental data. Thus, time-delayed IR-VIS pulses might be an opportunity to increase the spectral resolution of closeby peaks in SFG spectrum measurements. Finally, the study demonstrates the ability to perform time-resolved measurements with the accelerator-based light source at the sub-ps scale.

9 Summary and Perspectives

This thesis has focused on free-electron laser-based vibrational sum-frequency generation spectroscopy and its application to lattice vibrations in solid-state materials and nanostructures. To this end, a synchronized two-color optical setup was implemented using a femtosecond table-top oscillator in combination with the FHI FEL. By means of balanced optical cross-correlation, the low-jitter and low-drift pulse timing has been chracterized and verified. A study of the pulse dynamics within the long-wavelength FEL oscillator revealed the formation of sub-pulses and the occurrence of regular limit-cycle power oscillations, as corroborated by numerical simulations based on Maxwell-Lorentz theory. The second-order nonlinear response has been investigated in polar dielectric bulk media within the optical phonon spectral region. Supported by an analytical model, several dispersive and resonant contributions to the observed sum-frequceny spectra are identified. Revealing that the local electric field is crucial for the SFG intensity, localized surface phonon polaritons in nanostructures are examined as a way to modify the nonlinear optical response in the MIR range. Based on coherent second-order optical microscopy, the vibrational contrast imaging of sub-IR diffractional geometries is demonstrated with MIR radiation. Finally, the free-induction decay of the photoinduced electric polarization is studied in the time domain, revealing dephasing dynamics on the ps scale and resonance narrowing. In conclusion, the IR-VIS nonlinear light-matter interaction within dielectric media has been probed with spectral, temporal and spatial resolution.

The experimental investigations are performed with a newly established IR-VIS spectroscopy setup. While the intense, wavelength-tunable and narrowband MIR light is obtained from an accelerator-based light source, the upconversion radiation is provided by a separate laser. Crucial for nonlinear and time-resolved spectroscopy studies is the stability of the temporal pulse overlap. Thus, for monitoring of the pulse synchronization, the concept of balanced optical cross-correlation has been extended to the MIR region and applied to the FHI FEL. A timing jtter down to 100 fs has been revealed, with a pulse drift in the order of 3 ps per 30 min. The latter was found to be correlated with the fluctuations of the kinetic electron energy behind the linear accelerators. Application of the timing tool simultaneously to a time-resolved experiment allows for post-correction of the timing drift, improving the temporal resolution on the fs scale.

The pulse arrival time monitoring mitigates the requirement for a tight active synchronization, as it is implemented at other accelerator-based lasers [Sch15b]. Instead, the demonstrated balanced cross-correlation method extends the timing diagnostics available at fourth generation light sources [Cav05; Gah08; Har13; Kov17] and expands the spectroscopic possibilities at the FHI FEL to the time domain.

Prior to the SFG studies, the emitted FEL radiation has been characterized. Based on cross-correlation measurements, the detuning ΔL of the FEL cavity length L is found as critical parameter for the control of FEL pulse shape and bandwidth. The intensity envelope changes from a short Gaussian pulse close to zero detuning to a long asymmetric form at a strongly detuned resonator. In consequence, the relative bandwidth of the MIR radiation can be set as low as 0.3 %. Distinct oscillations of the FEL power during a macro-pulse have been observed at intermediate detuning values. This behavior is attributed to the nonlinear electron-light interaction in the FEL oscillator, modulating the gain provided by the free-electron medium, and thus resulting in the formation of regularly spaced sub-pulses within the ps-short FEL micro-pulse.

On the one hand, the measured characteristics are in line with observations at previous IR FELs [Col82; Jar93] and have to be taken into account in time-resolved experiments. Note that a single-pass X-ray FEL working without resonator [McN10] does not provide this tuning option. On the other hand, the performed Maxwell-Lorentz simulations of the emitted optical field, confirming the sub-pulse occurence and power oscillations, shed light on the fundamental interactions within the free-electron laser [Col90]. Known from other nonlinear dynamical systems [Man72], the self-sustained oscillations represent a limit-cycle solution of the differential equations.

Benchmarking of the homodyne IR-VIS SFG spectroscopy has been performed on polar dielectric materials providing strong second-order optical susceptibilities $\chi^{(2)}$. In the case of 4H-SiC, a spectrally broad Reststrahlen band was observed in the IR reflectivity, enclosed by the transverse and longitudinal optical phonon. Whereas resonant enhancement of the SFG is expected at vibrational modes possessing both IR and Raman activity, the strongest intensity in the spectra has been observed in the vicinity of the dipole-forbidden lattice vibration. The results were rationalized in terms of contributions from nonlinear and linear optical effects, yielding that the dispersive Fresnel factor as well as the phase mismatch between incident and generated optical waves strongly modify the SFG spectra. Similarly, the multi-phonon crystal of α-quartz showed a bulk-originating SFG response.

The results emphasize the different factors in the vibrational SFG signal when using non-centrosymmetric crystals. In this case, the resonant enhancement at certain phonon modes might be obscured due to the dominating linear optical properties of the medium [Bar94; Liu08a]. Moreover, the coherent nature of the SFG process limits the probed material volume, as a coherence length of at maximum 20 µm has been determined. Thus, even bulk-allowed SFG is restricted to a region close to the surface. Azimuth- and polarization-dependent measurements proved to be a reliable method to determine the symmetry of the crystal's quadratic susceptibility tensor. Applications might include the identification of structural or magnetic phase transitions in van der Waals heterostructures or ferroic crystals [Fie00; Li16].

Surface phonon modes hybridizing with the incident electromagnetic wave, i.e. phonon polaritons, have emerged as a way to manipulate the local electric field [Cal15], which is promising to enhance nonlinear optical effects in the MIR range. Employing polariton modes confined in sub-diffractional nanostructures of a polar dielectric material, manipulation of the SFG response at distinct frequencies has been observed, corresponding to the monopolar and dipolar modes of the nanoresonators. Further, the spectral sensitivity of the polaritonic field enhancement on the nanostructure geometry has been used in far-field SFG microscopy. In contrast to linear IR reflectivity images, an enhanced lateral resolution in the nonlinear SFG maps was achieved.

In a first attempt, the presented imaging of the nanophotonic structures extends the SFG microscopy beyond the IR wavelength $\lambda = 3.85\,\mu\text{m}$ [Han19] to the long-wave regime owing to the FEL IR source. While the applied scanning-probe approach of tightly focused beams has been capable of at best 10 µm resolution, the envionised method of wide-field microscopy will allow for spatial detection below the IR diffraction limit [Hof02; Chu13]. Then, studies might resolve e.g. molecular adsorbate structures [Nak09] or electrochemical interfaces [Liu14] with vibrational contrast.

Finally, the non-equilibrium dynamics of the IR-induced electric polarization of the material, leading to sum-frequency emission after upconversion with the VIS radiation, has been probed in time-domain SFG spectroscopy. There, the free-induction decay of the polarization is caused by a lost of the coherence. Depending on the excitation frequency, a faster dephasing was observed off-resonance ($T_2 = 0.3\,\text{ps}$) compared to the resonant case, with a factor ~ 10 in the time constants. Further, a narrowing of the resonance in the transient SFG spectra has been revealed at large time delays. Although the measured resonance has been due to the Fresnel factor, closely spaced vibrational modes in general might be better resolved in SFG spectroscopy when IR and VIS pulse are time-delayed, suppressing the non-resonant $\chi^{(2)}$-contribution.

The implemented timing post-correction demonstrated an increase of the temporal resolution on the sub-ps time scale. Further, time-domain SFG spectroscopy, although complementary to the frequency-domain measurements, can provide more detailed information about the lineshapes, comprising contributions from vibrational population decay and pure dephasing [GS91], when appropriate laser parameters are used [Rok03; Bor05].

In perspective, the implemented IR-VIS frequency-mixing setup allows for vibrational SFG spectroscopy with high spectral and temporal resolution, covering the entire molecular fingerprint region and extending down to low-energy phonon modes at 25 meV. Utilizing forthcoming higher power levels of the VIS radiation will allow for a better signal-to-noise ratio, enabling surface-sensitive vibrational spectroscopy. Thus, besides solid-state systems, molecules adsorbed on surfaces, the interfacial structure of liquids, or the electrochemistry of catalysts becomes accessible for all-optical investigations. Also, the dynamics of adsorption/desorption processes or chemical reactions could be studied with the provided correct time-delay information.

Appendix

A.1 Application of Group Theory to 4H-SiC

The symmetry properties of the lattice vibrations are classified by the point group of the crystal. Besides the identification of the lattice modes, the IR and Raman activity of the individual modes can be derived from a group theoretical analysis. Here, the case of uniaxial 4H-SiC is considered. The character table for the corresponding point group $6mm$ (Hermann-Mauguin) or C_{6v} (Schoenflies notation), respectively, is given in Tab. A.1.

Tab. A.1 Character table of point group $6mm$. Symmetry operations are stated in the first row, the irreducible representations are listed in the first column. Linear and quadratic basis functions are also given. Taken from Ref. [Dre08].

	E	C_2	$2C_3$	$2C_6$	$3\sigma_\mathrm{v}$	$3\sigma_\mathrm{d}$	linear functions, rotations	quadratic functions
A_1	1	1	1	1	1	1	z	x^2+y^2, z^2
A_2	1	1	1	1	−1	−1	R_z	
B_1	1	−1	1	−1	1	−1		
B_2	1	−1	1	−1	−1	1		
E_1	2	−2	−1	1	0	0	$(x,y)(R_x,R_y)$	(xz,yz)
E_2	2	2	−1	−1	0	0		(x^2y^2,xy)

The lattice vibrations of 4H-SiC obey the irreducible representations $4(A_1+B_2+E_1+E_2)$ [Pat68]. The IR activity of a certain phonon mode requires a permanent electric dipole moment, which changes under transition from the ground to the excited state. Thus, only the symmetry classes with a nonzero linear function are active in IR absorption, in this case, A_1 and E_1. Whereas the polarization of the E_1 modes is within the basal plane, the A_1 modes are polarized parallel to the optic axis. According to Ref. [Pat68], six IR-active lines are expected, with $2A_1+4E_1$.

The selection rule for the (first-order) Raman effect asks for a change in the (second-order) polarizability tensor. Therefore, irreducible representations with a quadratic function are relevant, being A_1, E_1 and E_2. The Raman-active modes are $3A_1+3E_1+4E_2$ [Fel68].

To observe vibrational modes in an SFG spectrum, both IR and Raman activity are requried. Hence, only A_1 and E_1-type lattice vibrations of 4H-SiC can contribute to a

resonant enhancement of the second-order susceptibility $\chi^{(2)}$. The necessary polarization conditions are obtained from the involved basis functions in the character table [Dre08].

A.2 Calculation of Electron and Optical Pulse Dynamics in an FEL Oscillator

The motion of the accelerated charges and the evolution of the optical power within the FEL oscillator are determined by the relativistic Maxwell-Lorentz equations of Eqs. (2.58) and (2.59) in Sec. 2.4, i.e.

$$\ddot{\zeta}_k = |a| \cos(\zeta_k + \varphi), \tag{A.1}$$

$$\dot{a} = -j \left\langle \mathrm{e}^{-\mathrm{i}\zeta_k} \right\rangle . \tag{A.2}$$

These are valid for weak and strong optical fields $a = |a|\mathrm{e}^{\mathrm{i}\varphi}$ and couple the dynamics of the electron particles, each with phase ζ_k and velocity $\nu_k = \dot{\zeta}_k$, with the development of the electromagnetic field via a nonlinear interaction. The theory has been developed by Colson at Stanford University [Col77] after the first experimental demonstration of the FEL in the 1970s and is described in detail in Ref. [Col90], including the assumptions made. To obtain the emitted optical pulse structure, see Fig. 5.5, and the electron phase space diagram, Fig. 2.7, the set of ordinary differential equations (ODEs) Eqs. (A.1) and (A.2) for the 2D FEL simulations is solved by numerical integration. All parameters are dimensionless and explained in Sec. 5.2.2. A script for calculation with Julia is given below. The Julia language [Bez17] has proven to be (about a factor of 10) faster in the performance than Matlab due to the demanding computation of the ODEs.

```
# ODE function
function fel(dy,y,p,t)

    nZ = Int(p[1]);
    N = Int(p[2]);
    j = p[3:end];

    dy[1:nZ*N] = y[nZ*N+1:2*nZ*N];  # ODE for zeta
    dy[nZ*N+1:2*nZ*N] = kron(y[2*nZ*N+1:2*nZ*N+nZ],ones(N,1)).*cos.(y[1:nZ*N
        ]+kron(y[2*nZ*N+nZ+1:2*nZ*N+2*nZ],ones(N,1))); # ODE for nu

    for zInd = 1:nZ
       indRange = (1+(zInd-1)*N):(N+(zInd-1)*N); # indices of electrons per
           z point
       dy[2*nZ*N+zInd] = -j[zInd]*mean(cos.(y[indRange].+y[2*nZ*N+nZ+zInd]))
           ; # ODE for a
       dy[2*nZ*N+nZ+zInd] = j[zInd]/y[2*nZ*N+zInd]*mean(sin.(y[indRange].+ y
           [2*nZ*N+nZ+zInd])); # ODE for phi
    end
end
```

```
# necessary packages
import Pkg
Pkg.add("Plots")
Pkg.add("Statistics")
Pkg.add("DifferentialEquations")
using Plots
using Statistics
using DifferentialEquations

# definitions
N = 50; # number of sample electrons per z point
zeta0 = range(-pi/2,3/2*pi,length = N)'; # initial phase zeta of electrons
zetaSigma = 1e-4; # random phase noise
nu0 = 2.6; # initial velocity nu of electrons
a0 = 1e-4; # initial amplitude a of optical field
phi0 = 0; # inital phase phi of optical field
j0 = 5; # electron current
jSigma = 2; # width of current profile
n = 500; # number of undulator passes
Q = 20; # cavity quality factor
W = 4; # width of z axis

tauStep = 0.05; # integration time step per undulator pass
tau = 0:tauStep:1; # integration axis
nTimes = length(tau)-1;

zResFac = 5;
zStep = timeStep/zResFac; # z axis step
z = -W/2:zStep:(W/2-timeStep); # z axis
zTimes = length(z);
z0 = 0.5; # peak position
d = 0.01; # cavity detuning
dInt = Int(d/zStep); # detuning integer
j = j0*exp.(-(z.-z0).^2/(2*jSigma^2)); # Gaussian electron bunch profile
j[j.<0] .= 0;

# preallocations
# variables during an undulator pass
zetaStep = zeros(nTimes+1,zTimes*N);
nuStep = zeros(nTimes+1,zTimes*N);
aStep = zeros(nTimes+1,zTimes);
phiStep = zeros(nTimes+1,zTimes);
tStep = zeros(nTimes+1,1);

# variables over multiple undulator passes
a = zeros(n+1,zTimes);
phi = zeros(n+1,zTimes);
P = zeros(n+1,zTimes); # optical power

# initialization
aStep[1,:] = a0*ones(1,zTimes);
phiStep[1,:] = phi0*ones(1,zTimes);

a[1,:] = aStep[1,:];
phi[1,:] = phiStep[1,:];
P[1,:] = a[1,:].^2;

# calculation
for nInd = 2:n+1 # multiple undulator passes
```

```
zetaStep[1,:] = repeat(zeta0,1,zTimes) + zetaSigma*randn(1,zTimes*N);
nuStep[1,:] = nu0*ones(1,zTimes*N);

aTemp = a[nInd-1,:];
phiTemp = phi[nInd-1,:];
if nInd > 2
   aTemp = circshift(aTemp,dInt); # detuning of optical field
   phiTemp = circshift(phiTemp,dInt);
end

aStep[1,:] = aTemp;
phiStep[1,:] = phiTemp;

for tInd = 2:nTimes+1 # integration steps during an undulator pass
   zetaInitTemp = zetaStep[tInd-1,:];
   nuInitTemp = nuStep[tInd-1,:];
   if tInd > 2
      zetaInitTemp = circshift(zetaInitTemp,-N*zResFac*1); # slippage of
          electrons
      nuInitTemp = circshift(nuInitTemp,-N*zResFac*1);
   end
   zetaInit = zetaInitTemp;
   nuInit = nuInitTemp;

   aInit = aStep[tInd-1,:];
   phiInit = phiStep[tInd-1,:];
   jStep = circshift(j,-1*zResFac*(tInd-2));

   # set ODE problem
   y0 = vcat(zetaInit, nuInit, aInit, phiInit);
   tspan = (tau[tInd-1], tau[tInd]);
   p = vcat(zTimes, N, jStep);
   prob = ODEProblem(fel,y0,tspan,p);
   alg = DP5(); # explicit Runge-Kutta formula

   # solve ODE problem
   sol = solve(prob,alg)
   y = sol.u[end];
   t = sol.t[end];

   # allocation of solution
   zetaTemp = y[1:zTimes*N];
   zetaTemp[zetaTemp.>3/2*pi] = zetaTemp[zetaTemp.>3/2*pi] .- 2*pi; #
       restrict phase to [-pi/2, 3/2*pi] range
   zetaTemp[zetaTemp.<-1/2*pi] = zetaTemp[zetaTemp.<-1/2*pi] .+ 2*pi;
   zetaStep[tInd,:] = zetaTemp;
   nuStep[tInd,:] =  y[(zTimes*N+1):(2*zTimes*N)];
   aStep[tInd,:] = y[(2*zTimes*N+1):(2*zTimes*N+zTimes)];
   phiStep[tInd,:] = y[(2*zTimes*N+zTimes+1):(2*zTimes*N+2*zTimes)];
   tStep[tInd] = t;
end

aTemp = aStep[nTimes+1,:];
pTemp = aTemp.^2*exp(-1/Q);
a[nInd,:] = sqrt.(pTemp);
phi[nInd,:] = phiStep[nTimes+1,:];
P[nInd,:]= pTemp;
```

```
    println("n=", nInd-1)
end

# phase space plot (evolution of electron bunching during pass)
C(g::ColorGradient) = RGB[g[z] for z=range(0,1,length = nTimes+1)]; #
    create color gradient
g = :plasma_r; # colormap
col = cgrad(g) |> C;
zSel = Int(zTimes/2); # selected z point
p = plot()
for i = 1:nTimes+1
    plot!(zetaStep[i,(zSel-1)*N+1:(zSel-1)*N+N],nuStep[i,(zSel-1)*N+1:(zSel
        -1)*N+N], color = col[i], markershape = :circle, markersize = 4,
        markerstrokecolor = false, linecolor = false, xlims = (-pi/2, 3/2*pi
        ), xlabel = "\\zeta", ylabel = "\\nu", title = "Phase Space")
end
display(p)

# optical power plot (evolution of subpulses over multiple passes)
heatmap(z,1:n+1,P)
title!("Optical Power")
xlabel!("z"), ylabel!("n")
```

A.3 Abbreviations

BOC	balanced optical cross-correlation
FEL	free-electron laser
FO	fiber oscillator
IR	infrared
NIR	near-infrared (ISO: $\lambda = 0.78\,\mu\text{m} - 3\,\mu\text{m}$)
MIR	mid-infrared (ISO: $\lambda = 3\,\mu\text{m} - 50\,\mu\text{m}$)
FIR	far-infrared (ISO: $\lambda = 50\,\mu\text{m} - 1000\,\mu\text{m}$)
linac	linear accelerator
PID	proportional - integral - derivative
PLL	phase-locked loop
PMT	photo-multiplier tube
RF	radio frequency
SFG	sum-frequency generation
VIS	visible

Publications

Author ORCID: 0000-0002-0946-1044

Journal Articles

R. Kiessling, W. B. Colson, S. Gewinner, W. Schöllkopf, M. Wolf, and A. Paarmann, "Femtosecond single-shot timing and direct observation of subpulse formation in an infrared free-electron laser", *Phys. Rev. Accel. Beams* 21 (2018), 080702, DOI: 10.1103/PhysRevAccelBeams.21.080702 (open access).

R. Kiessling, Y. Tong, A. J. Giles, S. Gewinner, W. Schöllkopf, J. D. Caldwell, M. Wolf, and A. Paarmann, "Surface Phonon Polariton Resonance Imaging Using Long-Wave Infrared-Visible Sum-Frequency Generation Microscopy", *ACS Photonics* 6 (2019), 3017, DOI: 10.1021/acsphotonics.9b01335 (open access).

R. Kiessling, M. Wolf, and A. Paarmann, "Resonance Narrowing in Time-Domain Sum-Frequency Generation", *in preparation.*

Conference Proceeding

R. Kiessling, S. Gewinner, W. Schöllkopf, M. Wolf, and A. Paarmann, "Synchronized Mid-Infrared Pulses at the Fritz Haber Institute IR-FEL", *Proc. 38th International Free-Electron Laser Conference, Santa Fe, NM, USA* (2017), 188, DOI: 10.18429/JACoW-FEL2017-MOP059 (open access).

Bibliography

[Abd75] G. B. Abdullaev, K. R. Allakhverdiev, L. A. Kulevskii, A. M. Prokhorov, E. Y. Salaev, A. D. Savel'ev, and V. V. Smirnov, "Parametric conversion of infrared radiation in a GaSe crystal", *Sov. J. Quantum Electron.* 5 (1975), 665, DOI: 10.1070/qe1975v005n06abeh011312.

[Ado00] B. Adolph and F. Bechstedt, "Influence of crystal structure and quasiparticle effects on second-harmonic generation: Silicon carbide polytypes", *Phys. Rev. B* 62 (2000), 1706, DOI: 10.1103/PhysRevB.62.1706.

[Ali96] A. P. Alivisatos, "Semiconductor Clusters, Nanocrystals, and Quantum Dots", *Science* 271 (1996), 933, DOI: 10.1126/science.271.5251.933.

[And03] M. S. Anderson, "Enhanced infrared absorption with dielectric nanoparticles", *Appl. Phys. Lett.* 83 (2003), 2964, DOI: 10.1063/1.1615317.

[Arn10] H. Arnolds and M. Bonn, "Ultrafast surface vibrational dynamics", *Surf. Sci. Rep.* 65 (2010), 45, DOI: 10.1016/j.surfrep.2009.12.001.

[Aut18] M. Autore, P. Li, I. Dolado, F. J. Alfaro-Mozaz, R. Esteban, A. Atxabal, F. Casanova, L. E. Hueso, P. Alonso-González, J. Aizpurua, A. Y. Nikitin, S. Vélez, and R. Hillenbrand, "Boron nitride nanoresonators for phonon-enhanced molecular vibrational spectroscopy at the strong coupling limit", *Light Sci. Appl.* 7 (2018), 17172, DOI: 10.1038/lsa.2017.172.

[Azi09] A. Azima, S. Düsterer, P. Radcliffe, H. Redlin, N. Stojanovic, W. Li, H. Schlarb, J. Feldhaus, D. Cubaynes, M. Meyer, J. Dardis, P. Hayden, P. Hough, V Richardson, E. T. Kennedy, and J. T. Costello, "Time-resolved pump-probe experiments beyond the jitter limitations at FLASH", *Appl. Phys. Lett.* 94 (2009), 144102, DOI: 10.1063/1.3111789.

[Bac05] E. H. G. Backus, A. Eichler, A. W. Kleyn, and M. Bonn, "Real-Time Observation of Molecular Motion on a Surface", *Science* 310 (2005), 1790, DOI: 10.1126/science.1120693.

[Bak94] R. J. Bakker, D. A. Jaroszynski, A. F. G. van der Meer, D. Oepts, and P. W. van Amersfoort, "Short-Pulse Effects in a Free-Electron Laser", *IEEE J. Quantum. Electron.* 30 (1994), 1635, DOI: 10.1109/3.299495.

[Bar01] S. Baroni, S. de Gironcoli, A. Dal Corso, and P. Giannozzi, "Phonons and related crystal properties from density-functional perturbation theory", *Rev. Mod. Phys.* 73 (2001), 515, DOI: 10.1103/RevModPhys.73.515.

[Bar94] M. Barmentlo, G. 't Hooft, E. Eliel, E. van der Ham, Q. Vrehen, A. van der Meer, and P. van Amersfoort, "Sum-frequency generation with a free-electron laser: A study of gallium phosphide", *Phys. Rev. A* 50 (1994), R14, DOI: 10.1103/PhysRevA.50.R14.

[Bel72] M. I. Bell, "Frequency Dependence of Miller's Rule for Nonlinear Susceptibilities", *Phys. Rev. B* 6 (1972), 516, DOI: 10.1103/PhysRevB.6.516.

[Ber06] C. Berger, Z. Song, X. Li, X. Wu, N. Brown, C. Naud, D. Mayou, T. Li, J. Hass, A. N. Marchenkov, E. H. Conrad, P. N. First, and W. A. de Heer, "Electronic Confinement and Coherence in Patterned Epitaxial Graphene", *Science* 312 (2006), 1191, DOI: 10.1126/science.1125925.

[Bez17] J. Bezanson, A. Edelman, S. Karpinski, and V. B. Shah, "Julia: A fresh approach to numerical computing", *SIAM Review* 59 (2017), 65, DOI: 10.1137/141000671, URL: https://julialang.org.

[Bha11] J. Bhattacharyya, M. Wagner, S. Zybell, S. Winnerl, D. Stehr, M. Helm, and H. Schneider, "Simultaneous time and wavelength resolved spectroscopy under two-colour near infrared and terahertz excitation", *Rev. Sci. Instrum.* 82 (2011), 103107, DOI: 10.1063/1.3653394.

[Bla15] J. Blau, K. Cohn, and W. B. Colson, "Four-dimensional models of free electron laser amplifiers and oscillators", *Proc. International Free Electron Laser Conference 2015* (2015), 607, DOI: 10.18429/JACoW-FEL2015-WEP008.

[Bon00] M. Bonn, C. Hess, S. Funk, J. H. Miners, B. N. J. Persson, M. Wolf, and G. Ertl, "Femtosecond Surface Vibrational Spectroscopy of CO Adsorbed on Ru(001) during Desorption", *Phys. Rev. Lett.* 84 (2000), 4653, DOI: 10.1103/PhysRevLett.84.4653.

[Bor05] A. N. Bordenyuk, H. Jayathilake, and A. V. Benderskii, "Coherent Vibrational Quantum Beats as a Probe of Langmuir-Blodgett Monolayers", *J. Phys. Chem. B* 109 (2005), 15941, DOI: 10.1021/jp051632g.

[Bor12] M. Born and T. von Kármán, "Über Schwingungen in Raumgittern", *Phys. Z.* 13 (1912), 297.

[Bor98] M. Born and K. Huang, *Dynamical Theory of Crystal Lattices*, Oxford: Oxford University Press, 1998.

[Bor99] M. Born and E. Wolf, *Principles of Optics: Electromagnetic Theory of Propagation, Interference and Diffraction of Light*, Cambridge: Cambridge University Press, 1999, DOI: 10.1017/CBO9781139644181.

[Boy08] R. W. Boyd, *Nonlinear Optics*, Burlington, MA: Academic Press, 2008, DOI: 10.1016/B978-0-12-369470-6.00001-0.

[Boy86] G. T. Boyd, Y. R. Shen, and T. W. Hänsch, "Continuous-wave second-harmonic generation as a surface microprobe", *Opt. Lett.* 11 (1986), 97, DOI: 10.1364/OL.11.000097.

[Bru82] P. Brueesch, *Phonons: Theory and Experiments I*, Berlin: Springer, 1982, DOI: 10.1007/978-3-642-81781-6.

[Bru86] P. Brueesch, *Phonons: Theory and Experiments II*, Berlin: Springer, 1986, DOI: 10.1007/978-3-642-52263-5.

[Cal13] J. D. Caldwell, O. J. Glembocki, Y. Francescato, N. Sharac, V. Giannini, F. J. Bezares, J. P. Long, J. C. Owrutsky, I. Vurgaftman, J. G. Tischler, V. D. Wheeler, N. D. Bassim, L. M. Shirey, R. Kasica, and S. A. Maier, "Low-Loss, Extreme Subdiffraction Photon Confinement via Silicon Carbide Localized Surface Phonon Polariton Resonators", *Nano Lett.* 13 (2013), 3690, DOI: 10.1021/nl401590g.

[Cal15] J. D. Caldwell, L. Lindsay, V. Giannini, I. Vurgaftman, T. L. Reinecke, S. A. Maier, and O. J. Glembocki, "Low-loss, infrared and terahertz nanophotonics using surface phonon polaritons", *Nanophotonics* 4 (2015), 44, DOI: 10.1515/nanoph-2014-0003.

[Cav05] A. L. Cavalieri, D. M. Fritz, S. H. Lee, P. H. Bucksbaum, D. A. Reis, J. Rudati, D. M. Mills, P. H. Fuoss, G. B. Stephenson, C. C. Kao, D. P. Siddons, D. P. Lowney, A. G. MacPhee, D. Weinstein, R. W. Falcone, R. Pahl, J. Als-Nielsen, C. Blome, S. Düsterer, R. Ischebeck, et al., "Clocking Femtosecond X Rays", *Phys. Rev. Lett.* 94 (2005), 114801, DOI: 10.1103/PhysRevLett.94.114801.

[Cha11] H. N. Chapman, P. Fromme, A. Barty, T. A. White, R. A. Kirian, A. Aquila, M. S. Hunter, J. Schulz, D. P. DePonte, U. Weierstall, R. B. Doak, F. R. N. C. Maia, A. V. Martin, I. Schlichting, L. Lomb, N. Coppola, R. L. Shoeman, S. W. Epp, R. Hartmann, D. Rolles, et al., "Femtosecond X-ray protein nanocrystallography", *Nature* 470 (2011), 73, DOI: 10.1038/nature09750.

[Che14] Y. Chen, Y. Francescato, J. D. Caldwell, V. Giannini, T. W. W. Maß, O. J. Glembocki, F. J. Bezares, T. Taubner, R. Kasica, M. Hong, and S. A. Maier, "Spectral Tuning of Localized Surface Phonon Polariton Resonators for Low-Loss Mid-IR Applications", *ACS Photonics* 1 (2014), 718, DOI: 10.1021/ph500143u.

[Che94] J. Chen, Z. H. Levine, and J. W. Wilkins, "Linear and nonlinear optical properties of four polytypes of SiC", *Phys. Rev. B* 50 (1994), 11514, DOI: 10.1103/PhysRevB.50.11514.

[Chu13] C.-Y. Chung, J. Boik, and E. O. Potma, "Biomolecular Imaging with Coherent Nonlinear Vibrational Microscopy", *Annu. Rev. Phys. Chem.* 64 (2013), 77, DOI: 10.1146/annurev-physchem-040412-110103.

[Cim06] K. Cimatu and S. Baldelli, "Sum Frequency Generation Microscopy of Microcontact-Printed Mixed Self-Assembled Monolayers", *J. Phys. Chem. B* 110 (2006), 1807, DOI: 10.1021/jp0562779.

[Col77] W. B. Colson, "One-body electron dynamics in a free electron laser", *Phys. Lett. A* 64 (1977), 190, DOI: 10.1016/0375-9601(77)90712-5.

[Col82] W. B. Colson, "Optical Pulse Evolution in the Stanford Free-Electron Laser and in a Tapered Wiggler", *Free-Electron Generators of Coherent Radiation*, ed. by S. F. Jacobs, G. T. Moore, H. S. Pilloff, M. Sargent III, M. O. Scully, and R. Spitzer, vol. 8, Physics of Quantum Electronics, Reading, MA: Addison-Wesley, 1982, 457.

[Col90] W. B. Colson, "Classical Free Electron Laser Theory", *Free Electron Lasers*, ed. by W. B. Colson, C. Pellegrini, and A. Renieri, vol. 6, Laser Handbook, Amsterdam: North Holland, 1990, 115.

[Cox10] J. A. Cox, A. H. Nejadmalayeri, J. Kim, and F. X. Kärtner, "Complete characterization of quantum-limited timing jitter in passively mode-locked fiber lasers", *Opt. Lett.* 35 (2010), 3522, DOI: 10.1364/OL.35.003522.

[Dai14] S. Dai, Z. Fei, Q. Ma, A. S. Rodin, M. Wagner, A. S. McLeod, M. K. Liu, W. Gannett, W. Regan, K. Watanabe, T. Taniguchi, M. Thiemens, G. Dominguez, A. H. C. Neto, A. Zettl, F. Keilmann, P. Jarillo-Herrero, M. M. Fogler, and D. N. Basov, "Tunable Phonon Polaritons in Atomically Thin van der Waals Crystals of Boron Nitride", *Science* 343 (2014), 1125, DOI: 10.1126/science.1246833.

[Dai15] S. Dai, Q. Ma, T. Andersen, A. McLeod, Z. Fei, M. Liu, M. Wagner, K. Watanabe, T. Taniguchi, M. Thiemens, F. Keilmann, P. Jarillo-Herrero, M. Fogler, and D. Basov, "Subdiffractional focusing and guiding of polaritonic rays in a natural hyperbolic material", *Nat. Commun.* 6 (2015), 6963, DOI: 10.1038/ncomms7963.

[Dea77] D. A. G. Deacon, L. R. Elias, J. M. J. Madey, G. J. Ramian, H. A. Schwettman, and T. I. Smith, "First Operation of a Free-Electron Laser", *Phys. Rev. Lett.* 38 (1977), 892, DOI: 10.1103/PhysRevLett.38.892.

[Deb99] A. Debernardi, C. Ulrich, K. Syassen, and M. Cardona, "Raman linewidths of optical phonons in 3C-SiC under pressure: First-principles calculations and experimental results", *Phys. Rev. B* 59 (1999), 6774, DOI: 10.1103/PhysRevB.59.6774.

[Dek03] T. Dekorsy, V. A. Yakovlev, W. Seidel, M. Helm, and F. Keilmann, "Infrared-Phonon-Polariton Resonance of the Nonlinear Susceptibility in GaAs", *Phys. Rev. Lett.* 90 (2003), 055508, DOI: 10.1103/PhysRevLett.90.055508.

[Din09] F. Ding, Q. Zhong, M. R. Brindza, J. T. Fourkas, and R. A. Walker, "Ti:sapphire, broadband vibrational sum-frequency generation spectrometer with a counter-propagating geometry", *Opt. Express* 17 (2009), 14665, DOI: 10.1364/OE.17.014665.

[Dlo91] D. D. Dlott and M. D. Fayer, "Applications of Infrared Free-Electron Lasers: Basic Research on the Dynamics of Molecular Systems", *IEEE J. Quantum Electron.* 27 (1991), 2697, DOI: 10.1109/3.104151.

[Dmi99] V. G. Dmitriev, G. G. Gurzadyan, and D. N. Nikogosyan, *Handbook of Nonlinear Optical Crystals*, Berlin: Springer, 1999, DOI: 10.1007/978-3-540-46793-9.

[Dre08] M. S. Dresselhaus, G. Dresselhaus, and A. Jorio, *Group Theory: Application to the Physics of Condensed Matter*, Berlin: Springer, 2008, DOI: 10.1007/978-3-540-32899-5.

[Dru87] P. Drude, "Ueber die Gesetze der Reflexion und Brechung des Lichtes an der Grenze absorbirender Krystalle", *Ann. Phys. (Berl.)* 268 (1887), 584, DOI: 10.1002/andp.18872681205.

[Ein07] A. Einstein, "Die Plancksche Theorie der Strahlung und die Theorie der spezifischen Wärme", *Ann. Phys. (Berl.)* 327 (1907), 180, DOI: 10.1002/andp.19063270110.

[Eli95] E. R. Eliel, E. W. M. van der Ham, Q. H. F. Vrehen, G. W. 't Hooft, M. Barmentlo, J. M. Auerhammer, A. F. G. van der Meer, and P. W. van Amersfoort, "Studies of interfacial regions by sum-frequency generation with a free-electron laser", *Appl. Phys. A* 60 (1995), 113, DOI: 10.1007/bf01538234.

[Fau66] W. L. Faust and C. H. Henry, "Mixing of Visible and Near-Resonance Infrared Light in GaP", *Phys. Rev. Lett.* 17 (1966), 1265, DOI: 10.1103/PhysRevLett.17.1265.

[Fel68] D. W. Feldman, J. H. Parker, W. J. Choyke, and L. Patrick, "Phonon Dispersion Curves by Raman Scattering in SiC, Polytypes $3C$, $4H$, $6H$, $15R$, and $21R$", *Phys. Rev.* 173 (1968), 787, DOI: 10.1103/PhysRev.173.787.

[Fie00] M. Fiebig, D. Fröhlich, K. Kohn, S. Leute, T. Lottermoser, V. V. Pavlov, and R. V. Pisarev, "Determination of the Magnetic Symmetry of Hexagonal Manganites by Second Harmonic Generation", *Phys. Rev. Lett.* 84 (2000), 5620, DOI: 10.1103/PhysRevLett.84.5620.

[Fis17] M. P. Fischer, J. Bühler, G. Fitzky, T. Kurihara, S. Eggert, A. Leitenstorfer, and D. Brida, "Coherent field transients below 15 THz from phase-matched difference frequency generation in 4H-SiC", *Opt. Lett.* 42 (2017), 2687, DOI: 10.1364/OL.42.002687.

[Fra06] A. Franzen, *ComponentLibrary*, 2006, URL: http://www.gwoptics.org/ComponentLibrary/.

[Fra61] P. A. Franken, A. E. Hill, C. W. Peters, and G. Weinreich, "Generation of Optical Harmonics", *Phys. Rev. Lett.* 7 (1961), 118, DOI: 10.1103/PhysRevLett.7.118.

[Fre11] H.-J. Freund, G. Meijer, M. Scheffler, R. Schlögl, and M. Wolf, "CO Oxidation as a Prototypical Reaction for Heterogeneous Processes", *Angew. Chem. Int. Ed.* 50 (2011), 10064, DOI: 10.1002/anie.201101378.

[Fuc65] R. Fuchs and K. L. Kliewer, "Optical Modes of Vibration in an Ionic Crystal Slab", *Phys. Rev.* 140 (1965), A2076, DOI: 10.1103/PhysRev.140.A2076.

[GS87] P. Guyot-Sionnest, J. H. Hunt, and Y. R. Shen, "Sum-frequency vibrational spectroscopy of a Langmuir film: Study of molecular orientation of a two-dimensional system", *Phys. Rev. Lett.* 59 (1987), 1597, DOI: 10.1103/PhysRevLett.59.1597.

[GS90] P. Guyot-Sionnest, P. Dumas, Y. J. Chabal, and G. S. Higashi, "Lifetime of an adsorbate-substrate vibration: H on Si(111)", *Phys. Rev. Lett.* 64 (1990), 2156, DOI: 10.1103/PhysRevLett.64.2156.

[GS91] P. Guyot-Sionnest, "Coherent processes at surfaces: Free-induction decay and photon echo of the Si-H stretching vibration for H/Si(111)", *Phys. Rev. Lett.* 66 (1991), 1489, DOI: 10.1103/PhysRevLett.66.1489.

[Gah08] C. Gahl, A. Azima, M. Beye, M. Deppe, K. Döbrich, U. Hasslinger, F. Hennies, A. Melnikov, M. Nagasono, A. Pietzsch, M. Wolf, W. Wurth, and A. Föhlisch, "A femtosecond X-ray/optical cross-correlator", *Nat. Photonics* 2 (2008), 165, DOI: 10.1038/nphoton.2007.298.

[Gan97] F. Ganikhanov and F. Vallee, "Coherent TO phonon relaxation in GaAs and InP", *Phys. Rev. B* 55 (1997), 15614, DOI: 10.1103/PhysRevB.55.15614.

[Ger74] F. Gervais and B. Piriou, "Anharmonicity in several-polar-mode crystals: adjusting phonon self-energy of LO and TO modes in Al_2O_3 and TiO_2 to fit infrared reflectivity", *J. Phys. C* 7 (1974), 2374, DOI: 10.1088/0022-3719/7/13/017.

[Ger75] F. Gervais and B. Piriou, "Temperature dependence of transverse and longitudinal optic modes in the α and β phases of quartz", *Phys. Rev. B* 11 (1975), 3944, DOI: 10.1103/PhysRevB.11.3944.

[Gho99] G. Ghosh, "Dispersion-equation coefficients for the refractive index and birefringence of calcite and quartz crystals", *Opt. Commun.* 163 (1999), 95, DOI: 10.1016/S0030-4018(99)00091-7.

[Gia91] P. Giannozzi, S. de Gironcoli, P. Pavone, and S. Baroni, "Ab initio calculation of phonon dispersions in semiconductors", *Phys. Rev. B* 43 (1991), 7231, DOI: 10.1103/PhysRevB.43.7231.

[Gre02] J.-J. Greffet, R. Carminati, K. Joulain, J.-P. Mulet, S. Mainguy, and Y. Chen, "Coherent emission of light by thermal sources", *Nature* 416 (2002), 61, DOI: 10.1038/416061a.

[Grg12] I. Grguras, A. R. Maier, C. Behrens, T. Mazza, T. J. Kelly, P. Radcliffe, S. Düsterer, A. K. Kazansky, N. M. Kabachnik, T. Tschentscher, J. T. Costello, M. Meyer, M. C. Hoffmann, H. Schlarb, and A. L. Cavalieri, "Ultrafast X-ray pulse characterization at free-electron lasers", *Nat. Photonics* 6 (2012), 852, DOI: 10.1038/nphoton.2012.276.

[Hah93] S. J. Hahn and J. K. Lee, "Nonlinear short-pulse propagation in a free-electron laser", *Phys. Rev. E* 48 (1993), 2162, DOI: 10.1103/PhysRevE.48.2162.

[Ham99] E. W. M. van der Ham, Q. H. F. Vrehen, E. R. Eliel, V. A. Yakovlev, E. V. Alieva, L. A. Kuzik, J. E. Petrov, V. A. Sychugov, and A. F. G. van der Meer, "Giant enhancement of sum-frequency yield by surface-plasmon excitation", *J. Opt. Soc. Am. B* 16 (1999), 1146, DOI: 10.1364/JOSAB.16.001146.

[Han19] A. M. Hanninen, R. C. Prince, and E. O. Potma, "Triple Modal Coherent Nonlinear Imaging With Vibrational Contrast", *IEEE J. Sel. Top. Quantum Electron.* 25 (2019), 6800411, DOI: 10.1109/JSTQE.2018.2846030.

[Har09] M. Harb, P. Labéguerie, I. Baraille, and M. Rérat, "Response of low quartz SiO_2 to the presence of an external static electric field: A density functional theory study", *Phys. Rev. B* 80 (2009), 235131, DOI: 10.1103/PhysRevB.80.235131.

[Har13] M. Harmand, R. Coffee, M. R. Bionta, M. Chollet, D. French, D. Zhu, D. M. Fritz, H. T. Lemke, N. Medvedev, B. Ziaja, S. Toleikis, and M. Cammarata, "Achieving few-femtosecond time-sorting at hard X-ray free-electron lasers", *Nat. Photonics* 7 (2013), 215, DOI: 10.1038/nphoton.2013.11.

[Has08] J. Hass, F. Varchon, J. E. Millán-Otoya, M. Sprinkle, N. Sharma, W. A. de Heer, C. Berger, P. N. First, L. Magaud, and E. H. Conrad, "Why Multilayer Graphene on 4H-SiC(000-1) Behaves Like a Single Sheet of Graphene", *Phys. Rev. Lett.* 100 (2008), 125504, DOI: 10.1103/PhysRevLett.100.125504.

[Hes02] C. Hess, M. Wolf, S. Roke, and M. Bonn, "Femtosecond time-resolved vibrational SFG spectroscopy of CO/Ru(001)", *Surf. Sci.* 502-503 (2002), 304, DOI: 10.1016/S0039-6028(01)01968-9.

[Hil02] R. Hillenbrand, T. Taubner, and F. Keilmann, "Phonon-enhanced light–matter interaction at the nanometre scale", *Nature* 418 (2002), 159, DOI: 10.1038/nature00899.

[Hof02] D. M. P. Hoffmann, K. Kuhnke, and K. Kern, "Sum-frequency generation microscope for opaque and reflecting samples", *Rev. Sci. Instrum.* 73 (2002), 3221, DOI: 10.1063/1.1499757.

[Hof94] M. Hofmann, A. Zywietz, K. Karch, and F. Bechstedt, "Lattice dynamics of SiC polytypes within the bond-charge model", *Phys. Rev. B* 50 (1994), 13401, DOI: 10.1103/PhysRevB.50.13401.

[Hor04] D. K. Hore, M. Y. Hamamoto, and G. L. Richmond, "Mid-infrared second-order susceptibility of α-quartz and its application to visible-infrared surface sum-frequency spectroscopy", *J. Chem. Phys.* 121 (2004), 12589, DOI: 10.1063/1.1826055.

[Hor19] D. K. Hore and E. Tyrode, "Probing Charged Aqueous Interfaces Near Critical Angles: Effect of Varying Coherence Length", *J. Phys. Chem. C* 123 (2019), 16911, DOI: 10.1021/acs.jpcc.9b05256.

[Hua94] M.-Z. Huang and W. Y. Ching, "First-principles calculation of second harmonic generation in α-quartz", *Ferroelectrics* 156 (1994), 105, DOI: 10.1080/00150199408215935.

[Hue11] H. Huebener, E. Luppi, and V. Véniard, "Ab initio calculation of many-body effects on the second-harmonic generation spectra of hexagonal SiC polytypes", *Phys. Rev. B* 83 (2011), 115205, DOI: 10.1103/PhysRevB.83.115205.

[Ins15] Instrumentation Technologies, d.d., *Clock Transfer System, Model: Libera Sync 3*, 2015, URL: https://www.i-tech.si/products/libera-sync-3/.

[Jar93] D. A. Jaroszynski, R. J. Bakker, A. F. G. van der Meer, D. Oepts, and P. W. van Amersfoort, "Experimental Observation of Limit-Cycle Oscillations in a Short-Pulse Free-Electron Laser", *Phys. Rev. Lett.* 70 (1993), 3412, DOI: 10.1103/PhysRevLett.70.3412.

[Jar94] D. A. Jaroszynski, R. Prazeres, F. Glotin, and J. M. Ortega, "Two-Color Free-Electron Laser Operation", *Phys. Rev. Lett.* 72 (1994), 2387, DOI: 10.1103/PhysRevLett.72.2387.

[Ji06] N. Ji, K. Zhang, H. Yang, and Y.-R. Shen, "Three-Dimensional Chiral Imaging by Sum-Frequency Generation", *J. Am. Chem. Soc.* 128 (2006), 3482, DOI: 10.1021/ja057775y.

[Juh89] T. Juhasz and W. E. Bron, "Subpicosecond-resolved polariton decay", *Phys. Rev. Lett.* 63 (1989), 2385, DOI: 10.1103/PhysRevLett.63.2385.

[Kai99] R. A. Kaindl, F. Eickemeyer, M. Woerner, and T. Elsaesser, "Broadband phase-matched difference frequency mixing of femtosecond pulses in GaSe: Experiment and theory", *Appl. Phys. Lett.* 75 (1999), 1060, DOI: 10.1063/1.124596.

[Kau12] M. Kauranen and A. V. Zayats, "Nonlinear plasmonics", *Nat. Photonics* 6 (2012), 737, DOI: 10.1038/nphoton.2012.244.

[Kie18] R. Kiessling, W. B. Colson, S. Gewinner, W. Schöllkopf, M. Wolf, and A. Paarmann, "Femtosecond single-shot timing and direct observation of subpulse formation in an infrared free-electron laser", *Phys. Rev. Accel. Beams* 21 (2018), 080702, DOI: 10.1103/PhysRevAccelBeams.21.080702.

[Kie19] R. Kiessling, Y. Tong, A. J. Giles, S. Gewinner, W. Schöllkopf, J. D. Caldwell, M. Wolf, and A. Paarmann, "Surface phonon polariton resonance imaging using long-wave infrared-visible sum-frequency generation microscopy", *ACS Photonics* 6 (2019), 3017, DOI: 10.1021/acsphotonics.9b01335.

[Kit05] C. Kittel, *Introduction to Solid State Physics*, Hoboken, NJ: Wiley, 2005.

[Kli15] P. Kling, E. Giese, R. Endrich, P. Preiss, R. Sauerbrey, and W. P. Schleich, "What defines the quantum regime of the free-electron laser?", *New J. Phys.* 17 (2015), 123019, DOI: 10.1088/1367-2630/17/12/123019.

[Kni95] G. M. H. Knippels, R. F. X. A. M. Mols, A. F. G. van der Meer, D. Oepts, and P. W. van Amersfoort, "Intense Far-Infrared Free-Electron Laser Pulses with a Length of Six Optical Cycles", *Phys. Rev. Lett.* 75 (1995), 1755, DOI: 10.1103/PhysRevLett.75.1755.

[Kni98] G. M. H. Knippels, M. J. van de Pol, H. P. M. Pellemans, P. C. M. Planken, and A. F. G. van der Meer, "Two-color facility based on a broadly tunable infrared free-electron laser and a subpicosecond-synchronized 10-fs-Ti:sapphire laser", *Opt. Lett.* 23 (1998), 1754, DOI: 10.1364/OL.23.001754.

[Kni99] G. M. H. Knippels, X. Yan, A. M. MacLeod, W. A. Gillespie, M. Yasumoto, D. Oepts, and A. F. G. van der Meer, "Generation and Complete Electric-Field Characterization of Intense Ultrashort Tunable Far-Infrared Laser Pulses", *Phys. Rev. Lett.* 83 (1999), 1578, DOI: 10.1103/PhysRevLett.83.1578.

[Kov17] S. Kovalev, B. Green, T. Golz, S. Mährlein, N. Stojanovic, A. S. Fisher, T. Kampfrath, and M. Gensch, "Probing ultra-fast processes with high dynamic range at 4th-generation light sources: Arrival time and intensity binning at unprecedented repetition rates", *Struct. Dyn.* 4 (2017), 024301, DOI: 10.1063/1.4978042.

[Laa11] J. E. Laaser, W. Xiong, and M. T. Zanni, "Time-Domain SFG Spectroscopy Using Mid-IR Pulse Shaping: Practical and Intrinsic Advantages", *J. Phys. Chem. B* 115 (2011), 2536, DOI: 10.1021/jp200757x.

[Lab07] F. L. Labarthet and Y. R. Shen, "Nonlinear Optical Microscopy", *Optical Imaging and Microscopy: Techniques and Advanced Systems*, ed. by P. Toeroek and F.-J. Kao, vol. 87, Optical Sciences, Berlin: Springer, 2007, 237, DOI: 10.1007/978-3-540-69565-3_9.

[Lag07] A. Lagutchev, S. A. Hambir, and D. D. Dlott, "Nonresonant Background Suppression in Broadband Vibrational Sum-Frequency Generation Spectroscopy", *J. Phys. Chem. C* 111 (2007), 13645, DOI: 10.1021/jp075391j.

[Lau71] A. Laubereau, D. von der Linde, and W. Kaiser, "Decay Time of Hot TO Phonons in Diamond", *Phys. Rev. Lett.* 27 (1971), 802, DOI: 10.1103/PhysRevLett.27.802.

[Lau78] A. Laubereau and W. Kaiser, "Vibrational dynamics of liquids and solids investigated by picosecond light pulses", *Rev. Mod. Phys.* 50 (1978), 607, DOI: 10.1103/RevModPhys.50.607.

[Li13] Y. Li, Y. Rao, K. F. Mak, Y. You, S. Wang, C. R. Dean, and T. F. Heinz, "Probing Symmetry Properties of Few-Layer MoS2 and h-BN by Optical Second-Harmonic Generation", *Nano Lett.* 13 (2013), 3329, DOI: 10.1021/nl401561r.

[Li15] P. Li, M. Lewin, A. V. Kretinin, J. D. Caldwell, K. S. Novoselov, T. Taniguchi, K. Watanabe, F. Gaussmann, and T. Taubner, "Hyperbolic phonon-polaritons in boron nitride for near-field optical imaging and focusing", *Nat. Commun.* 6 (2015), 7507, DOI: 10.1038/ncomms8507.

[Li16] D. Li, W. Xiong, L. Jiang, Z. Xiao, H. Rabiee Golgir, M. Wang, X. Huang, Y. Zhou, Z. Lin, J. Song, S. Ducharme, L. Jiang, J.-F. Silvain, and Y. Lu, "Multimodal Nonlinear Optical Imaging of MoS2 and MoS2-Based van der Waals Heterostructures", *ACS Nano* 10 (2016), 3766, DOI: 10.1021/acsnano.6b00371.

[Liu08a] W.-T. Liu and Y. R. Shen, "Sum-frequency phonon spectroscopy on α-quartz", *Phys. Rev. B* 78 (2008), 024302, DOI: 10.1103/PhysRevB.78.024302.

[Liu08b] W.-T. Liu and Y. R. Shen, "Surface vibrational modes of α-quartz(0001) probed by sum-frequency spectroscopy", *Phys. Rev. Lett.* 101 (2008), 016101, DOI: 10.1103/PhysRevLett.101.016101.

[Liu14] W.-T. Liu and Y. R. Shen, "In situ sum-frequency vibrational spectroscopy of electrochemical interfaces with surface plasmon resonance", *Proc. Natl. Acad. Sci. USA* 111 (2014), 1293, DOI: 10.1073/pnas.1317290111.

[Lyd41] R. H. Lyddane, R. G. Sachs, and E. Teller, "On the Polar Vibrations of Alkali Halides", *Phys. Rev.* 59 (1941), 673, DOI: 10.1103/PhysRev.59.673.

[MIT15] MITEQ, Inc., *Fiber Optic Link, Model: LBL-50K4P5G*, 2015, URL: https://nardamiteq.com/docs/MITEQ-LBL-50K4P5G.PDF.

[Mad01] "Aluminum arsenide (AlAs) phonon dispersion, phonon wavenumbers and frequencies", *Landolt-Börnstein - Group IV Elements, IV-IV and III-V Compounds. Part a - Lattice Properties*, ed. by O. Madelung, U. Rössler, and M. Schulz, vol. 41A1α, Springer-Verlag Berlin Heidelberg, 2001, DOI: 10.1007/10551045_60.

[Mad71] J. M. J. Madey, "Stimulated Emission of Bremsstrahlung in a Periodic Magnetic Field", *J. Appl. Phys.* 42 (1971), 1906, DOI: 10.1063/1.1660466.

[Mai07] S. A. Maier, *Plasmonics: Fundamentals and Applications*, New York, NY: Springer, 2007, DOI: 10.1007/0-387-37825-1.

[Man72] W. M. Mansour, "Quenching of limit cycles of a Van der Pol oscillator", *J. Sound Vib.* 25 (1972), 395, DOI: 10.1016/0022-460X(72)90190-3.

[McG96] J. F. McGilp, "A review of optical second-harmonic and sum-frequency generation at surfaces and interfaces", *J. Phys. D: Appl. Phys.* 29 (1996), 1812, DOI: 10.1088/0022-3727/29/7/016.

[McN10] B. W. J. McNeil and N. R. Thompson, "X-ray free-electron lasers", *Nat. Photonics* 4 (2010), 814, DOI: 10.1038/nphoton.2010.239.

[Mil64] R. C. Miller, "Optical second harmonic generation in piezoelectric crystals", *Appl. Phys. Lett.* 5 (1964), 17, DOI: 10.1063/1.1754022.

[Mit15] M. Mittendorff, F. Wendler, E. Malic, A. Knorr, M. Orlita, M. Potemski, C. Berger, W. A. de Heer, H. Schneider, M. Helm, and S. Winnerl, "Carrier dynamics in Landau-quantized graphene featuring strong Auger scattering", *Nat. Phys.* 11 (2015), 75, DOI: 10.1038/nphys3164.

[Mor18] A. Morita, *Theory of Sum Frequency Generation Spectroscopy*, Singapore: Springer, 2018, DOI: 10.1007/978-981-13-1607-4.

[Mos68] L. P. Mosteller and F. Wooten, "Optical Properties and Reflectance of Uniaxial Absorbing Crystals", *J. Opt. Soc. Am.* 58 (1968), 511, DOI: 10.1364/JOSA.58.000511.

[Mur09] B. N. Murdin, "Far-infrared free-electron lasers and their applications", *Contemp. Phys.* 50 (2009), 391, DOI: 10.1080/00107510902733856.

[Mut99] H. Mutschke, A. Andersen, D. Clement, T. Henning, and G. Peiter, "Infrared properties of SiC particles", *Astron. Astrophys.* 345 (1999), 187, URL: http://aa.springer.de/papers/9345001/2300187/small.htm.

[Nak09] I. F. Nakai, M. Tachioka, A. Ugawa, T. Ueda, K. Watanabe, and Y. Matsumoto, "Molecular structure and carrier distributions at semiconductor/dielectric interfaces in organic field-effect transistors studied with sum frequency generation microscopy", *Appl. Phys. Lett.* 95 (2009), 243304, DOI: 10.1063/1.3275805.

[Nak97] S. Nakashima and H. Harima, "Raman Investigation of SiC Polytypes", *Phys. Status Solidi A* 162 (1997), 39, DOI: 10.1002/1521-396X(199707)162:1<39::AID-PSSA39>3.0.CO;2-L.

[Ney18] P. Neyman, J. Blau, K. Cohn, W. Colson, S. Gottschalk, and A. Todd, "Free Electron Lasers in 2017", *Proc. International Free Electron Laser Conference 2017* (2018), 204, DOI: 10.18429/jacow-fel2017-mop066.

[Nie99] S. Niedermeier, H. Schillinger, R. Sauerbrey, B. Adolph, and F. Bechstedt, "Second-harmonic generation in silicon carbide polytypes", *Appl. Phys. Lett.* 75 (1999), 618, DOI: 10.1063/1.124459.

[Nih09] S. Nihonyanagi, S. Yamaguchi, and T. Tahara, "Direct evidence for orientational flip-flop of water molecules at charged interfaces: A heterodyne-detected vibrational sum frequency generation study", *J. Chem. Phys.* 130 (2009), 204704, DOI: 10.1063/1.3135147.

[Oep95] D. Oepts, A. F. G. van der Meer, and P. van Amersfoort, "The Free-Electron-Laser user facility FELIX", *Infrared Phys. Technol.* 36 (1995), 297, DOI: 10.1016/1350-4495(94)00074-U.

[Ohn16] P. E. Ohno, S. A. Saslow, H.-f. Wang, F. M. Geiger, and K. B. Eisenthal, "Phase-referenced nonlinear spectroscopy of the α-quartz/water interface", *Nat. Commun.* 7 (2016), 13587, DOI: 10.1038/ncomms13587.

[One15] Onefive GmbH / NKT Photonics, *Femtosecond Laser, Model: Origami 10 HP*, 2015, URL: https://www.nktphotonics.com/wp-content/uploads/sites/3/2017/09/onefive-origami-hp.pdf?1574285565.

[Paa15] A. Paarmann, I. Razdolski, A. Melnikov, S. Gewinner, W. Schöllkopf, and M. Wolf, "Second harmonic generation spectroscopy in the Reststrahl band of SiC using an infrared free-electron laser", *Appl. Phys. Lett.* 107 (2015), 081101, DOI: 10.1063/1.4929358.

[Par98] "SiC Materials and Devices", ed. by Y. S. Park, vol. 52, Semiconductors and Semimetals, Burlington, MA: Academic Press, 1998, DOI: 10.1016/S0080-8784(08)62843-4.

[Pat68] L. Patrick, "Infrared Absorption in SiC Polytypes", *Phys. Rev.* 167 (1968), 809, DOI: 10.1103/PhysRev.167.809.

[Per19a] K. Persson, *Materials Data on AlAs (SG:216) by Materials Project*, 2019, DOI: 10.17188/1197136.

[Per19b] K. Persson, *Materials Data on SiC (SG:186) by Materials Project*, 2019, DOI: 10.17188/1188302.

[Per19c] K. Persson, *Materials Data on SiO2 (SG:154) by Materials Project*, 2019, DOI: 10.17188/1272701.

[Per93] A. Peremans, P. Guyot-Sionnest, A. Tadjeddine, F. Glotin, J.-M. Ortega, and R. Prazeres, "Sum-frequency generation at surfaces using an infrared FEL synchronized with a YAG laser", *Nucl. Instr. Meth. Phys. Res. A* 331 (1993), ABS28, DOI: 10.1016/0168-9002(93)90174-G.

[Pet18] G. Petretto, S. Dwaraknath, H. P. Miranda, D. Winston, M. Giantomassi, M. J. van Setten, X. Gonze, K. A. Persson, G. Hautier, and G.-M. Rignanese, "High-throughput density-functional perturbation theory phonons for inorganic materials", *Sci. Data* 5 (2018), 180065, DOI: 10.1038/sdata.2018.65.

[Rag11] V. Raghunathan, Y. Han, O. Korth, N.-H. Ge, and E. O. Potma, "Rapid vibrational imaging with sum frequency generation microscopy", *Opt. Lett.* 36 (2011), 3891, DOI: 10.1364/OL.36.003891.

[Raz16] I. Razdolski, Y. Chen, A. J. Giles, S. Gewinner, W. Schöllkopf, M. Hong, M. Wolf, V. Giannini, J. D. Caldwell, S. A. Maier, and A. Paarmann, "Resonant Enhancement of Second-Harmonic Generation in the Mid-Infrared Using Localized Surface Phonon Polaritons in Subdiffractional Nanostructures", *Nano Lett.* 16 (2016), 6954, DOI: 10.1021/acs.nanolett.6b03014.

[Rei73] J. A. Reissland, *The Physics of Phonons*, London: Wiley, 1973.

[Ric02] G. L. Richmond, "Molecular Bonding and Interactions at Aqueous Surfaces as Probed by Vibrational Sum Frequency Spectroscopy", *Chem. Rev.* 102 (2002), 2693, DOI: 10.1021/cr0006876.

[Rok03] S. Roke, A. W. Kleyn, and M. Bonn, "Time- vs. frequency-domain femtosecond surface sum frequency generation", *Chem. Phys. Lett.* 370 (2003), 227, DOI: 10.1016/S0009-2614(03)00085-X.

[Sak40] B. D. Saksena, "Analysis of the Raman and infra-red spectra of α-quartz", *Proc. Ind. Acad. Sci.* A12 (1940), 93, URL: https://www.ias.ac.in/article/fulltext/seca/012/01/0093-0139.

[Sat09] H. Sato, M. Abe, I. Shoji, J. Suda, and T. Kondo, "Accurate measurements of second-order nonlinear optical coefficients of 6H and 4H silicon carbide", *J. Opt. Soc. Am. B* 26 (2009), 1892, DOI: 10.1364/JOSAB.26.001892.

[Sch00] M. Schubert, T. E. Tiwald, and C. M. Herzinger, "Infrared dielectric anisotropy and phonon modes of sapphire", *Phys. Rev. B* 61 (2000), 8187, DOI: 10.1103/PhysRevB.61.8187.

[Sch03] T. R. Schibli, J. Kim, O. Kuzucu, J. T. Gopinath, S. N. Tandon, G. S. Petrich, L. A. Kolodziejski, J. G. Fujimoto, E. P. Ippen, and F. X. Kärtner, "Attosecond active synchronization of passively mode-locked lasers by balanced cross correlation", *Opt. Lett.* 28 (2003), 947, DOI: 10.1364/OL.28.000947.

[Sch14] P. Schmüser, M. Dohlus, J. Rossbach, and C. Behrens, *Free-Electron Lasers in the Ultraviolet and X-Ray Regime*, Cham: Springer, 2014, DOI: 10.1007/978-3-319-04081-3.

[Sch15a] W. Schöllkopf, S. Gewinner, H. Junkes, A. Paarmann, G. v. Helden, H. P. Bluem, and A. M. M. Todd, "The new IR and THz FEL facility at the Fritz Haber Institute in Berlin", *Proc. SPIE* 9512 (2015), 95121L, DOI: 10.1117/12.2182284.

[Sch15b] S. Schulz, I. Grguras, C. Behrens, H. Bromberger, J. T. Costello, M. K. Czwalinna, M. Felber, M. C. Hoffmann, M. Ilchen, H. Y. Liu, T. Mazza, M. Meyer, S. Pfeiffer, P. Predki, S. Schefer, C. Schmidt, U. Wegner, H. Schlarb, and A. L. Cavalieri, "Femtosecond all-optical synchronization of an X-ray free-electron laser", *Nat. Commun.* 6 (2015), 5938, DOI: 10.1038/ncomms6938.

[Sch16] T. Schietinger, M. Pedrozzi, M. Aiba, V. Arsov, S. Bettoni, B. Beutner, M. Calvi, P. Craievich, M. Dehler, F. Frei, R. Ganter, C. P. Hauri, R. Ischebeck, Y. Ivanisenko, M. Janousch, M. Kaiser, B. Keil, F. Löhl, G. L. Orlandi, C. Ozkan Loch, et al., "Commissioning experience and beam physics measurements at the SwissFEL Injector Test Facility", *Phys. Rev. Accel. Beams* 19 (2016), 100702, DOI: 10.1103/PhysRevAccelBeams.19.100702.

[She16] Y. R. Shen, *Fundamentals of Sum-Frequency Spectroscopy*, Cambridge: Cambridge University Press, 2016, DOI: 10.1017/CBO9781316162613.

[She89] Y. R. Shen, "Surface properties probed by second-harmonic and sum-frequency generation", *Nature* 337 (1989), 519, DOI: 10.1038/337519a0.

[Spi61] W. G. Spitzer and D. A. Kleinman, "Infrared Lattice Bands of Quartz", *Phys. Rev.* 121 (1961), 1324, DOI: 10.1103/PhysRev.121.1324.

[Tam18] M. Tamagnone, A. Ambrosio, K. Chaudhary, L. A. Jauregui, P. Kim, W. L. Wilson, and F. Capasso, "Ultra-confined mid-infrared resonant phonon polaritons in van der Waals nanostructures", *Sci. Adv.* 4 (2018), eaat7189, DOI: 10.1126/sciadv.aat7189.

[Tha18] M. Thaemer, R. K. Campen, and M. Wolf, "Detecting weak signals from interfaces by high accuracy phase-resolved SFG spectroscopy", *Phys. Chem. Chem. Phys.* 20 (2018), 25875, DOI: 10.1039/C8CP04239J.

[Ueb97] H. Ueba, "Vibrational relaxation and pump-probe spectroscopies of adsorbates on solid surfaces", *Prog. Surf. Sci.* 55 (1997), 115, DOI: 10.1016/S0079-6816(97)00021-X.

[Val94] F. Vallee, "Time-resolved investigation of coherent LO-phonon relaxation in III-V semiconductors", *Phys. Rev. B* 49 (1994), 2460, DOI: 10.1103/PhysRevB.49.2460.

[Vid05] F. Vidal and A. Tadjeddine, "Sum-frequency generation spectroscopy of interfaces", *Rep. Prog. Phys.* 68 (2005), 1095, DOI: 10.1088/0034-4885/68/5/r03.

[Wan12] X. Wang, T. Nakajima, H. Zen, T. Kii, and H. Ohgaki, "Single-shot spectra of temporally selected micropulses from a mid-infrared free-electron laser by upconversion", *Opt. Lett.* 37 (2012), 5148, DOI: 10.1364/OL.37.005148.

[Wan13] S. Wang, M. Zhan, G. Wang, H. Xuan, W. Zhang, C. Liu, C. Xu, Y. Liu, Z. Wei, and X. Chen, "4H-SiC: a new nonlinear material for midinfrared lasers", *Laser Photonics Rev.* 7 (2013), 831, DOI: 10.1002/lpor.201300068.

[Wel00] J.-P. R. Wells, C. W. Rella, I. V. Bradley, I. Galbraith, and C. R. Pidgeon, "Coherent Dynamics of the Localized Vibrational Modes of Hydrogen in CaF_2", *Phys. Rev. Lett.* 84 (2000), 4998, DOI: 10.1103/PhysRevLett.84.4998.

[Win18] C. J. Winta, S. Gewinner, W. Schöllkopf, M. Wolf, and A. Paarmann, "Second-harmonic phonon spectroscopy of α-quartz", *Phys. Rev. B* 97 (2018), 094108, DOI: 10.1103/PhysRevB.97.094108.

[Zha19] Y. Zhang, D. Huang, Y. Shan, T. Jiang, Z. Zhang, K. Liu, L. Shi, J. Cheng, J. E. Sipe, W.-T. Liu, and S. Wu, "Doping-Induced Second-Harmonic Generation in Centrosymmetric Graphene from Quadrupole Response", *Phys. Rev. Lett.* 122 (2019), 047401, DOI: 10.1103/PhysRevLett.122.047401.

[Zho93] H. Zhong, Z. H. Levine, D. C. Allan, and J. W. Wilkins, "Band-theoretic calculations of the optical-activity tensor of α-quartz and trigonal Se", *Phys. Rev. B* 48 (1993), 1384, DOI: 10.1103/PhysRevB.48.1384.

[Zor15] S. Zorzut, M. Cargnelutti, and S. Hunziker, "Influence of Environment Changes on Libera Sync 3 Long-Term Stability", *Proc. International Free Electron Laser Conference 2015* (2015), 126, DOI: 10.18429/JACoW-FEL2015-MOP043.

Academic Curriculum Vitae

For reasons of data protection, the academic curriculum vitae is not included in the electronic version.

Acknowledgements

Before concluding the thesis, I would like to thank the numerous persons who made this project possible.

First of all, Prof. Martin Wolf as supervisor, providing me the opportunity to do my PhD studies in his department at the Fritz Haber Institute for about four years. I appreciate his efforts to create a scientifically and technically sound working environment.

In particular, Alex Paarmann for guiding the overall project with best possible care. I am grateful for his support, always taking the necessary time for discussions. Also, I acknowledge the possibility to persue my own research ideas.

I kindly thank Prof. Joachim Heberle from FU Berlin for taking the responsibility as the second thesis supervisor.

Importantly, I want to express my gratitude for scientific collaborations and exchange with various people. Namely, Bill Colson for his interest and support in the theoretical modelling of the FEL emission, as well as Prof. Josh Caldwell and Alex Giles, also from the United States, for providing the nanostructure samples. From the FHI, I thank Yujin Tong, for his practical experience in SFG spectroscopy, Prof. Kramer Campen, for the helpful comments on the time-domain measurements and Prof. Karsten Horn for his insights into the group-theoretical analysis of vibrational modes.

Without the reliable operation of the FHI FEL by Sandy Gewinner and Wieland Schöllkopf, the many beamtimes would not have been possible. Thanks also to Thomas Zehentbauer due to his electrical engineering competence and Heinz Junkes as programming expert required in the initial setup of the synchronization architecture. Wiebke Frandsen is acknowledged for realization of the SEM images.

Further, I thank the current and former members of the lattice dynamics group and colleagues in the 'Fermi' office, Nikolai, Chris, Marcel, Ilya and Christian, for the nice time and cooperative spirit we shared. Moreover, it has been a pleasure to organize the 'Fritz Sessions', together with Florian, Marcel, Max, Lorenz and Chris, inviting Prof. Johan Rockström to the Harnack House and discussing about the climate, a scientific topic of major relevance for society. Also, thanks to Alex for raising the awareness for sustainability within the institute.

I am thankful to my family for their continuous support throughout the PhD time.

Last but not least, I have to thank Prof. Jure Demsar for sparking my interest in ultrafast phenomena and the solid training in time-resolved and nonlinear spectroscopy.

Selbstständigkeitserklärung

Sämtliche verwendete Hilfsmittel, Hilfen und Quellen sind an der entsprechenden Stelle angegeben. Ich versichere, dass ich die Arbeit auf dieser Grundlage selbstständig verfasst habe. Diese Arbeit wurde bisher weder in gleicher noch ähnlicher Form einer anderen Prüfungskommission vorgelegt oder veröffentlicht.

Berlin, 18.11.2019

Riko Kießling